2020

Remote sensing of energetic electron precipitation

BOSTON UNIVERSITY

COLLEGE OF ENGINEERING

Dissertation

REMOTE SENSING OF ENERGETIC ELECTRON PRECIPITATION

by

NITHIN SIVADAS

B.Tech, Indian Institute of Technology Madras, 2013
M.Tech, Indian Institute of Technology Madras, 2013

Submitted in partial fulfillment of the

requirements for the degree of

Doctor of Philosophy

2020

Approved by

First Reader _____

Joshua L. Semeter, Ph.D.
Professor of Electrical and Computer Engineering

Second Reader _____

Meers M. Oppenheim, Ph.D.
Professor of Astronomy
Professor of Electrical and Computer Engineering

Third Reader _____

Min-Chang Lee, Ph.D.
Professor of Electrical and Computer Engineering

Fourth Reader _____

Yukitoshi Nishimura, Ph.D.
Research Associate Professor of
Electrical and Computer Engineering

Fifth Reader _____

Marilia Samara, Ph.D.
Research Astrophysicist
NASA Goddard Space Flight Center

"The true delight is in the finding out

rather than in the knowing"

Isaac Asimov

Acknowledgments

This Ph.D. dissertation is a result of several years of work sponsored by the Dean's Fellowship from Boston Univesity's College of Engineering, the NASA and Earth Space Science Fellowship, and the Air Force Office of Scientific Research.

Over the years, I was mentored by several astounding scientists who paved the path to my Ph.D. program at Boston University. I am deeply grateful to Dr. P. Sreekumar, Dr. Manju Sudhakar, and Dr. Umesh Kadhane. They saw in me potential when it was hard for many others and facilitated my pursuit of developing a nano-satellite program at the Indian Institute of Technology Madras. My introduction to my advisor Prof. Joshua Semeter would not have been possible without the generosity of Prof. Abas Sivjee, who went out of his way to bring me to the CEDAR 2013 Workshop in Boulder. There, I was lucky to have met two more exceptional scientists who would play important roles in my Ph.D. career - Dr. Sunanda Basu and Dr. Marilia Samara. Their advice on professional and moral decisions have made me a better scientist and a better human. Before beginning my Ph.D., I was fortunate to have met Dr. Upendra Desai and Hansa Desai. They had a long history of working at NASA Goddard Space Flight Center, and their friendship allowed me to observe the past and have a deeper appreciation of life.

My Ph.D. would not have started, nor made the contributions it has, without the mentorship of my advisor Prof. Josh Semeter. His faith in me as an incoming graduate student and the intellectual freedom he sustained in his laboratory were essential to my flourishing and well-being. The freedom and financial security directly contributed to my ability to explore uncharted territories in space physics, build and expand my network of colleagues, and develop a broader understanding of the near-Earth space system. I am incredibly grateful for his mentorship.

This document would not exist without the tireless guidance of Dr. Yukitoshi Nishimura. His in-depth and precise knowledge of space physics, the clarity of his explanations, and his infinite patience contributed towards my growth as a scientist. Toshi was a prominent causal factor of many of my achievements as a graduate student. Prof. Meers Oppenheim was another major influencer, whose space physics and plasma physics classes formed some of my core perspectives on doing research and presenting science. His willingness to provide honest and open feedback to his students contributed significantly to my development. I am also grateful to Prof. Min-Chang Lee for being available and agreeing to evaluate my work throughout my Ph.D.

I have been lucky to have mentors from the Coupling, Energetics, and Dynamics of Atmospheric Regions (CEDAR) and Geospace Environmental Modeling community, who have gone out of their way to expand my network. Marilia and Robert Michell have given a lot of their time and energy to bring me in contact with their colleagues in NASA, and the broader scientific community, in the interest of maximizing the value of my career and future contributions. I am incredibly grateful to Roger Varney for believing in me and investing his time in recommending me to the CEDAR Science Steering Committee. Without the two months at SRI International with him and learning the details of Incoherent Scatter Radar theory, my Ph.D. would not have been as fruitful. I am also grateful to Joe Borovsky, Larry Lyons, Robert Marshall, and David Sibeck, who helped me develop my ideas, improve my proposals, and directed me toward pursuing worthwhile projects. I also benefitted from the wise and kind Susan Nossal, and her encouragement, which allowed me to stay the course.

Through my experience representing students in the CEDAR Science Steering

Committee, I was grateful to have the company of my good friend and excellent colleague, Meghan Burleigh. Without her mentorship and support and Lindsay Goodwin's experience and positivity, I would not have been able to make the contributions I have. In the committee, I met Katrina Bossert, whose constant support, moral clarity, and scientific insights have kept me steady in my path towards being a better scientist. Similarly, the conversations and time Ying Zou gave me, through my last few years at Boston University, have helped me stay on the right path. And I am incredibly grateful to have them as my colleagues and friends.

On the other side of the Atlantic, I am very grateful to have colleagues who have helped me learn a diverse array of space physics topics. Stein Haaland, Noora Parthemis, and my cohort of students in the Polar magnetosphere substorms class in University Center in Svalbard (UNIS) - Justin Tonti-Filippini, Katie Herlingshaw, Anders Lindanger, Andreas Kvammen, Zoe Strimbeck Bazilchuck, and Erkka Heino. I am thankful for their continued support, and the enriching two months I have had with them in Svalbard. I am also grateful to Antti Kerro for his collaboration and opening the doors to build connections with the community of space physicists in Finland. I have been fortunate to work with the International Space Science Institute, Bern, during my Ph.D., which has allowed me to expand my horizons within Space Physics. In Bern, I am grateful to have Stein Haaland and Irmela Schweizer, whose mentorship and parenting are priceless, and have been an essential factor in keeping my spirits high through the last stages of my Ph.D.

I would not have been able to build this network of colleagues and friends and attain funding for travel and research, without the constant effort and support of Erin Reynolds, Mary Gordon, Thomas O'Connor from BU's Center for Space

Physics and Christine Ritzkowski from BU's Department of Electrical and Computer Engineering. They made all the challenging bureaucracy simpler. I realize that having the support of such excellent administrative staff is rare, and I am incredibly grateful for their presence. In Josh's lab, I was fortunate to work with Sebastijan Mrak, an excellent engineer and scientist, with whom I have had productive space physics discussions and collaborations.

As an international student, living in the United States under the current political climate is a challenge. Still, through career and personal stresses, I have always had Luisa Capannolo by my side. Having an excellent scientist such as her to discuss my work, and support me as a good friend and colleague, was a privilege for which I will always be grateful. I am also extremely thankful to my friends in Boston, whom I care for very much, and who have supported me through many of my personal and professional challenges over the years: Annie Bernard, Nehal Odedra, Ashkan Ghanbarzadeh-Dagheyan, Marcia Sahayalouis, Michael Obrien, and David Lloyd.

I am incredibly grateful to Chhavi Goenka, who has been there for me from my first day in Boston, who made Boston a home for me and made sure I felt safe and happy here. I have been lucky to receive the care and compassion from my other friends in Boston: Archana Balachandran, Maria Varghese, Ramesh Krishnan, Karthika Sankar, and Nithin Varma. I am also indebted to my friends around the world who have generously offered me their homes to stay during my travels, long and deep conversations, and given me their love and support regularly through the years: Prasanth Prahladan, Athreya Shankar, Nick Nardelli, Neesha R Schenpf, Jade Reidy, Dolon Battacharya, Jonathon Smith, Banfshe Ferdousi, Robert Irvin, Maxime Grandin, Maria-Theresia Walach, Florine Enengl, Poorya Hosseini,

Ananth Saran, and Vivek Bagaria. I am also extremely grateful to have Varsha Subramanyan, Girish Ananth, and Shameer Muhammed, as constants in my undergraduate life and continue to be my closest friends. Their presence pulled me through difficult times and allowed me to focus on this dissertation again.

In the last leg of my dissertation writing, where the vast and open beauty of space and time is not within view, I found that the intellectual air can get very thin. And in this time, I was lucky to have met Zach Beever, who reminded me of the beauty and depth of fundamental physics and mathematics through his curiosity and rigor. My parallel work with Oxford's Future of Humanity Institute on civilizational collapse introduced me to a vibrant research culture, with empathetic and intelligent individuals whose positivity and curiosity diffused into making the challenges of preparing for a Ph.D. defense a pleasurable exercise.

Ultimately, all of my pursuits were possible only because of my parents, Sivadasan P V and Lalitha S, who were my best friends from my childhood. They made sure to let me be free and uncontained and to explore where my mind takes me. They have been part of my journey throughout these years, and they continue to support me emotionally. Their patience and love have brought me so far, and I am grateful that I can share this journey with them.

REMOTE SENSING OF ENERGETIC ELECTRON PRECIPITATION

NITHIN SIVADAS

Boston University, College of Engineering, 2020

Major Professor: Joshua L. Semeter, Ph.D., Professor of Electrical and Computer Engineering

ABSTRACT

Charged particles trapped in Earth's magnetic fields slam or precipitate into the atmosphere during geomagnetic disturbances in the Near-Earth space environment. The particles ionize, excite, and heat the neutral gas, leading to the optical aurora. Below the peak of optical auroral emissions is the ionospheric D-region extending from 70–90 km. Here, in the night time, D-region ionization occurs mainly due to sub-relativistic (100–500 keV) and relativistic ($\sim$>500 keV) electron precipitation causing Ultraviolet, X-ray, and faint optical emissions. We can also detect its presence through electron density measurements from Incoherent Scatter Radars. Though the magnetospheric source regions of the precipitation are broadly known, a more constrained estimate of the location and mechanism is needed, especially during magnetic activity. Energetic electron precipitation is also known to cause changes in the upper atmospheric chemistry, increase in ionospheric conductance, and attenuation of radio signals in high-latitude regions. However, a quantitative estimate of these effects has been challenging to obtain due to sparse measurements.

This dissertation introduces techniques to measure energetic electron precipitation and its associated auroral forms in the ionosphere, and methods to constrain

its sources during magnetically active periods such as substorms. We primarily address the following questions: 1) What are the magnetospheric source regions of energetic electron precipitation observed during substorms? 2) What is the effect of these particles on the atmosphere?

By synthesizing measurements from Incoherent Scatter Radars, ground-based optical cameras, and satellites, we identify the two main sources of energetic precipitation during substorms: the near-Earth plasma sheet and the outer radiation belt boundary. The plasma sheet is a thin sheet-like region with a relatively high plasma density, close to the magnetic equatorial plane, between the dipolar field region and the stretched magnetotail. The outer radiation belts are regions of trapped high energy charged particles in the dipolar fields ranging from $\sim$3 to $\sim$10 R_E. For the first time, we identified the existence of the outer radiation belt boundary's auroral signature, which is present in at least 40% of strong substorms.These energetic electrons also cause the majority of the high-latitude ionosphere's peak Hall conductance during substorms.

The source regions of energetic electron precipitation explored in this dissertation lie in the nightside dipolar transition region - a relatively unexplored part of the magnetosphere. This work will be useful for future explorations of this region, especially for new missions such as the Transition Region Explorer (TREX). The remote sensing effort presented in this dissertation enhances the community's understanding of multi-scale processes that meet the scope of NASA's Heliophysics System observatory. This dissertation provides an extensive background of energetic particle precipitation and its role in the magnetosphere-ionosphere system and a detailed discussion on remote-sensing techniques to constrain precipitation sources using magnetically conjugate measurements.

CONTENTS

LIST OF TABLES

LIST OF FIGURES

LIST OF ABBREVIATIONS

AA .. Auroral Absorption

AAR . Auroral Acceleration Region

AEP .. Auroral Electron Precipitation

BBF .. Bursty Bulk Flows

CD .. Current Disruption

DASC . Digital All-Sky Camera

EAEP . Energetic Auroral Electron Precipitation

EEP .. Energetic Electron Precipitation

EFI .. Electric Field Instrument

e-IB .. Electron Isotropic Boundary

ELF .. Extra Low Frequency

EMIC . Electromagnetic Ion Cyclotron Waves

FGM . Flux Gate Magnetometer

GEO . Geostationary Orbit

GSM . Geocentric Solar Magnetospheric Coordinate Systemă

IGRF . International Geomagnetic Reference Field

IMF .. Interplanetary Magnetic Field

ISR .. Incoherent Scatter Radar

LEO .. Low Earth Orbit

LLBL . Low Latitutde Boundary Layer

MEPED Medium Energy Proton and ElectronăDetector

MI .. Magnetosphere-Ionosphere

MLAT . Magnetic Latitude

MLON Magnetic Longitude

MLT .. Magnetic Local Time

MR .. Magnetic Reconnection

NENL . Near Earth Neutral Line

NOAA National Oceanic and Atmospheric Administration

ORBB . Outer Radiation Belt Boundary

PAD .. Pitch Angle Distribution

PCA .. Polar Cap Absorption

PFISR . Poker Flat Incoherent Scatter Radar

POES . Polar Orbiting Environmental Satellite

REP .. Relativistic Electron Precipitation

SCA .. Sudden Commencement Absorption

SCW . Substorm Current Wedge

SDA .. Structured Diffuse Aurora

SEP .. Subrelativistic Electron Precipitation

T89 .. Tsyganenko 1989

T96 .. Tsyganenko 1996

THEMIS Time-History of Events & Macroscale-Interactions Spacecraft

TREX . Transition Region EXplorer

ULF .. Ultra Low Frequency

UV .. Ultraviolet

VLF .. Very Low Frequency

WTS . Westward Traveling Surge

CHAPTER 1

Introduction

The nearest astronomical body to our planet is the Moon, orbiting at an average distance of 60 earth radii (R_E) from the Earth. The intervening space between these bodies look deceptively empty. With an average ion density of only $\sim 10^7$ ions per cubic meter, the whole of the Earth's magnetosphere weighs less than a few tonnes. However, this is vastly more dense than the typical region in the universe - the intergalactic space, which is a mere $\sim$1 ion per cubic meter.

The near-Earth space is teaming with ions and electrons, whizzing around in the geomagnetic field. The plasma dynamics in this region lead to a zoo of phenomena. Although the total mass of the magnetosphere is small, the particle populations contain kinetic energy akin to a small nuclear bomb ($6 \times 10^{15} J$) (Dessler & Vestine, 1960). This may sound like a lot, but the amount of radiant solar energy input upon the Earth in one second is about 1.75×10^{17} J, which is two orders of magnitude higher than the total kinetic energy of these trapped particles. The most energetic charged particles reside in the radiation belts, a region in the magnetosphere roughly between 1.5-10 R_E. Further out, a region of stretched magnetic field lines contains higher density and lower energy particles - called the plasma sheet (See Figure 1.1).

These particles remain in trapped orbits around the Earth and within the magnetic field, as long as the temporal and spatial changes in the fields are not higher than the time-scales and spatial-scales of the particle's motion. Since the Earth's field is embedded in the solar magnetic field, it responds to plasma and magnetic fields escaping the sun - which is known as the solar wind. The interaction of

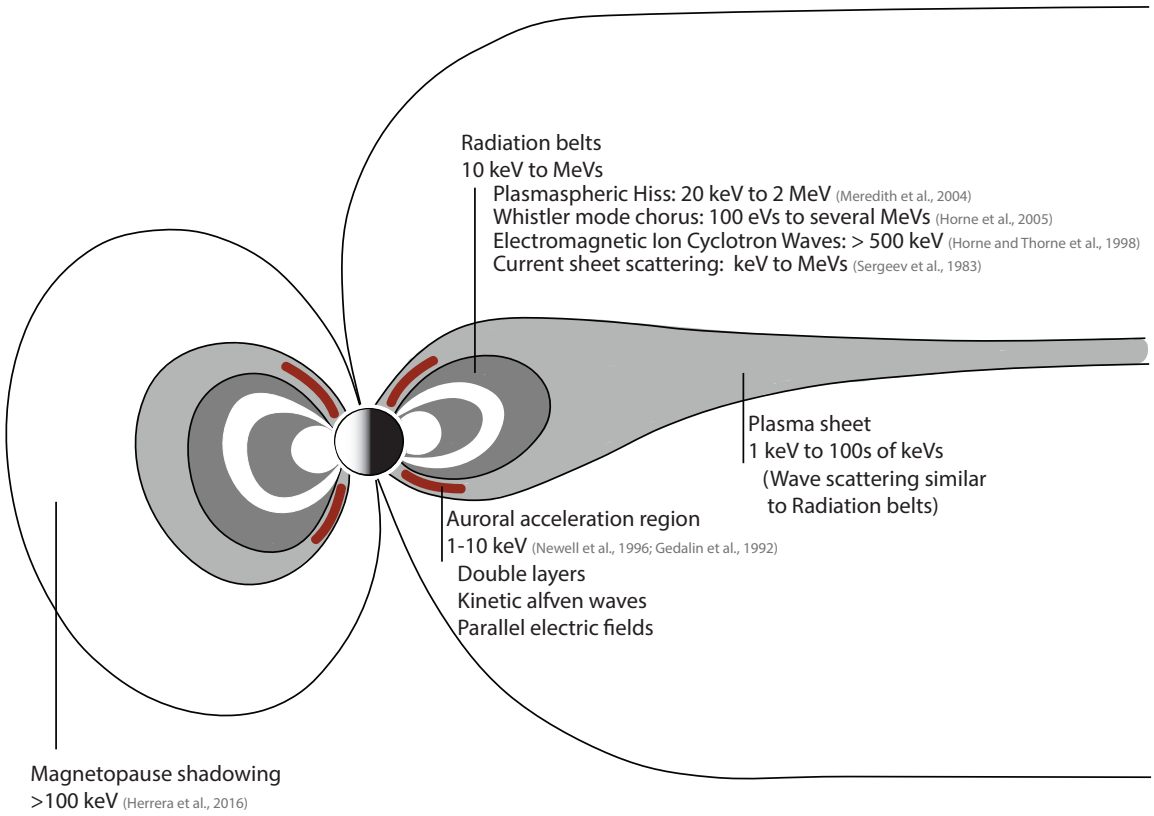

Figure 1.1: Known source regions and mechanisms of electron precipitation. (Lam et al., 2010; Herrera et al., 2016; Meredith et al., 2004; Horne et al., 2005; Horne & Thorne, 1998; Newell et al., 1996; Gedalin & Peter, 1992; Sergeev et al., 1983)

the Earth's magnetic field with the solar wind can result in a global change in the Earth's field configuration with accompanied release of energy into the charged particles within the magnetic field. Such disturbances, that includes temporally changing magnetic fields, spatial gradients in fields, and electromagnetic waves that interact with the particles, can cause the particles to be knocked out of their stable trajectories. Many of these particles make it down to the Earth's ionosphere in the polar regions, and cause spectacular visible emissions - known as the aurora.

1.1 The Problem

Scientists have come a long way in understanding the structure and dynamics of the near-Earth space environment. However, the interactions and coupling between the several distinct plasma populations and electromagnetic phenomena are an active area of research. Due to the system's complexity, a plethora of interesting phenomena lurks within data collected from the beginning of the space age. One plasma population that connects the Earth's magnetosphere to the ionosphere is the energetic particles ($>$ 10 keV electrons and $>$ 1 MeV protons). Their precipitation can produce optical, UV, and X-ray emissions in the atmosphere.

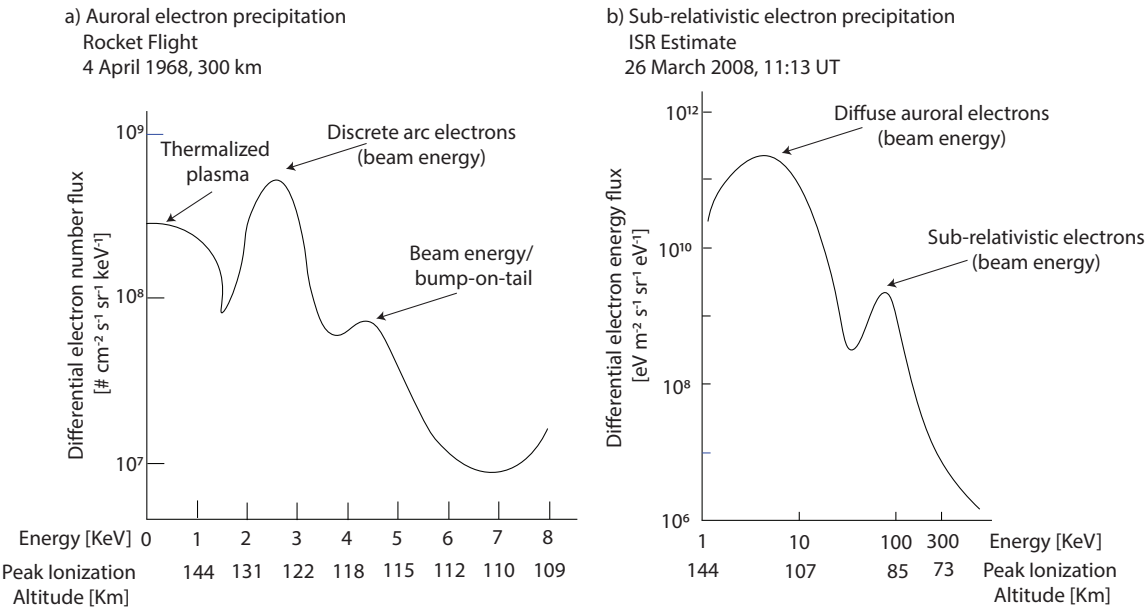

Figure 1.2: Typical energy spectra of precipitating electrons during a) substorm onset discrete arcs (Rees, 1969, adapted from figure 7a), and b) structured diffuse auroral during the growth phase of a substorm (Adapted from figure 6.8).

In this dissertation, we focus primarily on precipitating electrons and consider protons only occasionally. Therefore any mention of precipitation is that of elec-

trons unless specified. Figure 1.2 shows the type of energy spectra of precipitating electrons that we are concerned within this dissertation. By particle energy, we mean its kinetic energy. Thermalized plasma, for which we can define an equilibrium temperature, usually has an energy of tens of eV. However, charged particles that cause the aurora or ionize the atmosphere are mostly particle beams with kinetic energy aligned along the magnetic field line. They are not in equilibrium with the thermalized plasma. The higher the energy of a beam of particles, they cause deeper ionization of the atmosphere (See the peak ionization altitudes in figure 1.2). The canonical spectra shown in figure 1.2 were observed in the ionosphere using rocket flights, and incoherent scatter radars, respectively.

There are several reasons to be interested in this plasma population and its precipitation from the magnetosphere into the ionosphere. Firstly, prolonged exposure to these particles is potentially harmful to spacecraft and humans. The global economy currently depends heavily on the uninterrupted functioning of our satellite fleets – and will suffer substantial losses from space-weather related disruptions until our predictive abilities improve. Recent studies have shown that precipitation of these energetic particles into the ionosphere can cause a cascade of chemical reactions, which results in the loss of ozone in the mesosphere and stratosphere in the polar regions. Apart from this atmospheric effect, energetic particles interacting with the ionosphere can alter its conductivity, thereby affecting the current systems flowing through the ionosphere. Global ionospheric conductance affects the electrical coupling between the magnetosphere and ionosphere systems. Finally, increased energetic particle precipitation can lead to increased radio absorption, causing disturbances in high-frequency communications over the polar regions. Figure 1.3 shows the different altitude layers of the ionosphere, the typ-

ical electron density during the night and day during a solar minimum, and the types of radiation that dominates the cause of ionization in different layers, and the altitude dependence of predominant auroral emission spectra.

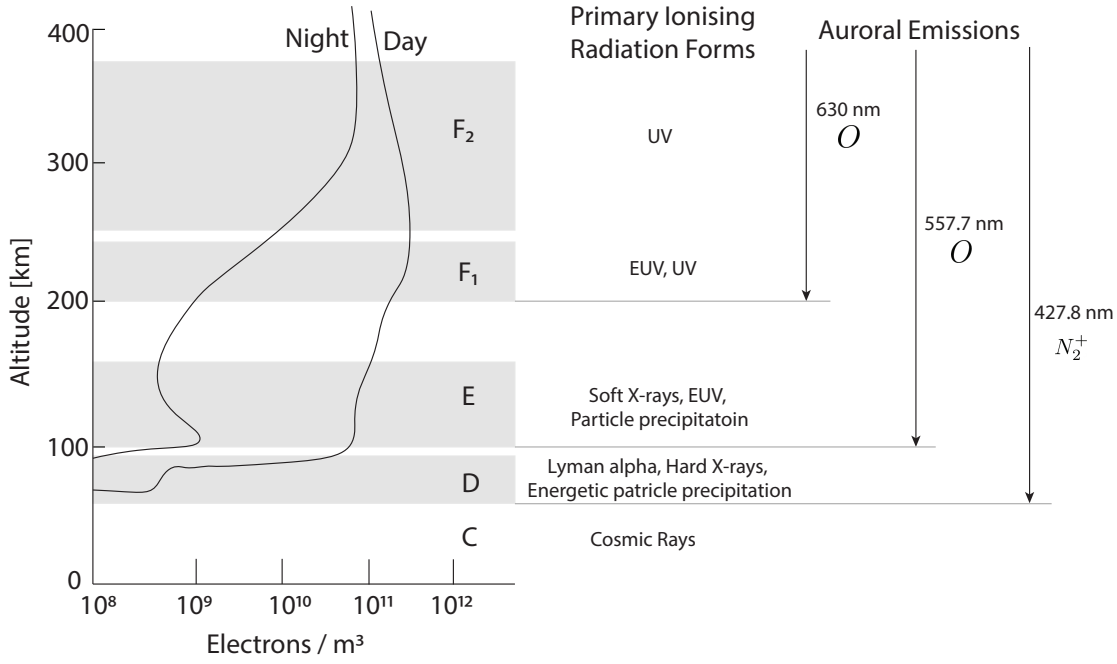

Figure 1.3: Typical ionosphere electron density during the night and day time, primary sources of ionization in different layers, and approximate altitude dependence of auroral emission spectra.

The first step to estimate the effect of energetic particles in Low Earth Orbit and the polar atmosphere is to characterize the source of these particles. Which region in the magnetosphere do these particles originate? What are the mechanisms acting on them? The next step would be to quantify the effects of precipitation. And finally, construct a model that takes into account all the magnetospheric sources of these particles and predict the precipitating particle flux, energy, and type at any given point on the Earth. At this moment in time, the knowledge or data we possess on the MI system is insufficient to develop such a model. In this dissertation,

we address the first step towards this ambitious goal, which are expanded below in the form of specific questions:

1. What are the magnetospheric source regions of precipitating energetic charged particles, especially during substorms?

2. What is the contribution of different acceleration mechanisms on energizing these particles?

3. What is the morphology and dynamics of precipitating energetic particles?

4. What are the effects of these particles on the ionosphere?

Figure 1.1 shows the most commonly known source mechanisms and regions for energetic electron precipitation. In this project, we address the source regions of energetic precipitation in more detail than what is represented in figure 1.1 for specific events. By studying particular energetic precipitation events observed by multiple instruments during magnetically active periods, we narrow down on the origin of precipitation for that specific event. We mainly limit our study to energetic electrons, and ignore the ions, as electrons make up a higher share of total precipitating flux than ions. Additionally, it narrows the scope of this study and makes it feasible. In this dissertation, we also explore methods to combine measurements from ground- and space-based sensors to demonstrate the simplest ways to constrain the source location and mechanism of these particles, even when the magnetosphere is highly dynamic. We develop methods to use incoherent scatter radar measurements as a remote atmospheric sensor to measure precipitating particle energies. We combine all these measurements with optical all-sky camera images to relate auroral observations to energetic precipitation and identify novel auroral structures with their magnetospheric sources.

Our analysis of one event revealed two main findings. a) The source of energetic precipitation during a substorm onset originated tailward of 9 R_E in the plasma sheet. b) A faint, structured aurora is associated with energetic precipitation from the outer boundary of the radiation belt before a substorm's onset. Analyzing multiple such events show that energetic precipitation from these sources accompanies strong substorms frequently. And that during magnetically active periods, energetic precipitation contributes substantially to ionospheric conductance.

1.2 Terminology

Due to the interdisciplinary nature of this work, before summarizing its key contributions, we define below the commonly used terms in the thesis for the benefit of the reader.

Magnetosphere: The region of space surrounding an astronomical body (in our case the Earth), in which charged particles are affected by the object's magnetic field. The source of the magnetic field is usually an internal dynamo.

Magnetic reconnection: A process by which the magnetic topology changes in highly conducting plasmas, resulting in the conversion of magnetic energy into kinetic energy of charged particles.

Plasma sheet: A sheet-like region in the Earth's magnetosphere, between the dipolar field regions and the magnetotail, near the equatorial plane, between the north and south magnetic lobes. The density of the charged particles are higher than in the lobes.

Radiation belts: Energetic electrons and protons trapped withing the Earth's dipole-like field lines and extending from 1.5 R_E to 10–15 R_E and overlapping with cold plasma.

Auroral acceleration region (AAR): A region between 0.5–2 R_E, on magnetic field lines conjugate with auroral latitudes, where quasi-static acceleration of charged particles occur through electrostatic potentials or other mechanisms.

Energetic electron precipitation (EEP): Electrons of energies $>$30 keV from the magnetosphere that are lost into the atmosphere. In the literature, some authors use different definitions based on their focus, mostly they range anywhere between 10 keV – 1 MeV.

Auroral electron precipitation (AEP): Electron precipitation of energies 1–10 keV, as these predominantly cause the visible aurora.

Energetic auroral electron precipitation (EAEP): Electron precipitation of energies 10–100 keV, as these energies are mostly energized and scattered by processes within the auroral acceleration region and the intervening space between the ionosphere and the plasma sheet. The upper energy limit of EAEP is limited by the maximum energization in the auroral acceleration region, which is in turn limited by the maximum polar cap potential that reaches up to $\sim$ 100 kV.

Sub-relativistic electron precipitation (SEP): Electron precipitation of energies 100–500 keV, as these are below the rest mass of an electron (~ 511 keV).

Relativistic electron precipitation (REP): Electron precipitation of energies $>$500 keV, as these are close to or above the rest mass of the electron.

Magnetic field aligned: Terminology used to refer to two or more points along a magnetic field line.

Magnetically conjugate: When two points are along or close to the same magnetic field lines, they are said to be magnetically conjugate.

D-region Ionosphere: The region of the ionosphere extending from 70 - 90 kms, the lowest region of the ionosphere with the highest concentration of neutrals.

Ionospheric conductance: The total integrated conductivity of the ionosphere, defined by the ion and electron mobility within the region. Usually, ionospheric conductance is separated into three parts. Conductance along the field line (Parallel conductance), conductance perpendicular the the field line and the horizontal electric field (Hall conductance), conductance perpendicular to the field line and parallel to the horizontal electric field (Pedersen conductance).

Incoherent Scatter Radar: ISRs are powerful ground-based radar systems that can measure various properties of the ionized part of the ionosphere, by using back-scattered radio waves from free electrons which are usually strongly influenced by the ions. ISRs can measure electron and ion number density, temperature and velocities (Sulzer, 2015).

In this dissertation, we use the Advanced Modular ISRs (AMISR). They are electronically steerable phased-array ISRs, one operational at Poker Flat, Alaska, and two at Resolute Bay, Canada (Nicolls, 2015). A standard AMISR face uses 128 panels, with each panel containing 32 antenna element unites (see figure 1.4). The electronically formed radar beam has a $\sim 1.1^{\circ}$ beamwidth and is steerable on a pulse-to-pulse basis over ten thousand preset locations within the field of view

of the radar. One such beam configuration used in chapter 4 and 5 is shown in figure 1.4 b-c. The AMISR system can discern small-scale spatial variability, and it provides the spatial context that is critical for this work.

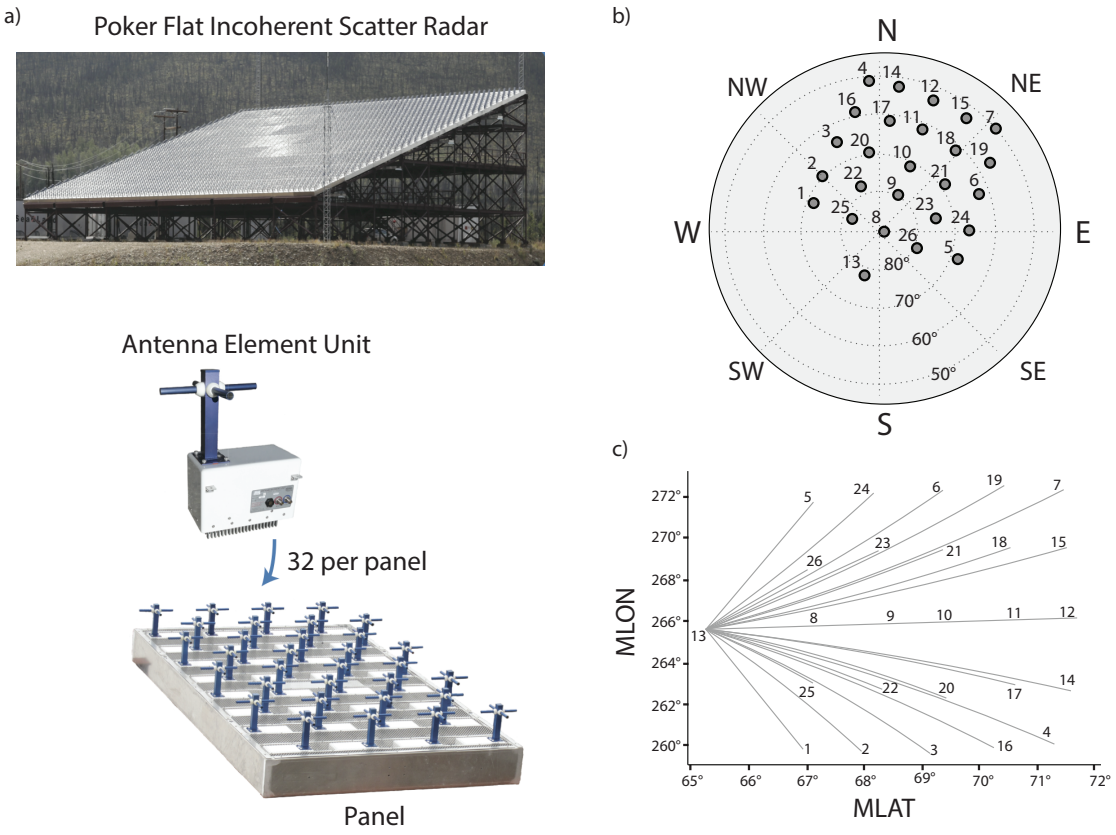

Figure 1.4: a) Show the face of Poker Flat Incoherent Scatter Radar (PFSIR), one of the AMISR systems, and its antenna element unit, assembled into one of its 128 panels (Nicolls, 2015); b) Polar plot of the beam pattern used in experiments discussed in chapter 4-5; c) The magnetic longitude and latitude of the range of each electronically constructed beam.

Substorm: Substorms are a global reconfiguration of the magnetosphere that occurs when the interplanetary magnetic field turns southward, and increased energy flows from the solar wind into the magnetosphere. They are usually brief,

and lasts for about 2–3 hours, and they manifest as magnetic disturbances in the ionosphere and magnetosphere, as well as aurora in the high-latitude ionosphere.

Growth phase: The phase of the substorm where energy is transferred from the solar wind to the magnetosphere, causing the polar cap and magnetic-lobes to expand, the aurora to move equatorward, and the plasma sheet to thin.

Onset: The end of the growth phase is usually marked by the breaking up of the equatorward most auroral arc, and an explosive release of electromagnetic and kinetic energy from the magneto-tail through magnetic reconnection.

Expansion phase: The onset is the beginning of a poleward expansion of the auroral arc, that fills the polar sky with bright and dynamic aurora, which in the magnetosphere manifests as dipolarization - where the plasma sheet expands and polar cap shrinks.

Recovery phase: The expansion phase ends with the recovery of the magnetospheric system to its original quiet-time conditions.

Aurora: Aurora are optical emissions caused by the ionization and excitation of the atmosphere caused by precipitation of charged particles from the magnetosphere.

Discrete Aurora: Aurora that appear like curtains, or discrete arcs with sharp edges, are called discrete aurora. They are often associated with field-aligned currents from the magnetosphere, with accelerated charged particles from the auroral acceleration region, and are stable over several minutes.

Diffuse Aurora: A region of glow without large-scale structures, that do not form rays or show shear or rotational motion is called diffuse aurora. They are thought to be caused by precipitation of particles from the plasma sheet due to scattering without additional field-aligned acceleration.

Black Aurora: Narrow regions within diffuse or discrete aurora that have a distinct lack of emissions, often associated with downward field-aligned currents.

1.3 Objective and Key Contributions

The primary goal of this project is to improve our physical descriptions of the magnetosphere-ionosphere system, and not to predict its behavior. However, improving our understanding of the workings of the system can aid in the development of models that approximate it better and, hence, allow for accurate predictions. In pursuing this goal, we have developed several techniques that will have utility in future studies of energetic particle precipitation, its sources, and its effects.

In this dissertation, we develop energy spectral estimates of precipitating particles by remote sensing the ionosphere using ISRs. Historically most measurements of energetic electron precipitation were made using in-situ measurements of LEO spacecraft with particle detectors. However, since LEO spacecraft are continually moving, they cannot observe a particular geographical location for an extended period. An alternative method was to use ISRs to measure ionization caused by energetic particle precipitation into the atmosphere Kirkwood & Eliasson (1990), and solve the inverse problem to estimate the energy spectra of the primary particles. There have been several methods to solve the inverse problem. We use a maximum entropy inversion technique Semeter & Kamalabadi (2005) and, for the first time, validate it with magnetically conjugate spacecraft measurements of loss-cone fluxes of energetic electrons. However, the technique of remote sensing the energy spectra of precipitating particles has the drawback of being agnostic regarding the species of incident particles, e.g., protons and electrons.

Using these data products and *in-situ* satellite measurements, we constrain sources of energetic precipitation during magnetospheric substorms. It is challenging to identify the magnetospheric source of precipitating particles during magnetic activity. One would need not only to identify spatio-temporal correlations between the energetic precipitation and the source mechanism in the magnetosphere but also to eliminate the presence of all other possible sources. Hence the approach we take is to constrain the mechanism and location of the origin of precipitation using multiple instruments along the same magnetic field line during substorms. This brings us to an additional challenge; the accuracy of magnetic field models is poor during substorms and other magnetically active periods. We address this by validating the accuracy of the model with spacecraft measurements and quantifying the variance in several magnetic field model predictions. Unfortunately, it is also rare to find magnetically conjugate measurements during particular events of interest. In our case, we were able to find an energetic precipitation event while THEMIS spacecraft were in the plasma sheet and magnetically conjugate to an ISR at Poker Flat, Alaska. Using them, we identified energetic precipitation due to EMIC waves near the central plasma sheet during substorm expansion and energetic precipitation from the radiation belts during the growth phase. We also recognized for the first time using optical white-light cameras and ISR measurements that the structured diffuse aurora seen during the growth phase correlates and marks the outer radiation belt boundary.

Finally, we quantify for the first time the effect of energetic electron precipitation on ionospheric conductance. Ionospheric conductance can be estimated using ionization measurements from the ISR and a model of the ionosphere's chemistry. There is very little information about D-region conductance in the literature, per-

haps because it contributes to ionospheric conductance only during brief periods of energetic precipitation or during the day. The complex D-region ion composition makes it challenging to incorporate the mobility of ions in its calculation. However, ion mobility in the D-region is very low due to ion-neutral collisions, and that of negative and cluster ions is even lower. Therefore, electrons are the predominant current carriers in the D-region, and using E-region chemistry is sufficient to calculate the D-region ionosphere's contribution to the ionospheric conductance during energetic precipitation events. The results suggest that D-region conductance makes up the majority of the ionospheric conductance during substorm onset and expansion.

Following list summarizes the main contributions of my dissertation research:

1. Validated a method of deriving energy spectra from Incoherent Scatter Radar measurements to electron energies between 5-300 keV using the THEMIS spacecraft.(Sivadas et al., 2017)

2. Developed 2-D energy flux maps using electronically steerable ISR at Poker Flat, to study the structuring in electron precipitation.

    - Observed latitudinal gradient in mean energy of precipitating electrons (that suggest current sheet scattering due to a thinning current sheet at the latitude of observation) (Sivadas et al., 2019)

3. Developed techniques to constrain the source of energetic precipitation using correlation of precipitating electron energy spectra between multiple instruments along a field line

- Identified energetic electron precipitation originating tailward of 9 R_E from the inner plasma sheet during substorm onset (Sivadas et al., 2017)
- Identified energetic electron precipitation originating from the outer boundary of the radiation belt during substorm growth phase (Sivadas et al., 2019)

4. Implemented techniques to estimate contribution of total ionosphere conductance caused by energetic precipitation (or D-region Ionosphere)
    - 60% of total hall conductance during substorm expansion comes from D-region ionization
5. Showed, for the first time, a particular visible auroral form marks the outer radiation belt boundary during substorm growth phases (Sivadas et al., 2019)
    - 2 out of 5 substorm growth phase events, over 10 years, that occur near Poker Flat, and have simultaneous clear all-sky and ISR measurements, show this feature associated with energetic precipitation from the outer-radiation belts.
    - Identified a source of this energetic precipitation to be current sheet scattering from the radiation belts (Sivadas et al., 2019)
    - Showed that loss of radiation belt electrons between 100-300 keV can reach $\sim$45% that of relativistic dropouts of the same electron energies during geomagnetic storms. (Sivadas et al., 2019)
    - Found that up to $\sim$50% of the optical emissions are contributed by energetic precipitation >30 keV - using GLOW model. (Sivadas et al., 2019)

1.4 Thesis Organization

This dissertation describes a study that narrows the source of energetic electron precipitation by remote sensing its energy spectra and synthesizing it with measurements of other relevant parameters. This work covers an extensive background on the near-Earth space environment and the underlying physics in Chapter 2, with a focus on the source locations and mechanisms of energetic particle precipitation. Chapter 3 describes the methods used to remote-sense energy spectra of electrons and combine data from multiple instruments. Chapter 4 describes energetic precipitation identified to originate from the plasma sheet during a substorm event. Chapter 5 details energetic precipitation from the outer radiation belt and its optical signature in the ionosphere. After this discussion of the sources of energetic precipitation, chapter 6 goes on to describe their effects on ionosphere conductance. In chapter 7, we present observations of multiple substorms that show energetic precipitation. A summary of this dissertation and ideas for future research projects are presented in Chapter 8. Chapter 3 - 5 includes work published in two journal articles in the *Journal of Geophysical Research - Space Physics* and *Geophysical Research Letters*.

CHAPTER 2

Near-Earth Space Environment

The space environment around the Earth is mostly composed of electromagnetic fields, plasma, and the occasional spacecraft debris. Hot plasma is continuously ejected from the giant nuclear fusion reactor at the center of the solar system that is the Sun. This expanding plasma is called the solar wind and is a consequence of the thermonuclear energy that pushes matter out, exceeding the gravitational and interstellar pressure that compresses it. The Earth's magnetic field, sustained by dynamos in the Earth's core, deflect most of the plasma in the solar wind. The cavity carved out of the solar wind by the geomagnetic field is known as the magnetosphere. An ecosystem of plasma and electromagnetic waves exist within this cavity. The Earthward boundary of the magnetosphere, is the ionosphere. It is created by the ionization of the upper atmosphere by solar irradiation and charged particles from the magnetosphere and interstellar space. The ionization and excitation of the neutral particles in the atmosphere can result in spectacular displays of light known as the aurora in the Earth's polar regions.

This dissertation's primary focus is just one part of this complex, interconnected system of the near-Earth space – energetic particle precipitation. In particular, we plan to examine its sources and effects. Hence, it is necessary to understand the physical processes and subsystems in this environment linked to energetic precipitation. Space physics textbooks broadly introduce many of the fundamental concepts; however, it is harder to find the necessary detail and depth in a single book written to introduce readers to a vast subject. Hence, this chapter presents concepts from many different areas of space physics in the level of detail necessary

to understand the source mechanisms and effects of energetic precipitation in the near-Earth environment. We start by discussing relevant fundamentals of charged particle motion in magnetic fields and introduce the concept of adiabatic invariants that naturally come out of a Hamiltonian description of a system that is in periodic motion. We note that causal agents of magnetic fields in a quasi-neutral plasma are fundamentally electric currents. We then briefly discuss the solarwind drivers of the magnetosphere-ionosphere system and describe the several subsystems of magnetospheric plasma coupled with each other. As we review the ionosphere, we focus on the D-region chemistry, which received far more attention in the early years of ionospheric discovery than in the past several decades. An important effect of precipitation that is a focus of this dissertation is ionospheric conductivity. We note that conductivity formulas used ubiquitously are first-order approximations from the simple gas kinetic theory and have some limitations. Next, we introduce substorms and their different manifestations, which significantly influence the generation and precipitation of energetic particles. We also discuss the apparent dichotomy between the competing theories of substorm onset and argue that the reality is likely a combination or sequence of both (and perhaps more) mechanisms. After this, we discuss different auroral forms caused by precipitation, and those particularly connected to energetic precipitation. In the final section, we dive deep into a background of the sources of particle precipitation, its morphology, and its effects on the ionosphere. We hope this review of topics inextricably linked to particle precipitation will be useful for the reader. If one is familiar with fundamental space physics and is only interested in reviewing the context of the results presented in later chapters, you can skip ahead to section 2.7.

2.1 Fundamentals of Magnetized Plasma

To understand the morphology of near-Earth space, we will briefly summarize the most relevant fundamentals of magnetized plasma.

Electric and magnetic fields are always generated by an underlying current or charge distribution. Maxwell's equations describe the relationship between electric current density **J** and magnetic field **B**, along with charge density ρ and electric field **E**.

$$\nabla \cdot \mathbf{E} = -\rho/\epsilon_o \tag{2.1}$$

$$\nabla \cdot \mathbf{B} = 0 \tag{2.2}$$

$$\nabla \times \mathbf{E} = -\frac{\partial \mathbf{B}}{\partial t} \tag{2.3}$$

$$\nabla \times \mathbf{B} = \mu_o \mathbf{J} + \epsilon_o \mu_o \frac{\partial \mathbf{E}}{\partial t} \tag{2.4}$$

These are instantaneous and local descriptions, where a change in the right-hand side of the equations results in a simultaneous, local change in the left-hand side. The electric and magnetic field caused by changes in the charge and current distributions can be described from the solution to Maxwell's equations in terms of retarded potentials. The form of these equations are as follows:

$$\mathbf{E}|_{r_1,t_1} = f(\rho, \mathbf{J}, \mathbf{r}))|_{r_0,t_0}$$

$$\mathbf{B}|_{r_1,t_1} = g(\mathbf{J}, \mathbf{r}))|_{r_0,t_0}$$

where r_0 and t_0 is the position and time at the source location, while r_1 and t_1 is the position and time instant of the field.

In the near-Earth space, charge density is seldom observed, as plasma is quasi-

neutral at scales larger than the Debye lengths. Beyond this length, any effect of charge separation is screened by the surrounding charges, and hence plasma at length-scales larger than the Debye length is charge-neutral. Therefore, the electric and magnetic fields that we observe in the Near-Earth space are mostly a result of current distribution, which occurs while quasi-neutrality is maintained, and not static charge distribution.

The geomagnetic field, generated by currents in the Earth's core, dominates the near-Earth space environment. Some charge particle that finds itself in this field undergoes periodic motion. The periodic motion has associated with it, quantities that remain approximately invariant. And if the conditions favor these adiabatic invariants described later in this section, the particle will remain trapped within the geomagnetic field.

The Lorentz force equation describes the motion of a charged particle in an electric and magnetic field.

$$m\frac{d\mathbf{v}}{dt} = q(\mathbf{E} + \mathbf{v} \times \mathbf{B}) \tag{2.5}$$

The trajectory of the particle in the Earth's magnetic field, governed by the above second-order differential equation, can follow a superposition of three types of periodic motions: (i) gyration around the magnetic field, (ii) mirroring before it reaches the atmosphere on both hemispheres, and (iii) longitudinal drift of these particles (see figure 2.1). If the magnetic vector potential (and therefore the magnetic field) is constant within the area enclosed by one complete gyration, the magnetic moment[1] of the particle averaged through the gyration remains more-or-less unchanged. These conserved quantities, in combination with the total conserved

[1] A discussion of the magnetic moment is presented later in this section.

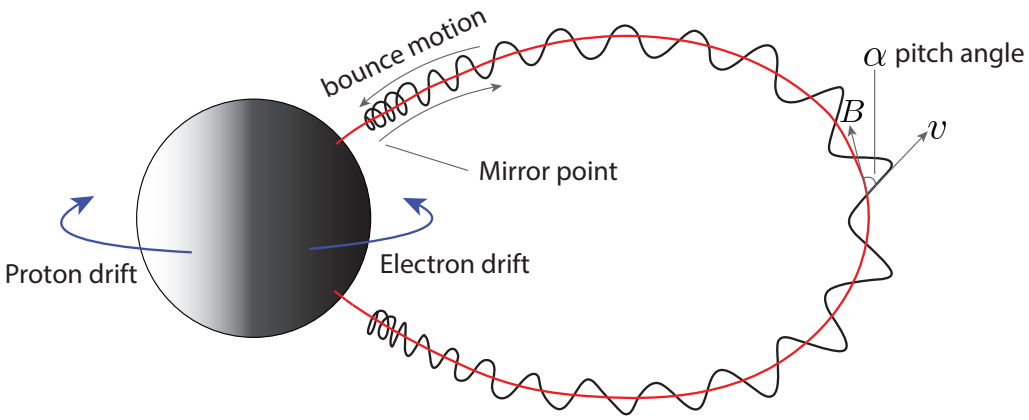

Figure 2.1: Single particle motion in the Earth's magnetic field: the superposition of gyration, bounce, and drift motion, and the defintion of the particle's pitch angle.

energy of the particle, results in the *mirror force* that slows down the particle's velocity along the magnetic field ($v_{||}$) as it moves out of the equatorial plane. The parallel velocity of the particle is maximum at the magnetic equatorial plane, and reduces to zero and then reverses its direction at its mirroring altitude close to the Earth. We can estimate its mirroring altitude, and its velocity distributions at any other point along the field line with the knowledge of the velocity distribution at the magnetic equatorial plane. The distribution is dependent on the magnetic field topology, provided the magnetic moment is conserved along the field line.

As expected, these approximations are seldom valid. The geomagnetic field is approximately a dipole field with a well-known magnetic field distribution within 6 R_E from Earth. Beyond 6 R_E, the magnetic field is usually highly stretched and is more uncertain as it changes based on the solar wind forcing. Furthermore, time-varying electric and magnetic fields, continuously interact with particles, resulting in deviations from the idealized periodic motion described above. However, work-

ing with the idealized dipole model of the geomagnetic field, space physicists have developed mathematical quantities that can be applied when the above approximations do not hold. These include the pitch angle distribution and the loss-cone angle, which are described in section 2.1.2. Also, to understand the system's deviations from its idealizations, we have the adiabatic invariants. Furthermore, we can track external forces acting on particle populations in the geomagnetic field by estimating diffusion coefficients in position-space and pitch-angle-space. Below we briefly highlight the most relevant physical concepts within space physics to our study.

2.1.1 Adiabatic invariant

For any system that obeys the Hamiltonian equations of motion, the phase-space density of a local bunch of trajectories is invariant through time, i.e., the convective derivative $\frac{d\rho}{dt} = 0$. This is Liouville's theorem, and it is true because a Hamiltonian system's velocity field ($X_i(\mathbf{q}, t) = \dot{q}_i$) is divergence-free. The theorem is analogous to the restatement of the continuity equation in terms of phase-space density in n-dimensions. A result of this property is that the following integral along a closed curve $C(t)$, composed of points in phase-space that move according to the equation 2.5, remains invariant.

$$I = \oint_{C(t)} \mathbf{p} \cdot d\mathbf{q} \tag{2.6}$$

Known as the Poincare linear invariant since $\frac{dI}{dt} = 0$, it is a fundamental property of any Hamiltonian system, i.e., systems that follow Hamiltonian equations and whose total energy is conserved. A strictly periodic system will follow a closed

curve in phase-space. Therefore, we can, in principle, find an invariant associated with it.

If, however, some parameter (λ) of the periodic system that affects its period, changes slowly compared to the period, all states of the system in the closed curve are affected similarly[2]. Therefore, the area within the curve remains mostly the same, and the invariant still holds with a transcendentally small error [3] $exp(-A\Delta t/T)$ (See figure 2.2)(Li, 1998). For charged particles in slowly varying electromagnetic fields, their motions are, therefore, periodic in only an approximate sense. And a strictly closed curve in phase-space may not exist. A gyrating charged particle has approximately the same guiding center only if the fields are changing slowly compared to the period of gyration. Therefore, we can obtain an approximate Poincare invariant by assuming the curve C to be a closed curve corresponding to the gyration period. The resulting invariant is one of the *adiabatic* invariants.

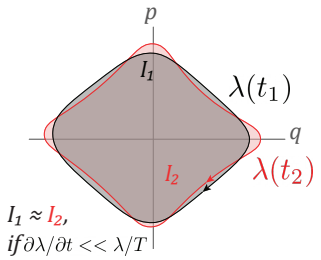

Figure 2.2: The volume of phase-space enclosed (I) by a periodic motion of period T, remains invariant if the rate at which a parameter λ changes is slow compared to the period. λ is a system parameter that affects the period T. After figure 66 in Tong (2005).

Adiabatic invariants are approximate constants of motion that are an asymptotic series of the form: $a_0 + \epsilon a_1 + \epsilon^2 a_2 + ...$ However, usually a_0 is referred to as *the adiabatic invariant* (Northrop, 1963)[4]. There are three adiabatic invariants associated with the three periods associated with charged particles trapped in the

[2]See the lecture notes by Tong (2005), Chapter 4, Section 4.6.1 for a discussion on Liouville's theorem and adiabatic invariants.

[3]Here A is a constant, Δt is the time interval of the change, T is the period of oscillation

[4]Northrop (1963) is a great resource to examine the definition and applications of the adiabatic invariants.

geomagnetic field. (i) Magnetic moment (M) associated with gyration, (ii) Longitudinal invariant (J) associated with the bounce motion parallel to the magnetic field, and (iii) Drift invariant (Φ) associated with the drift around the Earth in a closed surface as the particle bounces between the mirror points while maintaining constant M and J.

Magnetic moment (M) of a charged particle is $p_{\perp}^2/2mB$, and is one of the important parameters determining whether the particle will remain trapped in its orbit around the Earth. If M is constant throughout the bounce motion, charged particles in field lines with $M < M_{trap} = \frac{TE}{B_{max}}$ leak out of the magnetic confinement. Here TE is the particle's total energy, and B_{max} is the maximum magnetic field value where the charged particle mirrors. Since adiabatic invariants are only approximate invariants, M can change along a field line, especially when crossing the magnetic equator or the point of minimum field strength on its guiding-center path. The change ΔM across the magnetic equator is $\approx Aexp(-1/\epsilon)$, where ϵ is the system's adiabaticity and A depends on the particle's gyro-phase at the minimum-B point(Cohen et al., 1978). The adiabaticity ϵ is of the order of the ratio of the gyroradius to the field scale length at the magnetic equator (i.e., the radius of curvature): $\epsilon = \rho_0/R_c$ (Artemyev et al., 2013). A sufficiently sharp curvature increase of the magnetic fields near the magnetic equator (i.e., decrease in R_c), leads to a decrease in ΔM, which will result in the lowering of the mirror point of the particle and their loss from the magnetosphere.

2.1.2 Pitch angle distribution

Another critical parameter that allows us to keep track of a trapped particle's stability is the angle between the charged particle's velocity vector and the magnetic

field or its pitch angle (Figure 2.1). It changes along the trajectory of the particle. And in a dipolar field line, its minimum value is at the magnetic equator and maximum at the mirroring altitude. As described earlier, the pitch angle at the magnetic equator can be used to identify the particle's mirroring altitude. While studying particles on a magnetic field, analyzing its pitch angle distribution can prove useful. It allows us to reduce a 2-D velocity distribution of particles at a specific kinetic energy to a 1-D distribution, by imposing the axial symmetry of the particle gyrating about the magnetic field line. Due to Liouville's theorem of conservation of phase-space density and the approximate conservation of the magnetic moment, the pitch angle distribution at any point on the magnetic field line can be calculated from the distribution at the equatorial plane provided one knows the magnetic field distribution. As a result, the mirror altitude of a charged particle can also be calculated using its equatorial pitch angle.

The particles with a low equatorial pitch angle, have a larger parallel velocity than other particles and can go very close to the Earth's surface. These particles may not mirror back and instead collide with ionospheric particles and ionize neutral atoms or be captured by an oppositely charged particle. The particles can also be back-scattered, thereby changing its trajectory entirely and drifting on to another magnetic flux tube. The highest pitch angle below with the particle is lost from the current magnetic flux tube is called the loss cone angle. It is called a loss *cone*, because in the particles' 3D velocity distribution at the equatorial plane, those within a double cone with its vertex at the origin and axis aligned along the magnetic field direction, are lost either to the atmosphere or scattered to a different flux tube. The loss cone will be emptied in time if other sources do not replenish it. Time-varying electromagnetic fields can scatter charged particles in the pitch

angle space into the loss cone, and cause precipitation into the atmosphere.

Now that we are familiar with some of the useful mathematical concepts to understand charged particle motion, let us explore the reasons for the existence and dynamics of the magnetosphere-ionosphere system in the next section.

2.2 Drivers of the Magnetosphere-Ionosphere System

The Earth's magnetosphere-ionospheric (MI) system consists of plasma embedded in magnetic fields with a variable density and energy distribution in space and time. The motion of ionized fluid in the Earth's core relative to the existing magnetic field generates electric currents that result in the final geomagnetic field that we observe. Close to the Earth, these fields are relatively constant, with the most substantial changes being 150 nanoteslas per year. Farther away, in the upper atmosphere and beyond, influenced by electric currents in the plasma, the magnetic field is highly variable.

The plasma is a collective of electrons and ions that maintain overall charge neutrality. We can attribute its origin to solar-wind plasma entering in through openings in the field, and outflow from the ionosphere. However, in the ionosphere, plasma originates from upper atmospheric ionization from the ultraviolet light and impact of energetic particles from the magnetosphere (Borovsky & Valdivia, 2018). The ionospheric plasma is denser and less magnetized, while the magnetospheric plasma is less dense and highly magnetized. High magnetization implies that the magnetic field has a dominant influence on the motion of the charged particles. We observe such variations in density, energy, and magnetization across latitude, longitude, and altitude. The asymmetries result in convection of magnetic fields, plasma, and energy across the magnetosphere-ionosphere sys-

tem in a bid to eventually reach static equilibrium. However, since the solar wind continuously interacts with the M-I system, this state is never reached, and the system continuously cycles through its different states. The boundaries of the magnetic fields, and its deviations from that generated by the Earth's magnetic core, are **caused by**[5] global magnetospheric electric currents.

The solar wind is the primary source of asymmetry that creates convection in the magnetosphere-ionosphere (MI) system. It is also the main driver of magnetospheric dynamics. Closer to the atmosphere, the Earth's rotation causes convection of plasma. The solar ultraviolet rays play a role in ionizing the atmosphere. At the sunward most point of the magnetosphere, the magnetopause, the solar wind properties vary over time due to (1) the spatial variation in the wind's source on the Sun's surface, and the 27-day solar rotation and (2) the spatial structure of the solar wind plasma. As a result, the strength and properties of the driver of the MI system vary with time.

In 1961, H.W. Dungey proposed a theory that explains the global magnetospheric convection of magnetic field lines. Through magnetic field reconnection that changes the topology of the field, the geomagnetic field reconnects with the solar wind field at the dayside and is dragged around the magnetosphere. It meets and undergoes the nightside reconnection, and then the field lines move sunward from the magnetotail through the dipolar portion of the magnetosphere to exit at the dayside, thereby completing the cycle. Cold plasma tends to move along with the magnetic field lines due to the frozen-in flux condition being satisfied, and hence the convection of the field lines translates to convection of the cold plasma. Close to Earth, the dominant form of convection is caused by the rotation of Earth.

[5]See De Mees (2014) for a discussion on causality and Maxwell's equations.

As the global magnetospheric convection starts with dayside magnetic reconnection and depends on the properties of the magnetosphere, the solar wind parameters, and magnetospheric parameters that affect reconnection rates become most relevant in driving the convection. The solar wind parameters that affect convection are a function of solar wind number density (n_{sw}), velocity (u_{sw}), Alfven Mach number (M_A), IMF Clock angle (θ_{Bn}), and magnetic field (B). The density, plasma pressure, and magnetic pressure downstream of the solar wind will also affect the reconnection rates, and consequently, the convection.

2.3 Magnetosphere

The solar wind pushes the dayside magnetosphere inwards against the downstream plasma and magnetic pressure. The convection of magnetic fields from the dayside causes the piling up of the magnetic field on the nightside resulting in a stretched magnetotail. The interplay between the solar wind and the geomagnetic field ultimately determines the magnetosphere's morphology and dynamics. The solar wind and the ionosphere are sources of magnetospheric plasma, while the atmosphere and interplanetary space act as sinks. In this section, we briefly discuss the morphology of the magnetosphere.

Scientists have divided the magnetosphere and its surroundings into distinct regions that have unique plasma properties and dynamics. Figure 2.3, shows all the important regions that make up the MI system.

Bow Shock: The solar wind flows at supersonic velocities and is diverted around the magnetosphere through the formation of a shock front, which converts the supersonic flow to subsonic. Apart from deflecting the flow around the magnetosphere, the bow shock heats and compresses the solar wind plasma. It reflects

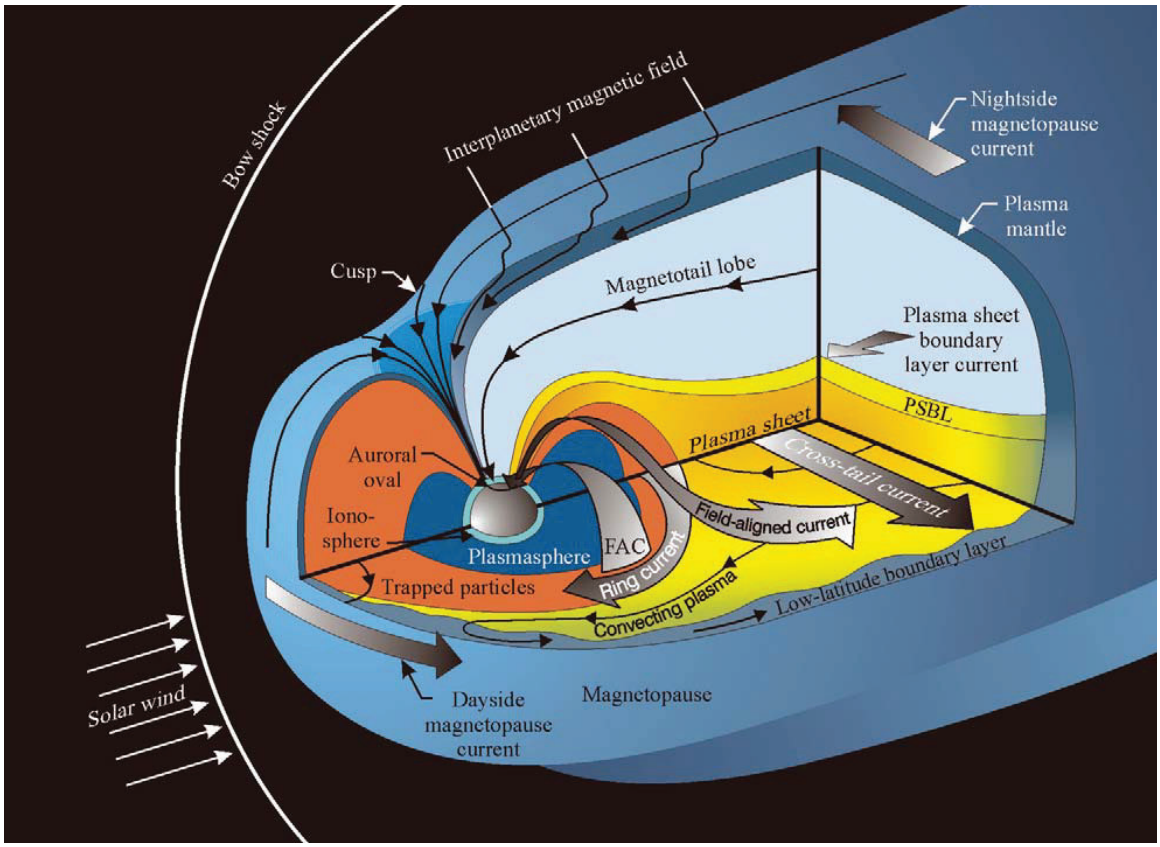

Figure 2.3: A schematic illustration of distinct plasma regimes and current systems of the Earth's magnetosphere. After Pollock et al. (2003).

and accelerates charged particles along magnetic field lines, back to the sun. These particles, mostly energetic protons of the order of keVs, are continuously swept back towards the shock by the solar wind, creating energy-dependent foreshock boundaries.

Magnetosheath: The subsonic, shocked solar wind plasma flows downstream of the bowshock and around the magnetosphere. The plasma in this magnetosheath eventually accelerates up to the solar wind speed and merges back where the shock weakens and disappears.

Magnetopause: The magnetosphere's outer boundary, which separates solar wind field lines from geomagnetic field lines that connect to the Earth, is the magnetopause. The magnetopause also separates the respective shocked solar wind plasma from the magnetospheric plasma. As the solar wind pressure squeezes the magnetopause, electric currents are flowing on this boundary. The formation of these currents is governed by Ampere's law of magnetism, where any distortion of the magnetic field is associated with an electric current. At low-latitudes, the magnetopause boundary between the solar wind plasma and the hotter magnetospheric plasma is characterized by a low latitude boundary layer (LLBL) (Rossolenko et al., 2008). At high latitudes, this boundary layer is called the plasma mantle, and it also separates the solar wind plasma from the magnetotail.

Magnetotail: On the night side of the Earth, the magnetosphere stretches into an elongated cylindrical volume of magnetic field lines ($\sim$100 R_E) connected to the Earth called the magnetotail. Within the magnetotail, there are two types of hot plasma: the ion plasma sheet (or ring current) and the electron plasma sheet. Both these plasma populations spatially overlap each other. These plasma sheets

are between magnetic lobes, which are mostly empty and contain low-density cold plasma. As magnetic flux piles up in the magnetotail, due to the convection driven by the solar wind, it is a reservoir of magnetic energy that powers several processes.

Dipolar magnetosphere: This is the inner dipolar region of the magnetosphere, dominated by Earth's internal dynamo. Mostly unaffected by distortions caused by the solar wind, the cold plasma close to the ionosphere corotates with the Earth. This region is the plasmasphere, and its corotation is a result of collisional coupling with the Earth's atmosphere. Further out, partially overlapping the plasmasphere, there are the radiation belts which constitutes energetic charged particles. This hot plasma is mostly brought in through energy-release processes in the magnetotail, such as bursty bulk flows and substorm injections.

Cusps: Close to the northern and southern magnetic poles, the magnetic field lines from the solar wind link up to the Earth's geomagnetic field lines. These open field lines allow the solar wind plasma to enter deep into the magnetosphere and interact with the Earth's atmosphere.

Auroral oval: Around the cusp region in the atmosphere, is a ring of visible air glow, that are produced by the impact of magnetospheric electrons and ions on the upper atmosphere. The oval is produced mostly by electrons from the plasma sheet. A weaker airglow is produced by protons from the ion plasma sheet, at slightly lower latitudes than the electron aurora. Aurora is a main source of power dissipation from the magnetotail. A similar but distinct term used in the literature is the Auroral Zone, which lies approximately along a circle of dipole latitude 67°. It is simply the locus of the midnight (MLT) part of the oval where intense auroral displays are frequent.

2.4 Ionosphere

The ionosphere is the ionized upper atmosphere ranging from 80 to 600 km in altitude, forming the electrically conductive inner boundary of the magnetosphere. It consists of a mixture of plasma and neutral particles created by ultraviolet light from the Sun and particle precipitation from the magnetosphere. The plasma density varies based on local time and latitude, as the intensity of sunlight changes. The ionosphere is a source of particles outflowing into the magnetosphere. The outflow attempts to maintain the magnetosphere's charge neutrality by compensating for the loss of charged particles to the atmosphere. The ionosphere also exhibits spatial and temporal variation in plasma density, temperature, flow velocities, and chemical composition both in space and time.

2.4.1 Spatial variation

The common distinctions that space physicists make regarding the spatial variation of the ionosphere are mostly based on altitude, latitude, and local time. These distinctions more-or-less translate to differences in the physics dividing vast regions of the atmosphere into sub-regions that can be studied more closely by different scientists.

2.4.1.1 Layers

Edward V. Appleton won the Noble Prize for the discovery of the Appleton layer of the ionosphere, which reflects radio waves and proved useful for communication (McElroy, 2012). He was responsible for the original naming scheme that divided the ionosphere based on altitude into D, E, and F layers (the F-region was later divided into F1 and F2 layers, see figure 1.3). As scientists usually describe

the electric field with the symbol E, he labeled the first layer of the ionosphere he studied as E to describe the electric field of the wave reflected from that layer. He identified a second layer at a higher altitude, F, and suspected the existence of a layer at a lower altitude, for which he used the symbol D. Though the nomenclature started off describing the field of the reflected waves, it is now associated with layers and has evolved to reflect our understanding of the underlying physics and chemistry.

D-region: The lowest region of the ionosphere, ranging from mostly 70-90 km, the D-region has a high density of neutral particles. The plasma here has high collision frequencies and effective recombination rates, with very low magnetization. It also has the most complex chemistry, with a large number of positive and negative ions (See section 2.4.3). Free electrons in the D-region are mostly removed by the process of attachment. It depends on the collisions between electrons and neutral atoms, which is highly probable in the lower D-region. In contrast, the free-electron loss is caused by recombination in the upper layers of the ionosphere, which depends on electron-ion collisions (Reid, 1964). The region is mostly produced by Solar EUV in the daytime and hence disappears very quickly at nighttime unless there are precipitating charged particles. Only particles with sufficiently high energy (electron >30 keV and protons >1 MeV) can penetrate the D-region. As a result, we focus heavily on this ionospheric layer in this dissertation.

E-Region: Spanning from 90-160 km, the E-region remains at night, although at a lower density. Dominated mostly by O_2^+ and NO_2^+ ions, the layer has a slower recombination rate and is home to bright auroral emissions.

F-Region: Located directly above the E-region, it extends up to 800 km. The

plasma density in the ionosphere reaches its highest value in the F-region around 350 km. During the daytime, two layers can be identified: the F_1 layer and the F_2 layer above it. F_1 is dominated by a mixture of molecular and atomic ions, while the F2 layers are composed mainly of atomic O^+ ions. During night time, the F_1 layer merges with the F_2 layer. This region is one of the primary layers that reflect high-frequency communications, allowing far-range terrestrial communications.

The ionosphere is also distinguished based on local time. The region exposed to sunlight referred to as the daytime or the dayside ionosphere, which are contrasted with the night time the nightside ionosphere. In addition to this, distinctions are made based on latitude: high-latitude, mid-latitude, and low-latitude, where different physical processes dominate because of the structure of the magnetic field, the variation of solar intensity and its cycle, and atmospheric circulation.

2.4.2 Temporal variation

Apart from the cyclical variation of solar radiation, the following sources cause both temporal and spatial variation, (i) charged particle precipitation from above, (ii) atmospheric gravity waves from below, and (iii) convection of plasma within the ionosphere due to induced electric fields.

The local temporal variation depends on the production rate of ionospheric plasma, its convection, and the rate at which it recombines to become neutral. This physics is captured in the following mass continuity equation.

$$\underbrace{\frac{\partial n_e}{\partial t}}_{\text{local change}} + \underbrace{\bigtriangledown \cdot (\mathbf{u} n_e)}_{\text{convection \& diffusion}} = \underbrace{P}_{\text{production terms}} - \underbrace{L}_{\text{loss terms}} \tag{2.7}$$

P refers to the electron production rate that, in the case of the ionosphere, is mostly

caused by ionization and hence is simply the ionization rate q ($m^{-3}s^{-1}$). The loss term L refers to the reverse process of recombination. Due to quasi-neutrality of plasma there are as many positive ions (n_i) as there are electrons (n_e) and therefore the electron loss rate $L = \alpha_D n_i n_e = \alpha_D n_e^2$, where α_D is the effective recombination rate ($m^{-3}s^{-1}$).

If the total change in electron density ($\frac{dn_e}{dt}$) is slow compared to the time constant of the loss ($\tau = 1/\alpha_D n_e$), which is true in the E- and D-region, then the left hand side of equation 2.7 can be ignored (Semeter & Kamalabadi, 2005). The effective recombination rates have a time scale of the order pf less than ~10s, and fluctuations in local electron density are considered to have larger time-scales. As a result the equation is sometimes simplified to $P = L$ i.e., $q = \alpha_D n_e^2$. However, this is, in particular, not true when n_e is very low, during quiet times, where τ can be larger than time-scales of local electron density variations.

For these cases, a more rigorous approach can be taken by finding an analytical solution for n_e (Virtanen et al., 2018), by integrating the following version of equation 2.7 in the time-scales of interest:

$$\frac{\partial n_e}{\partial t} = q - \alpha_D n_e^2 \tag{2.8}$$

This assumes that convection is negligible ($\bigtriangledown \cdot (\mathbf{u} n_e)) = 0$), a fair assumption at lower altitudes as the effective recombination rates α_D is high (due to increased collisions), and its corresponding time constant τ is low. As a result, the time scales of electron density fluctuations due to the plasma transport into or out of the volume of interest are mostly larger than τ.

An understanding of the dynamics of electron production and loss in the ionosphere is essential to detect these electrons. And measuring electrons produced by

precipitating energetic particles can be used to estimate their energy and flux, as we will see more in Chapter 3.

2.4.3 Composition and Chemistry

Overlapping with the ionosphere exists the neutral atmospheric region called the thermosphere ranging from 100 to 1000 km. This region is strongly coupled to the ionosphere's plasma and also dictates the chemistry of the region. The major neutral constitutes here are O, N_2 and O_2, accompanied by other minor constituents NO, N, H, He, Ar and CO_2. The abundance of N_2 and O_2 are a result of physical and chemical processes acting on the Earth's atmosphere through geological timescales. Oxygen atoms O are created by photo-dissociation of O_2 and destroyed by recombination reactions that are effective below 110 km.

In a steady-state, there is a balance between the pressure gradient and gravitational force leading to a stable equilibrium with atmospheric pressure decreasing exponentially with increasing altitude.

$$p = p_0 \exp\Big[- \int_{z}^{z_0} (\langle m \rangle g / kT) dz \Big] \tag{2.9}$$

The overall atmospheric pressure depends on average mass $\langle m \rangle$, altitude z, acceleration due to gravity g, and the temperature T. The quantity KT/mg is the atmospheric scale height and is a measure of pressure variation with altitude. It is different for each atmospheric constituent due to their differing masses. Therefore, the distribution of atmospheric constituents, with their different scale heights, usually differs based on their partial pressure as opposed to mixing into a uniform altitude distribution (Rees, 1989).

Photons and charged particles ionize the major neutral constituents into a variety of ions that may further dissociate into more ions and minor neutrals that form the ionosphere and thermosphere. The major ionospheric ions produced in this manner within the E-region are N_2^+, O_2^+, O^+, and N^+. At night, metallic ions such as Mg^+, Fe^+ with some Na^+, Al^+, Ca^+, and Ni^+ are produced by meteor ablation followed by photoionization during the day and charge transfer with other ions.

Energetic precipitation constitutes the dominant mode of ionization during the night-time in the D-region, where metallic ions and negative ions are observed. The concentration of negative ions in the lower ionosphere is high due to a greater probability of interaction of neutral particles with free electrons (electron attachment: $X + e^- \rightarrow X^-$). The reduction of negative ions happen through mechanisms such as reciprocal neutralization ($X^- + Y^+ \rightarrow X + Y$) and electron detachment ($X^- + M \rightarrow X + M + e^-$).

The presence of negative ions and charge neutrality implies that $n_i \neq n_e$, rather $n_i = n_e + n_{i^-}$. A useful way to describe the proportion of negative ions at a particular altitude is by using the parameter $\lambda_{i^-} = n_{i^-}/n_e$. The effective recombination rate in the presence of negative ions are therefore:

$$\alpha_D = \alpha^* + \lambda_{i^-}\alpha_{neut} + \frac{1}{n_e}\frac{d}{dt}\ln(1 + \lambda_{i^-}) \tag{2.10}$$

Here α^* is the electron recombination rate, α_{neut} is reciprocal neutralization rate. The continuity equation 2.8 becomes:

$$\frac{\partial n_e}{\partial t} = \frac{q(z)}{1 + \lambda_{i^-}} - \alpha_D n_e^2 \tag{2.11}$$

Details on the derivation of the above equations are described by Danilov (1970).

The negative ions through hydration can lead to negatively charged cluster ions produced overnight through hydration and other processes. In certain situations, like summer night-times, the cluster ions can be a dominant ion in the D-region. However, they are still lower than the total negative ion and electron abundance (Fritzenwallner & Kopp, 1998).

The effective recombination rate is, in general, higher in the D-region as compared to the E-region, due to its dependence on the abundance of negative ions. Models typically estimate that below 75 km, the abundance of negative ions exceeds that of electrons ($\lambda_{i^-} > 1$ for z $<$ 75 km), and hence results in increased α_D (Wisemberg & Kockarts, 1980; Danilov, 1970).

2.4.4 Conductance

Ionospheric chemistry plays an important role in determining another important ionospheric parameter – its conductivity. Conductivity of a plasma is a measure of the ease at which current can flow through the plasma. This is determined by the extent of collisions between charged particles and the neutral atoms within the ionosphere. Conductivity is a local measure, while conductance is the integrated conductivity along the path of interest (typically along a current) or across the length of a macroscopic material.

The conductivity of unmagnetized plasma is

$$\sigma_0 = \frac{n_e e^2}{m_e \nu_c} \tag{2.12}$$

where ν_c is the collision frequency. It is the constant in the microscopic relation

between current density and electric field known as the ohm's law

$$\mathbf{j} = \sigma_0 \mathbf{E} \tag{2.13}$$

For a magnetized plasma, there will be an additional force perpendicular to the magnetic field that modifies the ohms law as follows:

$$\mathbf{j} = \sigma_0(\mathbf{E} + \mathbf{v}_e \times \mathbf{B}) \tag{2.14}$$

where $\mathbf{v}_e$ is the relative velocity of electrons with respect to the ions. The magnetized plasma results in an anisotropic conductivity, with differing conductivity parallel and perpendicular to the magnetic field and electric fields. We can see this by writing the above equation in the form $\mathbf{j} = [\sigma] \cdot \mathbf{E}$, where $[\sigma]$ is a tensor. In Cartesian coordinates, with x-axis along a uniform background magnetic field **B**:

$$[\sigma] = \begin{bmatrix} \sigma_\parallel & 0 & 0 \\ 0 & \sigma_P & -\sigma_H \\ 0 & \sigma_H & \sigma_P \end{bmatrix} \tag{2.15}$$

In an arbitrarily directed uniform magnetic field, equation 2.14 can be written as:

$$\mathbf{j} = \sigma_\parallel \mathbf{E}_\parallel + \sigma_P \mathbf{E}_\perp - \sigma_H(\mathbf{E}_\perp \times \mathbf{B})/B \tag{2.16}$$

where,

$$\sigma_\parallel = \sum_s A_s \tan \alpha_s \tag{2.17}$$

$$\sigma_P = \sum_s \frac{A_s}{2} \sin 2\alpha_s \tag{2.18}$$

$$\sigma_H = -\sum_s A_s \sin^2 \alpha_s \tag{2.19}$$

and,

$$A_s = \frac{q_s n_s}{B_0}; \;\; \alpha_s = \frac{\omega_s}{\nu_s}; \;\; \omega_s = \frac{q_s B_0}{m_s}$$

Here n_s , q_s, m_s, ω_s, ν_s are the number density, charge, mass, gyrofrequency, and effective collision frequency of the charged particle of species s. These substitutions result in an elegant and concise description of the parallel ($\sigma_\parallel$), Pedersen (σ_P) and Hall (σ_H) conductivity (Maeda & Kato, 1966; Baker & Martyn, 1953). These equations are derived from simple gas kinetic theory and are only a first-order approximation. However, it provides a reasonable estimate of conductivity.

In the lower ionosphere, the ionosphere is lightly ionized, and hence the effective collision frequency ν_s can be approximated to just collisions of the charged particle species with the neutrals. However, at higher altitudes, the exclusion of ion-ion or ion-electron collisions can become significant.

The parallel conductivity ($\sigma_\parallel$) is the electric conductivity in the direction parallel to the magnetic field line; this is, in effect, the value of the conductivity of the plasma if it were unmagnetized (σ_0). If there were an electric field component ($\mathbf{E}_\perp$) transverse to **B**, then the conductivity along the transverse direction is reduced to the Pedersen conductivity σ_P, instead of the conductivity value observed in an unmagnetized plasma ($\sigma_\parallel$).

If the particle has collision frequency lower than its gyrofrequency, they undergo several gyrations before a collision. They hence can travel further in the $\mathbf{E}_\perp \times \mathbf{B}$ direction via the $\mathbf{E} \times \mathbf{B}$ drift. This is mainly true for electrons in the E-region. The ions in the same region collide more frequently and hence lag in the

$\mathbf{E}_\perp \times \mathbf{B}$ direction. The conductivity in the $\mathbf{E}_\perp \times \mathbf{B}$ direction is a result of enhanced electron mobility and is appropriately named the Hall conductivity σ_H.

Above 150 km altitude, the ions and electrons undergo $\mathbf{E} \times \mathbf{B}$ drift without significant collisions and hence produce no current. Here, Hall current is not produced since both particles are drifting along $\mathbf{E}_\perp \times \mathbf{B}$. While Pedersen current is also 0 since during the period of no collisions, the charged particles are unable to move in the direction of $\mathbf{E}_\perp$ and instead move transverse to it and the magnetic field. In altitudes close to 125 km, the Pedersen current peaks and is carried by the ions as they start colliding more frequently with the neutrals. The electrons continue their $\mathbf{E} \times \mathbf{B}$ drift and carry the hall current as the ions lag due to collisions, as mentioned above. At 100 km, the ion collisions become so high that they are coupled with the neutrals and are less likely to move along $\mathbf{E}_\perp$ and hence we see a decline in Pedersen current carried by ions. The hall current is still carried by electrons, which declines as we go into the D-region due to the decreased number density of electrons.

In the D-region, conductivity enhancements are observed through ionization caused by solar radiation in the day and energetic particle precipitation during the day and the night. Due to the complex chemistry, calculating D-region Hall and Pedersen conductance is challenging. The primary reason for this is the lack of an accurate estimate of collisional cross sections for the molecules predicted to exist in the region. In a deeper sense, calculating ionospheric conductivity is challenging due to the complexities of the collision integral in the momentum equation, and also since the formulas presented in equations 2.17-2.19 are first-order approximations. Non-linear effects due to plasma instabilities cause exponential enhancements in Pedersen conductivity, carried by electrons instead of ions in the

D-region Hosokawa & Ogawa (2010). We present a more detailed discussion of D-region conductivity, its estimate using ISR measurements, and the approximations we use to estimate their role in total ionospheric conductance in Chapter 6.

The transverse ionospheric conductance (i.e., σ_H, σ_P) plays a crucial role in determining the strength of magnetospheric currents that traverse it. Due to the very high conductivity along the magnetic field lines, the ionosphere is *electrically very close* to the currents in the Earth's magnetotail, even though distances of Earth radii separate it. Therefore, when the transverse ionospheric conductivity is sufficiently high, magnetospheric currents flow through them with greater strength. Though difficult to decipher, due to the lack of global datasets, ionospheric conductivity influences the magnetosphere's configuration and dynamics. Global modeling studies have been able to show that it affects the temporal history of the magnetospheric dynamics(Raeder et al., 1996), global cross polar cap potential (Hill & Rassbach, 1975; Siscoe, 2002), plasma pressure in the inner magnetosphere (Ridley et al., 2004), precipitation of auroral electrons (Ridley et al., 2004), and the timing and strength of magnetospheric substorms (Raeder et al., 2001).

2.5 Substorms

A substorm is a global reconfiguration of the magnetosphere-ionosphere current system. It is characterized by the release of stored magnetic energy from the solar wind in the form of kinetic and electromagnetic energy into the magnetosphere and the ionosphere. In the ionosphere, it manifests as an auroral substorm – vivid displays of aurora near midnight associated with strong magnetic perturbations from magnetospheric currents redirected into the ionosphere. The manifestation of the event in the magnetosphere is called the magnetospheric substorm. As dis-

cussed in section 2.2, the Dungey cycle is the steady-state convection of the magnetic field and plasma in the magnetosphere. And magnetospheric substorms occur due to an imbalance of reconnection rates in the dayside and the nightside. The reconnection rate immediately increases in the dayside when the interplanetary magnetic field (IMF) of the solar wind turns southwards (the opposite direction of the geomagnetic field direction at the magnetopause). However, it takes 10s of minutes for the reconnected magnetic fields to be transported towards the nightside by the surrounding flow. As the nightside reconnection rate remains the same as in the Dungey cycle, the higher dayside reconnection rate leads to a piling up of new magnetic flux in the tail. This growth of magnetic flux in the tail, and the corresponding increase in the polar cap size, is the **growth phase** of the substorm.

During the growth phase, the enhanced convection results in a thinning magnetotail and a highly thin current sheet along its equator. This configuration is increasingly unstable, and at some moment, magnetic reconnection initiates in the near-Earth magnetotail (20-30 R_E) (**onset**). This results in fast flows from the reconnection site towards and away from the Earth, accompanied by the dipolarization of the inner magnetosphere (**expansion**). The flows from the reconnection region in the magnetosphere couples with flows in the ionosphere through field-aligned currents, the net effect of which is a current-system termed the substorm current wedge (Kepko et al., 2015). Finally, over a couple of hours, the magnetosphere-ionosphere system returns to its initial state before the growth phase (**recovery**). This whole sequence of energy storage and its explosive release can repeat 2-3 times a day and is called the substorm.

The explanations of the origin of the substorm onset have been contentious. Several models were proposed over the years, and many have been disregarded,

and some modified. Two major groups of theories have emerged, attempting to explain all the observations associated with the phenomenon: The current disruption (CD) or "inside-out" model and the renovated Near-Earth Neutral Line or "outside-in" model or simply the magnetic reconnection (MR) model. These models attempt to explain two disparate observations that have eluded previous theories: 1) the auroral onset occurs near the most equatorward arc in the auroral oval, which maps close to the inner-plasma sheet boundary in the magnetosphere and 2) reconnection is associated with plasmoid releases that occur in the distant regions of the magnetotail which maps to the poleward-most boundary of the auroral oval in the ionosphere.

The inside-out model, proposed by Lui(1991), describes the initiation of the onset in the near-Earth region due to the growth of a current-sheet instability that leads to the tail-ward propagation of a rarefaction wave that destabilizes the distant thin current sheet region where X-line forms and a plasmoid is released. Therefore, the name comes from the fact that the model proposes that the activity starts close to the Earth and then propagates out to the distant tail. Several studies have offered observational evidence for this mechanism (Henderson, 2009; Lui, 2011; Murphy et al., 2014).

The revised NENL is characterized by an additional magnetic neutral line that develops in the mid-tail region (20-30 R_E). It undergoes magnetic reconnection at some moment of instability resulting in a rapid release of energy and earthward flows known as Bursty Bulk Flows (BBFs). Closer to the inner plasma sheet, the flow decelerates due to increased magnetic strength of dipolar field lines resulting in the substorm current wedge (SCW). SCW is a disruption in the cross tail current that forces partial current to redirect flow along the field lines and into the iono-

sphere. This is manifested as auroral breakup on or near the most equatorward arc. The name "outside-in" is appropriate for this class of models, as activity starts from the mid-tail and later induces near-Earth effects. The Time History of Events and Macroscale Interactions (THEMIS) spacecraft were instrumental in producing evidence for this mechanism (Angelopoulos et al., 2008; Lui et al., 2000).

The primary difference between the two categories of theories is the temporal order of processes within the substorm phenomena. The debate between the two groups of theories has been long and still somewhat remains a controversial topic. Picturing a dichotomy between the two proposed theories at this point is too simplistic. The current lack of measurement coverage may contribute to the ambiguity. However, given the evidence observed for both "inside-out" and "outside-in" mechanisms, perhaps it is time to acknowledge that there are at least two pathways for the magnetospheric system to evolve from pre-substorm to post-substorm. And the real question is about the system's probability of traversing these pathways, and the environmental conditions that increase or decrease the likelihood of one path. In a detailed study using both ionospheric and magnetospheric observations, Murphy et al. (2014) suggests that there are instances where both mechanisms can occur during a particular substorm onset, independent of each other, due to the storage of free energy at both the inner magnetosphere and the stretched tail during the substorm growth phase.

Particle acceleration processes in the magnetosphere are closely associated with substorms (Birn et al., 2012). A complete discussion of different acceleration processes is presented later in Section 2.7.1. The two primary sources of electron energization during substorms are the electric fields associated with magnetic reconnection and the induced electric fields related to the dipolarization of the stretched

field lines. *In situ* (spacecraft) observations of fields and charged particles can provide constraints to models that allow for the evaluation of relative importance of the different acceleration mechanisms. Apart from energization, charged particles can be scattered in velocity space due to the effects associated with the dynamic rapidly changing field lines and wave activity, lowering their mirror points and resulting in precipitation (Millan & Baker, 2012). Substorm dipolarization can result in $\sim$1–10 keV electrons from the plasma sheet to be accelerated and injected into the inner magnetosphere at energies of hundreds of keV. This, in turn, undergoes further acceleration through resonant wave interactions to reach $\sim$ MeV energies observed in the inner radiation belts.

2.6 Aurora

Substorms are associated with intense aurora in the Earth's polar regions. The more equatorward the aurora, the stronger the substorm is likely to be. The magnetic activity induced on the ground by auroral electrojets, the ionospheric part of the SCW, indicates the strength of the auroral substorm. A good proxy for this is the auroral electrojet index (AE index), a measure of the difference between the maximum westward and eastward auroral electrojets in the ionosphere (Davis & Sugiura, 1966).

Even when there are no substorms, the quiet and stable aurora is present in the auroral oval surrounding the polar regions. Electron precipitation from the plasma sheet produces these auroral emissions at ionospheric heights (Vasyliunas, 1972). Proton precipitation from the inner magnetosphere also produces faint and diffuse aurora (Spanswick et al., 2017). The auroral oval magnetically connects to a vast region of the magnetosphere ranging from 6–25R_E. Hence, distinctions in

auroral features may allow for differentiating regions of magnetosphere plasma. However, due to resistivity, induced electric fields, cross-field drift effects, Alfven waves, sparse measurements, and local changes in the field, accurate mapping of the aurora with magnetosphere source regions is a complex and challenging task (Otto, 1996; Kaufmann et al., 1993).

2.6.1 Auroral spectra

Precipitating charged particles produce visible auroral emissions when they excite atoms and molecules in the ionosphere. The aurora consists of emission lines and bands of neutral or ionized N_2, O, O_2, and N (Paschmann et al., 2003). The spectra of the aurora contain useful information about the energy of the precipitating particles. It is dependent on the depth to which the particles penetrate and the chemistry at that height range. Low energy electrons (<1 keV) that ionize altitudes above 200 km can produce red line emissions $630.0 - 636.4$ nm through long-lived atomic oxygen transitions with a lifetime of 110 s. The 630.0 nm emissions are also strongly quenched below 200 km due to higher collisions with atoms, and hence they are emitted only above 200 km. Electron energies between $1 - 10$ keV deposit their energy mostly between $100 - 150$ km, leading to green emissions at OI (557.7 nm) with a lifetime 1 s.

Given that most of the auroral electrons are between $1 - 10$ keV, the green color dominates the aurora's visual appearance. N_2^+ (427.8 nm) with a lifetime of 10^{-7} s is a prompt emission with excitation energy of 19 eV. Its short lifetime makes it less susceptible to quenching through collisions, and hence can be produced by most electron energies and is therefore proportional to the total energy flux. The minimum excitation energies required for the most common visible emissions lines

are below 10s of eV. Both the primary precipitating electrons and the secondaries they generate, produce these emissions.

Measurements of the auroral intensities are usually obtained as line-of-sight integrated quantities, and not altitude profile of the volumetric emission rates. We can use the ratios of the column emissions rates to estimate the characteristic energies of the spectra. For example, the ratio of $I_{630.0nm}$ and $I_{427.8nm}$ together with absolute emission rate $I_{427.8nm}$ provides an estimate of the energy flux and the mean energy of electron precipitation (Rees & Luckey, 1974). 630.0 nm emissions are proportional to low energy precipitation, and hence its ratio with the total energy flux provides an estimate of the hardness of the energy spectra. As conductivity also depends on the altitude of ionization and fluxes of precipitating electrons, the same principle can be applied to estimate height-integrated conductivity (a.k.a. conductance) from auroral spectroscopic measurements (Mende et al., 1984). Precipitating protons capture an electron producing an excited hydrogen atom leading to different auroral emissions: H_α (656.3 nm) and H_β (486.0 nm), which allow us to estimate the proportion of proton precipitation. The Doppler shift from these lines also enables the estimation of the energy of these protons.

2.6.2 Auroral structure

Given an ionospheric chemical composition, the altitude distribution of ionization determines the emission spectra. And the altitude of ionization provides us with information about the energy of the precipitating particles. The morphology of the aurora is indirectly tied to the precipitating particles' energy, as the auroral structure may be associated with its magnetospheric source, which is directly associated with the particle energy. For example, **discrete auroral arcs**, observed in

the evening and poleward sectors of the auroral oval, are mostly made of electrons with energy < 10 keV. Their source is primarily magnetic field-aligned electric fields produced by double layers or dispersive Alfven waves in the AAR. More details about the sources of precipitation are discussed in section 2.7. Another common auroral structure is the **diffuse aurora**. Observed typically in the equatorward portion of the auroral oval, they are associated with pitch angle scattering of plasma sheet electrons in the magnetosphere by chorus waves. They are faint, and diffuse, and cover a large area, at least 2000 km $\times$ 500 km. Their source electron population has energies within $0.1 - 30$ keV.

Fine-scale structures sometimes occur in diffuse aurora both in the dayside and nightside, often called the **Structured diffuse aurora (SDA)**. Two types of SDA were identified in the dayside: stripy or patchy forms that drift towards higher latitudes and forms adjacent to discrete aurora that moves slowly along with it; these are likely linked to particles from the magneto-sheath. Electrons of energy $\sim$ 1–10 keV are the likely source of the former type of aurora (Han et al., 2015). The patterns in SDA could be a result of the spatial distribution of whistler-mode wave and ambient plasma density near the magnetic equatorial plane (Nishimura et al., 2013). In the nightside, mostly during the recovery phase, the SDAs are regular, parallel auroral stripes brighter than the background (Sergienko et al., 2008). These aurorae are associated with electrons > 8 keV scattered from the magnetosphere (Samara et al., 2010). In Chapter 5, we analyze in detail one such SDA observation during a substorm growth phase. Nishimura et al. (2020) provides more background on SDAs.

2.6.3 Auroral dynamics

Apart from the varied structures, the aurora also exhibits a wide array of dynamics. During a substorm, the auroral oval follows a now-familiar dynamics described first by Akasofu (1964). Linked with the substorm cycle described in section 2.5, the auroral features slowly move equatorward and polar cap expands during the substorm's **growth phase**. This is due to the opening of the field lines on the day-side due to magnetic reconnection with solar wind field lines. As the field lines are dragged to the nightside and pile-up on the magnetotail, a quiet, steady, east-west aligned arc develops – called the growth-phase arc. The precise origin of the arc remains an open question. However, it does seem to map to the near-Earth plasma sheet boundary. The aurora moves equatorward up until the onset.

At the **onset**, the equatorward-most arc brightens up and then breaks up into many pieces. After this, the aurora explodes and fills the sky, and the oval rapidly expands poleward (**expansion phase**) as the polar cap shrinks. The onset is associated with the magnetotail reconnection and(or) current sheet disruption in the near-Earth plasma sheet. The expansion is related to the dipolarization of the inner magnetosphere, associated with fast earthward flows from the tail.

During the expansion, the poleward evolution of the aurora is called the substorm auroral bulge. At the westernmost border of the bulge, a growing vortex called western traveling surge (WTS) moves westward. This is a dynamic feature mostly made of electron energies ~ 10 keV but with a high-energy tail up to 100 keV. These are driven by upward flowing field-aligned currents, fed by horizontal currents of the westward auroral electrojet, and local current loops with downward field-aligned currents. Substorm onset and expansion phase includes a high flux of energetic electron precipitation as compared to the growth phase. An in-

creased hall conductance due to the energetic precipitation might be a cause for the WTS's westward motion (Ebihara & Tanaka, 2015, 2018).

After the expansion, the magnetosphere slowly over a couple of hours reverts to its original pre-growth-phase state known as the **recovery phase**. During this time, pulsating auroral patches are frequent in the auroral oval. The source of the pulsating aurora is likely precipitating electrons of a few tens of keV, caused by cyclotron resonance with lower-band chorus waves in the plasma sheet. However, there have been observations of electron precipitation up to 500 keV in the pulsating patches.

2.6.4 Energetic aurora

As mentioned earlier, electrons of energy < 10 keV cause most auroral emissions at visible wavelengths. Electrons > 10 keV produce a lower intensity of emissions since the number flux of these particles is usually low. The number flux of precipitating particles usually follows a power law with increasing energy ($j_E \propto c^{-E}$). However, such energetic precipitation produces measurable features in the ionosphere that can be studied. Such **energetic aurora**, and energetic electron precipitation that cause it is the focus of this dissertation.

Though the emissions intensities due to energetic precipitation are low, they result in an enhanced $I_{427.8nm}/I_{557.7nm}$ and $I_{427.8nm}/I_{630.0nm}$ ratio. Energetic precipitation can also produce bremsstrahlung X-rays. The flux of X-rays produced by high energy electrons is small; for example, there are about 5 X-ray photons produced per 1000 primary 200 keV electrons. Despite this low flux, studying bremsstrahlung emissions allows us to determine the primary precipitating particles' spectra and spatial and temporal structures. These X-ray emissions have been

measured using detectors onboard balloons, which reach altitudes of $20 - 40$ km, and X-ray imaging instruments onboard satellites such as the PIXIE camera on the Polar satellite (Cummer et al., 2000).

Apart from these emissions, we measure energetic aurora via the ionization produced in the D-region. One method to quantify the ionization is using the attenuation observed in the intensity of incoming cosmic radio noise. Most of the absorption occurs in the D-region, and hence the absorption corresponds to electron energies between 10-100 keV. Cosmic radio noise can be observed through relatively inexpensive measurement devices called riometers (Relative Ionosphere Opacity METER), which can also provide broad coverage. As a result, this technique is useful to explore large-scale morphology of energetic precipitation. ISRs can measure small-scale and high-resolution variations in energetic precipitation, through estimates of detailed altitude ionization profiles caused by energetic precipitation in small-scales. Chapter 3 discusses these measurement techniques in detail.

2.7 Particle Precipitation

Before we discuss the morphology of energetic aurora, we describe what we know about its source mechanisms and location in this section. Charged particles remain trapped in the Earth's magnetic field primarily because of the mirror force that pushes the particle away from increasing magnetic field gradients.

$$\mathbf{F}_{\parallel} = -\mu \nabla_{\parallel} B \tag{2.20}$$

Closer to Earth, the magnetic field gradients along the field lines are high, and

as a result of this geometry, the particles with an equatorial pitch angle greater than the loss-cone angle bounce back. Mechanisms that accelerates ($\frac{\partial \mathbf{v}}{\partial t}$) the charged particles, and scatter them into the loss cone (within velocity space) will increase particle precipitation. Processes that scatter particles so that the parallel component of the velocity decreases (and increases its perpendicular component) reduces precipitation.

2.7.1 Mechanisms

External to the magnetosphere, there are energetic protons (> 100 keV) emitted from the sun during brief bursts of energetic particles called Solar Proton Events (SPE), which makes its way through open-field lines into the polar caps. Galactic cosmic rays, composed of extremely high energy protons (GeVs), also continuously impact the Earth's atmosphere at a steady but low flux rate. Apart from these two primary sources, the rest of the precipitation can be traced to magnetospheric regions.

Particles trapped in closed magnetic field lines can be scattered into the loss-cone via processes such as (Birn et al., 2012; Lyons, 1997):

1. Field-aligned acceleration by parallel electric fields
2. Betatron acceleration
3. Current sheet acceleration or Fermi acceleration of type A or B
4. Wave-particle interactions
5. Turbulence

Direct acceleration can happen in **parallel electric fields** set up in the vicinity of reconnection sites, and field-aligned electric fields associated with auroral

acceleration (in the AAR). If the particles are drifting due to magnetic field curvature or gradient, they may gain energy in the presence of a dusk-ward electric field. Parallel electric-fields are sustained locally in the auroral acceleration zone through small charge imbalances forming a **double layer**, or parallel components of **disperive Alfven waves**.

Betatron acceleration is a result of spatially or temporally varying electromagnetic fields, such that the energy gained in one portion of the gyration is higher than the loss during the other portion (Birn et al., 2012). If the particle is still in the adiabatic limit (i.e., the variation in the field is smaller than the gyroscale of the particle), then a drift of the particle into a higher magnetic field will increase perpendicular energy since the magnetic moment is conserved: $\mu = W_\perp/B$. An earthward directed electric field or drift in the magnetotail can, therefore, cause betatron acceleration, which in effect can increase the pitch angle of the particles and cause precipitation flux to reduce.

Current sheet acceleration is the process by which a particle, in the adiabatic limit, crossing a neutral sheet along an earthward convecting field line, gains momentum in the earthward direction. This is also understood to be the first order **Fermi acceleration of type B** Northrop (1963). However, in the non-adiabatic limit, due to non-guiding center motion, the particles can undergo chaotic scattering resulting in increased precipitation.

Fermi acceleration of type A is associated with particle acceleration due to the shortening of the distance between magnetic mirror points of a trapped particle. This happens on an earthward convecting field line, as the length of the flux tube decreases as it moves earthward. If the second adiabatic invariant is conserved during this motion, then the increase in energy can be inferred from the invariant.

The earthward convection happens during dipolarization at substorm onset, as the stretched field-lines revert to its quiet-time dipolar configuration.

The first and the second adiabatic invariants can be violated due to particle interaction with **plasma waves** (Shprits et al., 2008). During quiet magnetic conditions, particles at $L > 2.5$ can interact with the plasmaspheric hiss. At lower L-values, the pitch angle scattering is dominated by Coulomb collisions and resonant interactions with lightning generated whistlers and anthropogenic VLF transmissions. During active times, in the plasma environment outside the plasmasphere, whistler-mode chorus waves can resonant-scatter. Day-side chorus more efficiently scatters MeV electrons into the loss-cone, while night-side chorus accelerates particles to MeV energies. Electromagnetic Ion Cyclotron wave can be present in small portions of the particle drift orbit, can produce very fast localized losses for relativistic electrons. ELF and VLF waves can also violate the first and second adiabatic invariants and cause pitch angle and energy diffusion of electrons.

Electromagnetic turbulence is another source of non-adiabatic scattering of the particle's pitch angle. They are fast (tens of seconds) and microscale (less than an ion gyroradius) fluctuations of magnetic and electric fields produced by various plasma instabilities. These magnetic field variations can result in inductive electric fields that cause non-adiabatic acceleration of particles (Milovanov & Zelenyi, 2001; Artemyev et al., 2009)

2.7.2 Source Regions

Lyons (1997) broadly classifies the magnetospheric source regions of precipitating particles into three groups:

1. Polar cap precipitation
2. Plasma sheet precipitation
3. Radiation belt precipitation

2.7.2.1 Polar cap precipitation

Over the polar caps, particles precipitate from the magnetosheath and interplanetary plasma along open-field lines that have one end connected to the polar cap and the other to the IMF. Uniform electron precipitation in the polar cap, known as polar rain is observed almost always with energies below a few hundred eVs. Since more interplanetary electrons move away from the Sun than towards it, the polar rain is more intense where the field lines come from the solar direction. At the equatorward boundary of the polar cap, the region transitions into field lines that map to the plasma sheet's outer boundary. There is a "soft electron zone" precipitation in between these two regions, which is seen as discontinuous > 1 keV electron precipitation with pronounced spatial and temporal structure. This layer maps to the low-latitude boundary layer and the dayside boundary plasma sheet.

Discrete auroral arcs are also present in the polar caps. These are narrow precipitation features of electrons that are accelerated towards the ionosphere by upward-directed magnetic-field aligned electric fields in the AAR 2000-3000 km above the ionosphere. See Lyons (1992) tutorial for more details on the mechanisms of generation of a stable auroral arc. Hosokawa et al. (2020) discusses the latest understanding of all auroral features that appear in the polar cap.

2.7.2.2 *Plasma sheet precipitation*

Charged particles populate the plasma sheet from the ionosphere, low-latitude boundary layer, and the mantle (or the magnetopause boundary layer). Particles that are in the plasma sheet interacts with the tail current-sheet, with a dawn-dusk current flow. At the current sheet, these particles undergo either current sheet acceleration or scattering. The nature of the particle's motion depends on the ratio κ^2 (Sergeev et al., 1983) of the minimum radius of field-line curvature to the maximum gyroradius of the particle.

$$\kappa^2 = \Big(\frac{TE_0}{TE}\Big)^{1/2}\Big(\frac{B_n}{1nT}\Big)^2\Big(\frac{L}{1000km}\Big)\Big(\frac{20nT}{B_{lobe}}\Big) \tag{2.21}$$

Here TE is the particle energy, TE_0 is 0.12 eV for protons and 220 eV for electrons. B_n is the magnetic field component perpendicular to the current sheet, B_{lobe} is the magnetic field strength in the lobes above and below the current sheet, L is the scale length for changes in the tangential component of B as it reverses direction across the current sheet. If $\kappa^2 >> 1$, the particle is still in the adiabatic limit as it crosses the current sheet, $\kappa^2 << 1$, the particle undergoes Speiser motion and gains energy. Pitch angle scattering does not occur for the above two cases. Particles with κ^2 between these two regimes undergo motion that is non-adiabatic with significant pitch angle scattering as they cross the current sheet. Since the particle energy $TE \propto \kappa^{-4}$, strong isotropic pitch angle diffusion is expected over a range of four order-of-magnitude of energies at any given location in the current sheet. According to Lyons (1997), electrons ranging from $0.14 - 90$ keV scatters at the distant tail. Closer to the Earth, the scattering energy increases, with the near-tail scattering $31 - 2 \times 10^5$ MeV. Since $TE \propto B_n^{-4}$, and B_n increases closer to the Earth,

the range of energies subject to strong scattering within the current sheet increases strongly toward the Earth. As a result, presumably during magnetically quiet periods, no electron precipitation is expected from the plasma sheet except at the outer boundary. Plasma sheet protons, on the other hand, are subject to strong scattering throughout the plasma sheet. The radial variation of B_n in the plasma sheet leads to a latitudinal energy dispersion in the energies of particles that are current sheet scattered.

Most of the plasma sheet electron precipitation is in a $0.3 - 20$ keV range. Since the gyroradius of these energies is not greater than the current sheet thicknesses observed in most of the plasma sheet, these energies are too low for current sheet scattering. One source of such precipitation is discrete narrow auroral arcs within the plasma sheet driven by magnetic field-aligned electric fields that accelerate electrons to maintain current-continuity in the ionosphere. The remainder of the $0.3 - 20$ keV electron precipitation leads to the "diffuse aurora." Precipitation that leads to the diffuse aurora is isotropic at low energies and anisotropic with increasing electron energy. The transition to anisotropy happens at ~ 5 keV. This variation in the pitch angle distribution is characteristic of pitch angle scattering by wave-particle interactions, and it has been shown that waves are responsible for the diffuse aurora. Nishimura et al. (2020) has reviewed the latest findings on diffuse aurora and its sources.

2.7.2.3 Radiation belt precipitation

Like the outer boundary of the plasma sheet, the outer boundary of the radiation belt can result in strong isotropic pitch angle scattering due to weak magnetic fields close to the current sheet. This is the primary mechanism and source region

discussed in Chapter 5. Additionally, in the radiation belt, there is anisotropic precipitation due to weak pitch-angle scattering in the plasmapause's vicinity due to the plasmaspheric hiss. This band of whistler-mode waves is present through the plasmasphere. This results in continuous precipitation of energetic electrons for $L \sim< 5.2$.

During magnetically active times, such as geomagnetic storms and substorms, enhanced fluxes of electrons in the radiation belt result from a direct injection of electrons from reconnection in the tail. Precipitating particle fluxes following storms are increased by approximately the ratio of the trapped fluxes to those during quiet times. Such loss of energetic electrons from the radiation belt affects the mid-latitude ionosphere and is believed to be an essential source of mid-latitude D-region ionization (Spjeldvik & Thorne, 1975).

2.7.3 Morphology of Energetic Precipitation

The precipitation into the ionosphere forms a statistical pattern in the Earth's magnetic coordinates, which is explained by the morphology of magnetospheric regions connected to it. Hartz & Brice (1967) developed an idealized averaged representation of soft ($\sim< 10$ keV) and energetic electron ($\sim> 40$ keV) precipitation which is pictured in figure 2.4. The energetic precipitation (black dots) is equatorward of the auroral oval, following the auroral zone boundary. Its defining feature is that it peaks in the morning side around 8 MLT. On the other hand, the soft electron (or auroral) precipitation follows the auroral oval with a pre-midnight peak around 23 MLT.

Our interest here lies in energetic precipitation and its morphology and its associations with auroral morphology and its magnetospheric source regions. As

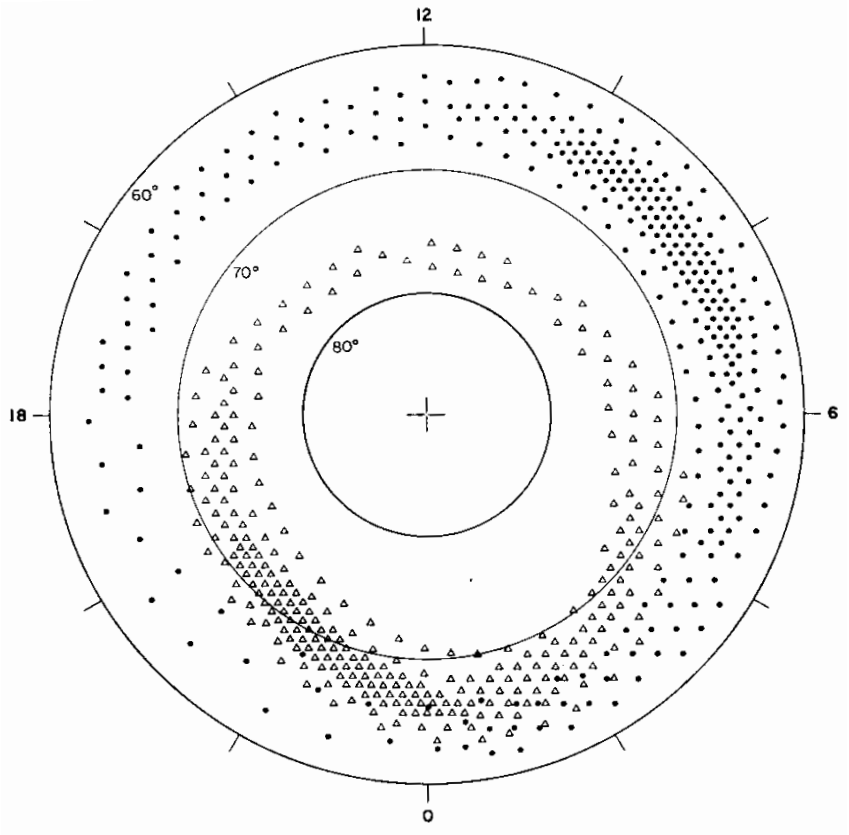

Figure 2.4: Idealized representation of soft and energetic electron precipitation in the northern hemisphere. The density of symbols indicates the average intensity of the flux on a geomagnetic grid. Triangles show the soft electron precipitation, and the dots show the energetic electron precipitation. (Adapted from Figure 19 from Hartz & Brice (1967))

discussed earlier, the auroral oval maps to the plasma sheet. The energetic precipitation seems to map to both the plasma sheet and the trapped particle regions found in the dipolar field lines. As a result, precipitation from the dipolar field lines is observed in the equatorward portion of the auroral oval. Average fluxes of precipitating electrons of energies 150 eV, 1.3 keV, 9.6 keV, and 22 keV for small Kp < 3 are shown in figure 2.5. For the low energy electrons ~ 150 eV in figure 2.5a, there are two peaks, one in the post-noon and another in the post-midnight

sector, which McDiarmid et al. (1975) relates to the magnetosheath electrons entering closed field regions at these MLTs. In figure 2.5b and c, for 1.3 and 9.6 keV a new peak of precipitation starts to form in the pre-midnight section with the magnetosheath electron peaks fading away with increasing energy. This third maximum is associated with auroral substorms and dispersion-less electron injections transporting electrons from the tail to the inner magnetosphere. Using the Combined Release and Radiation Effects Satellite (CRRES) data Friedel et al. (1996) found that the most probable location for electron injection to occur is around 21–23 MLT (pre-midnight) at L=~ 6. Finally, in figure 2.5d, for 22 keV electrons, only the morning maximum remains. This peak, which is the same as the one seen in figure 2.4 for energetic precipitation has two contenders as sources: 1) drifting of quasi-trapped particles during substorm injection and 2) scattering from lower band chorus waves that populate the entire dawn sector (00–12 MLT).

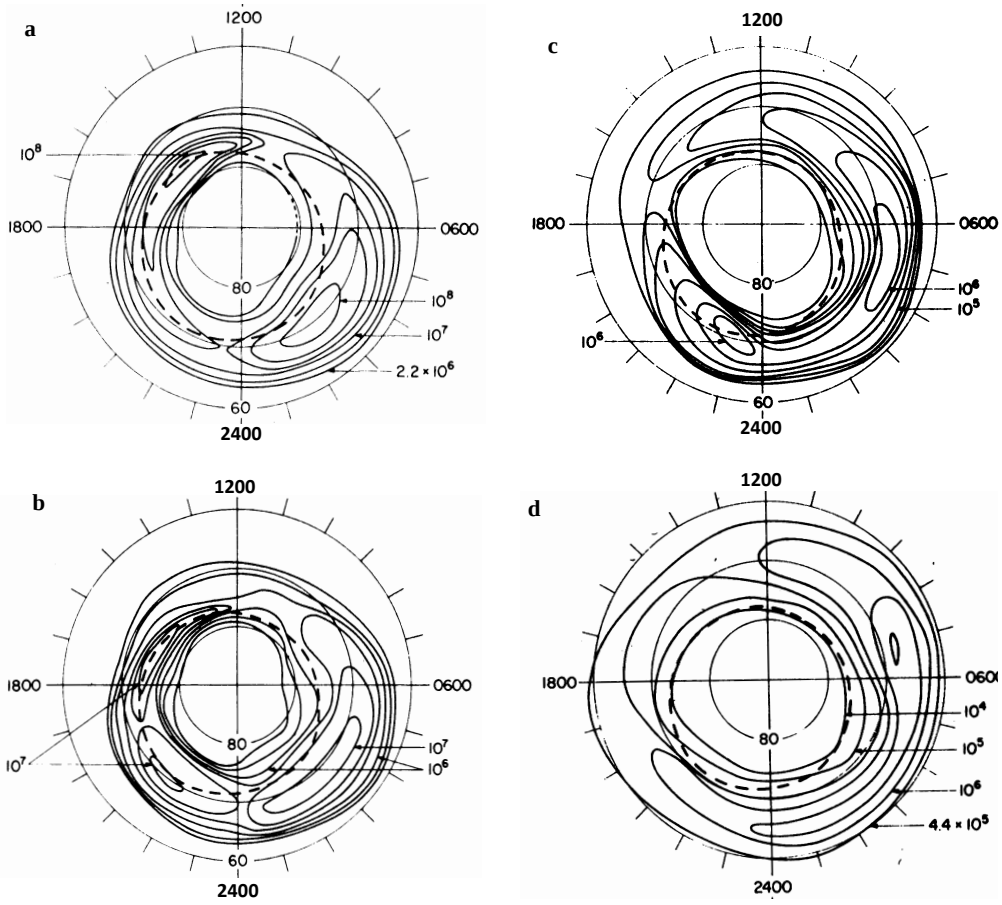

Figure 2.5: Average intensity contours for electrons of (a) 150 eV, (b) 1.3 keV, (c) 9.6 KeV and (d) 22 keV in [cm^2 s sr keV]$^{-1}$. Kp<3 and pitch angles $< 45°$. CGM grid is used for all plots, and noon MLT at top. Adapted from figures 4,6,8 and 9 from McDiarmid et al. (1975)

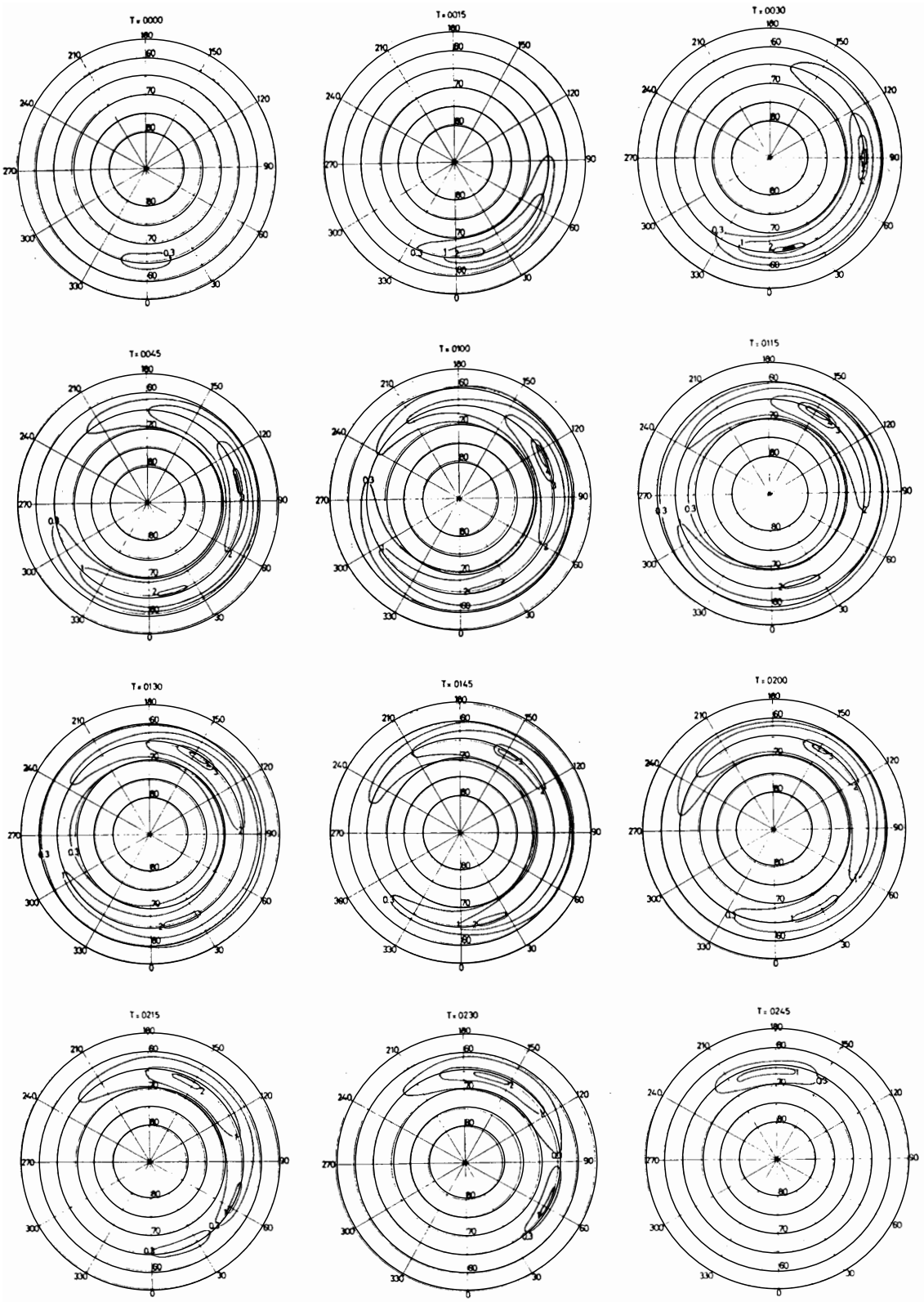
T = 0000
T = 0015
T = 0030
T = 0045
T = 0100
T = 0115
T = 0130
T = 0145
T = 0200
T = 0215
T = 0230
T = 0245

Figure 2.6: Isocontours of cosmic radio noise absorption, showing energetic precipitation intensity of an average substorm obtained from 60 substorms. The time resolution is 15 minutes, and CGM grid is used (Adapted from Figure 9 in Berkey et al. (1974))

Berkey et al. (1974) conducted the most extensive survey of energetic precipitation using a global network of riometers during 60 substorms measured through the solar minimum (1964-1965) and solar maximum (1969). The average expansion of energetic precipitation due to the substorms is captured in figure 2.6. Unlike the previous figures, this attempts to depict the average development of energetic precipitation during substorms, also known as the ionospheric substorm.

In auroral substorms, there is almost always a westward expansion of the auroral precipitation. Westward expansion associated with the WTS) was found in less than half of the substorms, indicating that this feature is not a common part of the energetic precipitation morphology during substorms. However, in almost all substorms, Berkey et al. (1974) found an eastward expansion of energetic precipitation with velocities independent of magnetic activity (i.e., Kp index). For most substorms, the expansion corresponded to the magnetic curvature and gradient drift of electrons in the energy range $\sim$ 50 - 300 keV, which would explain why increased magnetic activity did not affect the eastward expansion. However, the flux of these energies was much greater than what is normally observed in *in situ* measurements, which casts some doubt on drifting of injection electrons being the only source for the observed eastward expansion. The alternate possibility is that substorm dipolarization can increase magnetic field intensity in the inner magnetosphere, with a 100 fold growth of VLF chorus wave intensity (Foster et al., 2014). This sudden increase in chorus intensity can result in the acceleration and pitch an-

gle scattering of electrons from the inner magnetosphere (Bortnik & Thorne, 2007). Lower band chorus waves intensity is highest between 23 – 12 MLT, and for moderate magnetic activity (AE index $\sim 100 - 300$ nT) peaks around 6-12 MLT (Meredith et al., 2012). Therefore, this is the most likely explanation for the peak in energetic precipitation found in the morning sector. Ostgaard (1999) presents more details on the average statistical picture of energetic precipitation during substorms.

Moving forward from the statistical morphology, characterizing the spatial structure of energetic precipitation during dynamic events has been technically challenging due to the lack of instruments with global coverage and simultaneous high spatial and energy resolution. However, individual measurements of energetic precipitation associated with auroral features can give us insights into the spatial structure of energetic precipitation. Here we document a collection of such studies.

Soft electron precipitation $\sim< 10$ keV causes most of the auroral features such as discrete arcs, polar cap arcs, and streamers. **Discrete auroral arcs** are produced by field-aligned electric fields - generated by phenomena such as double layers, dispersive Alfven waves. A classic observation of conjugate electron precipitation associated with a band of multiple discrete arcs is shown in figure 2.7 from Stenbaek-Nielsen et al. (1998). However, sometimes conjugate with discrete arcs, precipitating electron energies have been found to reach energies over 100 keV. Swift & Gorney (1989) explains these as field-aligned electron beams exciting upper hybrid waves that causes pitch angle and energy scatter, resulting in electrons reaching higher energies.

Polar cap arcs, are discrete arcs observed within the polar cap and during quiet magnetic conditions. There are two main types, sun-aligned arcs and transpolar

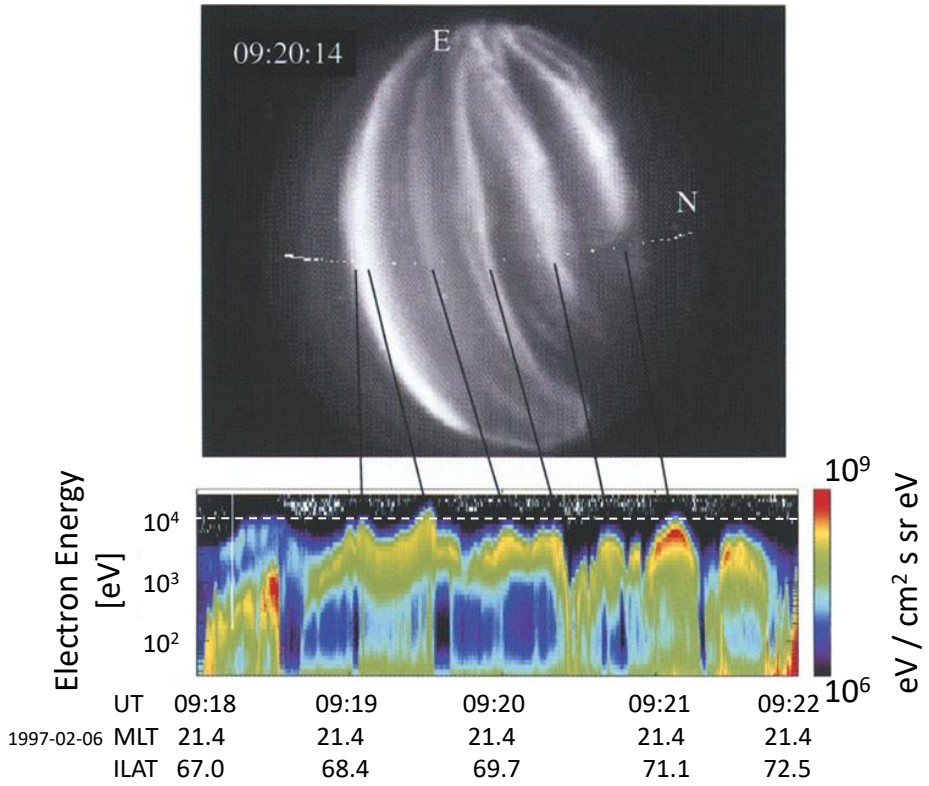

Figure 2.7: Adapted from Figure 2 of Stenbaek-Nielsen et al. (1998). Multiple discrete arcs as seen in the all-sky image and by FAST satellite. The 110 km conjugate is shown at 10s intervals as FAST passed across from left to right. The center panel is a "nodal" format of the electron energy spectrum (integrated over all pitch angles) and shows several inverted-V structures.

arcs. They have different magnetospheric sources depending on the type of the arc with low energy electrons ranging from 0.5 – 3 keV (Whalen et al., 1971). **Auroral streamers** that are found in the poleward boundary of the auroral oval, usually before substorm onsets, are caused by precipitating electron energies $\sim< 10$ keV. These streamers are ionospheric signatures of the earthward flow of plasma from the magnetotail, initiated by nightside reconnection. They are also called Bursty Bulk Flows (BBF). The plasma stream generated field-aligned current around its edges, where there is a plasma pressure gradient. The precipitating low energy

electrons that form the streamers are likely to be field-aligned electrons in the upward field-aligned current (Sergeev et al., 2004).

Omega Bands, Westward Travelling Surges (WTS), Pulsating aurora, and Diffuse aurora are auroral forms with characteristic energy higher than $\sim$10 keV and a substantial energetic tail are . **Omega bands** are wave-like structures that occur at the poleward boundary of the morning-side diffuse aurora (See figure 2.8). The spectra of the diffuse region equatorward of the edges of the omega band have electron precipitation of energies $\sim>$ 10 keV (Lyons & Fennell, 1986), while energies within the band are only about 2–5 keV (Amm et al., 2005). Omega bands are likely caused by Kelvin-Helmholtz instability driven by flow shears at the inner edge of the plasma sheet, or perturbation of the hot plasma torus boundary (Partamies et al., 2017).

Figure 2.8: Photograph of the omega band from Akasofu (2012).

Westward Travelling Surge (WTS) are the auroral forms found on the westernmost border of the evolving substorm auroral bulge during the substorm onset and expansion. MHD simulations by Ebihara & Tanaka (2018) suggest that a complex mechanism of field-aligned currents fed by horizontal currents of the westward auroral electrojet, and local current loops with downward field-aligned currents drive the surge. Though low energy auroral electrons from the plasma sheet dominate the surge, at 10 keV, there is shoulder in the precipitating electron energy spectrum, with considerable fluxes up to 100 keV (Olsson et al., 1996). The westward motion of the WTS might

Figure 2.9: Photograph of an auroral vortex associated with WTS Akasofu (2012).

be influenced by the increased hall conductance caused by this energetic precipitation (Ebihara & Tanaka, 2015, 2018). WTS can form large vortices along the western and poleward border, as seen in figure 2.9.

Associated with the substorm recovery phase, patches of diffuse aurora frequently oscillate in intensity. This is known as **pulsating aurora** (Nishimura et al., 2020). Cosmic noise absorption measurements (Grandin et al., 2017) and rocket observations (Saito et al., 1992) have shown that these are made of precipitating electrons of a few to tens of keV energy. The pulsation is likely due to cyclotron resonance of lower-band chorus waves with plasma sheet electrons in the equatorial plane (Nishimura et al., 2010; Li et al., 2012). Figure 2.10 from Nishimura et al. (2010) shows definitive evidence of the pulsating patches being driven by chorus wave intensity in the plasma sheet (right panel, red-line), with correlated pulsating auroral intensity at the satellite footpoint (left panel, right panel blue-line). Miyoshi et al. (2015) reports electron precipitation up to 200 keV observed through ionization by pulsating aurora as low as 60 km in altitude using ISR measurements. Confirming this (Oyama et al., 2017) observed up to 500 keV electron precipitation in pulsating aurora, with the highest energy appearing inside the auroral patch.

Finally, the **diffuse aurora** is made up of electron precipitation ranging from 0.1 – 10 keV, that extends beyond 30 keV frequently. In fact, the energetic precipitation in the average morphology represented in figure 2.4 is mainly associated with the diffuse aurora. As mentioned previously, scattering of inner plasma sheet electrons by chorus waves are the likely cause of such energetic electrons during magnetically active times (Thorne et al., 2010). Diffuse aurora is observed mostly in the equatorward portion of the auroral oval. It is usually an east-west aligned band with a considerable north-south thickness (~ 500 km) in the night sky. Figure

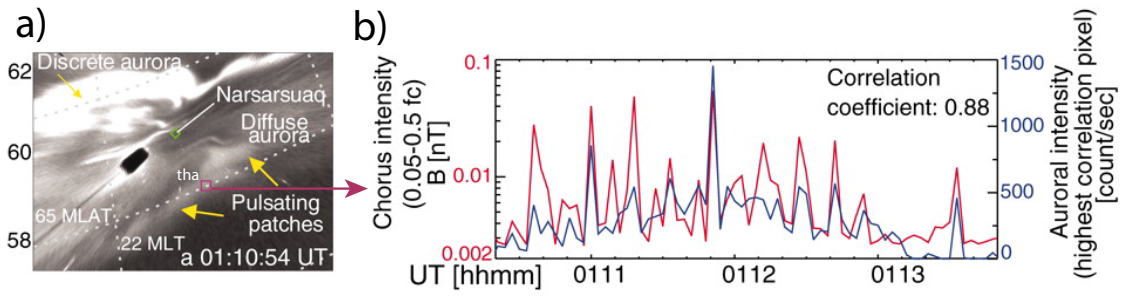

Figure 2.10: (a) Coordinated observation of pulsating aurora by the Narsarsuaq ASI and THEMIS-A spacecraft from 01:10:20 to 01:13:50 UT on 15 February 2009. (Right) Correlation of lower-band chorus integrated magnetic field intensity over 0.05 to 0.5 fc (red) and auroral intensity (b) at the highest cross-correlation pixel. The figure is adapted from Figure 1 of Nishimura et al. (2010).

2.11a) shows the diffuse aurora in the southern-hemisphere night sky, along with pulsating aurora on its equatorward border, and discrete auroral activity poleward of it. The magenta dotted line is the track of the SAMPEX satellite footprint. Figure 2.11b) shows how the auroral intensity varies along the satellite track, and figure 2.11c) shows how it correlates with an increase in energetic particle flux that peaks over the diffuse aurora. In this example, over the diffuse aurora, there is also an enhancement of relativistic electron precipitation greater than 1 MeV (Kurita et al., 2015).

2.7.4 Ionospheric Effects

2.7.4.1 Atmospheric Chemistry

Energetic particle precipitation affects the Thermosphere and Mesosphere, as these particles penetrate much deeper into the atmosphere due to their higher kinetic energy (Mironova et al., 2015). The four main sources of such precipitation are solar protons, galactic cosmic rays, auroral, sub-relativistic, and relativistic elec-

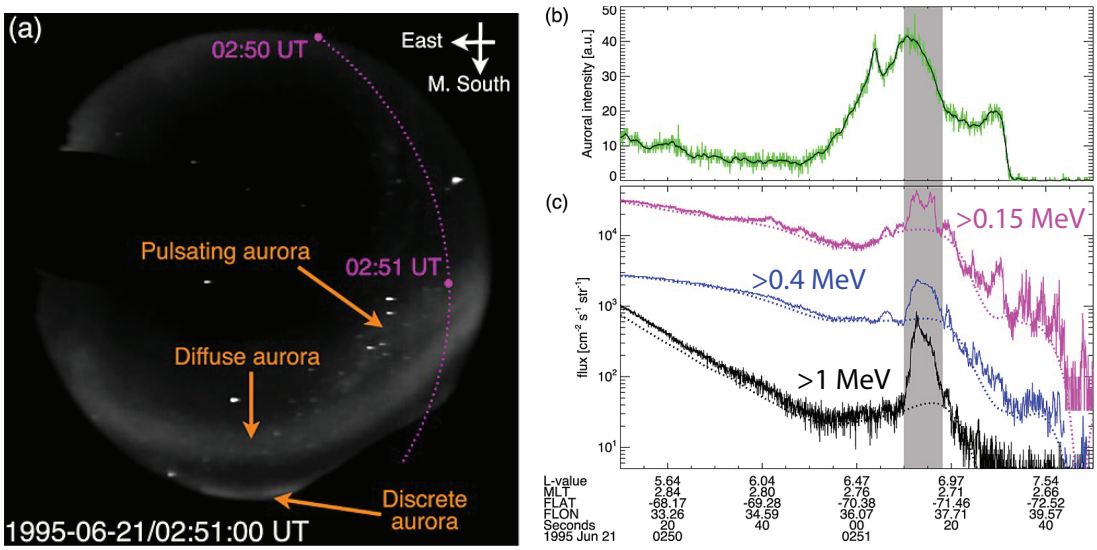

Figure 2.11: a) An all-sky imager at the Syowa station in Antarctica, showing diffuse, pulsating, and discrete aurora. The magenta dotted line shows the SAMPEX satellite track on the night sky, b) Auroral intensity observed along the SAMPEX track, c) Flux of energetic electrons measured by SAMPEX at Low Earth Orbit. The figure is adapted from Kurita et al. (2015).

tron precipitation from the magnetosphere. The role of auroral electrons that reach energies of ~ 30 keV on chemistry in these regions is well understood. Their penetration depth is above 90 km and represents one of the primary sources of nitrogen oxide in the thermosphere. During the polar night, NO_x can sink to lower altitudes and cause ozone depletion in the mesosphere. Though Seppälä et al. (2007) observed this with coordinated measurements of NO_2 and ozone using spacecraft, a study over an ensemble of many years is necessary to make a statement of statistical significance on this effect. One source of the drifting of NO_x down to the stratosphere is the polar vortex during polar nights. This hypothesis agrees qualitatively with observations and models, but not quantitatively. This effect may nevertheless be important for climate, due to the potential effect ozone depletion

has on polar surface temperatures.

Energetic electron precipitation from the magnetosphere (30 keV up to several MeV) also produces NO_x in the lower thermosphere and mesosphere. These particles penetrate to depths of 90 km down to 50 km. Sinnhuber et al. (2012) notes that there can be an impact of relativistic electron precipitation on ozone in the mid-stratosphere; however, the coupling mechanisms are unclear. Energetic electron precipitation, measured using the MEPED detector onboard NOAA/POES satellites during $2002 - 2012$, cause up to 90% destruction of mesospheric ozone at 60-80 km altitudes. Three other satellite instruments GOMOS, MLS, and SABER, independently observed this loss. There is no realistic model-based study of these effects because the ionization rate caused by radiation belt particles is unknown. As a result of this, and the lack of an understanding of the mechanism of coupling with the stratosphere, the role of radiation belt electrons and its effect on atmospheric chemistry remain unresolved.

2.7.4.2 Radio propagation

Energetic electron precipitation also leads to the absorption of radio waves in the D-region. A radio wave propagating through the ionosphere causes the electrons to oscillate. The collision of electrons driven by the waves, with more massive neutral particles, transfers the wave energy into the medium (Hargreaves, 1969). The rate of absorption depends on the number of collisions per oscillation of the wave (ν/ω). And the absorption is proportional to $exp[-(\kappa \cdot l)]$, where l is the distance of propagation, and κ is the attenuation rate.

$$\kappa = \frac{e^2}{2mc\epsilon_0}\frac{1}{\mu}\frac{N_e\nu}{\nu^2 + (\omega \pm \omega_L)^2} \tag{2.22}$$

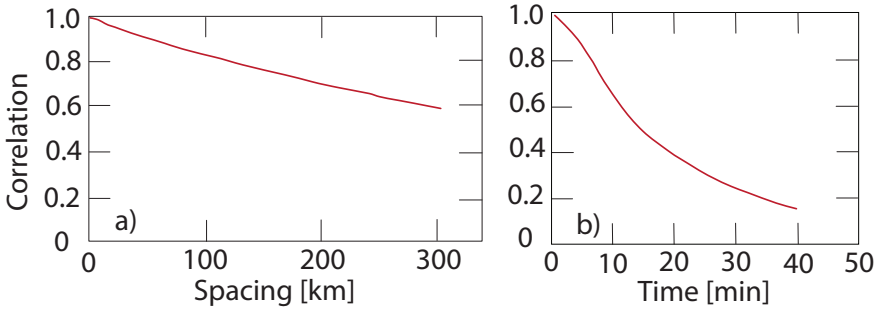

Figure 2.12: a) Cross-correlation between observed absorption at two stations versus distance between stations. b) Median autocorrelation function for observed absorption. After Holt et al. (1961); Hunsucker & Bates (1969).

Here N_e is the electron density, $\omega_L = \omega_H \cos\theta$, θ is the angle between the magnetic field and the direction of propagation of the wave, ω_H is the gyrofrequency. The strength of absorption falls as the square of the radio frequency. Hence, energetic electron precipitation affects the lower limit of HF (3-30 MHz) communications in the auroral zones. Radio waves in the hundreds of MHz or higher are immune from auroral absorption.

In high latitudes, two categories of absorption caused by electron precipitation have been defined: auroral absorption (AA) and sudden commencement absorption (SCA). AA's, as indicated above, refers to radio absorption caused by energetic or relativistic electron precipitation in the auroral zones. At the same time, SCA is radio absorption that occurs right after a substorm or storm onset. Solar energetic protons cause another prominent high-altitude absorption phenomenon that results in radio absorption through the whole polar cap known as 'polar cap absorption' or PCA.

Corresponding to the morphology of energetic precipitation in the auroral zones, AA peaks 1° to 2° equatorward of the auroral zone peak and sometimes extends to mid-latitudes. The highest absorption in MLT is observed during mid-day be-

tween 9 to 12 MLT. Interesting analysis by Holt et al. (1961) and Parthasarathy & Berkey (1965) showed structuring in AA over spatial scales of a few hundred kilometers and timescales of a few tens of minutes (See Figure 2.12).

The D-region property to attenuate HF waves (3 – 30 MHz) can be utilized to measure the ionization, and consequently, the hardness and flux of the precipitating particles that cause the ionization (Mitra & Shain, 1953). For example, the cosmic-noise method of measuring ionospheric absorption has led to the use of riometers to determine variation in energetic precipitation. They are stable receivers that continuously listens to cosmic radio emissions at around 30 MHz, whose flux remains constant over long periods. The apparent intensity variations of this noise, received by the riometers, represent corresponding variations of ionospheric absorption.

2.7.4.3 Conductance Enhancement

Charged particle precipitation increases the conductivity of the ionosphere by increasing the density of ions and electrons (See section 2.4.4). In high latitudes, therefore, conductance enhancement correlates with auroral structures. Global statistical models derived from satellite measurements of precipitation provide a crude approximation of ionospheric conductances that are inadequate in modeling the electric current flows during dynamic events like substorms (Brekke & Moen, 1993, and references therein). Kirkwood et al. (1988) used multiple instruments to approximate the ionospheric conductance during seven substorms (including both the E- and D-regions). Table 2.1 summarizes the quantitative effect of precipitation on conductance during different substorm auroral forms.

Precipitation associated with discrete arcs causes the highest conductance en-

	Σ_H [S]	Σ_P [S]	$\frac{\Sigma_H}{\Sigma_P}$
Growth-phase diffuse precipitation	2-15	1-8	1.6-2.0
Pre-onset discrete arcs (peaks)	20-60	18-28	1.0-2.5
Discrete arcs at onset (peaks): WTS	60-80	22-28	2.0-4.0
: AB	30-100	10-35	2.0-3.5
: WK	30-120	20-48	1.5-3.5
Expansion phase diffuse aurora	15-30	8-12	2.0-2.5

Table 2.1: Conductance associated with auroral forms during substorms. WTS: Westward traveling surge, AB: the northward edge of the auroral bulge, WK: bright rayed bands at the southern edge/ wake of WTS.

hancements. However, these are limited to within the thickness of the arc ($\sim$<10 km). On the other hand, diffuse precipitation spans large areas ($\sim 2000 \times 100$ km) though its local conductance is low. Therefore, the net contribution of ionospheric conductance is likely to be dominated by diffuse precipitation, which contains the greatest share of energetic precipitation. To the best of our knowledge, no detailed study has been conducted on the contribution of energetic precipitation towards the total ionospheric conductance. Chapter 6 of this dissertation addresses this question by estimating the altitude profiles of conductivity during different substorm phases using ISR measurements of D-region ionization.

CHAPTER 3

Measuring Energetic Particle Precipitation

3.1 Remote-sensing the Ionosphere

Now that we know that charged particle precipitation can affect the ionosphere, we introduce the different methods available to probe the ionosphere remotely from the ground. We restrict the discussion to the most popular ones, and those used for the analysis presented in chapters 4 - 7.

3.1.1 Incoherent Scatter Radar

Incoherent scatter radars are a powerful diagnostic tool used to estimate the properties of plasma in the Earth's ionosphere. The core principle is to utilize the phenomenon of incoherent scattering, which is the extremely weak back-scatter resulting from small fluctuations in the plasma density, caused by the discreteness and the random thermal motions of the ions and electrons. This weak scattering differs from the process of reflection of waves from plasma when the wave frequency is less than the plasma frequency.

Ionosondes operating at frequencies ranging from a few hundred kHz to 15–20 MHz, use the property of reflection. They are the predecessor to ISR's in terms of remote sensing techniques of the ionosphere. They transmit pulses while sweeping through a wide range of frequencies, and derives the shape of the altitude profile of electron density by measuring the echo time delay as a function of frequency.

Reflection and refraction are strong interactions between the radio wave and plasma, where theory can assume plasma is continuous. However, in reality, plasma is made of discrete electrons and ions, and the discreteness results in fluctuating

plasma densities at small spatial scales. These fluctuations vary in time due to the thermal motion of electrons and ions. When the radar frequency is above the plasma frequency, the waves can travel through the plasma without reflecting. However, the refractive index along the path of the wave fluctuates due to small-scale plasma density fluctuations, which causes weak scattering of the waves in different directions. This scattered wave contains information about the plasma density n_e, electron and ion temperatures (T_e, T_i), ion composition (n_s), bulk plasma motion (v_i) and other statistical properties of plasma. We can measure these plasma properties across the path of the radio wave traveling through the ionosphere. The ability to gain this wealth of information from the plasma makes the incoherent scatter radar technique powerful. However, the back-scattered signal is feeble and requires sensitive receiver systems to detect it.

3.1.1.1 ISR Theory

Scattering off free electrons

The primary scattering process ISRs rely on is Thomson scattering (the low-energy limit of Compton scattering). Here free electrons in a material scatter electromagnetic waves in a particular direction with a scattering cross-section of $\sum = 4\pi(r_e \sin\gamma)^2$ where $r_e = \mu_0 e^2/m_e$ is the electron radius, and γ is the angle between the direction of the incident electric field and the direction to the observer. For a direct back-scatter, the scattering angle will be 90° so that the scattering cross-section of an electron is $\sum_e \sim 10^{-28} m^2$. This is quite weak, and even if the transmitted wave is scattered off a volume of 1000 km ^{3}, the total effective scattering cross-section will only be 10^{-4} m^2. According to Ratcliffe (1972), the problem involved is equivalent to detecting a small coin at a range of several hundred kilometers.

Using simple scattering theory, we can argue that scattering of a transmitted signal with a wave vector $\boldsymbol{k}$ by plasma in a volume $A\ dz$ at height z with the total number of electrons in the volume being $N(z)\ A\ dz$ is

$$s(k \cdot z) = \text{constant} \times N(z) A\ dz \exp(2ik_z \cdot z) \tag{3.1}$$

And the total signal scattered from the range z_1 to z_2 is

$$S(k) = \text{constant} \times \int_{z_1}^{z_2} N(z) A\ dz \exp(2ik_z \cdot z) \tag{3.2}$$

which corresponds to the Fourier transform of $N(z)$ over the range, where the total phase change during the transmitted signal's path is $2\boldsymbol{k} \cdot \boldsymbol{z}$ (Beynon & Williams, 1978).

If the plasma consists of entirely free electrons distributed randomly with an average spacing of δ, where $|k| << 2\pi/\delta$, then the Fourier transform of $N(z)$ will be independent of k. This implies that when the electron motion is independent of each other, the incident wave is scattered equally for all wavelengths. Because of this random motion, the signals are scattered with random phases so that at the receiver, the signal powers add, and the scattering is truly incoherent. As a result, the total power scattered by a given volume is proportional to $\sum_e N(z)$, and by measuring the scattered power, we can determine the electron density $N(z)$. Furthermore, if the frequency of the transmitted wave is monochromatic, the scattered wave will have a spread in the frequency proportional to the electron's thermal velocity.

Electrons are not truly free in a plasma

Since ions attract electrons while repelling themselves, around each charged par-

ticle in the plasma, there is always a potential distribution different from the free space potential. The unlike charges, bring the plasma closer, while the repulsion between the like charges and the thermal velocities of the particles pull them apart. As a result, the ions form a shielding layer around each electron, and vice versa, the scale of which is represented by the balance of thermal energy and electrostatic potential energy. The Debye length λ_D quantitatively represents the scale.

$$\lambda_D = (\epsilon_0 k T_e / N_e^2)^{1/2} \tag{3.3}$$

For wavelengths that are much smaller than the Debye length, we can consider scattering from free electrons.

Quasi-coherent scattering

However, when the incident wavelength is much higher than the Debye length, the scattering is no longer from independent free electrons. The electrostatic coupling between ions and electrons generates waves in plasma, such as the ion-acoustic, electron-acoustic, or plasma waves. These waves cause spatial electron density variations that result in 'quasi-coherent' scattering of the incident radio waves (analogous to Bragg scattering). This type of scattering is much stronger than that from free electrons. If an upward traveling wave of velocity V and wavelength Λ scatters an incoming radio wave of frequency f, it will experience a Doppler shift of $\Delta f = -V/\Lambda = -F(\Lambda)$, where $F(\Lambda)$ is the frequency of the plasma or ion-acoustic wave. Therefore ISRs not only depend on truly incoherent scatter but quasi-coherent scatter that produces a much stronger scattered signal with a more complex and information rich-spectra.

The ion-acoustic and plasma waves occur over a wide and continuous spectrum of wavelengths propagating in all directions. However, waves in plasma of

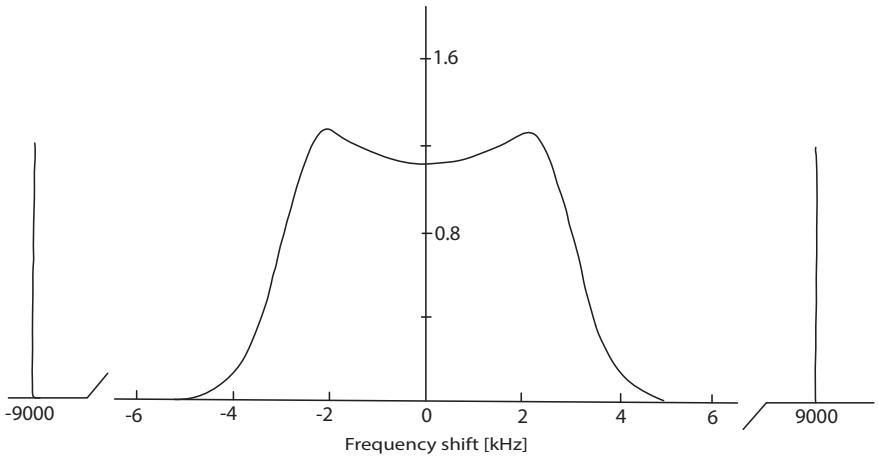

Figure 3.1: Theoretical ISR spectrum with the ion line (or ion spectra) and plasma lines, with the following properties $N = 10^{12}$ m^{-3}, $T_e = 1000$ K, $T_i = 1000$ K, $\lambda = 1$ m, $M_i = 16$. After Figure 6 of Beynon & Williams (1978).

wavelengths Λ can scatter the incident radio signals with wavelength ($\lambda = 2\pi/k$) if $\Lambda = \frac{1}{2}\lambda$. The scattered signal traveling away from the radar has a negative Doppler shift $-F(\Lambda)$, and those traveling towards the radar have a positive shift of $+F(\Lambda)$. Since both ion-acoustic waves and plasma waves that travel away and towards the radar exists, the spectrum of the scattered radio wave has four components centered at the frequencies: $f \pm F^{+}(\Lambda)$ and $f \pm F^{-}(\Lambda)$, where $F^{+}(\Lambda)$ is the frequency of the ion-acoustic wave and $F^{-}(\Lambda)$ is the plasma wave frequency (Beynon & Williams, 1978).

$$F^{+}(\Lambda) = \frac{1}{\Lambda}\Big[\Big(\frac{KT_i}{m_i}\Big)\Big(1 + \frac{T_e}{T_i}\Big)\Big]^{1/2} \tag{3.4}$$

$$F^{-}(\Lambda) = f_p\Big[1 + 12\pi^2\frac{D^2}{\Lambda^2}\Big]^{1/2} \tag{3.5}$$

Broadening of ion-acoustic lines

The degree of damping of the waves affects the shape of the spectral lines. The power spectrum of a signal is the Fourier transform of its autocorrelation function. (The autocorrelation function of a signal is the Pearson correlation of the values of the signal at different times as a function of the time lag between them $R_{XX}(\tau) = E[S(t)S(t+\tau)^*]$). The spectrum of a monochromatic (single-frequency or sinusoidal) signal is a Dirac delta function. Its autocorrelation function will, therefore, be a simple sinusoidal. If the waves are damped, then the monochromatic signal's amplitude and phase will not be correlated with that in the distant future. Therefore, its autocorrelation function is damped by a certain time constant and is no longer sinusoidal, which results in the broadening of the Dirac delta function.

In a plasma in thermal equilibrium, ion acoustic oscillations are inherently present. The fluctuation spectra at a given wave vector k, is altered by ion Landau damping. This damping process happens when waves transfer energy to particles with speeds slightly less than the wave velocity and moving in the same direction. The energy can be transferred in the opposite direction when the particles are moving at a slightly higher speed than the wave. It turns out that the ion-acoustic wave's velocity is well within the Maxwell distribution of thermal ions, so there are always more ions with a slightly lower speed moving in the direction of the wave than ions with higher speed. Therefore, the ion-acoustic waves are heavily damped. As a result, the ion-line is by no means a *line*, but rather a broad spectrum with a characteristic double-hump merging at the center frequency, as shown in figure 3.1. The plasma wave (Langmuir mode) has a much higher velocity than the thermal electrons and are not damped, and is seen as a 'plasma-line' in figure 3.1. They are weak but undamped and lies at the plasma frequency. When present, they provide an independent calibration point for plasma density.

Estimating plasma properties from the scattered spectra

From the power spectra, we can determine several plasma properties. The first and most relevant property for this dissertation is electron density varying with height $N_e(z)$. There are three different independent ways to determine this.

1. From the total power of the scattered wave from a height h, received by the radar (Beynon & Williams, 1978).

$$S(h) = K \sum N_e(z)/h^2 = K \sum_e sin^2\gamma N_e(z)/(1 + T_e/T_i)h^2 \tag{3.6}$$

   Here K is a constant dependent on the power transmitted and an effective collecting area of the receiving antenna. If the power scattered from a given height is measured, and if we know T_e/T_i, we can determine $KN_e(z)$. The constant K can be found by measuring $KN_e(z)$ for an F2 layer peak and independently measuring the critical frequency of the F2 layer ($foF2$) using an ionosonde.

2. From the polarization of a signal traveling through an ionized medium causing Faraday rotation (Ω), which provides an absolute measurement of N_e, but errors become high at high-altitudes since $d\Omega/\ dz$ is small at high altitudes (Beynon & Williams, 1978; Shpynev, 2017).

3. From the plasma lines, which have a frequency $fp \simeq \pm 9N_e^{1/2}Hz$. Here N_e is in the units of electrons/m^3.

Other properties that we can determine from the spectra are (Beynon & Williams, 1978):

- The electron-ion temperature ratio T_e/T_i from the sharpness of the ion line,

- The ratio of ion temperature and ion mass T_i/m_i from the separation of the two ion maxima,
- Ion mass m_i (Tepley & Mathews, 1985),
- Plasma velocity V_p through the mean Doppler shift of the scattered spectrum along three separate radar-look directions within the same scattering volume (Doupnik et al., 1972; Heinselman & Nicolls, 2008),
- Ion-neutral collision frequency ν_{in} which can be estimated at lower altitudes where $\nu_{in} >> F^{+}(\Lambda)$ from the spectral shape of ion-line (Dougherty & Farley, 1963; Lathuillere et al., 1983) and in the absence of neutral wind, from the relation between electric field and ion velocity (Nygrén et al., 1987),
- The spectrum of suprathermal electrons from altitude profiles of electron density derived from plasma frequency (Guio & Lilensten, 1999),
- Electric current density j, using the difference in the mean drift velocities of the ions and electrons, is reflected in the difference between the mean shift of ion spectrum and plasma lines, observed from three look directions within a volume (Thayer, 2000).

Impact of collisions on the spectra

In the D-region, the ion spectra become much narrower because ion-acoustic wave frequency reduces with decreasing T_i and an increasing m_i. With decreasing altitude, the ion-neutral collision frequency ν_{in} decreases sharply in proportion to the neutral density. As ν_{in} becomes much greater than $F^{+}(\Lambda)$, the ion-acoustic waves can no longer propagate, and it loses its double-humped appearance in the power spectra. As the radar observes through a wavelength λ, the shape of

the ion spectrum under this condition is determined by $\psi_i = \lambda/4\pi l_i$, where the ion mean free path is $l_i = (2\kappa T_i/m_i)^{1/2}/\nu_{in})$. It varies as shown in figure 3.2.

Deciphering the range of scattering

Though the shape of the ion spectra changes with increasing collisions in the D-region, the electron density is still proportional to the area under the spectra, which is the power of the scattered wave received by the radar. We can estimate the altitude profile of the electron density by determining the range of the scatter using the delay between the transmission and reception of the signal. There are several ways to structure the transmitted signal: it can be a continuous or short-pulsed signal. The short pulse or pulsed radar or monostatic method is the most commonly used as it requires only one antenna. We can achieve adequate spectral resolution by using multi-pulse techniques and improve the height resolution by reducing the individual pulse duration (τ). If τ is too low, the signal-to-noise ratio (SNR) will eventually become poor. We can improve the height resolution by maintaining adequate SNR by splitting each transmitted pulse into several subpulses with 180° phase shifts at the beginning of each subpulse. The patterns of phase changes within a pulse are determined by a series of codes known as Barker codes. They show significant improvement in height reso-

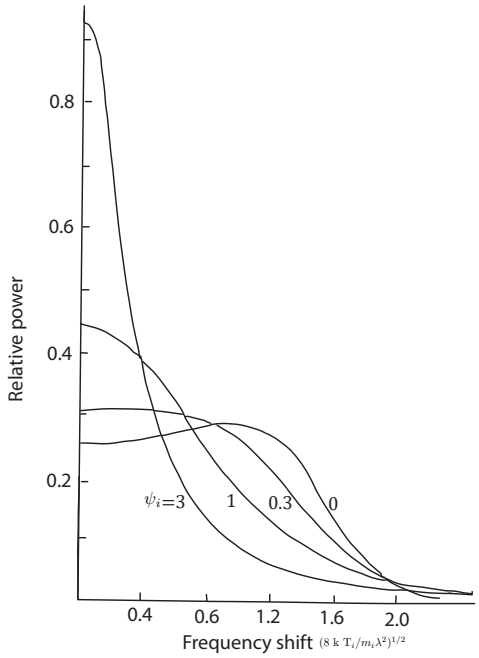

Figure 3.2: Impact of collisions on ion spectrum. $\psi_i \propto \nu_{in}(m_i/T_i)^{1/2}$. After figure 3 in Dougherty & Farley (1963).

lution without sacrificing SNR with the receiver, also coded the same way. With a thirteen-bit Barker code ($+++++--++-+-+$) we can determine electron density enhancements in D-region with an altitude resolution of $\sim$ 1.5 km.

In the following subsections, we describe the main techniques we have enlisted in chapter 4 - 5 to estimate the energy spectra of primary precipitating energetic electrons using altitude profiles of electron density measurements from ISRs.

3.1.1.2 Estimating precipitating electron flux

Energetic charged particles precipitating into the ionosphere collide with and ionize neutral atoms, independent of the presence of other precipitating particles. As a result, the ionization rate of the ionospheric plasma during precipitation is a linear function of the precipitating charged particle *flux*. A forward model A that transforms precipitating charged particle fluxes $\phi(E)$ to the ionization rate $q(z)$ it causes can be developed with the knowledge of charged particle transport, ionization of atmospheric gases and ionospheric chemistry (Kaeppler et al., 2019).

$$q(z) = A\,\phi = \sum_{E} A(E, z)\phi(E)\Delta E \tag{3.7}$$

The forward model A is a 2D matrix with the number of columns equal to the number of energy bins associated with the precipitating differential number flux. In contrast, the number of rows is equal to the altitude bins related to the altitude profile of the production rates.

$$\begin{bmatrix} q(h_1) \\ q(h_2) \\ . \\ . \\ q(h_M) \end{bmatrix} = \begin{bmatrix} a_{11} & . & . & a_{1N} \\ . & . & . & . \\ . & . & . & . \\ a_{M1} & . & . & a_{MN} \end{bmatrix} \begin{bmatrix} \phi(E_1) \\ \phi(E_2) \\ . \\ . \\ \phi(E_N) \end{bmatrix} \tag{3.8}$$

There are a total of N unknowns $\phi(E_n)$ in the equation 3.8, with a total of M equations associated with M range bins of production rates estimated by the radar. Usually, the system of equations might seem to be an over-determined system where $M > N$. However, having more measurements than unknowns does not guarantee an over-determined problem since often A is found to be rank deficient or ill-conditioned regardless of its dimensions.

Using ISR and equation 2.8, we can estimate $q(z)$. And if A is known, then to find $\phi(E)$, we cannot merely carry out a simple inversion. We must seek a pseudo-inverse of the forward model represented in equation 3.8.

$$\phi = A^{\dagger}\, q \tag{3.9}$$

There are two reasons for this: 1) as mentioned above, the number of measurements is not equal to the number of unknowns, 2) there is noise in the data. Standard inversion techniques from linear algebra that work on idealized data fail with noise or measurement uncertainties.

There are several methods to solve 3.8 to estimate $\phi(E)$, a summary of the general methods and techniques to calculate a pseudo-inverse ($A^{\dagger}$) found in section 7 of Semeter & Zettergren (2014) is presented here. To solve ill-posed problems

such as the current problem with non-unique solutions, a regularization process that adds information to prevent over-fitting is useful. Tikhonov regularization is one such technique that is particularly useful. The framework it provides can find unique-solutions to rank-deficient inverse problems. The approach estimates the unknown x of a forward model $y = Ax$ by minimizing the cost function of the form

$$\hat{x} = \arg\min_{x}\{||Ax - y||^2 + \alpha||Lx||^2\} \tag{3.10}$$

where α balances the cost function (modeled - measured data) and a constraint (L) on the solution behavior, which typically avoids overfitting.

Different constraints (L) make equation 3.10 equivalent to different inversion approaches. When $L = 0$ or $\alpha = 0$, equation 3.10 reduces to the least squares solution, given by $\hat{x}_{LE} = (A^T A)^{-1} A^T y)$. For rank-deficient problems, when there is insufficient information in the data to estimate the desired model, $\hat{x}_{LE}$ is highly sensitive to noise in measurements, including round-off error. Therefore, to limit solution variability and noise sensitivity, a truncated singular value decomposition (TSVD) inversion is used. This is equivalent to setting $L = I$ in equation 3.10. However, this approach does not allow for inclusion of prior knowledge (statistical or physical) about the solution. Bayesian approachs allow the incorporation of statistical prior information about x, for instance $L = I$ and $\alpha =$ ratio of data variance to model variance results in the minimum mean square estimator (MMSE): $\hat{x} = \sum_x A^T (A \sum_{xy} A^T A + \sum_e)^{-1} y$ where $\sum_x$ and $\sum_e$ are the error covariances for x and noise, while $\sum_{xy}$ is the cross-covariance of x and y.

Finally, if L is a measure of the entropy of x, then equation 3.10 reduces to a variant of the popular maximum entropy method (MEM). This method is used to

solve equation 3.9 and estimate precipitating electron flux from ISR measurements.

3.1.1.3 Maximum Entropy Inversion

The maximum entropy principle was first introduced by Jaynes (1957), extending the reach of the concept of 'entropy' discovered by C. E. Shannon by connecting information theory with statistical mechanics. The 'amount of uncertainty' of the outcome of an event is captured by a discrete probability distribution, where we can intuitively gather that a broad distribution represents more uncertainty than a narrow distribution. In this sense, we can define entropy for a probability distribution p_i, allowing us to consider the term 'entropy' to be synonymous with 'uncertainty.'

Shannon defined entropy by finding a quantity that is positive, increases with increasing uncertainty, and is additive for independent sources of uncertainty.

$$H(p_1...p_n) = -K \sum_i p_i \ln p_i \tag{3.11}$$

Probability theory has two main schools of thought. i) The frequentist or objective school regards the probability of an event as an objective property that can be empirically measured by observing frequency ratios in a random experiment. ii) The Bayesian or 'subjective' school of thought regards the probability of an event as an expression of our expectation that the event will or did occur based on whatever (prior) information is available. Here we adopt the subjective point of view by describing entropy as uncertainty.

Jaynes' maximum entropy principle suggests that if you were to infer the probability distribution of a process based on incomplete information, that *probability distribution must have maximum entropy subject to whatever is known* (Jaynes, 1957).

And this will be the only unbiased estimate that we can make, which is maximally noncommittal concerning the missing information. To use any other distribution would amount to arbitrarily assuming information that we do not have.

We estimate such a probability distribution p_i by maximizing $H(p_1...p_n)$ subject to the normalization condition:

$$\sum p_i = 1 \tag{3.12}$$

and prior information in the form of constraints on the moments of the distribution:

$$\langle f(x) \rangle = \sum_{i=1}^{n} p_i f(x_i) \tag{3.13}$$

Using the method of Lagrangian multipliers $\lambda_1...\lambda_m$, and $f(x)$ generalized to any number of functions $f_r(x)$, the maximum entropy probability distribution is given by

$$p_i = exp\{-[\lambda_0 + \lambda_1 f_1(x_i) + ... + \lambda_m f_m(x_i)]\} \tag{3.14}$$

in which the constants can be determined by

$$\langle f_r(x) \rangle = -\frac{\partial \ln Z}{\partial \lambda_r} \tag{3.15}$$

$$\lambda_0 = \ln Z \tag{3.16}$$

$$Z = \sum_i exp\{-[\lambda_1 f_1(x_i) + ... + \lambda_m f_m(x_i)]\} \tag{3.17}$$

and the entropy of the distribution in equation 3.14 reduces to

$$H_{max} = \lambda_0 + \lambda_1\langle f_1(x)\rangle + ... + \lambda_m\langle f_m(x)\rangle \tag{3.18}$$

It is interesting to note that several familiar probability distributions easily fall out from setting different constraints while maximizing the entropy of the distribution Kesavan (2008). If there is no prior information, i.e., the only constraint is $\sum p_i = 1$, then the probability distribution is simply the uniform distribution. This is the *Laplace's principle of insufficient reason*, which states that if an experiment has n possible outcomes, and we do not know anything about it other than that each probability $p_i \geq 0$ and $\sum p_i = 1$, then the most unbiased choice is the uniform distribution $(1/n, ..., 1/n)$. Similarly, the normal distribution is simply a maximum-entropy distribution resulting from maximizing the Shannon entropy by constraining the mean and the variance of the probability distribution and $\sum p_i = 1$.

Maximum entropy principle and linear inverse problems

We can apply this remarkably successful principle to a linear inverse problem, such as equation 3.7. The equation can be generalized by the Fredholm formulation Mohammad-Djafari (1993):

$$g(z) = \int_D p(r)h(r,z)dr + b(z) \tag{3.19}$$

where $g(z)$ is the measurement, $p(r)$ is the unknown quantity, $h(r,z)$ is the system function that we know perfectly, and $b(z)$ is the measurement noise. We observe $g(z)$ on a finite set of isolated points z_m, $m = 1, ..., M$ in the transform space. This implies

$$g_m = g(z_m) = \int_D p(r)h(r, z_m)dr + b(z_m) = \int_D p(r)h_m(r)dr + b_m \tag{3.20}$$

When discretized, the problem can be stated in terms of an unknown vector p = $[p_1, ..., p_N]$ representing the samples of the unknown function $p(r)$ using the data vector g = $[g_1, ..., g_M]$. This can be then recast into the familiar relationship between the discrete signal input and output of a linear system:

$$g_m = \sum_{n=1}^{N} H_{mn}p_n + b_n, \quad or \quad \mathbf{g} = \mathbf{Hp} + \mathbf{b} \tag{3.21}$$

The objective of the maximum entropy inversion is to obtain a unique and stable solution $\hat{p}$ from the data **g**. The main hypothesis for this is that the unknown function $p(r)$ has the properties of a probability density function, that is p_n in equation 3.21 is positive and normalized:

$$p_n \geq 0, \quad \sum_{n=1}^{N} p_n = 1 \tag{3.22}$$

The inverse problem is solved such that the entropy is maximized:

$$S(p_n) = -\sum_{n=1}^{N} p_n \ln p_n \tag{3.23}$$

Comparing equations 3.11 – 3.18, to equations 3.19 – 3.23, we can write the following explicitly

- **Hypothesis**: p = $\{p_n\}$, has the properties of a probability distribution p_i
- **Data**: g = Hp are exact linear constraints on p, where H or $h(r)$ is the same as $f(x)$, and $g(z)$ corresponds to $\langle f(x) \rangle$

- **Mathematical problem**: Given H and g, maximize $S(p_n)$ such that $g = Hf$, and $\sum_{n=1}^{N} p_n = 1$

- **Solution:**

$$p_n = \frac{1}{Z} exp\Big[- \sum_{m=1}^{M} \lambda_m H_{mn} \Big], \quad n = 1, ..., N \tag{3.24}$$

Lagrange multipliers $\{\lambda_1, ..., \lambda_M\}$ are obtained by solving the following set of equations

$$g_m = \sum_{n=1}^{N} \frac{1}{Z} exp\Big[- \sum_{m=1}^{M} \lambda_m H_{mn} \Big], \quad m = 1, ..., M \tag{3.25}$$

Computationally efficient implementation

To solve the inversion problem described by equation eq: ch3 inversion of forward model, we show how to implement the above method by using a multiplicative algebraic reconstruction technique (MART), specifically, the log-entropy MART technique (De Pierro, 1991). This algorithm minimizes the negative Burg's entropy $-\ln \phi$, instead of maximizing the Shannon entropy, subject to the constraint that the resulting error $q - A\phi$ matches the a priori noise distribution σ_q. The core principle of this algorithm is the same as that mentioned above. The iteration steps are as follows:

$$\phi_j^{k+1} = \frac{\phi_j^k}{1 - \phi_j^k \sum_{i=1}^{I} w_i c_i^k A_{ij}} \tag{3.26}$$

$$c_i^k = \beta_k \big(1 - \frac{\langle A_i, \phi^k \rangle}{q_i}\big) t^k \tag{3.27}$$

$$t_i^k = \min_j \left\{ \frac{1}{A_{ij}\phi_j^k} \mid A_{ij} \neq 0 \right\} \tag{3.28}$$

The parameter β_k controls the degree to which the solution is free to change each step. Semeter & Kamalabadi (2005) suggest a value of $\beta = 20$ for the ISR inversion problem. The w_i's are real numbers such that:

$$w_i >= 0 \; ; \; \sum_{i=1}^{N_q} w_i = 1 \tag{3.29}$$

with N_q being the number of elements of q.

The convergence of the solution is controlled through the equivalent of a χ^2 function:

$$\chi^2 = \sum_{N_q} \frac{|q - A\phi|^2}{\sigma_q^2} \tag{3.30}$$

where σ_q^2 is the estimated noise variance of the measurements. The noise variance of electron density is sampled and stored for each pulse; therefore, for each range, this information is available in the ISR data file. The iteration is allowed to continue till $\chi^2 = 1$. If it goes lower than that, it implies the estimated energy flux ϕ has over-fit the data, and if χ^2 is much higher than 1, then the model has under-fit the data.

3.1.1.4 Error Analysis

By measuring the variance in power received across several back-scattered pulses, ISR data records the variance or error in the measured electron density (σ_{n_e}). In this subsection, we derive the error (C_ϕ) in the estimated differential number flux (ϕ), and the error (σ_{j_E}) in the differential energy flux (j_E).

Estimating error in q

Assuming an equilibrium ionosphere, the ion production rate:

$$q = \alpha_{eff} n_e^2 \tag{3.31}$$

Before deriving the error C_ϕ, we need an estimate of the error propagation from n_e to q. Considering $\hat{n}_e$ and $\hat{q}$ to be Gaussian random variables, we can derive an estimate for the error in production rates (σ_q) as follows:

$$\begin{aligned}
\sigma_q^2 &= E[(\hat{q} - q)^2] \\
&= E[\hat{q}^2] - q^2 \\
&= E[\alpha_e f f^2 \hat{n}_e^4] - q^2 \\
&= \alpha_{eff}^2 E[\hat{n}_e^4] - \alpha_{eff}^2 n_e^4 \\
&= \alpha_{eff}^2 (n_e^4 + 6 n_e^2 \sigma_{n_e}^2 + 3\sigma_{n_e}^4) - \alpha_{eff}^2 n_e^4 \\
&= \alpha_e f f^2 (6 n_e^2 \sigma_{n_e}^2 + 3\sigma_{n_e}^4)
\end{aligned}$$

Here $E[\hat{x}]$ is the expectation of the random variable, which is defined as $\int xp(x)dx$ where p in this case is Gaussian normal distribution.

Therefore,

$$\sigma_q = \alpha_{eff} \sqrt{6 n_e^2 \sigma_{n_e}^2 + 3\sigma_{n_e}^4} \tag{3.32}$$

Estimating error in ϕ

Our forward model is $q = A\phi$, and the generalized inverse is $\phi = A^\dagger q$. With

this information, it is straightforward to develop the covariance matrix C_ϕ, which contains the variance in ϕ, as well as the cross-variance terms with all the elements of the random vector $\hat{\phi}$.

$$\begin{aligned}
C_\phi &= E[(\hat{\phi} - \phi)^2] \\
&= E[\hat{\phi}\hat{\phi}^T] - E[\hat{\phi}]E[\hat{\phi}^T] \\
&= E[A^(\dagger)\hat{q}\hat{q}^T A^(\dagger)^T] - E[A^(\dagger)\hat{q}]E[\dagger q^T A^(\dagger)^T] \\
&= A^(\dagger)E[\hat{q}\hat{q}^T]A^(\dagger)^T - A^(\dagger)(E[\hat{q}]E[\hat{q}^T])A^(\dagger)^T \\
&= A^(\dagger)(E[\hat{q}\hat{q}^T] - E[\hat{q}]E[\hat{q}^T])A^(\dagger)^T \\
&= A^(\dagger)C_q A^(\dagger)^T
\end{aligned}$$

Here $C_q = diag(\sigma_q^2)$, assuming q measured at each altitude is independent of that measured at other heights, and therefore there are no cross-covariance terms

However, this does not take into account the effect of prior probability, i.e., the constraint enforced through the Burg's entropy maximization. If we have more confidence in the prior probability, C_ϕ will have a lower value. Hysell (2007) describes a method to estimate the error in ϕ calculated with the maximum entropy method and Bayesian statistics.

$$C_\phi^{-1} = \frac{\partial^2 E}{\partial^2 \phi} \tag{3.33}$$

where $E = -\frac{S}{\Gamma} + \frac{1}{2}e^T C_q^{-1} e \propto \ln(p(\phi|q))$ is proportional to posterior probability. Here, $e = A\phi - q$ and Burg's Entropy is defined as $-S = -\ln\frac{\phi}{\Phi}$ where $\Phi = \sum \phi_i$.

To estimate C_ϕ, we take the double derivative of E as per equation 3.33. First, we take the double derivative of the initial term $-S/\Gamma$, which is a function of the

prior probability $\ln(p(\phi))$ that contains the model information irrespective of the measurement:

$$-\frac{\partial}{\partial\phi}\Big(\frac{\partial}{\partial\phi}S\Big) = -\frac{\partial}{\partial\phi}\Big(\frac{\partial}{\partial\phi}\Big(\ln\frac{\phi}{\Phi}\Big)\Big) = -\frac{\partial}{\partial\phi}\Big(I\phi^{-1}\Big) = \Big(I\phi^{2}\Big)^{-1}$$

$$-\frac{1}{\Gamma}\frac{\partial^2 S}{\partial^2\phi} = \big(\Gamma I\phi^{2}\big)^{-1} \tag{3.34}$$

Before taking the double derivative of the second term, $\frac{1}{2}e^T C_q^{-1} e$, the distributed measurement error, which is a function of the transitional probability $\ln(p(q|\phi))$, we introduce the following proposition.

Proposition 1: *For the special case where* $\boldsymbol{A}$ *is a symmetric matrix and*

$$\alpha = \mathbf{x}^T\mathbf{A}\mathbf{x} \tag{3.35}$$

where $\boldsymbol{x}$ *is* $n \times 1$ *,* $\boldsymbol{A}$ *is* $n \times n$*, and* $\boldsymbol{x}$ *is a function of the vector* $\boldsymbol{z}$*, while* $\boldsymbol{A}$ *does not depend on* $\boldsymbol{z}$*. Then*

$$\frac{\partial\alpha}{\partial\mathbf{z}} = 2\mathbf{x}^T\mathbf{A}\frac{\partial\mathbf{x}}{\partial\mathbf{z}} \tag{3.36}$$

If we assume $\mathbf{x} = \mathbf{e}$, $\mathbf{A} = C_q^{-1}$ (which is diagonal hence symmetric), $\mathbf{z} = \phi$ then

$$\frac{\partial^2}{\partial^2\phi}\Big(\frac{1}{2}e^T C_q^{-1} e\Big) = \frac{1}{2}\frac{\partial}{\partial\phi}\Big(2e^T C_q^{-1}\frac{\partial e}{\partial\phi}\Big) = \frac{\partial}{\partial\phi}\Big(e^T C_q^{-1} A\Big) = A^T C_q^{-1} A \tag{3.37}$$

Therefore adding equations 3.34 and 3.37 we get the covariance matrix for ϕ we set out to estimate

$$C_{\phi}^{-1} = A^T C_q^{-1} A + [\Gamma I \phi^2]^{-1} \tag{3.38}$$

here $I\phi^2$ is a diagonal matrix with the diagonal terms being the square of each element in the vector ϕ. Since both terms in equation 3.38 are positive, the first term is always lesser than the sum of the two terms

$$A^T C_q^{-1} A < A^T C_q^{-1} A + [\Gamma I \phi^2]^{-1}$$

Therefore, it is safe to regard the maximum error covariance matrix to be

$$max(C_{\phi}) = (A^T C_q^{-1} A)^{-1} \tag{3.39}$$

The magnitude of the off-diagonal elements, the cross-covariance terms, are considered to be small. Hence, the estimated error for the ISR inversion estimate of the number flux will not exceed

$$\sigma_{\phi_{max}} = \sqrt{Diag(A^T C_q^{-1} A)^{-1})} \tag{3.40}$$

and to calculate the error in the differential energy flux from differential number flux, you can use the following equation

$$\sigma_{j_E} = \frac{ebin}{2\phi} \times \sqrt{Diag(A^T C_q^{-1} A)^{-1})} \tag{3.41}$$

To estimate a more accurate and smaller error by incorporating the prior probability distribution, one needs to use equation 3.38, but choose a value for Γ. Like the regularization parameter α in Tikhonov regularization (See equation 3.10), the Γ factor weights the importance of two probabilities. 1) The entropy for the prior

probability and 2) the chi-squared prediction error for the transnational probability. The value of Γ remains a subjective statement of one's personal beliefs in the confidence in one's a priori information, which will result in more confidence in one's posterior information, i.e., the estimate of ϕ. If Γ is ∞, it means we have no confidence in the a priori information (i.e., entropy maximization constraint), and the error tends to the maximum possible error $\sigma_{\phi_{max}}$.

A more accurate estimate of Γ can be set using a few methods - all of which are contested. One way is to equate Γ to the expected value of chi-squared, which is $E[e^T C_q^{-1} e] = N - 1$ where N is the number of data points of q. The result follows from the fact that $e^T C_q^{-1} e$ is a normalized chi-squared random variable with $N - 1$ degrees of freedom. The second method is to tune the Γ parameter using an L-curve (Hansen, 2005), which is a log-log plot of norm of the regularized solution (e.g. first part of equation 3.10, $||Ax - y||^2$) vs. the corresponding residual norm (e.g. second part of equation 3.10, $||Lx||^2$) for a particular α or in this instance Γ. The appropriate Γ value will be the corner point of the curve, where the curvature is maximum, where the Γ is not too large, and the inversion result doesn't underfit the data, nor is Γ too small that it overfits and captures the noise in the data.

3.1.1.5 Other inversion techniques

In this dissertation, we have relied heavily on the technique described by Semeter & Kamalabadi (2005) to estimate precipitating electron energy spectra from ISR measurements. However, several other methods to invert the forward model in equation 3.7 can be found in the literature. We summarize all of the techniques that have been developed so far to the best of our knowledge. Kaeppler et al. (2019) presents a review of most of them.

- Vondrak & Baron (1977) developed an iterative method called UNTANGLE to invert the forward model, by calculating the ionization at the highest energy bin and subsequent energy bins relying on the previous energy bin estimate. As this can result in uncertainty propagating through each step, the method is prone to errors.

- Brekke et al. (1989) obtained the solution by minimizing the difference in the altitude profile of ionization measured by the ISR, and the forward model results using a least-squares approach. This routine is called CARD.

- Kirkwood et al. (1988) developed SPECTRUM, which attempts to match the dimensions of the energy grid to the altitude observations to make a square matrix and apply standard inversion techniques. If they are unable to formulate a square matrix, they fall back on the least-squares method. One feature that sets this program apart from the previous ones is that it incorporates temporal variations in electron density.

- Doe et al. (1997) solved equation 3.9 using the method of singular value decomposition, but this approach can lead to negative electron differential number fluxes.

- Semeter & Kamalabadi (2005), as we have mentioned, uses an iterative maximum entropy method that maximizes Burg's entropy, which has the advantage of the estimated electron differential number flux being a positive definitive quantity since the estimate has the properties of a probability distribution. Additionally, there are no implicit assumptions made about the nature of the precipitating spectra.

- Simon Wedlund et al. (2013) compared the results of the above method, with a more traditional approach of maximizing the Shannon entropy $H_S = -\sum_i \phi_i \log \phi_i$ instead of the Burg's entropy $H_B = \sum_i \log \phi_i$. They found that the technique based on Burg's entropy tends to produce smoother results. This could be because the variance in the a priori probability that contributes to the covariance matrix (second term of equation 3.38) is smaller ($\Gamma I \phi^2$) in the case of maximizing Burg's entropy as compared to the term obtained while maximizing Shannon's entropy ($\Gamma I \phi$). $\Gamma I \phi^2 < \Gamma I \phi$ since $\phi_i < 1$, and when this term is higher, it implies we are more uncertain about the a priori distribution, and therefore more uncertain of the resulting estimate of ϕ.

- Turunen et al. (2016) developed a method for inverting D-region electron density measurements using a Metropolis-Hastings Markov Chain Monte Carlo (MCMC) technique and the full Sodankyla Ion Chemistry (SIC) model. The SIC model is a complex D-region ion chemistry model that can output the chemical composition given input solar radiation or particle fluxes. Turunen et al. (2016) iteratively determined the altitude profile of ionization using the SIC model for a given observed electron density profile. After this, the differential number flux was estimated using the MCMC algorithm to optimize a cost function with a Gaussian regularization term. The estimates derived by this method are also positive definite quantities, and the model is capable of fitting over a large dynamic range of energies.

- Virtanen et al. (2018) developed an inversion technique based on the integration of the electron continuity equation and a spectrum model selection using the Akaike information criterion. The method is called ELSPEC for electron spectrum estimation from incoherent scatter radar measurements. This is the

most recent technique at the time of writing this dissertation. The advantage of this approach is that it allows the use of data with any time resolution. It can estimate the spectrum with dense energy grids, avoids noise amplification in numerical derivatives, and provides statistical error estimates for all output parameters, including number and energy fluxes. However, unlike the previous models, the output of ELSPEC is a lower-dimensional nonlinear parameter estimation where a set of parameters describes the precipitating energy spectra. The simplest model with one parameter can produce Maxwellians, while a higher number of parameters can produce very good matches with observed distributions. They use the Akaike information criterion to obtain the optimal model, with the optimum number of parameters.

3.1.1.6 Advantages and limitations of ISR measurements

Incoherent scatter radars allow for measurements of energetic particles within the loss-cone of the pitch angle distribution. These are highly sensitive to the magnetospheric mechanisms that cause the loss of energetic particles to the ionosphere. Since ISR measures the effect of precipitation in the ionosphere, by definition, they give us detailed measurements of particle populations within the loss-cone that are difficult to measure with satellites. They provide high-resolution local measurements in time and good energy resolution. Using electronically steerable radars such as Poker Flat Incoherent Scatter Radar (PFISR), we can study variations in small spatial-scales $\sim 5 - 10$ km with a < 100 km coverage of a region in the sky. They provide a variety of measurements, such as line-of-sight ion velocity, electron and ion temperature, plasma density, conductance, horizontal electric fields, and currents, in tandem with energy spectra of precipitating electrons. This richness of

the data allows for a more detailed picture of M-I coupling. However, we must admit that very few studies exploit all that ISRs have to offer due to the complexity of the analysis and processing of higher-level data products. Additionally, since ISRs are ground-based systems, it can, in principle, be operated continuously without data interruption, i.e., 24/7.

However, PFISR being one of the most recent ISRs, was the first to provide 24/7 coverage. This allows sampling across all MLT sectors at a fixed latitude. Currently, there are only about ~ 10 active ISR facilities in the world, and hence the global coverage of ISRs is abysmal[1]. This is one of its significant limitations, especially since there is a push towards predicting space weather that requires an understanding and measurement of the global magnetosphere-ionospheric system. Among the ISRs, the most rapid measurements with moderate spatial coverage is currently achieved through PFISR (and other AMISRs). At 100 km altitude, the horizontal range can extend from north-south to about ~ 157 km and east-west ~ 122 km. Each PFISR beam has a beamwidth of ~ 1.1 degrees, which at 100 km has an actual size of about 1.9 km.

Another limitation, like any other sensor, is its sensitivity or detector threshold for observing energetic particle precipitation. An SNR of -10 DB would be detectable, as it will result in a received signal variance of about 20% for averaging 3025 pulses. This is estimated form the following relation derived by Farley (1969) for the statistical variance of the received signal for uncorrelated pulses:

$$\frac{\langle \hat{S} \rangle}{\hat{S}} = \frac{1}{\sqrt{N}} \Big(1 + \frac{1}{SNR} \Big) \tag{3.42}$$

[1]However, there are efforts to make inexpensive ISRs with less capabilities, to allow for more global coverage (Lind et al., 2001).

where N is the number of samples integrated. Due to the received signal's statistical nature, the power spectrum will differ from the theoretical spectrum shown in figure 3.1. This noise results from random statistical errors and systematic distortions due to the finite transmitted pulse length, finite receiver bandwidth, receiver bias, and other distortions. The scattered signal incident on the receiver generates a complex voltage $V(t)$ that is a Gaussian random variable. If we assume that the scattered signal is statistically stationary within the measurement time, the signal is completely specified by its autocorrelation function or the power spectrum. To separate the noise from the signal, we also need to gather the noise statistics. Therefore, two separate measurements are taken: the signal $\hat{S}$ with the noise S_N, and the just the noise alone. We then subtract the two estimates, each of which will have an independent error associated with it, to get an estimate of the signal power. It is advantageous to take more samples of the noise than the signal with noise since the noise is generally independent of range or time. Doing this, we get the normalized error as shown in equation 3.42. This normalized error is factored in on the error in the ISR electron density estimates σ_{n_e}, and the error in production rates σ_q of equation 3.32.

Calculations by Kaeppler et al. (2019) suggest an altitude dependence on the detectability of ionization caused by energetic precipitation, which decreases with energy and energy flux. Energy flux of $0.5 - 10$ mW/m^2 of electrons of energy $30, 70, 100$ and 300 keV all seem to be within the detectability threshold assumed above.

With ISRs, we have to contend with the inability to distinguish between different types of charged particle precipitation fluxes. Our current analysis assumes that proton precipitation is confined to higher altitudes (upper E-region and above)

due to their higher collisional cross-sections. We presume that electrons mostly cause the ionization measured in the lower E-region and D-region. There are likely improvements in the forward model and inversion techniques that can allow for the estimation and separation of proton precipitation from electron precipitation using the following two factors (See section 8.3). Protons and electrons with the same peak ionization altitude, and the same energy flux, will cause different altitude profiles of ionization. This is because the protons ionize much more of the atmosphere at higher altitudes than the electrons. This distinction, coupled with simultaneous optical measurements characteristic to proton precipitation such as H_β, can be used as additional constraints for the pseudoinverse problem to estimate proton energy spectra and electron energy spectra.

3.1.2 Optical Measurements

Optical measurements through ground-based all-sky images have been an essential diagnostic tool from the beginning of modern space physics. Historically auroras have been observed directly through human eyes, photographic plates and images, all-sky cameras, television and image intensifier camera systems, meridian scanning photometers, and spectrometers. Technological advances made in the past few decades have replaced photographic films used by all-sky camera networks with digital cameras that have solid-state optical detectors. The MIRACLE network in Scandinavia and the THEMIS Ground-based Observatory (GBO) in North America (Mende et al., 2008) are the two major operating networks made of scientific-grade CCDs that can measure both weak and intense emissions simultaneously. We present a summary of the state-of-the-art of optical measurements in Section 2.1 of Nishimura et al. (2020). In this dissertation, we use the THEMIS

GBO cameras and the Digital All-sky Camera installed at the Poker Flat Research Range by the University of Alaska Fairbanks.

Another vital instrument class that we have used for our work are meridian scanning photometers. Photometers are a simple instrument with a tube consisting of a lens, filter, and a detector that is capable of measuring the intensity of light that falls on it. Photometers that scan the magnetic meridian, with filters, are called meridian scanning photometers. They can produce meridional or elevation profiles of auroral emissions at different wavelengths typically: O^+ 557.7 nm and 630.0 nm, N_2^+ 427.8 nm, H_β 486.1 nm. Section 2.6 contains a brief discussion of how the spectral information of auroral emissions can illuminate the energy and the species of precipitating charged particles. We provide more details of specific instruments that we use in chapters 4 and 5 before discussing our findings.

This section will focus on a particular problem related to processing data from all-sky cameras, which have broader applications in other space-physics and astronomy studies.

3.1.2.1 Calibrating the pixel positions of an all-sky camera

If one is interested in studying simultaneous measurements of a spatial region from more than one instrument, then accurately recording the position and time of the measurement made by each device is essential. All-sky camera data is usually accompanied by calibration files that specify where each pixel of the image points to in the sky in terms of elevation and azimuth. The THEMIS GBO all-sky imagers, which record white light, is distributed in the Common Data Format (CDF) through the web-link[2], which also includes the calibrated latitude and longi-

[2]http://themis.ssl.berkeley.edu/data/themis/thg/l1/asi/

tude information of pixels. However, the Digital All Sky Camera (DASC) at Poker Flat Alaska does not have an easily accessible calibration file. Furthermore, DASC has undergone several modifications through the years in terms of its filters, and CCDs. Hence its orientation and location have also been altered several times in the past decade. A new calibration file is necessary every time there is some disturbance in the setup.

Fortunately, there is a way to calibrate the camera image pixels by using the position and brightness of the stars it observes in the night provided we know the Geo-location of the camera in question. With image processing done on images of the night sky, the camera's location and orientation can be determined, including the azimuth and elevation values of each pixel (Klaus et al., 2004). Astrometry.net[3] is an example of such a tool available to the public. However, these cannot be readily applied to all-sky camera calibration since they use fisheye lenses that produce strong visual distortions allowing the imaging of an entire hemisphere. Therefore, we developed a technique that merges the image processing methods to identify stars in the night-sky image with a genetic algorithm [4] to determine the lens distortion, camera orientation, and field of view by fitting the positions of the identified stars with a sky chart. Since the camera position is approximately known, we fix those parameters. However, in principle, they can also be free parameters to be determined by the fitting process.

Here we summarize the methodology we used to calibrate the digital all-sky, white-light camera at Poker Flat Research Range in Alaska. The procedure can be used for all other white-light all-sky cameras but is unlikely to work well with

[3]http://astrometry.net/

[4]We chose a genetic algorithm to allow for the fitting process to identify the global minimum in the cost function, and not end up in the large numbers of local minima that are likely to exist given the large space and number of fitting parameters.

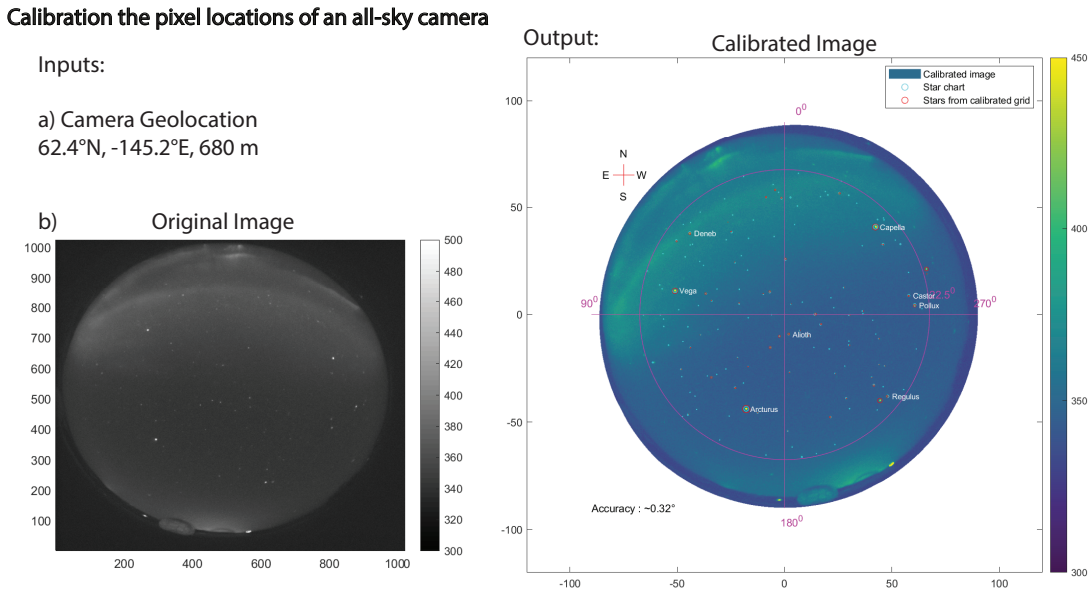

Figure 3.3: The input and output of the all-sky camera calibration algorithm summarized below. It provides a calibration accuracy of $\sim$0.32°, which is an error of about 0.55 km at 100 km altitude.

cameras with a spectral filter, as the star chart we use is only for white-light images. However, modifications to this algorithm can add this functionality. (See intensity calibrations on monochromatic CCDs (Grubbs et al., 2016)).

Steps for calibrating the pixel positions of an all-sky camera

1. Use a star catalog to estimate the position of all bright stars. We used the Hipparcos extended catalog.

2. Identify a night sky image with the least clouds or obstructions, and process it to remove the background, hot pixels, and noise spikes.

3. Extract the remaining star-like features, and record its centroid in the image coordinates.

4. Order the stars from the star chart and the stars extracted from the image, in

two separate lists, in their ascending order of magnitude (brightness). Match the top 10 stars, and label the centroid of star-like features extracted from the image with the star IDs and names of those from the star chart.

5. Use the genetic algorithm to estimate the coefficients of the functional relationship between the azimuth and elevation of stars from the star chart and its projection on the image pixels. The cost function to minimize is the distance between the paired stars. Equation 3.43 shows the functional relationship between the azimuth and elevation values of a star and its projection on to the image-pixel space (or CCD).

6. The initial projection of the stars from the star chart onto the image-pixel space is done by assuming an initial nominal value for all the parameters. This initial value also corresponds to the initial azimuth-elevation value for all the image pixels. Therefore, once we estimate the bold-faced parameters in equation 3.43, the initial azimuth and elevation values corresponding to the image pixels can be rotated to the calibrated values. The results are shown in figure 3.3. The algorithm achieves a calibration accuracy of about $\sim$0.32°, which corresponds to a 0.55 km error at 100 km altitude.

$$
\begin{aligned}
x &= \boldsymbol{x_0} + \boldsymbol{spin}(r\sin(\phi - \boldsymbol{d\phi})) \\
y &= \boldsymbol{y_0} + r\cos(\phi - \boldsymbol{d\phi}) \\
r &= 90^{\frac{\boldsymbol{k}-1}{\boldsymbol{k}}}(90-\theta)^{\frac{1}{\boldsymbol{k}}}
\end{aligned}
\tag{3.43}
$$

Here, x and y are the horizontal and vertical pixel indices, ϕ and θ are azimuth and elevation values in degrees associated with the pixel, $\boldsymbol{x_0}$ and $\boldsymbol{y_0}$ is the translation of the center point of the image, which is equivalent to the tilt of the camera

orientation along the elevation, in its polar projection, $d\phi$ rotation of the camera orientation along the azimuth, $spin$ can hold two values $+1$ or -1, which suggest anti-clockwise or clockwise labeling of the azimuth values. (Sometimes, all-sky camera images can follow two different directional conventions. This parameter takes it into account by recording defining image flipping.), k is the radial distortion parameter that takes into account the lens distortion that we assume is radial only.

3.1.3 Riometer

Before describing the techniques used to probe the magnetosphere, it is worth discussing briefly one more powerful technique to measure energetic precipitation - riometer. A riometer is a passive radio receiver operating in the range of $30 - 40$ MHz. It uses the absorption in cosmic noise background to estimate D-region ionization, and hence the hardness of the precipitating electron spectra and its relative intensity. Since riometers are cheap to build, it has been used to obtain global coverage of energetic precipitation that is not currently possible with ISRs (Berkey et al., 1974; Hargreaves, 1969). Kero et al. (2014) developed a spectral riometer technique that can invert the absorption spectrum to estimate altitude profiles of electron density. An international collaborative program called The Global Riometer Array (GLORIA) to track the global evolution of high-energy electron population through a substorm cycle exists, with 50 riometer including 22 imaging systems (Alfonsi et al., 2008).

Imaging riometers were a significant technological advancement that allows us to measure the spatial variation of absorption signatures using a set of riometer beams across the sky (Honary et al., 2011). Kosch et al. (2001a) developed a

technique to produce high-resolution maps of characteristic energy of precipitating electrons by fusing 2D-imaging riometer data with optical data at 557.7 nm from the Digital All-Sky camera at Poker Flat Research Range. This is the first of its kind small-scale characteristic energy map of particle precipitation. However, it has relatively poor energy resolution and energy range compared to the ISR-based 2D energy flux maps developed in chapter 5.

Rodger et al. (2012) compared the sensitivity of riometers to energetic particle precipitation with two other remote-sensing techniques: subionospheric radio wave propagation measurements (VLF) and GPS-produced total electron content (vTEC). They concluded that riometers responded to energetic precipitation the most, while VLF and vTEC seem to have measurable perturbations.

3.2 Probing the Magnetosphere

In this section, we discuss the different types of measurements made in the magnetosphere by spacecraft, and the phenomena they can illuminate. There are three categories of *in situ* measurements to study the sources of energetic precipitation: 1) solar wind measurements, 2) measurement of magnetosphere plasma properties, and 3) upper ionospheric measurements.

3.2.1 Measuring solar wind parameters

Spacecraft such as the Advanced Composition Explorer (ACE) and its successor, the Deep Space Climate Observatory (DISCOVR), are stationed at the L1 point ($X_{GSM} = +235R_E$). They measure solar-wind properties such as the IMF due to the solar-wind proton density, dynamic pressure, speed, and temperature at high temporal resolutions. These properties have a direct effect on the dynamics of

the magnetosphere. However, the assumption here is that the above spacecraft measures the solar-wind when the solar-wind hits the magnetosphere's nose. It is not always the case since the solar-wind has a mesoscale structure (1-100 R_E) and the aberration in the solar wind, directional variability of the solar-wind velocity vector, and the movement of the spacecraft orbit around L1 can affect the error in measurements (Borovsky, 2018). Keeping this caveat in mind, knowledge of the plasma parameters of the solar wind at the magnetopause allows us to predict the magnetosphere's state. For example, Murayama & Hakamada (1975) showed through a statistical analysis of 175 substorms the following.

- A significant southward IMF component can lead to increases in the total auroral electrojet (AE) current, which is proportional to the time integral of the southward component.
- The azimuthal part also affects the AE magnitude.
- AE intensity is proportional to the square of the velocity.

Therefore, ACE and DISCOVR allow us to measure drivers of the magnetospheric dynamics.

3.2.2 Measurements in the Magnetopshere

There are many spacecraft missions in LEO, MEO, and GEO orbits, to probe magnetospheric plasma and electromagnetic fields. They generate vast amounts of data. Despite this fact, we still lack global, spatial, and continuous coverage of the near-Earth space environment to address major outstanding questions. In this subsection, we discuss important *in situ* measurement parameters and the type of

physical insights we can derive from them. The list is by no means exhaustive. We intend to introduce the kind of analysis that can be done with these measurements.

3.2.2.1 Magnetic field measurements

Measuring the magnetic field vector in the magnetosphere allows one to estimate currents based on the temporal and spatial variation of the field (See Ampere-Maxwell's law, equation 2.4). With a small constellation of satellites measuring the magnetic field, a more accurate reconstruction of the currents can be made from the curl of the magnetic field (Parham et al., 2019). The deviation of the DC magnetic field from that predicted by empirical models provides a measure of the magnetic field dynamics (i.e., the stretching and dipolarization of the fields). A sudden and opposite change in the direction of the static field might suggest crossing a magnetic neutral line and regions where magnetic reconnection is possible. Changes in the curl of the magnetic field can also indicate passing current sheets. The magnetic field magnitude also contains approximate geographical information, based on our understanding of the magnetosphere and the Earth's magnetic field model. The frequency spectra of the magnetic field, also tell us about the intensity and type of plasma waves in the Earth's magnetosphere. Most scientific spacecraft missions that do heliophysics studies contain a magnetometer. There are several types of them; the most common magnetometers are fluxgate and search coil magnetometers. The THEMIS spacecraft, Van Allen probes, MMS, GOES, ACE, and DISCOVR, measure the magnetic fields.

3.2.2.2 *Electric field measurements*

Electric fields play an essential role in the ionosphere and magnetosphere plasma convection, through the $E \times B$ drift. Therefore, measuring E can provide quantitative estimates of the plasma convection. Using electric field measurements, one can study the following regions and mechanisms:

1. Auroral acceleration region with parallel electric fields in the form of double-layer, or kinetic Alfven waves

2. The magnetopause and the magnetotail with small-scale electric fields associated with magnetic reconnection

3. Global electric fields such as the polar-cap electric field driven by the Dungey cycle and sub-auroral polarization drift [5]

The AC component of the electric fields is usually associated with PC5 pulsations, which have as much impact on plasma transport as DC fields (Junginger et al., 1984; Matsui, 2003). Double probes can measure electric fields. Other measurement techniques include ion-drifts along spacecraft trajectory and electron drift instruments that use the drift of test electrons in the ambient electric field (Matsui, 2003).

3.2.2.3 *Particle measurements*

We can divide charged-particle measurement into two categories based on energy: low and high energy particles. The exact point of separation between the energy

[5] Sunward electric fields at the earthward boundary of the plasma sheet cause sub-auroral polarization drifts.

ranges is ambiguous, and historically it seems to have been determined by instrument limitations. We suggest an alternate set of labels that utilize our knowledge of the source mechanisms that drive electron precipitation in section 1.2. However, in literature, low energy electrons range from a few eV to a few keV, while high energy electrons range from a few keV to MeV. The low energy particles are mostly measured using Langmuir probes, Retarding potential analyzers (RPA), and sector-field or curved plate analyzers. These could measure electrons from a few eV to a few KeVs, mostly based on measuring the current flow through a potential difference or electric field as the particle passes through it. While high energy particles are measured using solid-state detectors, usually made up of semiconductors or scintillator materials.

Cold plasma detectors can usually measure the density, temperature, and spacecraft potential. The plasma density and temperature are useful to locate the magnetospheric region of the spacecraft. The spatial or temporal variations in plasma density also may indicate acceleration or scattering mechanisms. The temperature and energy spectra of the particles, especially high energy particles, have information regarding the acceleration mechanisms affecting them. We can use the directional flux or velocity distribution to understand: 1) the pitch angle scattering processes, 2) conditions of wave-instabilities, 3) loss of particles into the ionosphere, or diffusion across L-shells, and 4) transport of particles within the magnetosphere-ionosphere system. By measuring the periodicity of detected particle counts, we can also study resonant wave-particle interactions (Watkins et al., 2013). There are many satellites with low and high energy particle detectors in the magnetosphere: THEMIS, Van-Allen Probes, Cluster, FAST, SAMPEX, GOES, POES, MMS, etc. However, there are very few current missions that can measure high energy

particles from Low Earth Orbit. Currently, it can be done only by the POES mission with poor energy resolution, and a few other CubeSat missions such as FIREBIRD, ELFIN, Foresail-1. A need exists for future LEO missions to measure high energy particles, as this is a reliable way to quantify energetic precipitation into the atmosphere. This is extremely difficult to do from deep within the magnetosphere since we do not yet have detector systems with sufficient pitch angle resolution to resolve the loss-cone.

3.2.2.4 Imaging from space

We complete our discussion of probing different regions of the magnetosphere, by discussing missions designed to record images of the aurora from orbit. Spacecraft have measured a range of wavelengths starting from optical to far ultraviolet and X-rays. Some measurements are narrow FoV, while others provide a global image. Ostgaard (1999) contains two detailed tables 1 and 2, that summarize the properties of the imagers and satellites that recorded the aurora from space. The IMAGE spacecraft and the small satellite mission REIMEI are new additions to this list.

Such measurements are useful in the case of Ultraviolet or X-ray emissions since they are much easier to measure from space rather than the ground. The intervening atmosphere causes the UV and X-rays to be scattered and attenuated before reaching ground instruments, while those scattered into space are detected without much attenuation. Satellites can provide a simultaneous global view of the whole auroral oval, which can give unique insights into the global reconfiguration of the magnetosphere (i.e., substorms and storms), indicate regions of current closure, provide a precise estimate of the polar cap and the amount of open magnetic flux, and so on. Such instant global snapshots can help derive global estimates

of ionospheric conductances that capture spatial variability to improve global MI coupling models.

3.3 Techniques to Constrain the Sources of Precipitation

In this dissertation, to constrain the source of energetic precipitation, we use a broad technique based on magnetic conjunction: where we compare measurements made at the ionosphere with those made simultaneously in the magnetosphere along the same field line.

3.3.1 Magnetically Conjugate Measurements

3.3.1.1 Identifying field lines

Charged particles in slowly varying uniform or non-uniform magnetic fields gyrate about the field lines and drift within magnetic-field surfaces (the two-dimensional extension of the field line). Two points along the same field line are said to be magnetically conjugate to each other. If all the adiabatic invariants are conserved, then the part of the charged particle population within the loss-cone is observed, unchanged, at both these points (provided the measurements are in the same hemisphere). Under these conditions, the precipitating charged particles that originate at a particular *drift-shell* will remain confined to it.

The arc length s covered by the trapped particle along a field line represents its *bounce phase*. Averaging over the bounce phase through the bounce period results in only the drift motion of the field lines occupied by the particle's bouncing guiding center. This field line where the particle is bouncing at a particular time is called the *guiding field line*. The guiding field lines form a surface, called the drift

shell, with two limiting curves generated by the mirror points.

The McIlwain's L parameter is an idealized but an effective coordinate to identify a field line. It is defined for a purely dipolar field, where the L value of a field line is the radial distance of the intersection of the field line with the magnetic field minimum surface in units of Earth radii (R_E). It can be described with the following set of equations, and with figure 3.4.

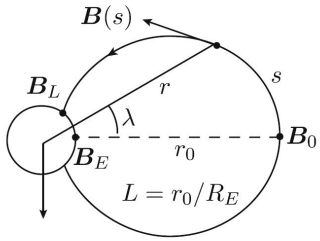

Figure 3.4: Dipole field line parameters. After Roederer & Zhang (2014).

$$R = L\cos^2\Lambda \tag{3.44}$$

$$B = \frac{B_E}{R^3}\sqrt{4 - \frac{3R}{L}} \tag{3.45}$$

$$\Lambda = \arccos\sqrt{1/L} \tag{3.46}$$

Here B is the local magnetic field value, L is the McIlwain's L value, Λ is the invariant latitude, and $R = r/R_E$. The L-shell value will be highly inaccurate at high latitudes (corresponding to $L > 5$) since the field lines are not dipole-like. In non-dipole equipotential field lines (no parallel forces) with trapped particles, we can still assign an L-value to a particle of given I and B_m values. Where $I = \int_{s'_m}^{s_m}[1 - B(s)/B_m]^{1/2}ds$ is a field-geometric integral connected to the second adiabatic invariant of the particle, where B_m is the mirror point magnetic field and s_m is the mirror point of the particle on the field line. With these in mind, equation 3.47 can be used to identify *quasi-dipole* fields like the magnetosphere out to about $L = 7$ during quiet times, giving an intuitive idea of the radial extension of a drift

shell (Roederer & Zhang, 2014).

$$L = \left(\frac{B_E}{B_m}\right)^{1/3} f\left(\frac{I^3 B_m}{R_E^3 B_E}\right) \tag{3.47}$$

This relation defines the L parameters as a function of a pair of I, and B_m. Values of the function $f(I^3 B_m / R_E^3 B_E)$ are the cubic root of the function found in published tables in Appendix VI in Roederer & Zhang (2014). Note that this L value is ascribed to the particle since it is not a constant for a given field line.

A more general reference representation of particles found stably trapped in any non-symmetric magnetic field configuration is given by what is called *adiabatic reference parameters*: "L-star" L^* (see equation eq: L-star), "B-star" B_m^* and the particle's kinetic energy T^*. These are the L, B_m and T value of a particle when the non-dipolar sources of a *real* magnetic field are slowly turned off, such that the final field is a pure central dipole of moment $B_E R_E^3$. The particle will end up in a symmetric dipole drift shell defined by the above adiabatic reference parameters while conserving the values of its adiabatic invariants.

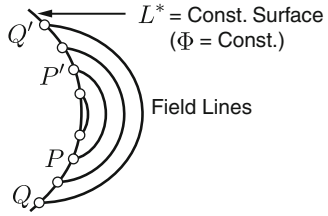

Figure 3.5: Mirror points on different field lines for which the trapped particles have the same L^* value. After Roederer & Zhang (2014).

$$L^* = \frac{2\pi B_E R_E^2}{\Phi} \tag{3.48}$$

In equation 3.48, the third adiabatic invariant $\Phi = \int_\pi \boldsymbol{B} \cdot \boldsymbol{dS}$ is the flux over the polar cap Π. However, it is important to note that the surface of constant L does not represent a particle drift shell or field line. It is simply the locus of all mirror points (P,P',Q,Q', etc.) of particles with drift shells with the same Φ value.

All mirror points show in figure 3.5 will assemble on one single dipole field line and shell surface (with different energies, if they initially had the same) after the adiabatic transformation into a pure dipole field.

3.3.1.2 Magnetic field models

A way to identify and label field lines is helpful during quiet periods, and regions where the magnetic field is near-dipolar. However, deviations from the dipolar field (at $L \sim> 5$ R_E) make it very difficult to use these labeling schemes and maintain the physical significance of associating them with a single field line. In this dissertation, we mostly attempt to link a region of space to another region, using magnetic field models that estimate the field geometry and the knowledge that charged particle guiding centers track the field line while the adiabatic invariants are conserved. Fortunately, we can do this without worrying about labeling the field lines and merely using a coordinate system to locate these two magnetically connected regions. To identify such magnetic conjunctions, we rely on external magnetic field models.

The Earth's internal magnetic field caused by the core can be represented by a spherical harmonic series, with the first term being that of a simple dipole. From repeated measurements and magnetic surveys, the main field is captured by the International Geomagnetic Reference Field (IGRF) model. While dealing with the auroral zone, which is magnetically connected to $L > 5$, we need to take into account the following magnetospheric currents that determine the shape of the external field

1. the current system on the magnetopause (Chapman-Ferraro current),

2. the current system in the neutral sheet of the magnetotail (cross-tail current),

and

3. the current system around the Earth, flowing along the equatorial magnetic minimum surface (ring current).

During magnetic activity that includes storms and substorms, the fields contributed by the currents change substantially, with new currents forming such as field-aligned currents in and out of the ionosphere. Several models have been developed to capture the external field: Mead-Farfield [1975], Tsyganenko 89, 96, 01, 04, Olson-Pfitzer quiet, Olson-Pfitzer dynamic, etc. Tsyganenko's models are the most popular. These are semi-empirical representations of the magnetic field, constructed with a large number of satellite observations (IMP, HEOS, ISEE, POLAR, Geotail, etc.).

3.3.1.3 Error in Magnetic Conjunction Estimates

Error in magnetic field models: Though the magnetic field models do not provide an error bar in their estimates, we can validate them on a case-by-case basis, based on real measurements from satellites whose data are not included in the model development. A method to quantify the uncertainty in the model estimates is to calculate the variance in the estimates made by many different models. Such a technique was used to derive an error estimate for magnetic conjunctions described in chapter 5. For the particular case, during a substorm growth phase, the standard error ($\sigma/\sqrt{n}$) is $\sim< 3R_E$, with the model variance calculated across 11 magnetic field models.

Cross-field drift: We have discussed the scenario where the gyro center of particles follows the magnetic field lines, as long as the adiabatic invariants are conserved. However, when magnetic fields have a spatial gradient or temporal vari-

ation greater than the spatial or temporal scales of the periodic motion associated with the invariants, the particles can drift out of the initial magnetic field line or scatter in velocity space. The third adiabatic invariant (Φ) is hard to conserve. Since it is associated with the azimuthal drift of a charged particle with the largest period (τ_Φ) amongst the three periodic motions, most magnetic fluctuations can lead to its violation and cause radial diffusion of the charged particle across magnetic field lines.

Walt (1971); Lejosne & Kollmann (2020) reviews radial diffusion and its sources. Magnetic field fluctuations are the primary source of radial diffusion. However, electric field fluctuations can induce magnetic field disturbances through current variations. The solar wind interaction can drive them within the magnetosphere, and also variations in the coupling with the ionosphere and thermosphere, turbulence (Minnie et al., 2009), or ULF waves (Li et al., 2017). Ultimately the sum of all these different field fluctuations drives the particle cross-drift shell motion. Figure 3.6 shows the radial diffusion coefficient (D_{LL}) estimated and observed at different L-shells. The maximum diffusion based on these estimates is $D_{LL} = 10^2 R_E^2/day$, which corresponds to a cross-field drift of about 0.1 R_E within one bounce period ($\tau_J = 10$ sec) of 1 keV electrons. Higher energy electrons have shorter bounce periods and therefore drift for a lesser time before being absorbed into the ionosphere. Therefore, for precipitating electrons (electrons within the loss-cone), radial diffusion causes only a very modest cross-shell drift of $\sim< 0.1$ R_E, which is comparable to the gyro-radii of these particles (~ 0.1 R_E).

Therefore, the magnetic field mapping uncertainty in the radial direction is clearly dominated by the uncertainty in modeling the magnetic fields, as opposed to cross-field drifts. It is also worth mentioning the error in mapping is much

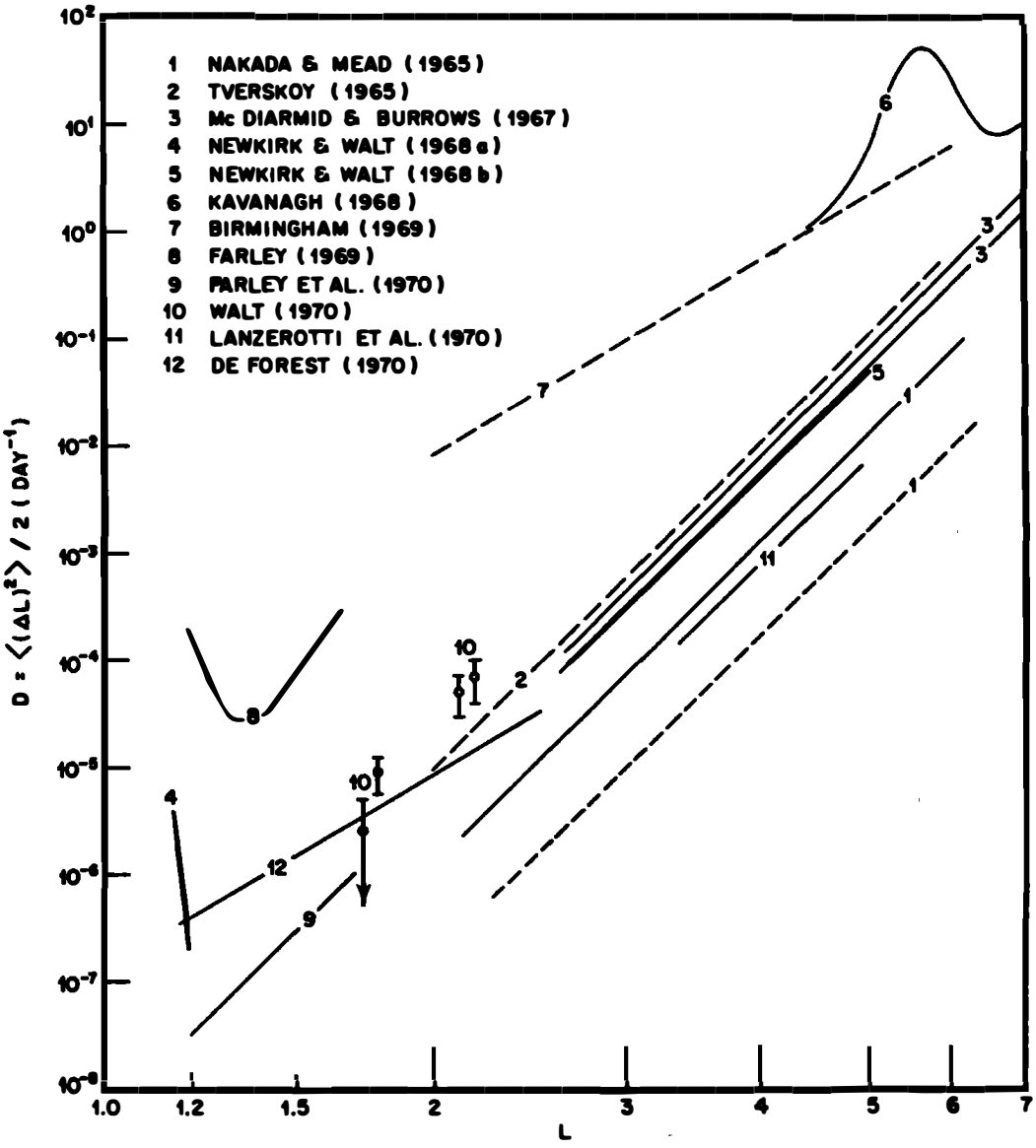

Figure 3.6: Collected values of radial diffusion coefficients, dashed lines are theoretical values, and solid lines and symbols are experimentally determined. After Walt (1971)

higher along the azimuthal or (MLT) direction. This is because magnetic field gradients, curvature, or electric fields cause the charged particles to drift azimuthally. The azimuthal drift speeds can be much higher than radial drift rates. For gradient and curvature drift, the drift speeds depend on the energy and charge of the particle. It results in temporal dispersion in the precipitating particles' energy, the slope of which will be proportional to the duration the particles have spent drifting in the magnetosphere.

3.3.1.4 Correlation and causation

Causation is established through correlation of measurements and theory of particle motion in magnetic fields. If the properties of the charged particle distribution correlate between two magnetically conjugate regions, we can conclude that the plasma populations are the same. The validity of this conclusion is contingent on the truth of our model of charged particle motion in a magnetic field. To confirm this further, one can also show that the properties of plasma do not correlate with neighboring regions that are not magnetically conjugate.

Even now, we cannot establish causality, as our knowledge of the direction of physical connection is missing. Do changes happen in the magnetosphere, which we then observe in the ionosphere or vice-versa? We address this by relying on our knowledge of single-particle motion. Only charged particles within the loss cone at the magnetic equatorial plane reach down to the atmosphere. Therefore, an increase in precipitation necessarily needs a disturbance in the pitch angle distribution tailward of the point of interest along the magnetic field line.

Causality cannot be identified from statistics without a causal assumption. According to the causal inference theory (Pearl, 2009), there is nothing in the distribu-

tion functions that would tell us how it would change if external conditions were to differ. Statistics or probability theory alone cannot tell us how a property of the distribution would change when another property of it is modified. This information must come from a *causal assumption*, which identifies relationships that remain invariant when external conditions change. Therefore, behind every causal conclusion, there must lie some causal assumption that is not testable in observational studies.

Here, the causal assumption is that the charged particles follow the physics of motion in magnetic field lines, and perturbation in the flux is ultimately caused by changing electromagnetic fields in the magnetosphere or transport of particles from some external source. Based on this assumption, we can use correlation with magnetospheric plasma and the lack of correlation with external conditions to establish a causal connection between magnetospheric sources and ionospheric effects of particle precipitation.

Therefore, the source mechanisms of precipitation are assumed to be acting somewhere in the magnetosphere rather than the ionosphere. However, one could rightly argue that there might be changes in the ionosphere that activate magnetospheric mechanisms resulting in the disturbance of fields that eventually precipitate particles. We address this by clarifying that our definition of the source of precipitation is merely the previous step in the long chain of transformations of energy (and information) in the magnetospheric system. Ultimately, discussing the source of a phenomenon in the magnetosphere-ionosphere system or any complex dynamic system for that matter will be ambiguous. A dynamic system is always responding to changes in its environment and within it from the moment of conception. Therefore, it constitutes a series of processes that take the system from one

state to another. **Sources are links in a long chain of processes.** Any attempt to identify the sources of a process within the system is merely referring to noticing the previous link in the chain of processes that constitutes the system.

3.3.1.5 Constraining magnetospheric source of precipitation

As charged particles undergo bounce motion along its guiding field line, the pitch angle of the particle varies according to equation 3.49 derived from the conservation of magnetic moment.

$$\frac{sin(\alpha)}{\sqrt{B}} = \frac{sin(\alpha_{eq})}{\sqrt{B_{eq}}} \tag{3.49}$$

This suggests that the differential number flux pf particles associated with a particular pitch angle along the field line (α_λ at latitude λ) is the same as its corresponding pitch angle at the magnetic equator ($\alpha_{\lambda=0} = sin^{-1}(\sqrt{B_{\lambda=0}/B_\lambda} sin(\alpha_\lambda))$):

$$j(\alpha_\lambda, E) = j(\alpha_{\lambda=0}, E) \tag{3.50}$$

As a result, the flux of precipitating electrons measured at the ionosphere is equal to the loss-cone flux measured by a probe at the minimum magnetic field surface (approximately the magnetic equatorial plane). An additional consequence of this is that the observed flux in the ionosphere will be equal to that of the magnetic equator if the pitch angle distribution (PAD) of the charged particle of energy (E) is isotropic. It will be less if PAD at the equatorial plane is a pan-cake distribution, and greater if it is bi-directional. Therefore, the measurement of precipitating particles in the ionosphere allows us to estimate the flux within the loss cone precisely at the magnetic equator. And also, by knowing the type of PAD at the magnetic

equator, we can determine if the total flux at the magnetic equator is greater than or less than the precipitating particles' flux.

The above arguments hold only as long as there is no violation of first adiabatic invariants. If there is any acceleration process between measurements at the ionosphere and the magnetic equatorial plane, then the flux within the loss-cone can be different in these two regions. That is, if $\langle j(\alpha, E)_{iono} \rangle_{\alpha} \neq \langle j(\alpha_{eq}, E)_{eq} \rangle_{\alpha_{eq} < \alpha_{losscone}}$, then there is some energization or scattering process happening between the two regions along the magnetic field line that connects them. Figure 3.7 describes the causal assumption made from the principles of charged particle motion in the magnetic field. Figure 3.7a) shows two probes, both earthward of the source of acceleration, measuring correlated energy spectra of loss-cone particles. Figure 3.7b) shows the case of the source of acceleration occurring between the two probes, resulting in differences in the loss-cone energy spectra measured by the probes. For this method to work, both probes have to be on the same magnetic hemisphere (in this case, the northern hemisphere), unless the source of acceleration is symmetrically located in both hemispheres. As mentioned earlier, this is because changes in the loss-cone flux are communicated earthward, not tail-ward, since most of the loss-cone particles are lost into the atmosphere and do not mirror back. Some of the loss-cone particles do get scattered back into the magnetosphere via elastic collision with neutrals, and undergo more bounces, to eventually be absorbed by the atmosphere (Khazanov et al., 2018).

a) Correlated spectra

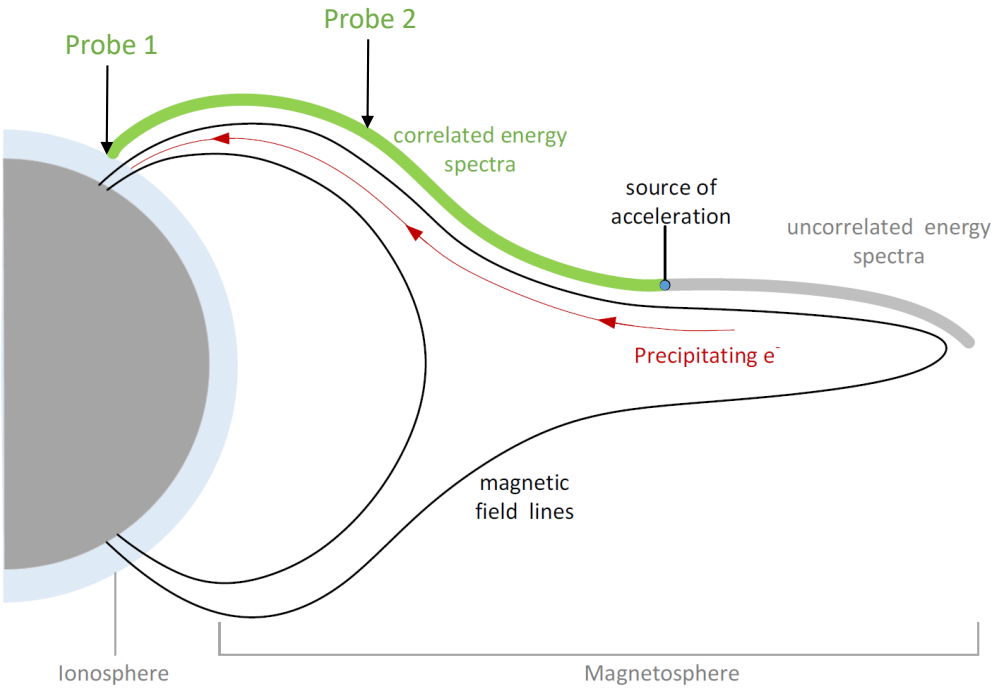

b) Uncorrelated spectra

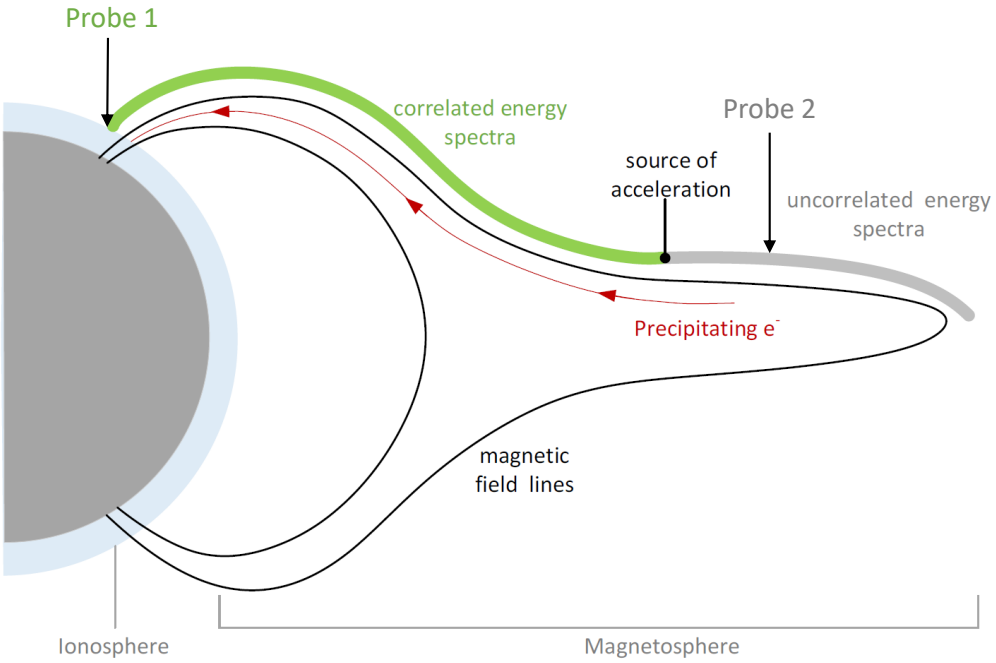

Figure 3.7: Cartoon illustrating the location of two probes along a magnetic field line with a source of acceleration relative to them and the resulting association between the energy spectra of loss-cone particles measured by the probe.

Reiff et al. (1988) analyzed data from two spacecraft: the Dynamics Explorer -1 and -2, which had orbits at an altitude of $\sim$ 11,000 km and 700 km respectively. This puts the spacecraft at a trajectory that crosses the earthward and tail-ward regions of the auroral acceleration region (AAR). The AAR extends between 4,000–12,000 km (Shelley, 1995). It is the region where the quasi-static acceleration of charged particles occurs due to electrostatic structures with electric fields parallel to the magnetic field (Sadeghi & Emami, 2018). Measurements during magnetically conjugate time periods of the satellites with a < 1 min, $\delta\lambda \sim 0.1°$, and $\delta MLT \sim 45$ mins were considered. From the differences observed in the energy spectra of particles with $\alpha \sim 0°$ by both satellites, Reiff et al. (1988) was able to extract the potential drop in the auroral acceleration region that accelerates electrons. Figure 3.8 a) shows a model of the differential number flux of precipitating electrons $j(\alpha = 0°)$ as a function of energy (E). The distributions measured by DE-1 and DE-2 can be described by equations 3.51 - 3.52.

$$DE-1:\ j(\alpha=0°,E) = const.\ \exp -\frac{E}{kT} \tag{3.51}$$

$$DE-2:\ j(\alpha=0°,E) = const.\ \exp -\frac{E-e\phi_{Tot}}{kT}\ for\ E \geq e\phi_{Tot} \tag{3.52}$$

According to Reiff et al. (1988) ϕ_{Tot} can be approximated to the potential drop across the AAR, and they calculate it from the differences in the peak flux values of the two measured distributions. We show the relative positions of the satellites to the AAR and the quasi-static potential structure in figure 3.8 b.

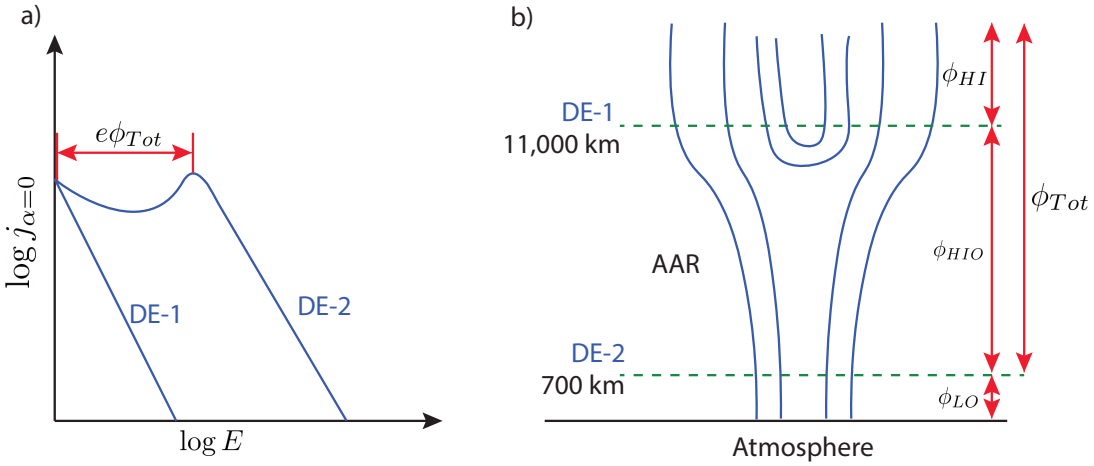

Figure 3.8: The model of the energy spectra observed by DE-1 and DE-2 satellites (panel a), and their corresponding locations in the auroral acceleration region with a quasi-static electric potential structure (panel b). After Reiff et al. (1988).

Finally, before describing specific studies that we have conducted using the above techniques, we should mention that the relative position of source mechanisms with known auroral or precipitation structures or boundaries can help narrow the magnetospheric location of the source. Newell et al. (1996) undertook an instrumental and detailed characterization of precipitation boundaries. For example, the electron stable trapping boundary b_2t was identified in chapter 5 using specific structural variations in energy spectral measurements predicted by the theory of current-sheet scattering. It allowed us to attribute the precipitation to the outer-radiation belt boundary. The surrounding regions did not have the same energy spectra. And based on our causal assumptions of charged particle motion in magnetic fields, we were able to conclude that a causal connection exists between the observed ionospheric features and the outer radiation belt boundary.

CHAPTER 4

Energetic Precipitation from the Plasma Sheet

Particles precipitating from the plasma sheet during substorms can contain a mixture of essentially two energetic particle population: one produced by the near-Earth auroral acceleration region (AAR) and the other arising from the direct precipitation of the plasma sheet electrons. The former is associated with the discrete aurora and the latter with the diffuse aurora (Mironova et al., 2015).These visual signatures, a result of ionization driven by precipitating particles, are an ionospheric reflection of energy exchange in the magnetosphere. Thus, ionospheric measurements can be used to remote sense these processes, which are difficult to quantify using *in situ* measurements.This chapter is based on Sivadas et al. (2017), where we discuss source locations of electron precipitation of different energies and contributions of particle acceleration in different regions during a substorm event using the Poker Flat Incoherent Scatter Radar (PFISR) in combination with *in situ* measurements by the Time History of Events and Macroscale Interactions during Substorm (THEMIS) spacecraft.

Precipitating electrons associated with aurora are mostly in the energy range 1–10 keV. However, as described in 2.7, precipitating electron population can contain a high-energy tail of electrons of primary energies ranging from 10 to 100 keV that cause X-ray emissions (Brown, 1966). This high-energy tail, sometimes referred to as energetic electron precipitation (EEP), was first measured indirectly by rockoons (small rockets carried by balloons and ignited in the stratosphere) with onboard Geiger tubes and scintillation counters that measured the X-rays (Meredith et al., 1955). EEPs have been measured in the past using cosmic radio noise absorption

by riometers e.g., (Berkey et al., 1974; Hartz & Brice, 1967), X-ray measurements from balloon campaigns e.g., (Barcus & Rosenberg, 1966; Pytte & West, 1978), ionosphere electron density measurements from incoherent scatter radar e.g., (del Pozo et al., 1993; Osepian et al., 1996), particle measurements in space e.g., (McDiarmid et al., 1975; Collis & Korth, 1985), and X-ray measurements from low-altitude satellites e.g., (Imhof et al., 1978). Simultaneous ground- and space-based observations have been used to study temporal and spatial evolution of EEPs and their source in the plasma sheet during substorms (Kosch et al., 2001a; Kurita et al., 2015; Pytte & West, 1978).

In previous literature, no consistent definition of the EEPs has been followed, as authors have chosen the definitions of electron energies depending on their foci: 10–100 (Brown, 1966), 25–100 (Anderson & Enemark, 1960), >30 (Lam et al., 2010), and 4.65–1,050 keV (Callis et al., 1998). In our study, we classify energy ranges of precipitating electrons based on phenomenological grounds. Electron precipitation of energies 1–10 keV is termed auroral electron precipitation, as this population is predominantly the cause of the visible aurora. We identify electron precipitation between 10 and 100 keV in the auroral region as energetic auroral electron precipitation, as this population is mostly energized and scattered by processes within the auroral acceleration region and the intervening space between the ionosphere and the plasma sheet. The upper energy limit of energetic auroral electron precipitation is limited by the maximum energization in the auroral acceleration region, which is in turn limited by the maximum polar cap potential that reaches up to $\sim$ 100 kV (Borovsky, 1993; Boyle et al., 1997). As we discuss later in this chapter, the precipitating electrons of energy >100 keV are likely to originate from sources within the plasma sheet or the magnetotail. Utilizing the fact that rest mass

of an electron is 511 keV, we define electron precipitation between 100 and 500 keV as subrelativistic electron precipitation and that greater than 500 keV as relativistic electron precipitation.

However, the source of energization of electrons is not uniquely determined by electron energy, as different sources of energization could contribute to the precipitation of electrons of similar energy. *In situ* measurements can provide energy spectra that reflect particle acceleration processes in the plasma sheet, whereas radar measurements can reconstruct precipitating particle spectra that are subject to both plasma sheet and auroral acceleration processes. Using combined ground- and space-based measurements, we can distinguish different energization processes and identify source locations

Here, we present observations of a substorm in the near-Earth plasma sheet with simultaneous variations in magnetic field, electron energy spectra, pitch angle distribution (PAD), and particle anisotropy in conjunction with the occurrence and motion of electron precipitation in the ionosphere. Nearly magnetically conjugate measurements were made in the ionosphere by PFISR and at the plasma sheet by the THEMIS spacecraft. The magnetic conjugacy of these measurements provides a unique opportunity to address the question of the source location and morphology of the precipitating subrelativistic electrons (>100 keV). To estimate the energy spectra of precipitating electrons, we use a maximum entropy-based inversion technique (Semeter & Kamalabadi, 2005) to invert altitude profiles of electron density measured at the ionosphere, as described in section 3.1.1.3. This inversion technique applied to PFISR measurements provides us with quantitative estimates of precipitating electron energy spectra with a spatial and energy resolution that superior to *in situ* measurements.

In this chapter, we present a quantitative comparison of different energy ranges of precipitating electrons as observed from the ionosphere and the plasma sheet. Our work reveals a close spatial and temporal correlation between the magnetic reconfiguration of the plasma sheet and the electron precipitation >10 keV observed from the ground. The energy spectrum and time variation of the 10–100 and 100–500 keV electrons broadly constrain the source region and acceleration processes within the magnetosphere that generate them. This work demonstrates the feasibility of establishing this source partitioning using incoherent scatter radar (ISR)-based remote measurements of the D and E region ionosphere in conjunction with *in situ* plasma sheet measurements.

4.1 Experiment Overview

Clear signatures of the 10–10 and 100–500 keV populations in the high latitude ionosphere were observed during a large substorm of AE ∼1400 nT at ∼11:44 UT on 26 March 2008. Figure 4.1 illustrates the relative positions of PFISR, THEMIS All Sky Imagers, and THEMIS-D spacecraft during the growth phase (∼11:15 UT) when the magnetic field configuration was tail-like. *In situ* measurements of PADs and magnetic fields provide insight into magnetic field topology and the spacecraft location with respect to the plasma sheet. Among the three THEMIS probes (C, D, and E) that were in the plasma sheet at most times, THEMIS-D's northern magnetic footprint estimated using the T89 magnetic field model (Tsyganenko, 1989) was at PFISR MLT at ∼9:47 UT and ∼1.5 hr in MLT to its west during the early expansion phase (∼11:45 UT). The longitudinal extent of the substorm is much larger (∼5 hr in MLT) than the longitudinal separation between the satellite footprint and PFISR. The latitudinal separation between them is ∼0.5° at 9:47 UT and grows to

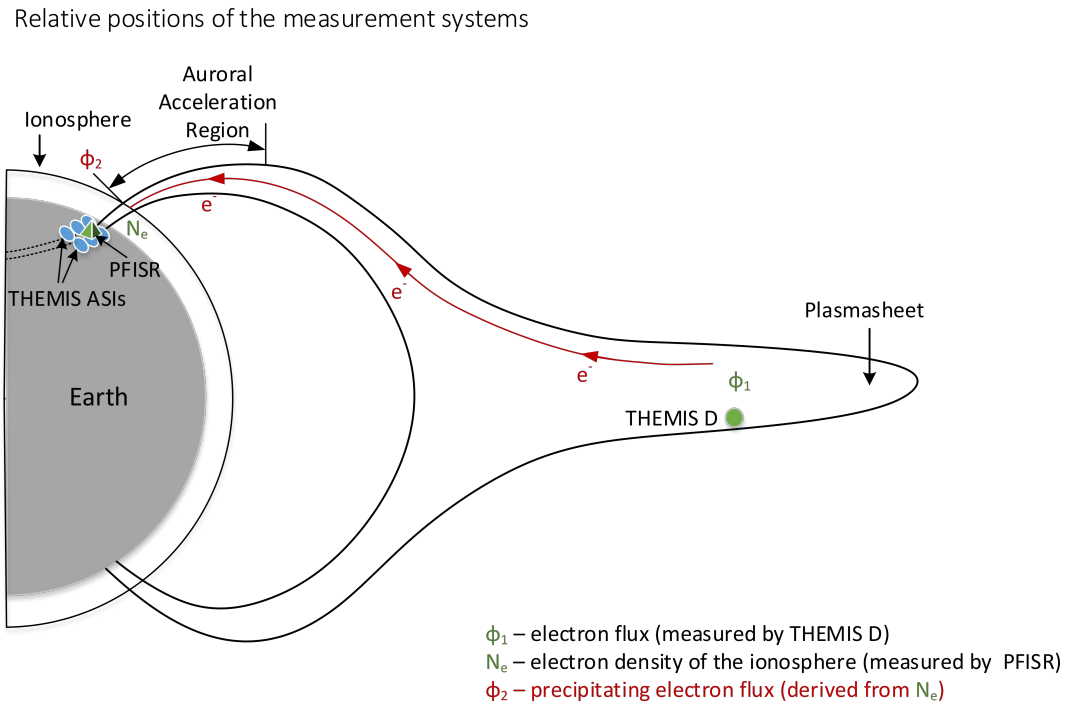

Figure 4.1: The relative positions of measurements and derived quantities made during the 26 March 2008 substorm. THEMIS-D is within the near-Earth plasma sheet at a distance of 7–11 R_E and is also ~ 1 R_E southward of the neutral sheet. After Sivadas et al. (2017).

$\sim$4° toward the end of the substorm. This configuration offers a unique opportunity to examine transport of plasma from the plasma sheet to the ionosphere during a substorm. Convective flows in the ionosphere during this substorm were previously studied by Semeter & Kamalabadi (2005).

Figure 4.1 depicts the type of measurement made by each instrument from ground and space and their relative positions in the magnetosphere-ionosphere system. Comparing differential electron fluxes measured by THEMIS-D ($\phi_1(E)$) and precipitating electrons estimated at the ionosphere ($\phi_2(E)$) enables us to infer

the source location of particle acceleration and precipitation. $\phi_2(E)$ is estimated from the altitude profiles of PFISR electron density ($N_e(z)$)) using the inversion technique described by Semeter & Kamalabadi (2005). This technique in combination with ion-chemistry models is summarized in the following subsection.

4.1.1 Estimating the Precipitating Electron Energy Spectrum

Precipitating charged particles cause ionization at different altitudes depending on their incident energy. Although both electrons and protons precipitate in high-latitude regions, we assume negligible contribution toward ionization from proton precipitation for altitudes <110 km because of the extreme energies required for protons to penetrate to these altitudes (Fang et al., 2013). With this assumption, we estimate the ion production rates due to electron precipitation from altitude profiles of electron density measured by PFISR. Alternatively, we could estimate the production rates with prior knowledge of precipitating electron energy spectra using Monte Carlo models that evaluate the effect of EEP on the neutral atmosphere (Sergienko & Ivanov, 1993). This approach constitutes the inversion of a forward model, where the causal factor is the energy spectra of the precipitating electrons and the resulting observation is the altitude profile of the production rates. However, because we do not have prior knowledge of the energy spectra of precipitating electrons, we solve the inverse problem using estimated production rates from PFISR as an input to determine the precipitating electron energy spectra that caused it.

Using the principle of conservation of mass and neglecting transport processes, we estimate the production rate of electrons in the ionosphere with measured electron density as described in equation 2.8. Here we assume quasi-neutrality, i.e.,

$N_e \sim N_i$. Here N_e is the electron density, N_i is the ion density, and α_{eff} is the effective recombination rate (See section 2.4.2). The effective recombination rates in the E region of the ionosphere may be represented by empirical models such as those proposed by Vickrey et al. (1982). Vickrey's model assumes $\alpha_{eff} = 2.5 \times 10^{12} e^{(\frac{z}{51.2})}$ [$m^3 s^1$], where z is the altitude in kilometers, which is obtained as a reasonable fit to the various profiles of effective recombination rates measured or computed by several authors for the E region. However, recombination in the D region requires a more sophisticated approach that considers the complex ion chemistry (See section 2.4.3). The Sodankylä Ion Chemistry (SIC) model developed at the Sodankylä Geophysical Observatory computationally solves concentrations of several ions, negative ions, and neutral species between the altitude of 20 to 150 km, with 1 km resolution, taking into account several hundred chemical reactions and external forcing due to electron precipitation (Turunen et al., 1996, 2016).

The SIC model predicts higher recombination rates at altitudes lower than 85 km as compared with the empirical model by Vickrey et al. (1982). Hence, for the same input electron density below 85 km in the D region, the SIC model estimates production rates that are several orders of magnitude higher than that of Vickrey et al. (1982). The SIC model is initialized by simulating only photoionization for a few days before the substorm. The model is then adapted to the PFISR measurements by searching for a production rate profile $q(z)$ that produces the observed electron density N_e. This is done independently for each altitude of the measurement and in the same time resolution as the ISR measurement. When the required $q(z)$ is found, it is smoothed and interpolated to the native altitude resolution and range of SIC and is used to obtain the production rate for the next instant of time. The model does not explicitly estimate the effective recombination rate, as it uses

numerous independent reaction rates, a negative ion chemistry scheme, and ion-ion recombination coefficients to determine the electron production rates. Several studies in the past have validated the SIC model by comparing observations with the model's predictions (Verronen et al., 2005, 2015).

With a known incident energy spectrum of precipitating electrons, the forward model of the production rates computed directly using the Monte Carlo model proposed by Sergienko & Ivanov (1993) can be expressed as a system of linear equations with coefficient matrix A: $q = A\phi$. Here A is the production rate profile per incident electron flux and is calculated by evaluating the production rate induced by a unit flux of monoenergetic electron beam precipitating into the neutral atmosphere, and ϕ is the incident differential electron number flux to the ionosphere.

With production rate q estimated from electron density measurements and the forward model A evaluated using the Sergienko & Ivanov (1993) Monte Carlo model, the differential number flux of electrons can be calculated by solving the inverse problem: $\phi = A^{\dagger}q$.

The pseudoinverse $A^{\dagger}$ is realized through the Maximum Entropy Method described in chapter 3. The method maximizes Burg's entropy $-\sum_{j}^{j=1} log(\phi_i)$, and the algorithm is as described by equation 3.28. According to Semeter & Kamalabadi (2005), the inverse problem is generally ill posed. However, the Maximum Entropy Method effectively handles the ill-conditioned nature of the ISR inversion problem and preserves sharp gradients in the density during reconstruction. The inversion performs well even when a mildly underdetermined problem is posed and is insensitive to the manner in which the energy bins are distributed.

The Vickrey and SIC models estimate production rates, which are inputs to

the inversion algorithm, based on the measured ionization profiles. Using the SIC model results in a higher production rate below 85 km and consequently a higher flux of precipitating electrons >50 keV, as compared with Vickrey. During quiet times, the noise power below 85 km is comparable to the signal power and calls into question the accuracy of the inferred energy spectra above 50 keV. Both models produce similar results for altitudes above 85 km and for electron energies less than 50 keV. The quality of the inversion procedure and the effect of using Vickrey and SIC model is discussed in detail in section 4.2.2.

In order to validate the estimated electron energy flux, a comparison between the estimate and measurements from low Earth orbit satellites is necessary. Such a comparison has been described by Semeter & Kamalabadi (2005), with FAST satellite measurements for electron energies <30 keV. The inversion procedure has also been evaluated by Zettergren et al. (2008) who used simultaneous ISR and optical spectroscopy measurements to test the internal consistency of the forward model. Currently, we do not have an independent validation of estimates of electron energies >30 keV using low Earth orbit satellites.

4.1.2 Instrument Configurations

Electron density measurements used to estimate the energy spectra of precipitating electrons in the ionosphere were made using PFISR, an electronically steerable phased-array ISR located at Poker Flat Research Range near Fairbanks, Alaska (65°N, 147.5°W). During the substorm, the phased-array system used 26 narrow beams, with a width of 1.1°, steered in a pulse-to-pulse basis within a field of view spanning from 64°N to 66°N latitude and 145°W to 149°W.

We use the THEMIS all-sky white light imagers (ASIs) to observe the evolution

of the substorm from the ground. Twenty ASIs cover the higher latitudes in North America, each with a circular field of view of about 9° latitude, to ensure accurate determination of substorm onset locations to within ∼1 hr of magnetic local time (Mende et al., 2008). We use three of the THEMIS ASIs situated in Gakona, Fort Yukon, and Whitehorse.

Figure 4.2 is a selection of mosaics of THEMIS ASIs, together with instrument locations during our event. Details of the auroral dynamics pictured in the figure is described in section 4.2.1. Here we note the PFISR beam configuration mapped at 110 km altitude displayed with green dots and its relative position with respect to the ASIs and magnetic footprints of the THEMIS spacecraft at the same altitude. The single beam outside the square pattern points along the local magnetic field, which is at 77.5° in elevation. A digital pulse compression technique is used, in particular a 13-baud Barker code with 10μs bauds, for a better altitude resolution. With a pulse length of 130 μs, the altitude resolution of the measurements of electron density can be estimated to be 1.5 km. The temporal resolution of the final data product after processing the ISR spectra is 124 s. The post-processing assumes the equality of ion and electron temperatures, which is valid at lower altitudes considering the rapid energy exchange between particles through collisional processes.

We also use a suite of instruments onboard the THEMIS-D spacecraft to study the source of the precipitating electrons. We use the Electro-static Analyzer (ESA) and Solid State Telescope (SST) to measure electron energy flux from 5 eV to 1 MeV (Angelopoulos, 2008). These instruments can also measure the PAD of electron and ions with an angular resolution of 22.5°. The SST and ESA Level-2 data products are calibrated and have undergone improvements to mitigate contamination. We

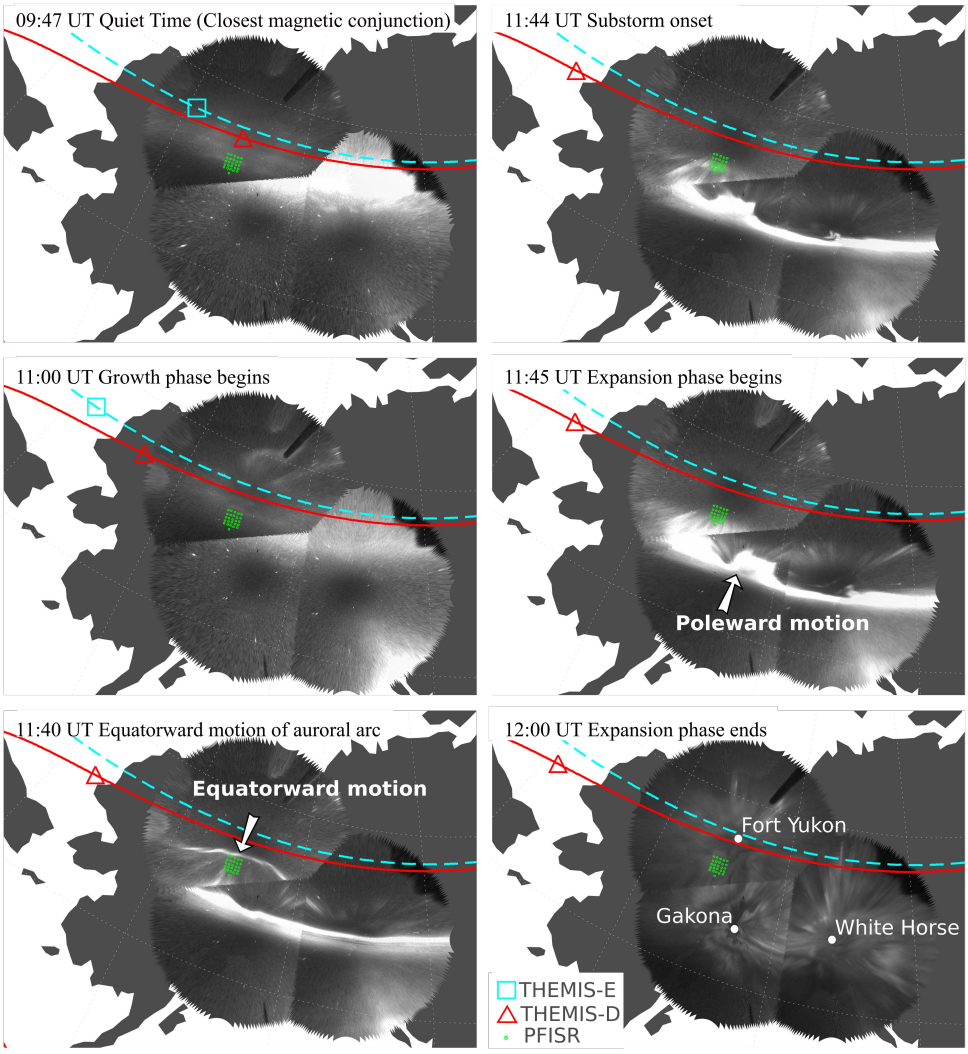

Figure 4.2: THEMIS all-sky image mosaics with the magnetic footprints of THEMIS-D and E along with the projection of PFISR beams, all at 110 km altitude, at different time instances during the evolution of the substorm on 26 March 2008.

use the latest calibrated and corrected data uploaded on January 2014 with a temporal resolution of 96 s. The Fluxgate Magnetometer (FGM) onboard THEMIS produces vector magnetic field measurements of the background DC magnetic fields with a 3 pT resolution and ±25,000 nT range (Auster et al., 2008), which can be used to study the reconfiguration in the Earth's magnetosphere during the substorm. We also use the FGM measurements to estimate wave power along the GSM-X axis for frequencies below 1 Hz. The Electric Field Instrument (Bonnell et al., 2009), which has a sensitivity of 10^4 mV m^{-1} Hz$^{-0.5}$ at 10 Hz, was used simultaneously to estimate wave power along the GSM-Y axis for the same frequencies. The Search Coil Magnetometers can make measurements between 0.1 Hz and 4 kHz with sensitivities of 0.8 pT Hz$^{-0.5}$ at 10 Hz and 0.02 pT Hz$^{-0.5}$ at 1,000 Hz (Roux et al., 2008). We use the Search Coil Magnetometers data to estimate wave power for frequencies between 1 and 1,000 Hz.

4.2 Observation

In this section, we describe measurements made by the THEMIS ASIs, THEMIS spacecraft, and PFISR along with estimates of precipitating electron spectra made by inverting measured electron densities during the substorm event on 26 March 2008.

4.2.1 Substorm Overview

In the first snapshot of Figure 4.2 at 9:47 UT, the sky within the PFISR field of view is relatively quiet and dominated by diffuse aurora as the preceding substorm concludes. At this time, the THEMIS-D magnetic footprint is closest to PFISR. From about 11:00 UT, the diffuse aurora starts to move equatorward signaling the be-

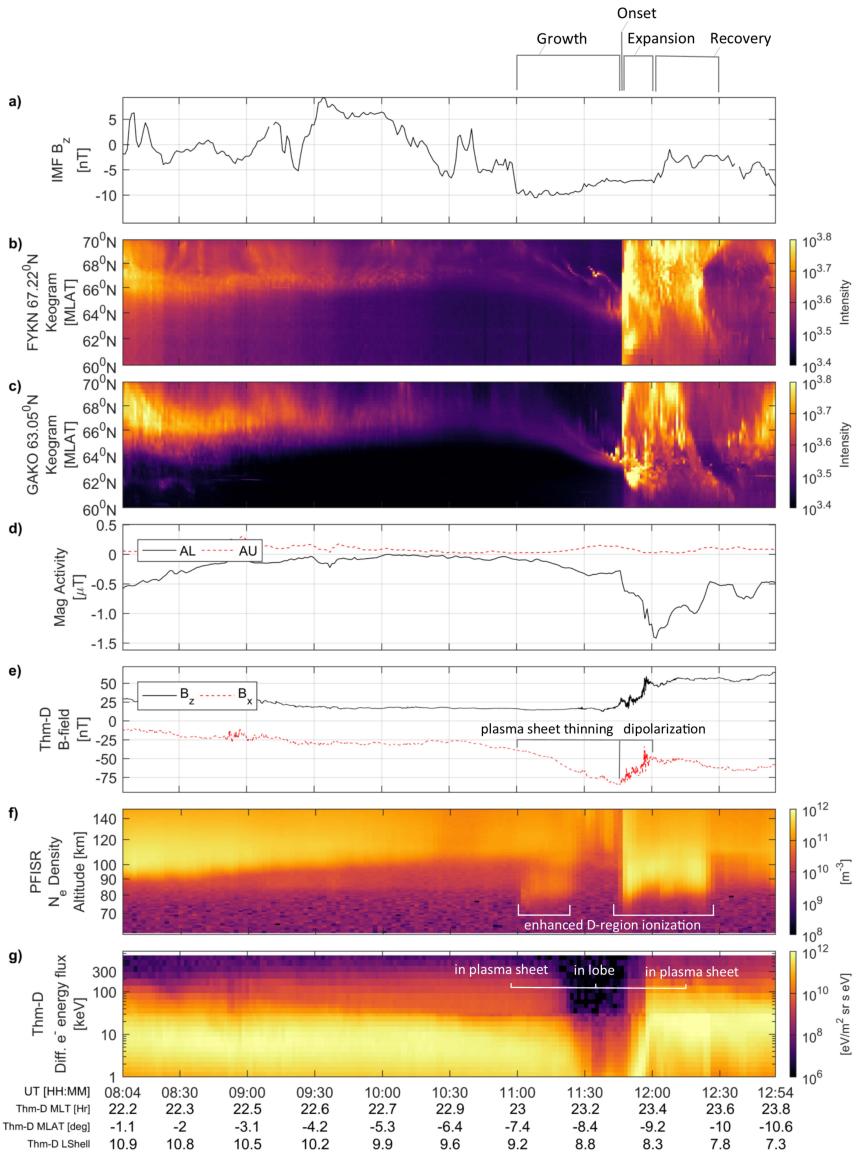

Figure 4.3: Overview of relevant ground- and space-based measurements during the substorm on 26 March 2008: (a) Northward IMF component from ACE spacecraft time-shifted to the bow shock nose; (b) optical keogram from an ASI at Fort Yukon; (c) same from Gakona; (d) auroral electrojet indexes AL and AU; (e) measurements of z and x components of the DC magnetic field in GSM coordinates from THEMIS-D; (f) altitude profiles of electron density by PFISR (averaged across 26 beams); and (g) differential energy flux of electrons from THEMIS-D.

ginning of the growth phase. A few discrete arcs are also observed moving equatorward during the growth phase. Note a bright one at 11:40 UT moving equatorward through the PFISR field of view. A sudden brightening of the equatorward arc occurs at ∼11:44 UT and continues to increase in intensity followed by poleward expansion from 11:45 UT, signaling the onset and expansion phase of the substorm. The expansion phase lasts until about 12:00 UT, after which the aurora starts to become fainter–indicating a transition into the recovery phase that ends at about 12:30 UT after which the intensity and activity in the night sky returns to what was observed before the growth phase.

Figure 4.3 presents a global perspective of the substorm using both space- and ground-based measurements. Figure 4.3a shows the interplanetary magnetic field (IMF) along the GSM-Z axis measured by the ACE satellite and time-shifted to the bow shock nose. At 10:40 UT, the IMF turns southward, which presumably created conditions for reconnection in the dayside and hence initiating the growth phase of the substorm at ∼11 UT. Around this time in Figure 4.3b, the keogram from Fort Yukon (FKYN) THEMIS ASI located at 66.56°N–145.21°E close to Poker Flat clearly shows a decaying diffuse aurora. From about 11:00 UT, the auroral intensities move equatorward as seen in the keogram from FYKN and also Gakona (GAKO) THEMIS ASI located equatorward of PFISR at 63.05°N–145.16°E (Figure 4.3c). The AL index in Figure 4.3d and the earthward component of the magnetic field (Bx) measured by THEMIS-D in Figure 4.3e decrease (or increase in magnitude), suggesting formation of ionospheric currents and tail-like magnetospheric configuration. Figure 4.3f is an altitude profile of the electron density obtained by spatially averaging across all 26 beams of PFISR, also making the assumption that the ion and electron temperatures are the same throughout. The averaging

allows for better statistics while limiting the spatial resolution to about $\sim$0.5° in magnetic latitude. For altitudes less than 85 km, the electron density observed is typically below 10^{10} m^3, and they have comparatively poor signal-to-noise ratio. As the diffuse aurora crosses the PFISR field of view, we observe substantial D region ionization in Figure 4.3f between 11:00 and 11:30 UT, suggesting a hardening of the precipitating electron energy spectra. However, in Figure 4.3g, we observe a softening of the THEMIS-D electron energy spectra during this period. The apparent disparate behavior of the energy spectra of plasma sheet and precipitating electrons during this period, probably because of the longitudinal and latitudinal separation between THEMIS-D magnetic footprint and PFISR, is discussed further in section 4.3. There is beam-to-beam variation observed during this period that may contribute in part to the lack of correlation with plasma sheet electrons. However, the spatial averaging across beams is more valid during the expansion phase and before the growth phase as there are no significant beam-to-beam variations.

Toward the end of the growth phase $\sim$11:37 UT, we see signatures of a pseudo-breakup from GAKO ASI keogram. Following this at $\sim$ 11:44 UT,B_x and B_z start to increase rapidly, signaling dipolarization. This coincides with a further auroral brightening, followed by poleward expansion and thus the substorm onset. Based on the white light images measured by THEMIS ASIs displayed in Figure 4.2, the onset location was identified to be westward of Poker Flat. During the expansion phase, enhanced ionization is observed by PFISR over altitudes as low as 70 km (Figure 4.3f), indicating enhanced precipitation of electrons with energies greater than 100 keV. The expansion phase of the substorm continues up to 12:00 UT, where the AL index reaches its peak value, and the substantial low-altitude ionization continues to be observed by PFISR. From 12:00 UT, the recovery phase

begins with the AL index and auroral intensities at FYKN gradually returning back to the pre-substorm configuration at about 12:30 UT.

During the expansion phase, sharp increase in electron energy flux greater than 100 keV was also observed by the THEMIS-D spacecraft. Figure 4.3g shows the time series energy spectra of electrons of ∼1 to 1,000 keV in the plasma sheet, developed by combining energy spectra measurements from ESA (electrons <25 keV) and SST (electrons >25 keV) onboard the THEMIS-D spacecraft. The energy spectra observed by THEMIS-D between 11:00 to 11:44 UT is characteristic of plasma sheet thinning known to occur during the growth phase (Pytte & West, 1978). As the plasma sheet thins, the plasma sheet boundary layer passes through the spacecraft, and the spacecraft finds itself in the magnetospheric lobe region after 11:30 UT, where the density of electrons is very low. The satellite's position relative to the plasma sheet during different phases of the substorm is described in Figure 4.4. From 11:44 to 11:55 UT during the expansion phase, the satellite re-enters the plasma sheet as the tail undergoes dipolarization and the plasma sheet expands, and the measured energy flux is much higher than before the onset.

4.2.2 Inversion Results

In Figure 4.5, we compare the time series differential energy flux of precipitating electrons in the ionosphere with that measured by THEMIS-D in the plasma sheet. Figure 4.5a,b shows the results of the inversion carried out using the Vickrey and SIC models, respectively. They provide a comparison of the inversion technique carried out by two different ion-chemistry models, which resulted in similar energy fluxes for energies less than 100 keV. Figure 4.5c, which is the same as Figure 4.3g, shows the differential energy flux of plasma sheet electrons measured by

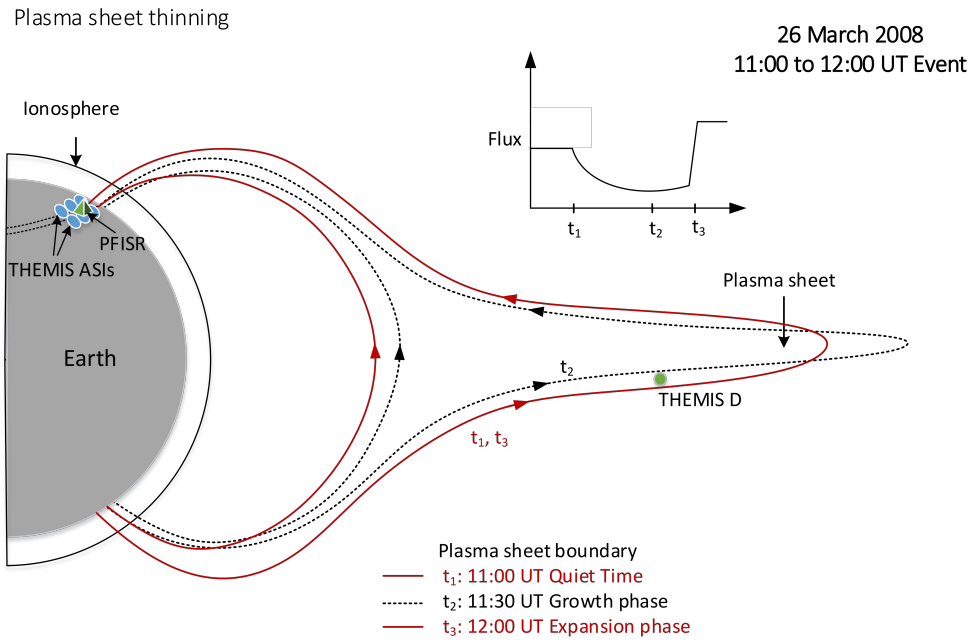

Figure 4.4: Diagram of plasma sheet thinning and expanding before and after the substorm onset. At time t1 before the growth phase, the plasma sheet extends up to about $5R_E$ from the neutral sheet. This phase is not represented in the diagram. However, after t_1, during the growth phase, the plasma sheet starts thinning, and the spacecraft THEMIS-D finds itself in the lobe region by t_2. At t_3, the substorm onset causes rapid expansion of the plasma sheet, because of dipolarization of the magnetic field, and the spacecraft suddenly finds itself within the central plasma sheet with an increased energetic electron flux.

THEMIS-D. It is repeated here to highlight the temporal correlation observed between the energy spectra estimated in the ionosphere and the plasma sheet. The THEMIS-D spacecraft measures the trapped particle population, as it is located close to the magnetic equator and is within the plasma sheet, where the loss cone is less than the angular resolution of the particle detector. However, by definition, PFISR measures particles within the loss cone as they precipitate into the ionosphere. The population of electrons greater than a few tens of kilo-electron volts is mostly higher in THEMIS-D measurements than in PFISR, as indicated by the difference in the energy spectra between the trapped particles and loss cone particles (Figure 4.5c). Figure 4.5a–c shows at least an order of magnitude increase in the net energy flux across all energies after the onset at 11:44 UT as compared with the growth phase. Between 11:00 and 11:30 UT in Figure 4.5a,b, we observe energy flux enhancements of ∼70–100 keV electrons associated with the enhanced D region ionization mentioned in the previous section. This enhancement is not observed in the THEMIS-D energy spectra (Figure 4.5c) because of a lesser degree of magnetic conjugacy during growth phase.

Figure 4.5d,f shows the corresponding cumulative energy flux distribution of the differential energy flux in Figure 4.5a–c, normalized to the highest total energy flux estimated in the time span of the corresponding result. The color indicates the percentage of energy flux of electrons below a particular energy, relative to the highest total energy flux observed within the time span. The median energy of the energy spectra is represented with a cyan line in Figure 4.5d,f. During the growth phase at PFISR from 11:00 to 11:44 UT, the distribution has a median energy value of 5 keV, which increases to 30 keV after the onset (Figure 4.5d,e). This is roughly consistent with THEMIS-D measurements in the plasma sheet with a 7 keV median

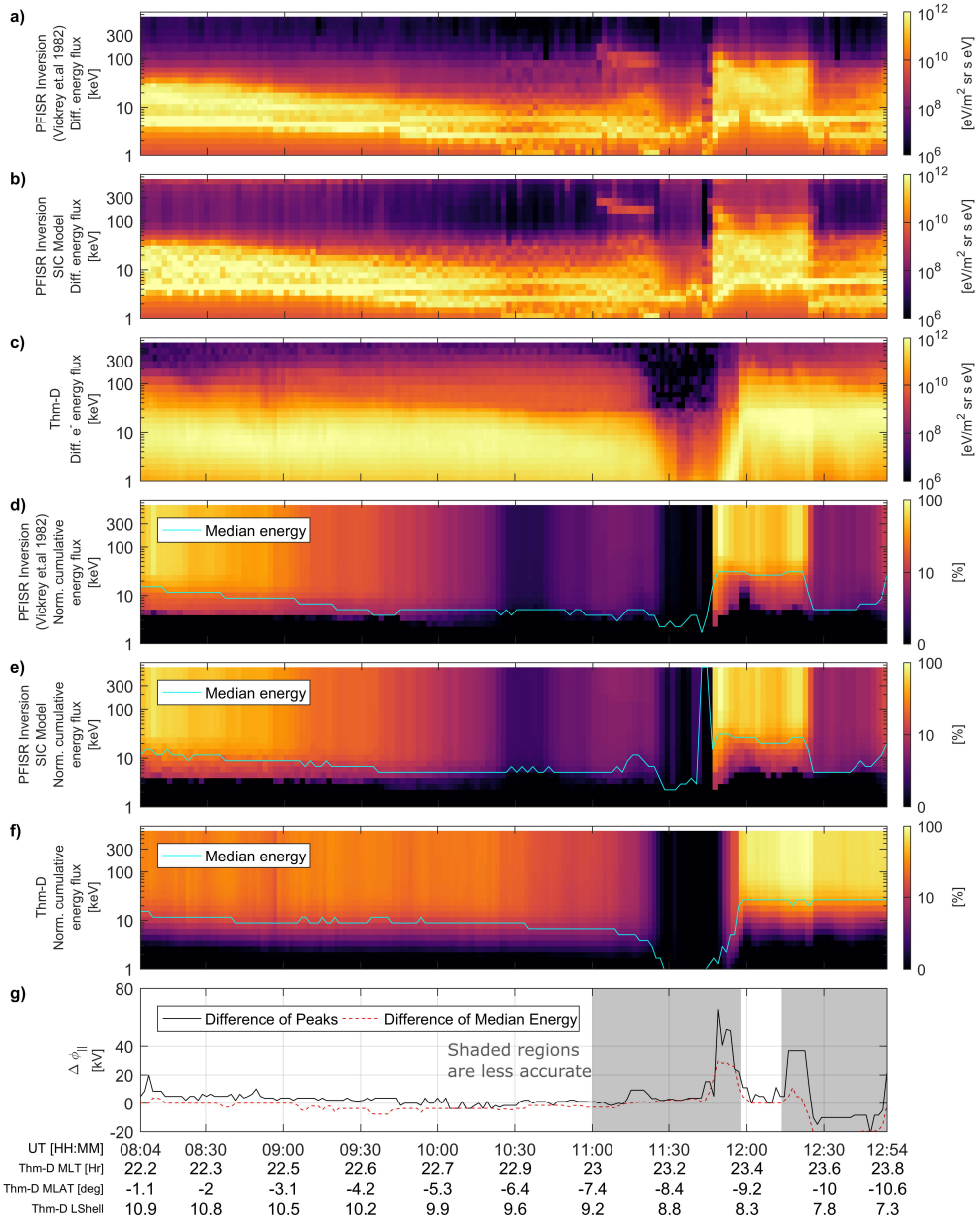

Figure 4.5: Inversion results of PFISR electron density measurement in comparison with THEMIS-D energy spectra: (a–c) Differential electron energy spectra estimated from PFISR measurements using Vickrey model, the same using SIC model, and measured using THEMIS-D, respectively; (d, f) normalized cumulative energy spectra of the same; and (g) maximum potential drop estimated from the differences in peak and median energy in the differential electron energy spectra between PFISR and THEMIS-D.

for the electron energy spectra during the growth phase and 25 keV after the onset (Figure 4.5f).

Note the qualitative agreement between the differential energy flux in Figure 4.5a–c and normalized cumulative energy flux in Figure 4.5d,f. Comparing the differences in the energy distributions in the plasma sheet and the ionosphere, we can estimate the maximum parallel potential required to accelerate the loss cone electrons. Figure 4.5g displays the maximum parallel potential between the plasma sheet and the ionosphere estimated from the differences in the high-energy peaks (black solid line) and the median energy (red dashed line) of the loss cone energy spectra. In reality, the parallel potential drop is likely to be less than this value because of simultaneous pitch angle diffusion effects that may affect the median energy or high-energy peaks. Before the substorm onset, the estimated parallel potential drop is a few kilovolts. After the onset, it is as high as ∼10–20 kV, indicating an active AAR. However, beyond 11:00 UT, the estimate has a lot of uncertainty as longitudinal separation between THEMIS-D and PFISR increases substantially even though latitudinal variability remains small. Because of this separation, the spacecraft is within the magnetic lobes during 11:44 to 11:55 UT and sees little or no electron flux at higher energies, leading us to inaccurately estimate a higher potential drop (∼70 kV) between the plasma sheet and the ionosphere. Between 11:55 and 12:15 UT, the satellite finds itself moving into the plasma sheet and observes the same population as observed by PFISR – estimating ∼10–20 kV potential difference. At about 12:20 UT, the potential difference estimated from energy peak differences reaches about 35 kV, probably because of enhanced precipitation of subrelativistic electrons associated with diffuse aurora observed toward the end of the expansion phase rather than increased parallel electric fields. Time spans

with less reliable estimates have been shaded grey. Although the shaded region spans most of the time of interest, the panel demonstrates that a time series estimate of parallel potential difference between the plasma sheet and the ionosphere can be developed with magnetically conjugate energy spectra measurements from ISR and spacecraft.

Figure 4.6a,b displays the electron density directly measured by PFISR (solid black line) and the uncertainty in the ISR electron density measurements σ_{N_e} (dashed black line). The dashed magenta line is the forward modeling of the inverted electron flux estimated using Vickrey model, which when compared with the electron density directly measured by PFISR indicates the quality of the inversion technique. The dotted blue line is the forward modeling of the THEMIS-D measurement, also using the Vickrey model of effective recombination rates. Comparing this with the PFISR electron density measurement, we can evaluate the degree to which the ionization caused by precipitating loss cone electrons resembles the ionization that may be caused by the precipitation of the entire electron population in the plasma sheet measured by the spacecraft.

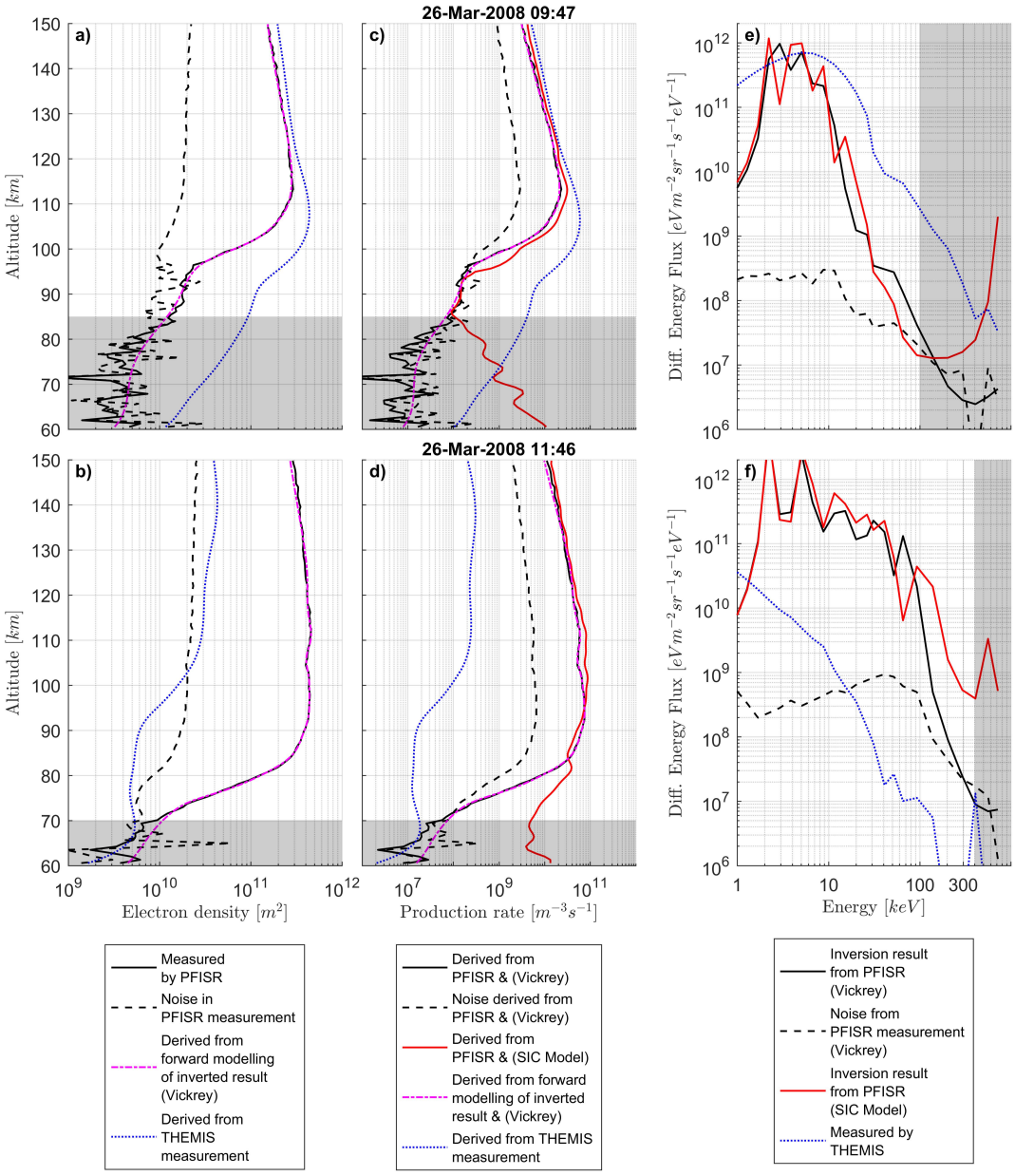

Figure 4.6: Electron density, production rate, and differential energy spectrum estimates from PFISR and THEMIS-D measurements contrasted against each other at two time instances 9:47 UT and 11:46 UT. THEMIS-D's magnetic footprint was closest to PFISR at 9:47 UT, and the highest auroral intensities after the substorm onset was observed at 11:46 UT. The shaded areas have poor signal-to-noise ratio.

Figure 4.6c,d displays data that go through similar processing as that in Figure 4.6a,b, except that they display the production rates derived from the PFISR measurements using Vickrey (black solid line) and SIC models (red solid line). The uncertainty in terms of the production rate, σ_q (black dashed line), is derived by differentiating $q = \alpha_{eff} N_e^2$ so that $\sigma_q = 2\alpha_{eff} N_e \sigma_{N_e}$. It is propagated through the Vickrey model and results in an order of magnitude or more uncertainty in the production rate derived from PFISR measurements below ~8595 km altitude at 09:47 UT and below ~70 km altitude at 11:46 UT. The altitudinal variability is high below ~85 km at 09:47 UT and ~70 km at 11:46 UT. The same is true for the measured electron density in Figure 4.6a,b. In Figure 4.6a, between 85 km and 95 km, the uncertainty only becomes comparable to the signal at a few points. The ISR measurement uncertainty causes the production rates estimated by the SIC model to increase substantially and abruptly below 85 km altitude at 09:47 UT and below 70 km altitude at 11:46 UT. Thus, this increase cannot be considered a result of primary electron precipitation. These altitudes correspond to peak production rates caused by 100 keV at 09:47 UT and ~400 keV at 11:46 UT. Because of low signal to noise ratio and large variability in density with altitude, we consider the regions of the plot that are shaded grey as unreliable.

Figure 4.6e,f shows the results of the inversion process in the form of differential energy flux. The black solid line represents the inversion result from PFISR measurements estimated using the Vickrey model, whereas the black dotted line represents the estimated noise in the energy flux using the same model, and the red solid line represents the inversion result estimated using the SIC model. The error in energy flux is estimated using the diagonalized covariance matrix C_ϕ, where $C_\phi^{-1} = A^T C_q^{-1} A + [Diag(\Gamma\phi)]^{-1}$ (Hysell, 2007). We compare all of these with the closest

magnetically conjugate measurement of differential energy flux by THEMIS-D. In Figure 4.6f, we observe that the energy flux of electrons in the ionosphere greater than 10 keV increases by several orders of magnitude at 11:46 UT, compared with the energy flux before the substorm.It is also important to note that the Vickrey and SIC models predict almost the same production rates and differential energy flux above 85 km (below 100 keV), respectively. However, between 70 and 80 km in Figure 4.6d, the SIC model predicts 1–2 orders of magnitude higher production rates and consequently predicts a higher precipitating energy flux for energies >100 keV as compared with the Vickrey model in Figure 4.6f.

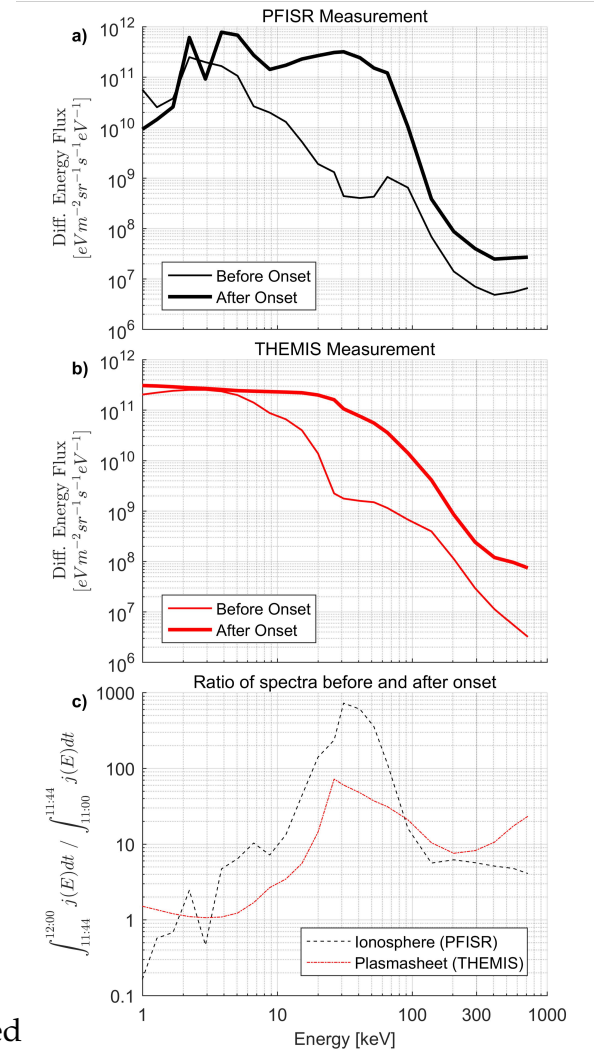

Figure 4.7: Time-averaged energy spectra during (a) the growth phase of the substorm (11:00 UT to 11:44 UT), (b) the expansion phase of the substorm (11:44 UT to 12:00 UT), and (c) their ratio.

Figure 4.7a,b shows the time-averaged electron energy spectra before and after the substorm onset, both in the ionosphere and the plasma sheet, respectively. These panels present the effect of acceleration processes during the substorm on the electron energy spectra measured in the ionosphere and the plasma sheet. The spectra before onset are av-

eraged across 11:00 to 11:44 UT and after onset are averaged across the period 11:44–12:00 UT. Apart from the peak observed at around 2–5 keV before the onset, corresponding to the energy range of visible auroral precipitation, a secondary peak at about 70 keV with lower flux is observed during growth phase. However, after the onset, during the expansion phase, the peak shifts to about 30 keV, with a precipitating high-energy tail that extends higher than 100 keV. Figure 4.7c shows the ratio of the time-averaged energy spectra before and after the onset in the ionosphere and the plasma sheet. This panel compares the changes in the time-averaged energy spectra due to the onset in the ionosphere and plasma sheet. For energies between 2–5 and $>\sim$100 keV, the ratio of the energy flux before and after the onset remains within an order of magnitude in the ionosphere and the plasma sheet. However, for energies between $\sim$4 and 60 keV, the ratio is nearly an order of magnitude higher in the ionosphere compared with that measured in the plasma sheet.

Figure 4.8a,b shows the normalized cumulative energy spectra before and after the onset in the ionosphere and plasma sheet, respectively, averaged across the same period mentioned above. These panels provide an estimate of the proportion of energy within different electron energy ranges before and after the onset. The dashed lines represent the median energy flux value and can be used to find the corresponding median energy. The median energy increases from about 3 to 30 keV in the precipitating electron flux within the ionosphere and from about 5 to 20 keV in the plasma sheet. The total time-averaged energy flux increase measured after the substorm onset is about 20 times in the ionosphere and five times in the plasma sheet, suggesting a substantial increase in the loss cone population. The proportion of energy flux contributed by 10–100 keV electrons increased from less

than 15% of the total energy flux before the substorm onset to about 75% after the onset.

4.2.3 Pitch-angle Anisotropy and Wave Power

To identify possible mechanisms of enhanced precipitation of ∼100 keV electrons, we examine pitch angle anisotropy and wave power at THEMIS-D. Figure 4.9a,b displays the ion and electron pitch angle anisotropy ($A = \frac{V_\perp}{V_\parallel} - 1$) calculated from the PAD obtained from THEMIS-D ESA and SST instruments through the duration of the substorm. An anisotropy value of $A \sim 0$ implies the particles have almost equal perpendicular and parallel energy and hence have an isotropic distribution. $A > 0$ implies greater perpendicular energy or a pancake-type PAD. $A < 0$ implies greater parallel energy or a field-aligned PAD. For electrons greater than 30 keV, from 8:00 to 11:00 UT we observe a bidirectional and field-aligned PAD, characteristic of the plasma sheet boundary layer (PSBL; Parks et al. (1984)). At 11:03 UT, the probe is in the outer edge of the PSBL, where the energy flux starts to drop, and the electron

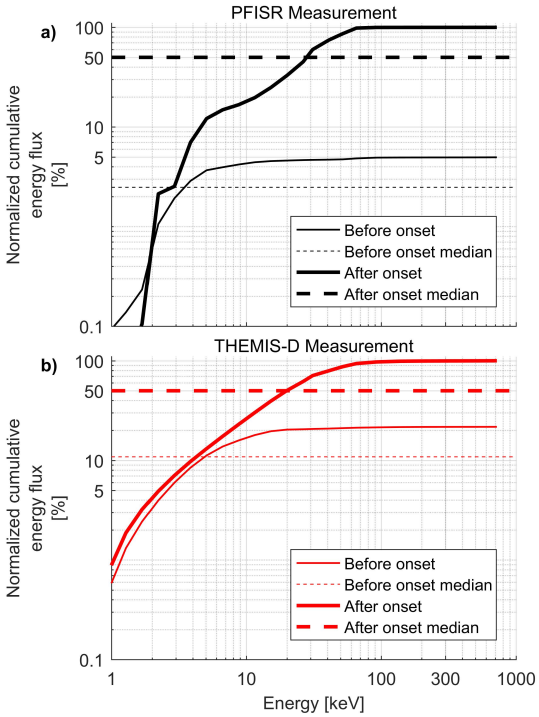

Figure 4.8: Normalized cumulative energy spectra (in percentages) during the growth phase (11:00–11:44 UT) and expansion phase (11:44–12:00 UT) of the substorm estimated from (a) PFISR measurement and (b) THEMIS-D measurement.

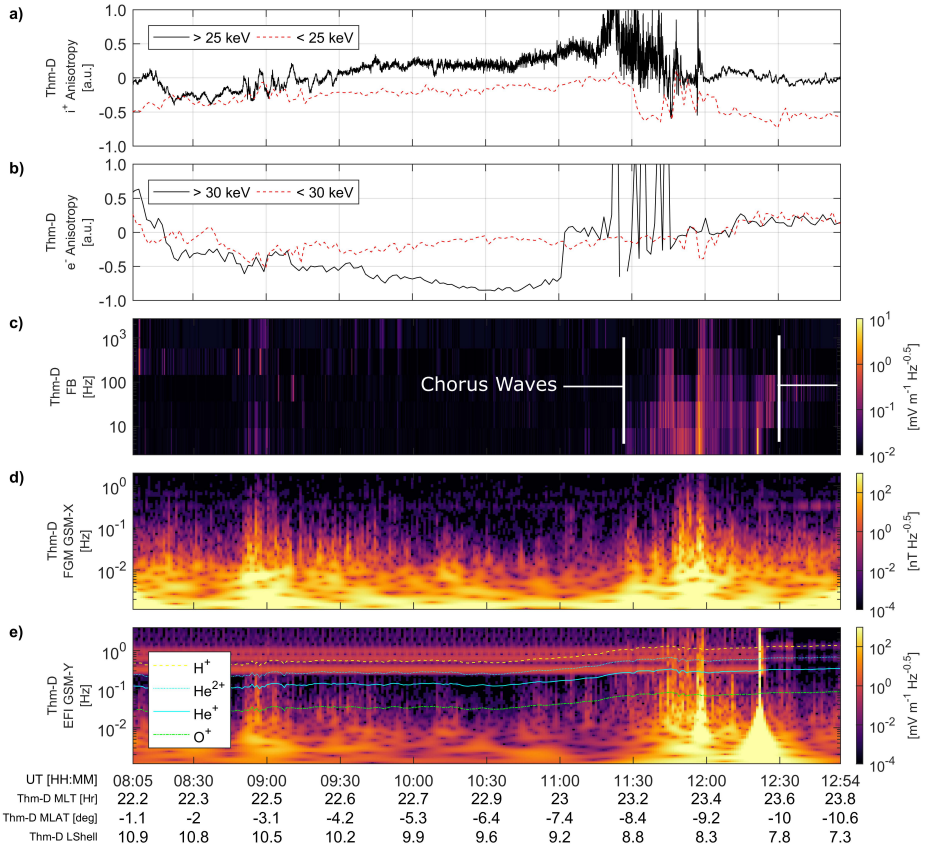

Figure 4.9: Particle anisotropy and wave energy measured by THEMIS-D during the 26 March 2008 substorm: (a) Ion anisotropy and (b) electron anisotropy measured at the plasma sheet; (c) power spectra of high-frequency waves from THEMIS-D filter bank measurements; (d) power spectra along GSM-X axis of low-frequency waves from THEMIS-D FGM measurements; and (e) the same along GSM-Y axis from THEMIS-D EFI measurements overlaid with estimated local ion gyrofrequencies.

PAD is isotropic. Up to 11:44 UT, the flux is too low to determine the nature of the PAD. Immediately after 11:44 UT, the probe finds itself moving through the PSBL into the central plasma sheet, where the distribution is isotropic–as the particles scatter off the neutral sheet (Pytte & West, 1978). After several minutes, the PAD settles down to a pancake-type distribution, with lower flux at pitch angles outside 70–110°.

The energetic ions >25 keV show a positive anisotropy, during the growth phase, and become more isotropic as the expansion phase proceeds. A positive ion anisotropy can lead to generation of electromagnetic ion cyclotron (EMIC) waves. Figure 4.9c,e displays the power spectra of high frequency waves (1–1,000 Hz) and low frequency waves (1–1,000 mHz) along the GSM-X and GSM-Y axes. Figure 4.9e also displays the ion cyclotron frequencies of the major ions present in the plasma sheet. EMIC waves may account for enhanced wave power below ion cyclotron frequencies displayed in Figure 4.9d,e. The minimum cyclotron resonance energies are low enough for electrons to be scattered by EMIC waves with the upper cutoff frequency (ω_{UC}) estimated using the ion densities measured in the plasma sheet (Albert, 2003). The observed wave frequencies are also high enough to meet the minimum resonant energy condition. The EMIC wave amplitudes are enhanced substantially during the substorm expansion between 11:46 UT and 12:30 UT, increasing their efficiency in scattering electrons with subrelativistic energies or higher. Figure 4.9c also shows signs of possible chorus waves close to the substorm onset time.

4.3 Discussion

4.3.1 Correlation in the Energy Spectra

As IMF turns southward at 10:40 UT (Figure 4.3a), the favorable conditions for dayside reconnections cause magnetic fluxes of open field lines to increase in the tail lobes, accompanied by an increase in the earthward component of the tail magnetic field, B_x (Figure 4.3e), during the growth phase. This is causally linked to the thinning of the plasma sheet as observed by THEMIS and the simultaneous equatorward motion of the auroral oval crossing the field of view of PFISR. We observe temporally correlated decrease in the electron energy fluxes up until 11:44 UT (Figure 4.5a-c) as THEMIS-D and PFISR are nearly magnetically conjugate. However, the transport of magnetic flux and frozen in particles associated with the plasma sheet thinning causes this decrease in energy flux. As the plasma sheet thins down, the spacecraft finds itself moving toward the outer boundary of the plasma sheet as described in Figure 4.4. Measurements of PADs from THEMIS further support this conclusion.

The bidirectional and field-aligned PAD of electrons >30 keV observed before the growth phase (Figure 4.9b from 9:45 to 11:00 UT) is characteristic of the energetic electrons drifting into the nighttime magnetosphere while the field is more or less in a dipole configuration (Pytte & West, 1978). From 11:00 to 11:44 UT during the growth phase of the substorm (see Figure 4.3a), the AL index increases to very high magnitudes from -285 to -1403 nT, signaling the shunting of the cross-tail currents through the ionosphere typical of the substorm onset (Baker et al., 1996). Closer to the outer boundary of the PSBL at about 11:03 UT, the PAD of electrons >30 keV immediately transitions to an isotropic distribution. These isotropic dis-

tributions are typically observed when electrons encounter a more tail-like magnetic field configuration, and the first and second adiabatic invariants break down because of the large electron gyroradius ρ in the vicinity of the neutral sheet crossing in comparison to the field curvature $R_c(\rho >\sim \frac{R_c}{10})$ (Alfvén & Fälthammar, 1963). Between 11:20 UT to 11:50 UT in Figure 4.3g, we observe extremely low flux at higher energies (characteristic of the magnetic lobe) and consequently an erratic PAD because of the low number of samples. Because of their near magnetic conjugacy, the effect of the outer layer of the plasma sheet boundary crossing THEMIS and PFISR was observed almost simultaneously by both as the plasma sheet thins down and the foot of the outer boundary of the plasma sheet in the ionosphere moves equatorward till about 11:44 UT. We speculate that the secondary peak of ∼70 keV electrons observed at the ionosphere in the early part of the growth phase ∼11:0011:30 UT (see Figure 4.7a) may be caused by precipitation from the equatorward-moving trapping boundary, located between the outer-radiation belt and the plasma sheet (Kirkwood & Eliasson, 1990). The outer boundary of the plasma sheet moves across the spacecraft at ∼11:55 UT, bringing with it a high intensity of isotropic/pancake PADs characteristic of the inner plasma sheet during the expansion phase (Parks et al., 1984). This increase in intensity was a result of dipolarization and was delayed by about 11 min with respect to PFISR observations of the poleward boundary swiftly moving northward across the ionosphere at the substorm onset (∼11:44 UT). This delay is due to the MLT difference between the THEMIS footprint and PFISR.

4.3.2 Source Location of Energetic Particles

In this section, we use the following arguments to gauge the source location of the precipitating particles and qualitatively identify the contribution of pitch angle scattering and energization processes affecting them. A correlated variation in the energy spectra at two magnetically conjugate locations, being on opposite sides of the magnetic equatorial plane, suggests that processes between these two locations caused no variations in the pitch angle distribution. It also suggests that the source of these particles lies tailward of the measurement location closest to the magnetic equator. A shift in the median or peak energy in the energy spectra between the two magnetically conjugate locations suggests energization processes acting between the two locations. An uncorrelated variation in the energy spectra without any clear change in the median or peak energy indicates processes that cause pitch angle diffusion between the two magnetically conjugate locations.

In Figure 4.7c, the time-averaged energy flux of electrons >100 keV within the plasma sheet increases up to about five to eight times after the onset whereas that of electrons around 30 keV increases up to 60 times. However, the time-averaged energy flux of low energy electrons of about 3 keV does not change much. The same trend is more or less reflected in the ionosphere, with the exception that the increase in precipitated electron energy flux for ∼30 keV electrons is about 700 times that before the onset. This uncorrelated increase in energy flux for 10–100 keV electrons precipitating in the ionosphere suggests pitch angle scattering due to processes in the AAR or tailward. We estimate the parallel potential drop (Figure 4.5g) by calculating the difference in median and peak energies between the loss cone electrons in the ionosphere and the plasma sheet. Figure 4.5g confirms the increase in parallel potential drop after the onset with a maximum of ∼10 kV,

suggesting energization of cold electrons by the AAR to ∼10 keV. The increase in the energy flux of subrelativistic electrons >100 keV seen in Figure 4.7c at both the ionosphere and plasma sheet suggests the location of the source of these electrons to be at or tailward of ∼9R_E. Figure 4.8 shows the normalized cumulative energy spectra, time-averaged during the growth phase (thin line) and the expansion phase (thicker line), which can be used to estimate the percentage of energy flux up to a particular energy value. We observe a considerable hardening of the spectra after the substorm onset, with an increase in median energy of ∼15 keV in the plasma sheet and ∼25 keV in the ionosphere compared with that before the onset.

4.3.3 Substorm Motion

The time difference of enhanced particle flux in the beginning of the expansion phase observed by PFISR and THEMIS-D is about 11 min (∼11:44 UT at PFISR and ∼11:55 UT at THEMIS-D). THEMIS-D's magnetic footprint is at 68°N, 169.3°W, which is about 22° westward of PFISR. Moreover, THEMIS-E and THEMIS-C are also within the plasma sheet during our period of interest, and further westward of THEMIS-D, they measure the arrival time to be ∼12:00 UT and ∼12:30 UT, respectively. The westward delay in arrival of the energetic particles suggests that the substorm onset is located at an MLT very close to Poker Flat and expands westward. The substorm also expands eastward, to a lesser degree from Poker Flat. Evidence for this can be seen in Figure 4.2, which shows intense auroral brightening at ∼11:44 UT longitudinally close to Poker Flat expanding eastward in ∼11:45 UT.

4.3.4 Distribution of Energetic Electrons within the Plasma Sheet and Corresponding Auroral Arc

One interpretation of the data is that the outer boundary of the plasma sheet maps down to the poleward region of the diffuse auroral arc (Lui et al., 1977). During the growth phase, THEMIS ASIs observe equatorward motion of the arc in the ionosphere, whereas both PFISR and THEMIS observe precipitating electron population from the inner to the outer boundary of the plasma sheet. At 11:00–11:25 UT, the outer boundary of the plasma sheet moves across THEMIS, and the poleward edge of the auroral arc moves equatorward across PFISR's field of view. During this period, Figure 4.5a-c shows the flux of energetic electrons to be decreasing rapidly 1–2 min earlier than the flux of the lower energy electrons in both the ionosphere and the plasma sheet. This observation suggests that the inner boundary of the plasma sheet has a harder spectrum as compared with the outer boundary, and similarly, the equatorward edge of the auroral arc has a harder spectrum than the poleward boundary. The median energy of precipitating electrons in the equatorward boundary is $\sim$5 keV, which reduces to $\sim$3 keV in the poleward boundary. However, a contradictory interpretation is discussed in chapter 5, where evidence suggests that the equatorward boundary of the diffuse aurora maps to the outer radiation belt boundary. While, the poleward border of the diffuse aurora maps to the inner boundary of the plasma sheet.

4.3.5 Pitch Angle Anisotropy

The pitch angle anisotropy of a particle distribution is a useful indicator of wave growth. A sufficiently positive anisotropy of the electron or ion pitch angle distribution can cause growth of either the whistler mode or ion cyclotron mode. The

anisotropy also gives clues to the type of acceleration or scattering mechanism that is acting on the distribution. Processes that act along the field-aligned direction like Fermi acceleration, field aligned potential drops, Alfven waves, or Speiser motion (Wang et al., 2013) are likely to cause negative anisotropy, whereas processes like betatron acceleration cause an increase in the perpendicular energy resulting in a positive anisotropy. Fermi acceleration of the kind described in Ganguli et al. (1995) can cause acceleration during the growth phase along the cross-tail electric field, leading to positive anisotropy. The highly bidirectional pitch angle distribution of the high energy electrons is likely caused by Fermi acceleration type B (or current sheet acceleration) during plasma sheet thinning (Hada et al., 1981).

4.3.6 Wave Scattering and Energization

An analysis of the wave power measured by THEMIS-D confirms the presence of EMIC waves during the growth phase, produced probably due to the positive anisotropy of high-energy ions. EMIC wave interactions with electrons have been proposed to account for the bursty precipitation following substorms by Lorentzen et al. (2000). An estimate of the minimum kinetic energy needed by the electron for cyclotron resonance with the EMIC wave produced by different ion species, made using equation 19 from Albert (2003) is included in figure 4.10. Up to two orders of magnitude increase in the wave power is observed at almost all frequencies from growth phase ($\sim$10:40 UT) to expansion phase (11:51 UT), suggesting a possible increase in pitch angle scattering of electrons $>$100 keV due to EMIC waves produced by H^+ or O^+ ions. O^+ ion concentrations are higher during substorms (Lennartsson, 1987), reaching proportions up to about 20%, thereby increasing the probability of electron scattering. An additional mechanism for scattering could

be bounce resonance with EMIC waves, which Shprits (2009) suggests is most efficient for nearly equatorially mirroring electrons.

The presence of kinetic Alfven waves (KAWs) is highly likely, as the ratio of the low-frequency electric and magnetic perturbations almost equals the local Alfven speed $\sim 10^6$ m/s.Generation of KAWs is closely related to particle injections from the magnetotail. The parallel electric fields associated with KAWs can drive waveparticle interactions that trap electrons in a potential well and accelerate them along the field lines in the plasma sheet. The energy gain is limited to several kilo-electron volts Artemyev et al. (2015) but may be a contributor toward the parallel potential drop pictured in Figure 4.5g. Additionally, parallel electric fields generated by electrostatic double layers can contribute toward accelerating electrons in the AAR. Parallel electric fields increase the parallel energy of the electrons – and therefore contribute to scattering them into the loss cone as well. Figure 4.5g indicates that the combined effect of energization processes between

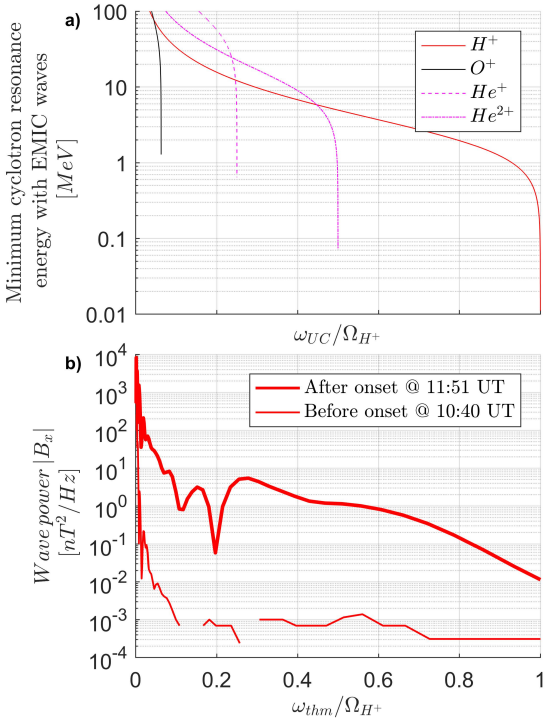

Figure 4.10: a) Minimum resonant energy of electrons estimated using Equation 19 from Albert (2003) for the plasma sheet ion densities measured by THEMIS-D, b) Maximum wave power observed after the onset at ∼11:51 UT and minimum wave power observed at ∼10:40 UT before the onset measured by THEMIS-D in the relevant frequency range showing an increase by two orders of magnitude.

the ionosphere and the plasma sheet may accelerate electrons up to ~10 keV.

Using the same principle in figure 3.8, we develop figure 4.11a, which shows the AAR potential. The potential difference is assumed to be the median energy difference between the energy spectra of loss-cone electrons measured at near-magnetically conjugate locations in the magnetosphere (THEMIS-D) and the ionosphere (PFISR), as shown in figure 4.11b.

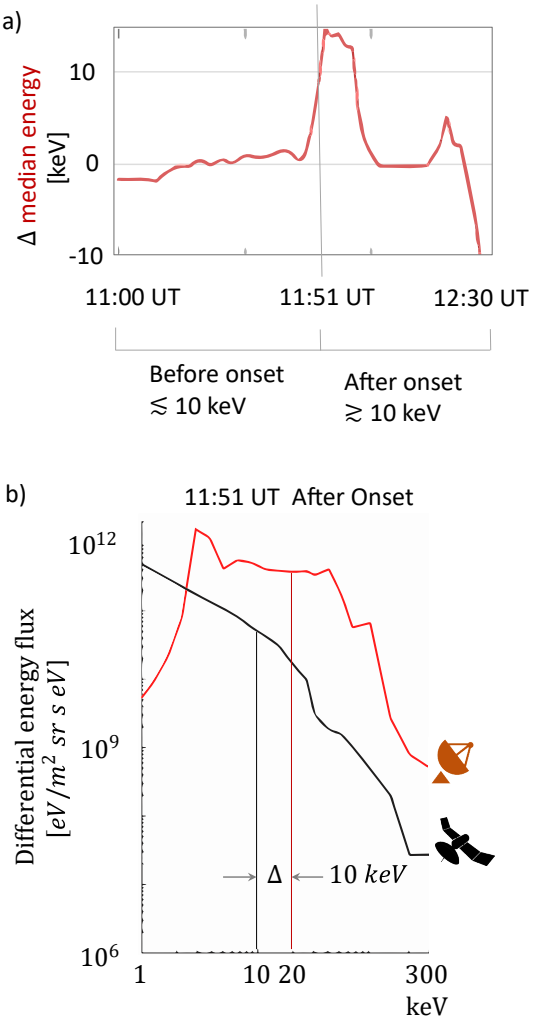

Figure 4.11: a) An estimate of the potential drop along the magnetic field in the AAR at 11:51 UT, b) Energy spectrum of loss-cone electrons measured in the ionosphere (red) and that measured at the near-magnetically conjugate location in the magnetic equatorial plane by THEMIS-D (black).

4.4 Conclusion

This chapter demonstrates the utility of combining ISR-based measurement of energetic particle precipitation with conjugate spacecraft measurements. It begins to address a few specific unresolved problems in our understanding of substorm dynamic (1) the connection between ionospheric signatures and magnetotail processes; (2) energy transmission through the magnetosphere during substorms; and

(3) location of the magnetospheric particle acceleration regions. The subrelativistic electron precipitation observed by PFISR, and its correlation with plasma sheet energetic electron flux measurements after the onset, suggest a direct link between the low altitude ionization and pitch angle scattering of electrons from within the plasma sheet. The substorm onset originates very close to Poker Flat and primarily expands westward at an average rate of 2° per minute longitudinally. The substantial increase in these electron fluxes after the onset and large earthward convection during the onset suggest that they originate tailward of THEMIS-D in the near-Earth plasma sheet and a result of magnetotail reconnection.

In this particular substorm, the electron populations that transfer energy from the magnetosphere to the ionosphere were substantially different before and after the substorm onset. Before onset, the energy is transported predominantly by electrons $<$10 keV, which originates from pitch angle scattering within the plasma sheet. After onset, 75% or more of the energy flux is carried by electrons between 10 and 100 keV. They originate predominantly from pitch angle diffusion caused by parallel electric fields in the AAR and other processes that cause pitch angle scattering within and tailward of the AAR. We speculate the cause of the prolonged precipitation of subrelativistic electrons $>$100 keV after the onset of the substorm to be pitch angle scattering of these electrons in the plasma sheet and beyond ($>\sim 9R_E$) through bounce and cyclotron resonance with EMIC waves.

Key Findings

- Electron precipitation greater than $\sim$100 keV after the onset originate tailward of the near-Earth plasma sheet
- Electrons between 10 and 100 keV are scattered into the loss cone by processes in and tailward of the AAR

- Cold electrons are accelerated up to 10 keV after the substorm onset by the parallel potential drop in the AAR
- Electron cyclotron and bounce interaction with EMIC waves within the plasma sheet may play a role in scattering subrelativistic electrons ($>\sim$100 keV) into the loss cone during the expansion phase of the substorm

Our work validates the ability of ISR measurements to estimate the plasma-sheet loss-cone electron population reliably during a substorm (See also section 6.3). We extend the ISR inversion technique to study two-dimensional transport of electron precipitation across the ionosphere using multibeam measurements made by electronically steerable ISR in the next chapter. Furthermore, magnetically conjugate wave measurements from within the plasma sheet may allow us to estimate the average wave power required for scattering energetic electrons into the loss cone. Unlike spacecraft measurements, the ISR inversion technique provides remote measurements of the plasma sheet with good spatial and temporal coverage that one may use to carry out continuous diagnostics of the phenomenon in question.

CHAPTER 5

Energetic Precipitation from the Radiation Belt

In the nightside magnetosphere, the outer boundary of the outer radiation belt coexists with a non-dipolar and tail-like magnetic field. The field is stretched thin during substorm growth-phase due to enhanced tail current. Radius of curvature of these field lines at the magnetic equator is sometimes as low as the gyroradius of radiation belt electrons (Sergeev et al., 2012). This results in isotropic pitch angle scattering of these electrons into the loss-cone as their first adiabatic invariant (magnetic moment) is no longer conserved. The earthward (equatorward) boundary of this region of isotropic pitch angle distribution is referred to as the isotropic boundary (IB). The electron IB (e-IB) borders such a region of energetic electrons ($\sim$>30 keV) that precipitate down to the lower E- and D-regions of the ionosphere (Sergeev et al., 2008). Low Earth Orbit (LEO) spacecraft measurements of such isotropic energetic electron precipitation located near the outer radiation belt boundary has been referred to as an energetic electron arc (EEA) (Sergeev et al., 1983, 1996). During the growth-phase, the precipitation occurs equatorward of the growth-phase arc (sometimes referred to as a pre-breakup arc) and within the poleward shoulder of the diffuse aurora, and is simultaneously observed as an absorption arc in riometer measurements (Kirkwood & Eliasson, 1990). The absorption arc and the EEA mark the inner edge of the outer boundary of the outer radiation belt during substorm growth-phase (Kirkwood & Eliasson, 1990; Sergeev et al., 2012). Under such conditions the ionization caused by the EEA is an ionospheric signature of the outer radiation belt boundary.

The EEA was first observed using stratospheric balloons measuring bremsstrahlung

X-rays (Rossberg, 1976) and LEO spacecraft (Fritz, 1968; McCoy, 1969). The equatorward moving front of X-ray emissions had a latitudinal extent of 1° stretching as far as 2000 km in longitude and moving at a rate of 5–10 km/min (Pytte et al., 1976). The peak fluxes of precipitating electrons showed a dependence on the magnetic rigidity of the particles, with higher energies reaching a maxima at lower L-shells (Imhof et al., 1978, 1979). Sergeev et al. (1983) were the first to propose that the non-adiabatic scattering of energetic particles in the equatorial current sheet is the most likely mechanism for the isotropy observed at the IB, and consequently the precipitation of energetic protons and electrons poleward of it. Optical signatures associated with the EEA has not been identified in previous literature, however, Opgenoorth et al. (1983) mentions in passing a faint optical arc in overexposed images coincident with an absorption arc. Recently optical pulsating patches were reported in the equatorward edge of the growth-phase arc, coincident with the EEA (McKay et al., 2018).

In this work we present a detailed study of the optical signature that marks the outer boundary of the outer radiation belt during the growth-phase of a strong substorm. We describe simultaneous small-scale observations of a structured diffuse aurora (SDA) correlated with the EEA, spanning spatial, temporal and energy dimensions. We found that the SDA spans at least 1° in latitude and ∼2000 km in longitude, consistent with X-ray emissions observed by Pytte et al. (1976). It is faint and diffuse with highly structured east-west aligned features in the poleward shoulder of the nighttime diffuse aurora. The SDA is composed of ∼5–300 keV electrons mapping to distances of ∼9–12 R_E. It marks the nightside transition region where the outer radiation belt particles overlap with the plasma sheet particles, and we speculate that this might be used as an optical tracer of the radiation

belt boundary during substorm growth-phase. The energy spectrum of precipitating electrons within the SDA was derived from analysis of ionization profiles observed by Poker Flat Incoherent Scatter Radar (PFISR). Using the GLobal airglOW (GLOW) model we confirmed that direct precipitation of electrons >30 keV from the radiation belt is sufficient to produce detectable optical signatures in 4278 and 5577Å emissions.

5.1 Multi-instrument Measurement of Electron Isotropic Boundary

5.1.1 Instrumentation

As described in 4, during the substorm on 26 March 2008, two THEMIS probes D, and E were on the nightside close to the equatorial plane (-1 $R_E > Z_{GSM} > -2$ R_E). The growth-phase of the substorm extends from ∼11:00 to ∼11:44 UT, with substorm onset at ∼11:44, and expansion phase continuing to ∼12:00 UT. The timings were determined using Geomagnetic Auroral Electrojet (AE) Index and auroral observations (Akasofu, 1964; Tanskanen, 2009; Sivadas et al., 2017). According to the T96 model (Tsyganenko, 1995), the northern magnetic footprints of THEMIS-D and -E, were near Poker Flat, Alaska where a digital All-sky camera (DASC) recorded white-light images at 20 second cadence. The T96 model was calculated using the International Radiation Belt Environment Modeling (IRBEM) library with inputs of Dst, solar wind dynamic pressure, interplanetary magnetic field B_y and B_z measurements at 1-min cadence. The magnetic field model estimates were compared with *in-situ* THEMIS-D measurements to verify accuracy.

During the substorm, PFISR was measuring high resolution altitude profiles

of ionization down to 60 km at a temporal resolution of 15 seconds using interlaced barker coded pulses along 26 different beam directions (Nicolls et al., 2007). This allowed us to develop 4-D electron density fields within PFISR's field of view (FOV) varying in latitude, longitude, altitude and time (Semeter et al., 2010). Magnetic field-aligned electron density profiles were inverted to derive an energy spectral map of the precipitating electrons within PFISR's FOV using the technique described by Semeter & Kamalabadi (2005) and applied to the 26 March 2008 substorm by Sivadas et al. (2017). Co-located with the PFISR and the DASC a digital meridional scanning photometer (MSP) recorded emissions of 4861, 5577, and 4278 Å. A LEO spacecraft, NOAA-17, was at a magnetically conjugate location in the southern hemisphere during late growth-phase. The northern magnetic foot point estimated using T96 has a standard error of $\sim 1.5^{\circ}$ in latitude. In order to improve precision, we used the assumption that precipitating electron energy flux causes the optical emissions observed at the foot point. Hence, we moved the northern foot print of the spacecraft to be morphological consistent with the measurements from the Total Energy Detector (0.05 – 20 keV electrons) on-board the satellite and the magnetically conjugate pixels from the all-sky camera at McGarth, Alaska (MCGR). Using the above instruments we tracked the evolution of energetic electron precipitation through the substorm growth-phase. The magnetospheric and ionospheric location of the instruments are depicted in figure 5.1, and detailed in table 5.1.

Table 5.1: Details of instruments used in this study.

Instrument	Data Product	Location	Time
THEMIS-D	Differential energy flux of e^- (1-900 keV)	~7-12 R_E 22-24 MLT	8-13 UT
THEMIS-E	Differential energy flux of e^- (1-900 keV)	~9-11 R_E 22-23 MLT	""
NOAA-17	Integrated number flux of e^- (>30 keV, >100 keV, >1 MeV)	60°S - 65°S MLAT 23-24 MLT 850 km	11:29-11:31 UT
PFISR	Loss-cone differential energy flux (1-300 keV)	65.3°N MLAT 20.5-1.6 MLT	8-13 UT
DASC	White light intensity of auroral emissions	65.3°N MLAT 20.5-1.6 MLT	""
MSP	Keogram of H_β(4861 A°) N_2^+(4278 A°) and O^+(5577A°)	""	""
THEMIS-GBO	4 all-sky camera white light images	GAKO 63.06°N MLAT FYKN 67.42°N MLAT MCGR 61.72°N MLAT WHIT 63.66°N MLAT	""

[a] Digital All-sky Camera at Poker Flat, Alaska.
[b] Meridian Scanning Photometers at Poker Flat, Alaska

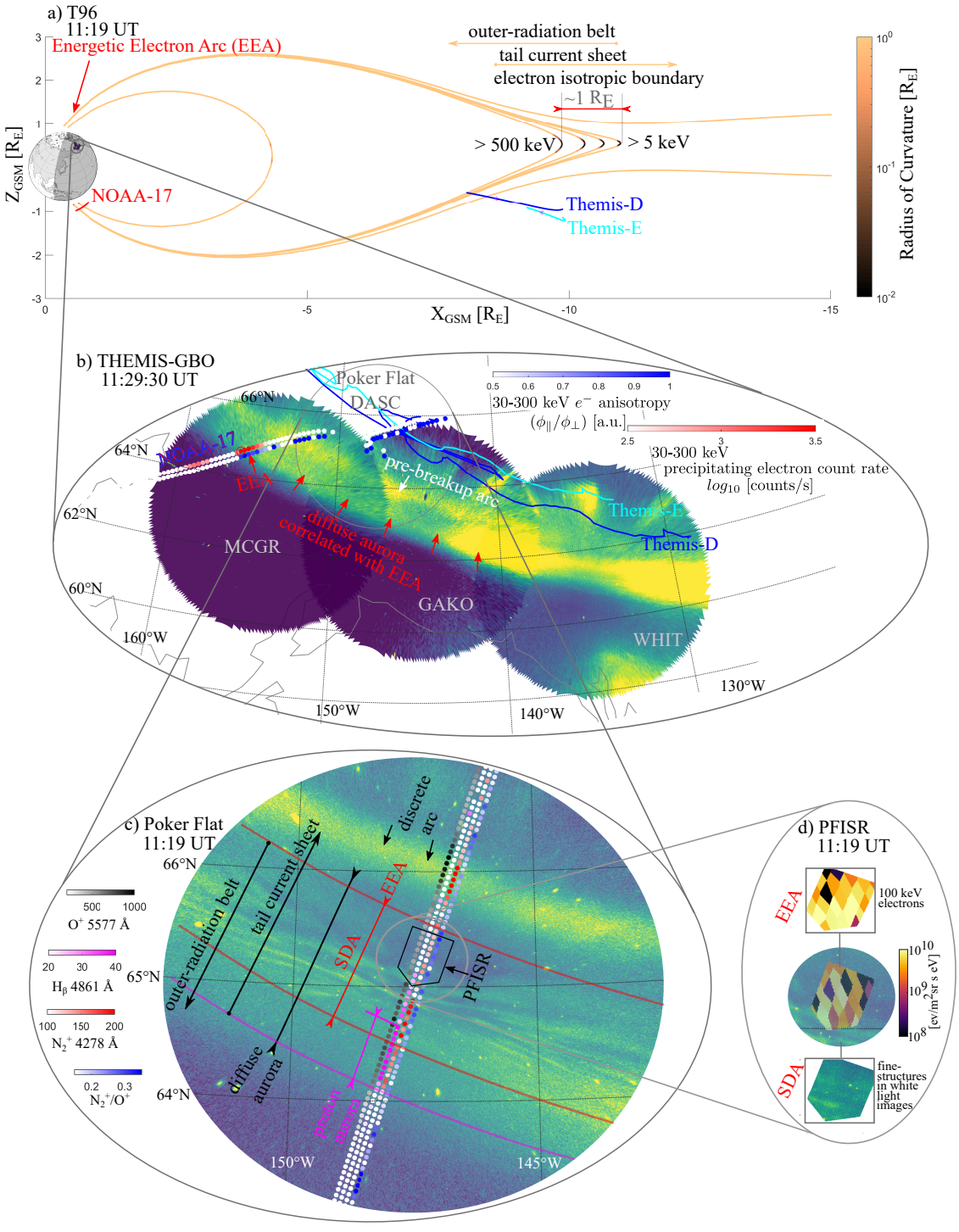
a) T96
11:19 UT
Energetic Electron Arc (EEA)
outer-radiation belt
tail current sheet
electron isotropic boundary
~1 RE
> 500 keV
> 5 keV
NOAA-17
Themis-D
Themis-E
ZGSM [RE]
XGSM [RE]
Radius of Curvature [RE]
b) THEMIS-GBO
11:29:30 UT
Poker Flat
DASC
30-300 keV e− anisotropy
(ϕ∥/ϕ⊥) [a.u.]
30-300 keV
precipitating electron count rate
log10 [counts/s]
NOAA-17
EEA
pre-breakup arc
diffuse aurora
correlated with EEA
MCGR
GAKO
WHIT
Themis-E
Themis-D
66°N
64°N
62°N
60°N
160°W
150°W
140°W
130°W
c) Poker Flat
11:19 UT
O+ 5577 Å
Hβ 4861 Å
N2+ 4278 Å
N2+/O+
outer-radiation belt
tail current sheet
discrete
arc
EEA
SDA
PFISR
diffuse
aurora
proton
aurora
65°N
64°N
150°W
145°W
d) PFISR
11:19 UT
EEA
100 keV
electrons
SDA
fine-
structures
in white
light
images

Figure 5.1: Measurements in the context of the magnetosphere-ionosphere system: a) T96 magnetic field lines with radius of curvature reaching a minimum near the magnetic equatorial plane - with the THEMIS-D, -E and NOAA-17 orbit tracks. b) All-sky cameras with northern magnetic footprints of spacecrafts, showing the large-scale structure of the diffuse aurora correlated with the EEA overlaid with electron count-rates and anisotropy measurements from NOAA-17 at 11:29:30 UT. c) DASC at Poker Flat, overlaid with MSP measurements, showing the ionospheric location of the EEA overlapping with the SDA with respect to the proton aurora. d) Energy flux map of 100 keV electrons estimated from PFISR measurements, correlated with the fine-scale optical signatures of the SDA.

5.1.2 Methodology

The EEA was identified in the ionosphere by virtue of low-altitude ionization reaching ∼70 km altitude, observed by PFISR during substorm growth-phase. The e-IB associated with the EEA was identified in the magnetosphere using precipitating electron flux measurements from NOAA-17 in LEO which maps to the nightside transition region (Figure 5.1a). Here the magnetic topology transitions from a dipole-like field to a stretched tail-like configuration. The diffuse aurora coincident with the EEA was observed with the THEMIS-GBO (Figure 5.1b), and small-scale structures of the SDA were measured with the DASC and MSP at Poker Flat (Figure 5.1c). To constrain the source mechanism of the small-scale structures, we examined the energy spectral maps of precipitating electrons estimated using PFISR (Figure 5.1d) and carried out a correlation analysis of its spatial structure with the corresponding structure observed in the DASC. We also used the PFISR-based energy flux estimates as input to the GLOW model to gauge the contribution of energetic precipitation towards optical emissions in the ionosphere (Solomon, 2017).

Our conclusions are mainly supported by measurements from PFISR, DASC, and MSP. Measurements from the spacecraft NOAA-17 established the proximity of EEA to the outer radiation belt boundary, and THEMIS-D measurements verified the magnetic field model accuracy. In order to estimate the magnetic field mapping error, we compared the *in-situ* magnetic field measurements from THEMIS-D to the T96 model estimates, and evaluated the variability of the northern magnetic foot point of the spacecraft with 11 different magnetic field models. During early growth-phase, the model is more or less accurate with a Bx mostly within 25% of the measured value. A maximum standard error of $\sim$1.5° was observed while mapping the satellite footprint to its northern foot print. See supplemental figure A.1, A.2 and text A.1 for a more detailed discussion.

5.2 Results and Discussion

5.2.1 Overview

Figure 5.1 shows the different scales of the EEA within the magnetosphere-ionosphere system. The magnetic field lines (brown-black lines) are computed using the T96 magnetic field model at 11:19 UT, with the night-side transition region between $\sim$10 R_E < X_{GSM} <$\sim$11 R_E. The radius of curvature (R_C) within this region is less than 0.1 R_E, which is $\sim$8 times the gyro-radius of 5–500 keV electrons. This can cause non-adiabatic pitch angle scattering and with an EEA mapping to a thickness of $\sim$1 R_E in the magnetic equatorial plane for that energy range (Sergeev et al., 1983). The energy range was calculated by using the criteria for non-adiabatic current sheet scattering $K_C = R_{Cmin}/\rho$ $\sim$<8 (Sergeev et al., 1983). Figure 5.1b shows the spatial context of the EEA within the diffuse aurora marked by red arrows.

At 11:29:30 UT, during the late growth-phase, the NOAA-17 satellite footprint (the red circle) is magnetically conjugate with the EEA. Count rates of precipitating 30–300 keV electrons and its anisotropy (ratio of the precipitating flux with trapped flux) is shown as red and blue dots respectively with color proportional to intensities. The EEA is seen as highly isotropic precipitation within the diffuse aurora. Poleward of the EEA, the growth-phase arc or pre-beakup arc is brightening.

Figure 5.1c shows the small-scale structures of the SDA coincident with the EEA, measured 10 minutes earlier as compared to figure 5.1b. Similar SDA has been observed in the nightside auroral oval during different substorm phases, but has not been linked to a magnetospheric source (Samara et al., 2010). The four stripes of filled circles from left to right represent, OI(5577Å), H_β, N_2^+ emissions and N_2^+/OI emission ratios measured by the MSP. The EEA is seen as enhancement in the both the N_2^+ emissions and N_2^+/OI ratio, with low OI emissions. The multiple small-scale features are observed only when the SDA is over the zenith of DASC's FOV. They become diffuse and brighter at lower elevations due to line of sight integration. The intensity of the structure is about $\sim$4% above the background night sky. Overlapping with the equatorward edge of the SDA, is the proton aurora, observed as enhancements in the H_β emissions (magenta dots) caused by current sheet scattering of protons (Spanswick et al., 2017). The region equatorward of the poleward boundary of the EEA (high N_2^+/OI ratio) is the outer radiation belt. The region poleward of the equatorward edge of the proton aurora is the tail current sheet. The proton aurora and the equatorward edge of the EEA make up the diffuse aurora. Poleward of the EEA and within the tail current sheet is a discrete auroral arc seen wider than it is owing to the off-magnetic-zenith line of sight integration. The center of DASC's FOV overlaps with the PFISR FOV and

is detailed in figure 5.1d. The pixelated trapezoidal structure is a map of electron energy flux of 100 keV electrons overlaid on to the DASC image. The uncertainties and caveats of the energy flux estimation are explained in detail in earlier works (Semeter & Kamalabadi, 2005; Sivadas et al., 2017).

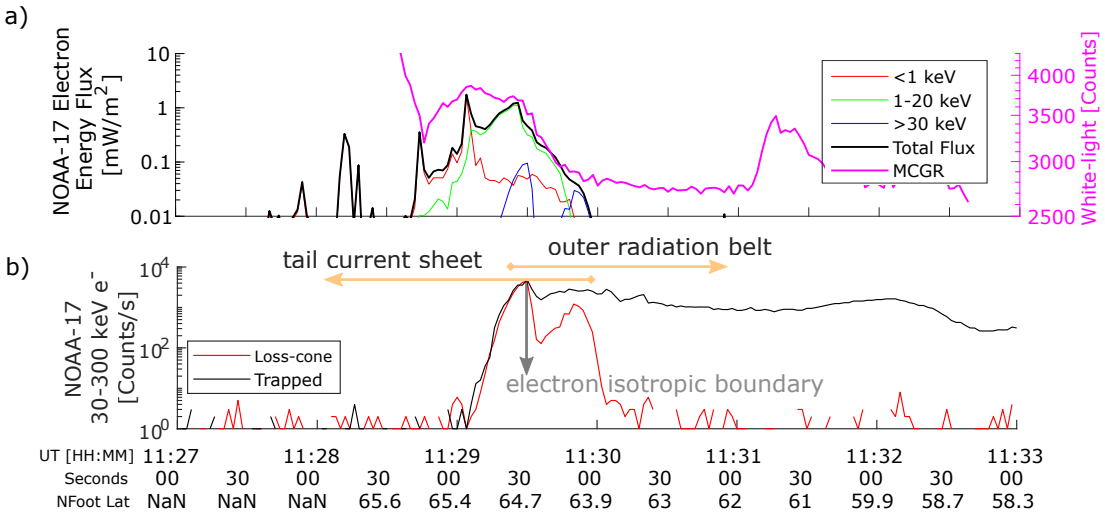

Figure 5.2: Electron isotropic boundary from space: a) Electron energy flux from NOAA-17 measurements along with optical emissions measured by MCGR all-sky camera at NOAA-17's northern magnetic foot-point estimated by T96 model and adjusted to be morphologically consistent with the emissions, b) NOAA-17 count rates of field-aligned and trapped 30–300 keV electrons.

Figure 5.2a shows line plots of electron energy flux estimated from NOAA-17 measurements of electrons <1 keV, 1–20 keV, >30 keV, the total energy flux and white-light emission counts at its northern magnetic foot point from MCGR all-sky camera. The T96 model was adjusted such that the foot point of NOAA-17 was shifted equatorward by ∼1.25° latitude to maintain morphological consistency with the white-light emissions and total energy flux. Before 11:28:40 UT, the white-light emissions measured by MCGR are not auroral. At 11:29:05 UT and

11:29:20 UT there are two peaks in both the NOAA-17 total energy flux and MCGR white-light counts. The former is likely a developing growth-phase/ pre-breakup arc driven by $<$1 keV electrons, and the latter is the peak of the diffuse aurora. Coincident with the latter (equatorward) peak is the EEA. Figure 5.2b shows the line plots of NOAA-17 loss-cone and trapped count rates of 30–300 keV electrons. The loss-cone flux maximum, which is equal to the trapped flux, indicates the e-IB at $\sim$64.7°N MLAT. The sharp drop of trapped electrons count-rates at $\sim$ 65°N suggests that the e-IB and the equatorward boundary of the EEA marks the outer-boundary of the outer-radiation belts.

5.2.2 Equatorward Motion of the EEA and the SDA

Figure 5.3a shows snapshots in time of the equatorward motion of the SDA in three all sky cameras FYKN, DASC (at Poker Flat) and GAKO. From 10:21 UT to 11:35 UT, the SDA moves equatorward at a rate of $\sim$5 km/min. At 11:18:50 UT, the SDA is observed to be coincident with the EEA measured by PFISR. The fine-structure is only visible when the arc is at the zenith of the camera, and is seen as a diffuse arc when at smaller elevation angles. This suggests that the structured precipitation is narrow in latitude, and east-west aligned. Figure 5.3b shows both the DASC image within PFISR's FOV and an under-sampled DASC image in accordance with PFISRs 26 beams. Figure 5.3c shows slices of energy flux maps derived from PFISR for 3, 8, 30, and 100 keV electrons. The diffuse arc enters PFISRs FOV in the DASC image from the poleward edge at 11:04 UT (Figure 5.3b), and moves equatorward when the sharp east-west enhancement of the precipitation is observed in the 100 keV electrons (Figure 5.3c). At 11:18 UT, as the arc continues its equatorward journey it reveals small-scale structure in the DASC image, with

corresponding structural variations in the electron energy fluxes. At ∼11:25 UT, the region of enhanced 100 keV electron fluxes leave PFISR's FOV, and a low energy (∼3 keV) band of discrete aurora enters from the poleward edge. During this period, the EEA had a latitudinal width of ∼1°, with a harder spectra towards the equatorward-edge. The precipitating electrons estimated by PFISR go up to about 300 keV (See supplemental figure A.3b). Sivadas et al. (2017) describes the precipitating electron energies measured during this substorm in detail. Figure 5.3b and 5.3c suggests that the small-scale structures are correlated with electrons >30 keV.

5.2.3 Non-adiabatic Pitch Angle Scattering a Major Source of EEA

Overlaid on the white-light keograms from DASC in figure 5.4a, are line-plots of the maximum energy flux latitudes of 30, 70 and 100 keV electrons estimated from PFISR energy flux maps. The line-plots were smoothed using 1 min moving average filter. The flux of higher energies reaches the peak value equatorward of the lower energy fluxes. This is strong evidence of non-adiabatic scattering from a thinning magnetotail (current sheet scattering), and it is consistent with the minimum electron energy of scatter depicted in figure 5.1a, with lower energies scattered poleward (or tailward) and higher energies scattered equatorward (or earthward). The latitudinal separation between 30 and 100 keV maximum energy fluxes is ∼0.25°, which is consistent with a separation of ∼0.15-0.3° inferred from a temporal separation of ∼2–4 seconds observed with NOAA measurements by Sergeev et al. (2012). Other scattering mechanisms, such as plasma waves co-located with a thinning current sheet, may be acting on the electrons in the transition region and we have not ruled them out. See supplemental figure A.4 and text A.2 for additional discussion.

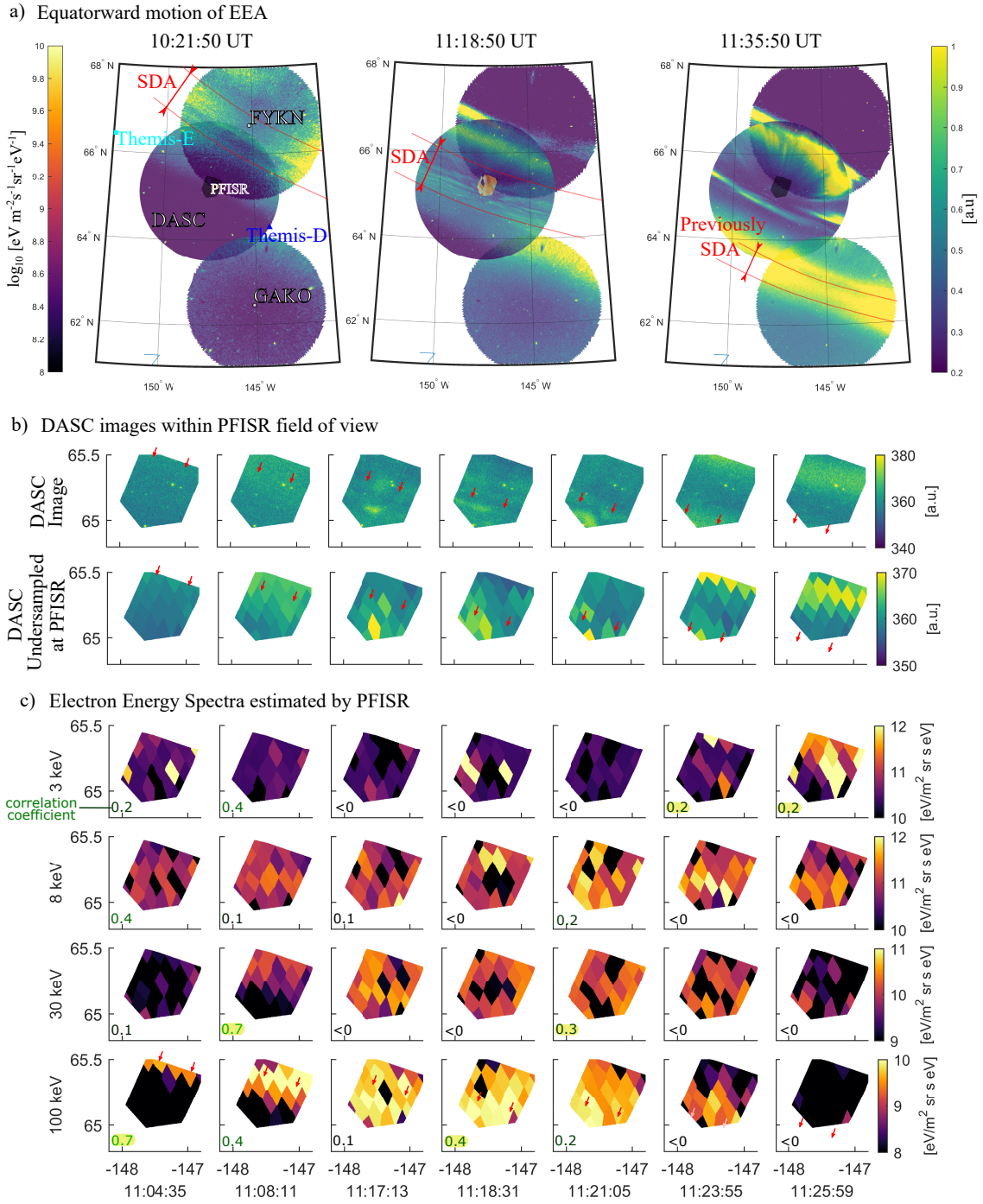
a) Equatorward motion of EEA
10:21:50 UT
11:18:50 UT
11:35:50 UT
SDA
FYKN
Themis-E
PFISR
DASC
Themis-D
GAKO
Previously
SDA
log10 [eV m-2s-1sr-1eV-1]
[a.u]
b) DASC images within PFISR field of view
DASC Image
DASC Undersampled at PFISR
[a.u.]
c) Electron Energy Spectra estimated by PFISR
correlation coefficient
3 keV
8 keV
30 keV
100 keV
[eV/m2 sr s eV]
11:04:35
11:08:11
11:17:13
11:18:31
11:21:05
11:23:55
11:25:59

Figure 5.3: Equatorward motion of the EEA: a) SDA moving equatorward during substorm growth-phase, b) optical images within PFISR's FOV in original resolution and undersampled at conjugate PFISR beam locations, c) electron energy flux at different electron energies estimated from PFISR measurements. The red arrows indicate the motion of the SDA.

5.2.4 Significant Outer Radiation Belt Electron Loss through the EEA

Figure 5.4b shows an estimate of 4278Å emissions made using the GLOW model with PFISR-based estimates of energetic electron spectra at 65.4°N as input. The emissions caused by electrons >100 keV and >30 keV coincide with the diffuse auroral emissions, with a larger contribution from electrons >30 keV within the SDA. The maximum intensity caused by electrons >30 keV is about 406 Rayleigh at ∼11:20 UT, and contributes ∼46% of the total emission intensity at that time. This suggests that the EEA alone can produce detectable optical signatures. Figure 5.4c shows the energy flux in units of power of electrons from 1–10, 10–30, 30–100, and 100–300 keV estimated at ∼65.4°N. The loss through non-adiabatic scattering within the e-IB precipitating into the atmosphere is F_E∼0.4 mW m^{-2} and F_{atm}∼2.8×10^6 cm^{-2} s^{-1} for 100–300 keV electrons. This is a conservative estimate, as the inversion technique underestimates the energy flux of electrons >30keV since the technique used to estimate precipitating energy flux from PFISR measurements extrapolates the E-region chemistry into the D-region (Sivadas et al., 2017). Furthermore, the ionization caused by electrons >300 keV are below the noise floor and are not captured in the PFISR estimate (Sivadas et al., 2017).

The loss of energetic electrons into the ionosphere within the EEA is comparable to the loss observed during relativistic electron dropouts at magnetospheric

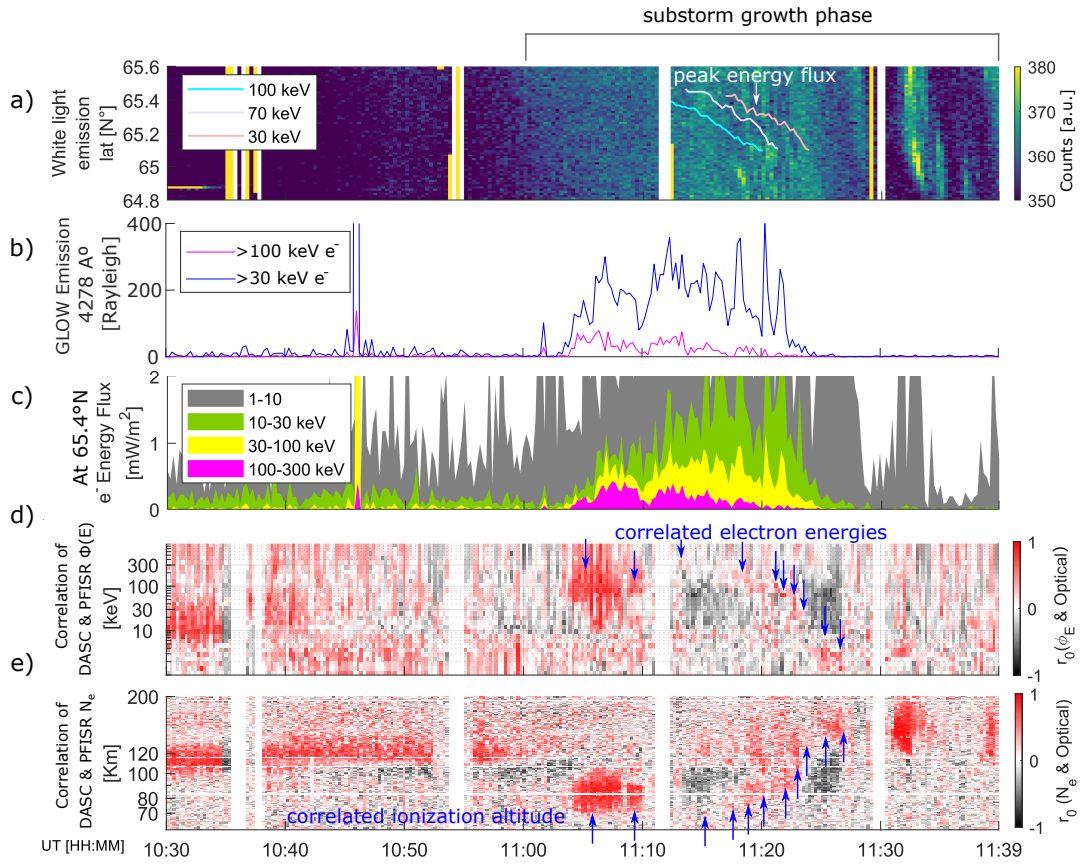

Figure 5.4: Comparing precipitating electrons and optical emissions: a) Keogram of DASC, overlaid with maximum energy flux estimates of 30, 70, 100 keV electrons from PFISR, b) estimate of 4278Å emissions made using the GLOW model with input electron energy spectra of electrons >30 and >100 keV from PFISR, c) integrated electron energy flux of 1–10, 10–30, 30–100 and 100–300 keV estimated at 65.4°N in PFISR's FOV (along the magnetic field aligned beam), e) Spatial correlation coefficient of differential electron energy flux and white-light intensity at the conjugate DASC pixel along PFISR's magnetic field aligned beam d) Spatial correlation of electron density with DASC white-light intensity.

storms. Energetic electrons of characteristic energy ∼170 keV are lost at a rate of F_E∼0.9 mW m^{-2} during storms (Borovsky & Denton, 2009). These dropouts are transient in nature, but the EEA is a more permanent conduit for loss that intensifies during tail-stretching, and has an energy flux of electrons >30 keV close to F_E∼1 mW m^{-2} needed to produce visible airglow (Borovsky & Denton, 2009; Seaton, 1954).

5.2.5 Optical Structure of EEA is Correlated with Structuring in Energetic Electron Fluxes

The above analysis suggests that electrons >30 keV in the EEA is capable of producing optically detectable signatures. However, in the event presented in our work, the brightest emissions are dominated by electrons <30 keV with F_E∼3 mW m^{-2}. Figure 5.4c shows that between 11:00–11:39 UT both low and high energy electron fluxes are present within the EEA. In order to narrow down on the electron energies that contribute to the SDA, we carried out a correlation study. Figure 5.4d shows the spatial correlation coefficients between the DASC image and electron energy fluxes within the PFISR FOV varying with the energy of precipitating electrons. The DASC image is projected to 110 km and is interpolated to the latitude and longitude coordinates corresponding to the energy flux map. The energy flux map is projected to the peak ionization altitude of a given precipitating electron energy. The correlation is carried out between this interpolated DASC image and the energy flux map for a given energy. Careful attention was paid to extract DASC pixels within the PFISR beam-widths after a star-calibration of the DASC pixel locations. Positional error is likely <5 km between the PFISR measurements and DASC images. Figure 5.4e shows the spatial correlation coefficient of PFISR

electron densities at different altitudes with the DASC image estimated in a similar manner. In this case, we used electron density maps at specified altitudes instead of energy flux maps. Between 11:04–11:10 UT, while EEA enters PFISRs FOV, there is a significant positive correlation starting from energies >100 keV (<90 km) to >10 keV (<120 km). This region in the DASC image is diffuse, and has no structure (See Movie A.1). The gaps in data from 11:11 to 11:12 UT (and other times), are due to corrupted DASC images. Right afterwards, during the time period of high fluxes of energetic precipitation and structuring within the DASC image, the high correlation continues in the high energies of 300 keV, slowly dropping to 10 keV by 11:24 UT. This decreasing correlation with energy (marked by the blue arrows) is what we expect if the electrons were precipitating due to non-adiabatic scattering from a tailward thinning current sheet. Simultaneously, there is a constant positive correlation with 8 keV electrons through the entire time span from 10:30 to 11:39 UT that are possibly scattered from the near-Earth plasma sheet due to wave-particle interactions. In Figure 5.3c, the bottom left hand corner of every electron energy flux map is labelled with their corresponding spatial correlation coefficient. They are highest for the 30 and 100 keV electrons when the EEA (and SDA) is in PFISRs FOV. The spatial correlation can be seen by visual inspection between the DASC undersampled image and 30, 100 keV electron energy flux maps. From the above analysis, we conclude that the structure of electron precipitation >30 keV within the EEA is correlated with the fine structures embedded in the SDA.

5.3 Conclusion

The precipitation of nightside outer radiation belt boundary of 30–300 keV electrons (EEA) is correlated with the SDA in the ionosphere. The loss of energy flux from the radiation belts within the EEA of electrons $\sim$>100 keV during this particular substorm growth-phase is $\sim$0.4 mW m^{-2}, which is comparable to loss of energetic electrons during relativistic electron dropouts during geomagnetic storms. Electrons >30 keV contributes to $\sim$46% of the total 4278Å emissions within the SDA. However, the total intensity within the SDA is dominated by lower energy electrons. In summary, the SDA marks the interface between the outer boundary of the outer radiation belt and the inner plasma sheet.

PFISR measurements of energetic electrons within the SDA show latitudinal energy dispersion with higher energies precipitating equatorward. This is a consequence of the non-adiabatic pitch angle scattering due to a thinning current sheet. The latitudinal separation between the peak energy fluxes of 30 and 100 keV electrons ($\sim$0.25° latitude) were consistent with previous findings (Sergeev et al., 2012). Other non-adiabatic mechanisms, such as chorus or electromagnetic ion cyclotron (EMIC) wave interactions, can also scatter electrons into the loss-cone within the same location. In fact, pulsating patches probably driven by such interactions have been observed within the EEA during several substorm growth-phases (McKay et al., 2018).

Though the latitudinal width of the EEA is only $\sim$100 km, it may map to spatial scales larger than $\sim$1 R_E within the nightside transition region (according to T96). The SDA provides us with a window into the structure and dynamics of this less-explored region of the magnetosphere. We speculate that identifying this SDA in all-sky cameras during substorm growth-phase bolstered with simultaneous radar

measurements may allow us to map the radiation belt boundary - and further constrain magnetic field models. Measurements of the e-IB from LEO satellites, linked to the EEA, have already been identified as a morphological boundary by Newell et al. (1996) with the label b2t. Furthermore, with a correlated optical signature in all-sky cameras we may be able to circumvent space-time ambiguity of in-situ spacecraft measurements, and also capture the longitudinal extent of the boundary simultaneously.

The faint, east-west aligned features in the SDA may be a projection of the structuring of the radiation belt and plasma sheet source populations. They may be caused by non-uniform thickness of the current sheet or wave instabilities developing at the interface of these two populations with different mean energies. We believe that understanding the cause of the fine structure is a worthwhile goal for future studies. Furthermore, the outer radiation belt boundary causes low-altitude ionization which might be a region of enhanced conductance, and hence may play a role in field-aligned current closure during substorm growth-phase. In fact, the outer radiation belt boundary may have a role to play in solving the mystery of the growth-phase arc generation mechanism.

CHAPTER 6

Ionospheric Conductance from Energetic Precipitation

Energetic precipitation has a direct effect on the ionosphere's chemistry, its conductance, and radio wave propagation (See section 2.7.4). In this chapter, we focus on the impact of energetic precipitation on ionospheric conductance. Ionospheric conductivity is an essential parameter that determines the amount of current redirected from the magnetosphere. Therefore, it is a crucial parameter that determines the coupling between the magnetospheric and ionospheric plasma.

To model MI coupling, a global conductance model is essential. Several statistical/empirical conductance models have been developed using satellite measurements of particle precipitation (Fuller-Rowell & Evans, 1987; Hardy et al., 1987). These models have been beneficial to the scientific community, and as a result, they are extensively used three decades later. However, they have a few drawbacks. Due to the limitation of particle detectors onboard satellites, conductance estimates are limited to the energy range and resolution of charged particle detectors, therefore not all energy ranges are incorporated in estimating the conductance empirically. As the spatial coverage of satellite precipitation is also limited, these models use large averaging of the data over space and time. Hence, they do not provide a good instantaneous picture of high-latitude dynamics, which is important during magnetically active events such as storms and substorms.

The poor spatial and temporal resolution results in the averaging out of small-scale dynamics. For example, conductance enhancement of discrete auroral arcs is not represented in these global models - even though they couple strongly with the magnetosphere through field-aligned currents. ISR measurements are by their

very nature small-scale, and unlike satellite measurements of particle precipitation, they provide a more direct estimate of conductivity through electron density measurements. This technique is at least several decades old. However, by using electronically steerable radars like PFISR, we can develop small-scale maps of Hall and Pedersen conductivities to explore the conductivity structure varying with altitude. We can potentially use such 3-D conductivity estimates to study current closure in the high-latitude ionosphere.

Energetic precipitation ionizes the D-region, resulting in enhancements in the D-region conductivity. Though global conductance models, such as Fuller-Rowell & Evans (1987); Hardy et al. (1987), incorporate energetic electrons from POES spacecraft, MI coupling models such as Global Ionosphere Thermosphere Model use self-consistent conductance boundary conditions that are associated with only auroral electron precipitation ($\sim$ 1–30 keV). Lu (2016) showed that the proportion of peak global conductance that electron $\sim> 30$ keV contribute is at least twice that of the peak conductance contribution from auroral electrons ($\sim< 30$ keV). Furthermore, Hosokawa & Ogawa (2010); Buchert et al. (2008) showed that D-region Pedersen conductivity behaves differently from E-region because collisions with the neutrals influence more electrons in the D-region. This results in a Pedersen conductivity that is predominantly contributed by electrons than ions (Hosokawa & Ogawa, 2010). Also, electron Pedersen conductivity in the D-region is non-linear at large electric fields, and the Pedersen conductance was $\sim 60\%$ higher than when assuming the classical ohms law (Buchert et al., 2008).

Considering the likely importance of D-region ionization's contribution to the total conductance, this chapter is devoted to quantifying the small-scale D-region conductivity structures and its contribution to total ionospheric conductance dur-

ing different phases of a substorm. We start with the methodology used to estimate D-region conductivity and its limitation. Then we describe observations of D-region conductivity enhancements during the 26 March 2008 substorm growth-phase and expansion phase. Finally, we discuss insights we can gain from the observations. A very conservative estimate during the expansion phase shows that the maximum D-region contribution to the Pedersen conductance is more than 15%, and the Hall conductance is more than 60%.

6.1 Methodology

The formulas for calculating parallel, Hall, and Pedersen conductivity are described in section 2.4.4. Developed in the 1920s-1950s, they are derived from mean-free path theory and assuming the plasma is in thermodynamic equilibrium. These conductivity's are therefore only accurate to first order. To calculate the ion-neutral collision frequencies (nu_{in}) we used the formula $\nu_{in} = K_{in} n_n$, for nonresonant ion-neutral interactions. With $K_i n$ values from the table 4.4. in Schunk & Nagy (2009) multiplied by 10^{-16} to convert the coefficients into SI units. And for resonant ion-neutral interactions, we used formulas from table 4.5 in Schunk & Nagy (2009). The electron collision frequency ν_e can be thought of as a contribution from electron-neutral interactions (ν_{en}) and electron-ion interactions (ν_{ei}) (See equation 6.1). The electron-neutral collision frequencies ν_{en} were derived from table 4.6 of Schunk & Nagy (2009) and ν_{ei} from equation 2.29 b of Kelley (2009), rewritten here as equation 6.2.

$$\nu_e = \nu_{ei} + \nu_{en} \tag{6.1}$$

$$\nu_{ei} = [34 + 4.18 \ln(T_e^3/n_e)] n_e T_e^{-3/2} \tag{6.2}$$

Notice that these equations depend on neutral density (n_n), ion temperature (T_i), electron temperature (T_e), electron density (n_e), and ion concentration (C_i). In the D-region, it is possible to measure n_e, T_e, T_i, using ISR. However, we do not fit the D-region spectra here and instead rely on ISR only for estimating the electron density (n_e). Algorithms that can reliably fit the ISR power spectra in the D-region ionosphere are being developed at SRI International. Until then, we fall back on using the International Reference Ionosphere Model (IRI-2016) for the ion composition and temperatures, and the Mass Spectrometer Incoherent Scatter model (MSIS-00E) for neutral atmosphere composition. Based on the uncertainties in the neutral atmosphere and collision frequency estimates, conductance estimated by different authors has a variance of about 100% (Brekke & Moen, 1993).

All inputs into the formula are based on physical or empirical models, except for the electron density, which is estimated by ISR. As described in 5, by using the electronically-steerable phased-array radar - PFISR, we can develop a 3-D volumetric profile of conductivity in the lower-ionosphere, which varies with time at a resolution of 15 seconds. Altitude slices of the time-varying 3-D data set produce a 2-D map of conductivity per measurement instance. The process for developing such maps is summarized in figure 6.1.

Figure 6.1a, shows the beam pattern in the sky of the Sporadic04 mode that uses the barker code to make measurements across the different beam positions several times in 15 seconds. An average of these measurements provides us with estimates of electron density along the beam (26 profiles, one for each beam). These beams are not field-aligned. Since precipitating electrons that cause the ionization are field-aligned, we interpolate the 3-D data set on to a set of points along the field

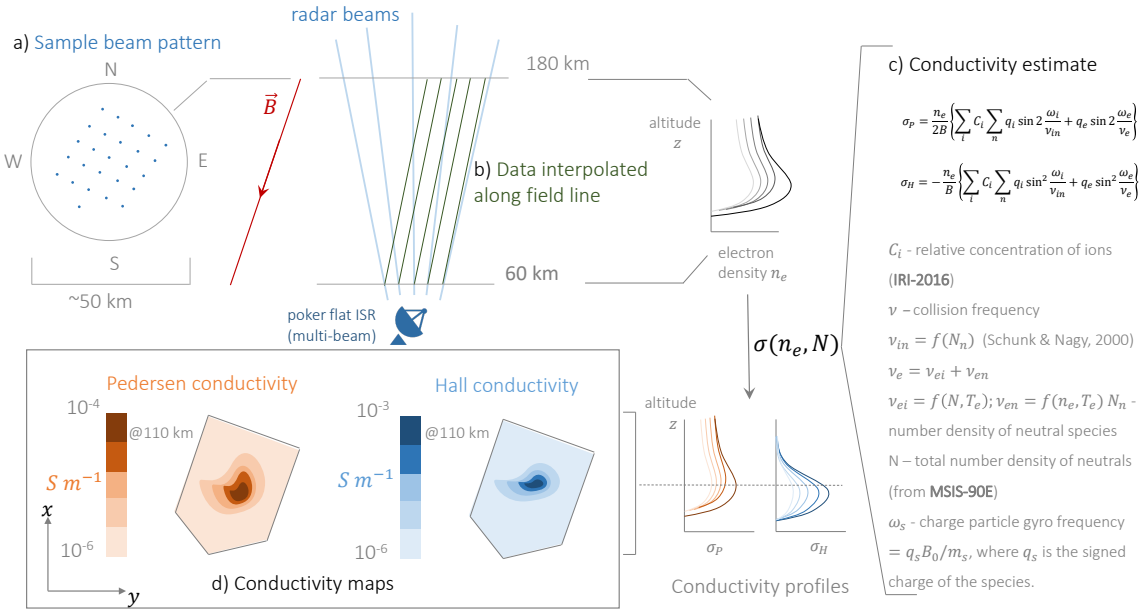

Figure 6.1: Process of developing small-scale ionosphere conductivity maps from PFISR.

line. This provides us with 26 altitude profiles of electron density, each parallel to the magnetic field line estimated from the IGRF model. After this, the electron density profiles are plugged into the conductivity formulas shown in figure 6.1 and equations 2.18-2.19. No direct validation of conductivity estimates is currently possible. However, we verified our estimates for the period with estimates derived by Yu et al. (2018) independently, and it is within 100%. This error bar is considered acceptable, given our lack of precise measurements of T_i,T_e,N_n and C_i.

There is an additional issue while estimating the D-region conductivity. The chemical composition of IRI is insufficient, as it does not include D-region chemistry. The D-region has complex chemistry of ions, negative ions, cluster ions with recombination reactions, electron attachment, reciprocal neutralization, and electron detachment (See section 2.4.3). Since we do not have reliable estimates of the collision frequencies of the negative and cluster ions, incorporating this complex

chemistry is challenging even with the availability of D-region chemistry models such as the Sodankylä Ion Chemistry model. From rocket measurements, it is clear that the maximum N^-/N^+ ratio is about 1 (Arnold et al., 1971; Amemiya & Nakamura, 1996). This implies to maintain quasi-neutrality in the D-region $N^+ = N_e + N^-$. However, ISR directly measures electron density, as electrons cause the bulk of the back-scattered radiation. And electron mobility is the dominant factor influencing electric conductivity in the D-region below $\sim$ 97 km. Therefore, negative and cluster ion mobility, which is likely lower than positive ion mobility due to its higher collisional cross-section and mass, is unlikely to alter our estimate of conductivity in the D-region. In other words, in the D-region, the neutral density is high enough that ions, both negative and positive, are bound to the neutrals, and electrons are the only charge carriers. However, if we calculate conductivity from satellite measurements of energetic precipitation, we will need to use an ion chemistry model to estimate the resulting electron density caused by the precipitating particles. In this case, not incorporating the complex D-region chemistry can cause an error in conductivity estimates of about 20% (Yu et al., 2018).

6.2 Observations

For the 26 March 2008 substorm discussed in chapters 4 and 5, we applied the methodology described in the previous section, to develop 3-D conductivity data structures that vary as a function of time. Figure 6.2 a, shows small-scale maps of hall conductivity, with a coverage of 50 km and spatial resolution of 5 km. In this example, we see steep conductivity gradients at 82 km and 11:08 UT, when the energetic electron arc (i.e., the outer radiation belt boundary) moves equatorward through PFISR's field of view, during the substorm growth phase (figure 6.2 b).

We do not see such a steep gradient at 120 km at 11:08 UT. This suggests that the physical mechanisms scattering lower energy electrons $1 - 10$ keV (which ionizes high altitudes) are different from current-sheet scattering that has a stronger effect on precipitating high energy electrons due to their higher gyro-radius (See section 2.7.2.2). If there is sufficient electric field in the D-region, equation 6.3 shows that energetic precipitation that causes high conductivity gradients can result in an increased field-aligned current flowing into this boundary (Kosch et al., 2001b). The Poynting flux form the magnetosphere communicates the electric field along the magnetic field down to the ionosphere. The electric field attenuates as it penetrates to lower altitudes, as the energy is lost to accelerating free electrons and ions and joule heating. However, 90% of DC electric fields perpendicular to the magnetic field can penetrate down to 70 km (Vanhamäki et al., 2015), which is at the altitudes of the conductivity gradient described here.

$$J_{\parallel} = \sigma_P \nabla \cdot \boldsymbol{E} + \nabla \sigma_P \cdot \boldsymbol{E} + \nabla \sigma_H \cdot \hat{\boldsymbol{b}} \times \boldsymbol{E} \tag{6.3}$$

In equation 6.3, $J_{\parallel}$ is the current density along the magnetic field line, where $\hat{b}$ is the magnetic field-line direction.

The difference in the sources of low-energy and high energy electron precipitation during this growth phase can be visualized more clearly by comparing measurements of differential energy spectra from PFISR with that of near magnetically-conjugate THEMIS-D and -E satellites. Figure 6.3d) shows the northern magnetic footpoint of THEMIS spacecraft and their relative position to the PFISR radar system. Figure 6.3e) shows the equatorial distance of the magnetically conjugate point of the instruments on the magnetic equatorial plane. We see that the closest magnetic conjunction achieved by the radar with the satellites is between 11:03 - 11:10

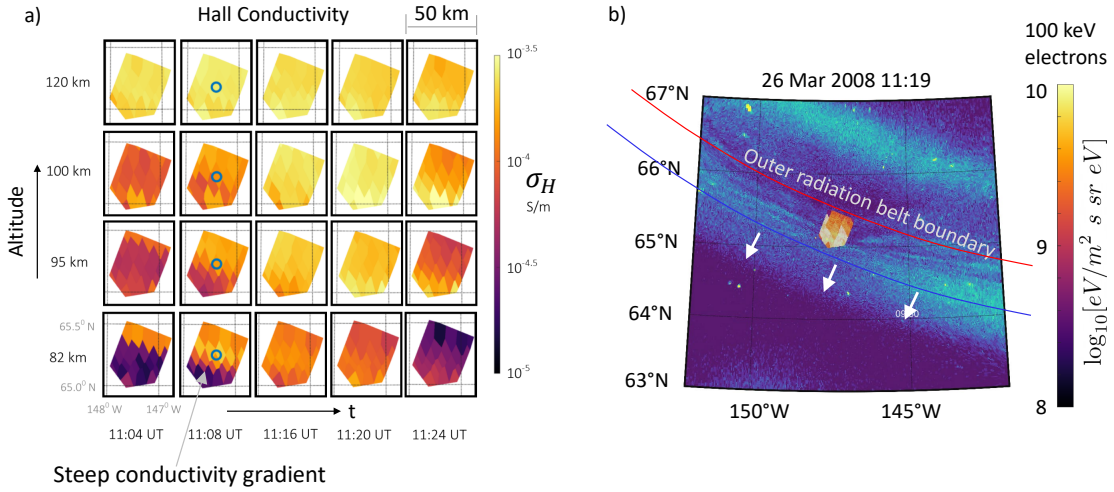

Figure 6.2: Hall conductivity maps derived from PFSIR, induced by energetic electron precipitation from the outer radiation belt boundary moving equatorward during a substorm growth phase. Panel a) Small-scale maps of conductivity with each sub-panel at increasing height along the vertical axis and increasing time along the horizontal axis. Sub-panel (4,2) shows a steep latitudinal conductivity gradient as the energetic electron arc passes through PIFSR's field of view. Panel b) shows the optical emissions associated with the outer radiation belt boundary at 11:19 UT, and overlayed on it is the PFISR energy flux map of 100 keV electrons from the outer radiation belt boundary.

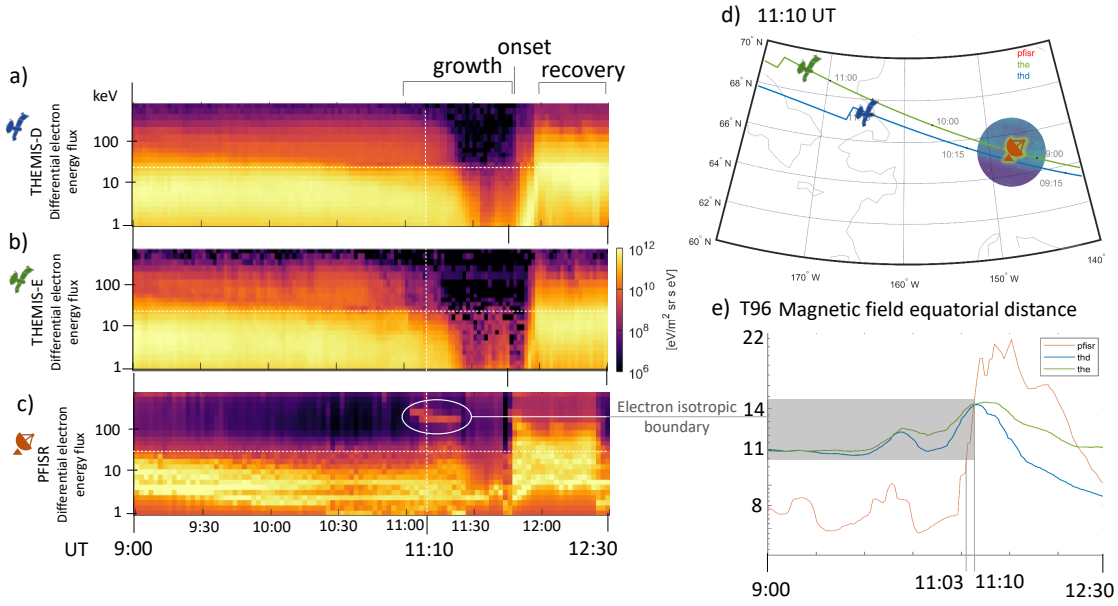

Figure 6.3: a) differential energy flux of loss-cone electrons measured by THEMIS-D at the equatorial plane, b) differential energy flux of loss-cone electrons measured by THEMIS-E at the equatorial plane, c) differential energy flux of precipitating electrons estimated by PFISR at the ionosphere, d) magnetic footpoints of the satellite trajectory and PFISR location, e) the radial distance of the magnetically conjugate point in the magnetic equator of the satellites and ISR, calculated using T96 model.

UT. During this short period, figure 6.3c) shows the differential electron energy flux estimated by PFISR. Marked by a white-circle, we can observe an increase in 100-300 keV electrons, which indicate the electron isotropic boundary that marks the outer radiation belt boundary. Figures 6.3a-b) shows the differential electron flux estimated within the loss-cone of particle detectors onboard THEMIS. It was near the equatorial plane and magnetically conjugate with Poker Flat at the time. However, the equatorial magnetic region associated with THEMIS-D and -E from 9:00 UT to 11:10 UT is similar to the region associated with PFISR between 11:03 UT to 11:10 UT. We show this in figure 6.3e) using the gray shaded box. As a result, differential energy flux of electrons $\sim 30-300$ keV seen in figure 6.3a-b) is likely associated with current sheet scattering. The flux values and time evolution between the satellite and PFISR measurements are remarkably similar once corrected for the magnetic conjunction.

The 9:00 – 11:10 UT of loss-cone particle measurements made by THEMIS-D and -E satellites is the same plasma population as PFISR measurements from 11:03-11:10 UT. Keeping this in mind, we now turn to the conductivity estimates from precipitating electrons observed by THEMIS satellites, and PFISR. Figure 6.4 shows the variation of hall conductivity with time. Figure 6.4a-b) shows hall conductivity calculated by estimating the ionization caused by THEMIS measurements of loss-cone electrons at the magnetic equatorial plane and using the conductivity formula described in section 6.1, 2.4.4. Figure 6.4c) shows the conductivity profile estimated using PFISR measurements of electron density along the magnetic field-aligned beam. The primary feature to notice here is that there seems to be a separate layer of conductivity in the D-region, distinct from the E-region, as seen in figure 6.2. The source for this separation of the layer at about 90–95 km

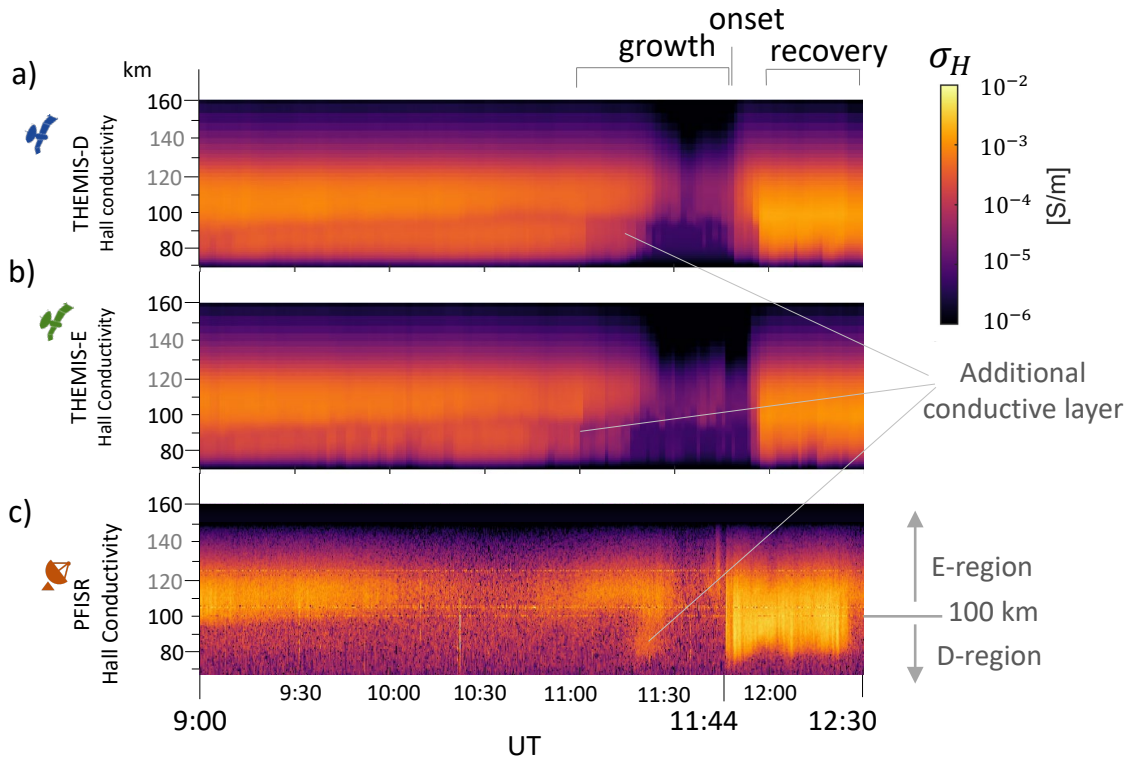

Figure 6.4: Hall conductivity estimated from loss-cone particles measured by THEMIS-D and -E, agrees with measurements made by PFISR. The conductivity between 9:00 – 11:10 UT of panel a-b) is magnetically conjugate with panel c) from 11:03-11:10 UT, according to the T96 model.

seems to be the separation of sources of energetic electrons at about 30–40 keV as seen figure 6.3. Apart from this feature, notice that the Hall conductivity in the D-region is also comparable to the Hall conductivity in the E-region during the growth phase. During the substorm onset and expansion, the D-region hall conductivity seems higher than in the E-region.

A different reason causes the separation between the additional Pedersen conductivity layer induced by energetic precipitation in the D-region and the Pedersen conductivity in the E-region. Figure 6.5 shows a characteristic altitude at around 97 km above which ions dominate Pedersen conductivity, and below that by elec-

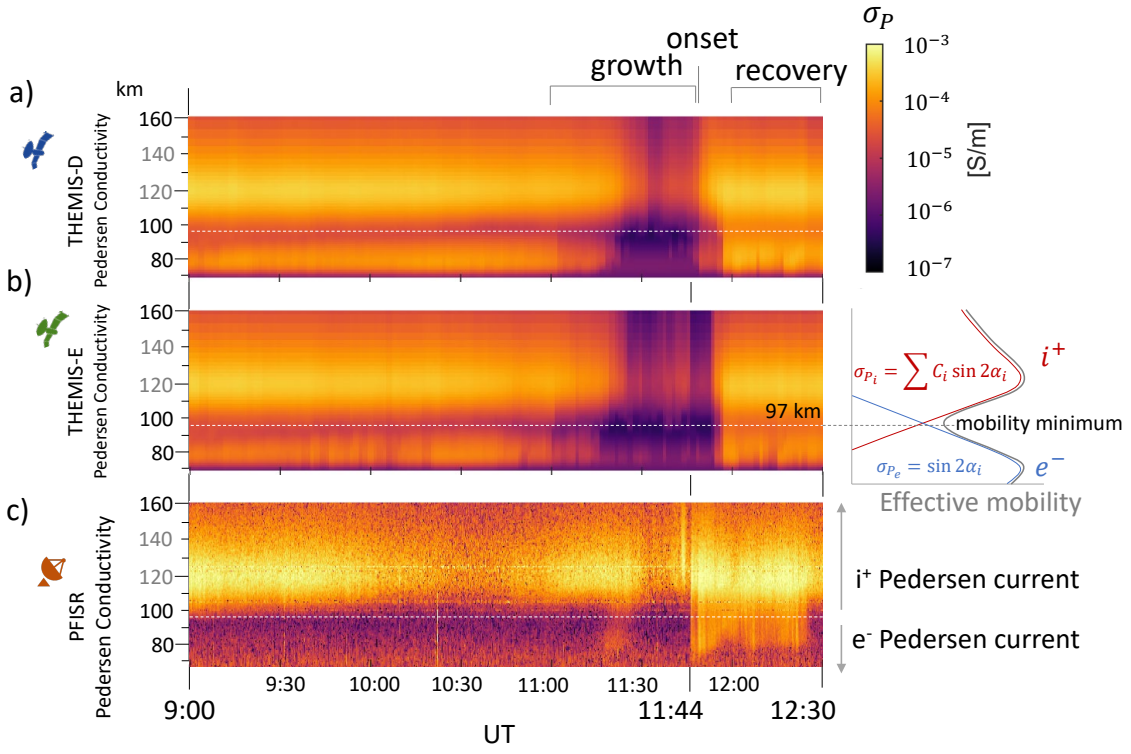

Figure 6.5: Pedersen conductivity estimated from loss-cone particles measured by THEMIS-D and -E, agrees with measurements made by PFISR. The conductivity between 9:00 – 11:10 UT of panel a-b) is magnetically conjugate with panel c) from 11:03-11:10 UT, according to the T96 model. A net mobility minimum induces the minimum in Pedersen conductivity at 97 km. Below this ion-neutral collision constrains the ions to the neutrals. An increase in electron-neutral collisions steers the electrons from purely the Hall direction and more along the electric field direction.

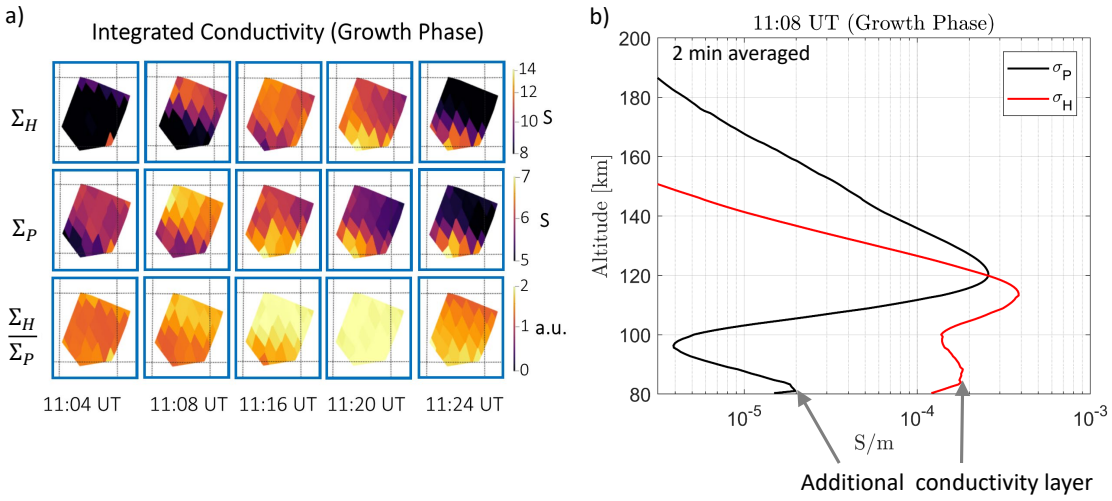

Figure 6.6: Panel a) the First row shows integrated Hall conductivity across the range of the radar (60–140 km), i.e., Hall conductance. The second row shows the Pedersen conductance, and the third row shows the ratio of the Hall and Pedersen conductance. Each column is a time instant. Panel b) shows the altitude profile of the Hall and Pedersen conductivity at 11:08 UT during the growth phase. The profile is averaged across 2 minutes.

trons. At about 125 km altitude, the ions are only partially coupled to neutrals, and as a result, they move in the direction of the electric field $\boldsymbol{E}$ and carry the ion Pedersen current. However, electrons are unaffected by collisions and therefore drift in the $\boldsymbol{E} \times \boldsymbol{B}$ direction. Below ∼97 km, the ions are completely dominated by collisions with the neutrals, and they follow the neutral wind. The electrons start to become partially coupled to the neutrals through collisions and hence start drifting in the $\boldsymbol{E}$ direction causing an electron Pedersen current. The obvious minimum at $\sim$ 97 km is perhaps also enhanced by a minimum in the precipitating electrons at $\sim 30 - 40$ keV, which is a result of the two distinct source mechanisms driving the low and high energy precipitation.

Figure 6.6 a) shows the Hall and Pedersen *conductance* (height integrated conductivity), and their ratio. The Hall conductance value shows a moderate conduc-

tance gradient at 11:08 UT. Let us recall that in figure 6.2, the Hall conductivity was uniform in the E-region ($\sim$ 120 km) but had a steep gradient in the D-region ($\sim$ 82 km) at 11:08 UT. Therefore, a moderate conductance gradient suggests that D-region Hall conductivity, during energetic precipitation from the outer radiation belt boundary, contributes significantly to the total ionospheric conductance. The third row in figure 6.6 shows the Hall to Pedersen conductance ratio, which peaks at around 11:20 UT. Hall to Pedersen conductance ratio is high when there are more energetic particles precipitating (Robinson et al., 1987). This is because the Hall conductance is affected by higher-energy electrons that ionize lower altitudes ($<$100 km), as compared to lower-energy electrons that ionize high altitudes ($>$100 km).

Figure 6.6 b) shows an altitude profile of Hall and Pedersen conductivity at 11:08 UT, averaged over 2 minutes of ISR measurement along the magnetic field-aligned beam. The primary peak of the Pedersen conductivity is as expected to be – about 120 km. The Hall conductivity peak is slightly lower at around 115 km. However, there is a second, additional, smaller peak around 80 and 82 km. This is a clear sign of the additional D-region conductivity enhancements, though the conductivity is one order of magnitude lower than the E-region maximum.

Finally, we can view the figure 6.7 as quantifying the contribution of D-region towards total ionospheric conductance. In both panels, about 10:30 UT is the quietest time in terms of precipitation. As a result, the conductance values we see during that time is very close to the quiet background. Total Hall and Pedersen conductance have a value of 8 S and 3.5 S, respectively. During the growth phase, when the outer radiation belt boundary passes through the PFISR field of view, the Hall conductance reaches 40 S and the Pedersen conductance 15 S. It is an almost

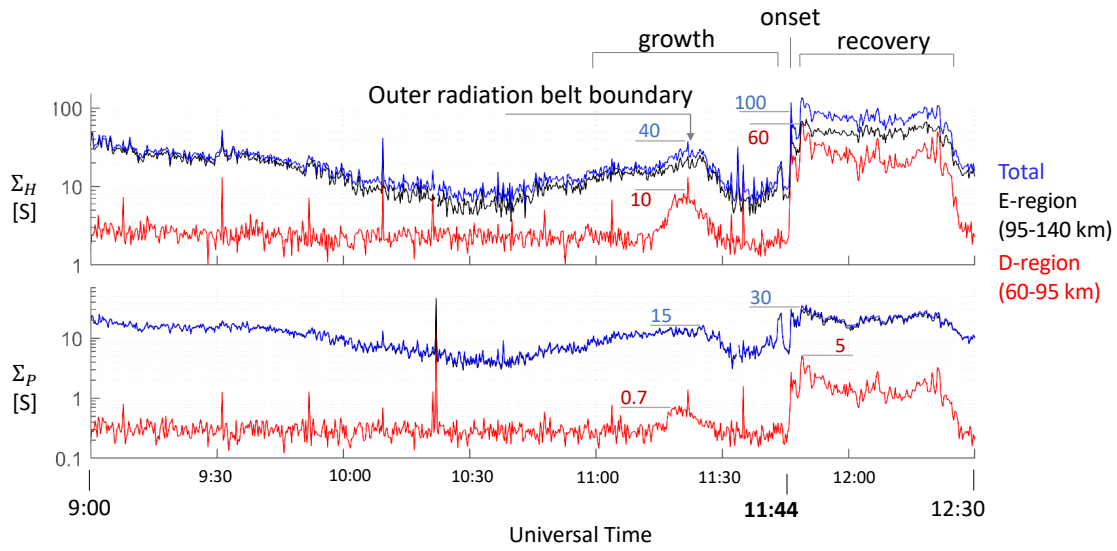

Figure 6.7: Hall and Pedersen conductance from the D-region, the E-region, and the total ionosphere.

five-fold increase. D-region contributes about 10 S of the Hall conductance and 0.7 S of the Pedersen conductance. This is about a 25% and a 5% increase. During the substorm onset, the Hall conductance rises to 100 S, and the Pedersen conductance to 30 S. This is more than a ten times increase from the quiet period. And here, the D-region Hall conductance contribution increases to 60% (60 S) and the Pedersen conductance contribution to 15% (5 S) of the total conductance. This enhanced D-region contribution is a result of energetic precipitation. The D-region Pedersen conductance contribution is likely higher than the above estimate if we incorporate the non-linear increase in Pedersen conductivity with large electric fields (Buchert et al., 2008). It is also important to note that the small-scale Hall conductance observed over the outer radiation belt boundary is 40% of that seen during substorm onset.

6.3 Discussion

Steep conductance gradients emphasize the need to improve the spatial and temporal resolution of global conductance models.

Figure 6.6 and 6.7 makes clear that there are steep conductance gradients in both space ($\sim$ 1 S/km) and time ($\sim$2 S/min). Such gradients are completely smoothed out in global conductance models, where the spatial and temporal resolution are in the order of hundreds of kilometers or hundreds of minutes. Such small-scale and mesoscale descriptions of conductances are required to model field-aligned currents that electrically couple the ionosphere and magnetosphere.

Conductivity estimated from loss-cone measurements in the magnetosphere correlates well with measurements in the ionosphere.

Panels a), b), correlate well with panel c) in figures 6.4 and 6.5, considering the magnetic conjugacy described in figure 6.3e) and associated text. It is a direct result of correlation in loss-cone particles and precipitating electrons in the magnetically conjugate period between THEMIS satellite and PFISR measurements (See figure 6.3a-c). Figure 6.8 shows the remarkable correlation between the loss-cone flux of electrons at the magnetic equatorial plane measured by THEMIS-D and flux of precipitating

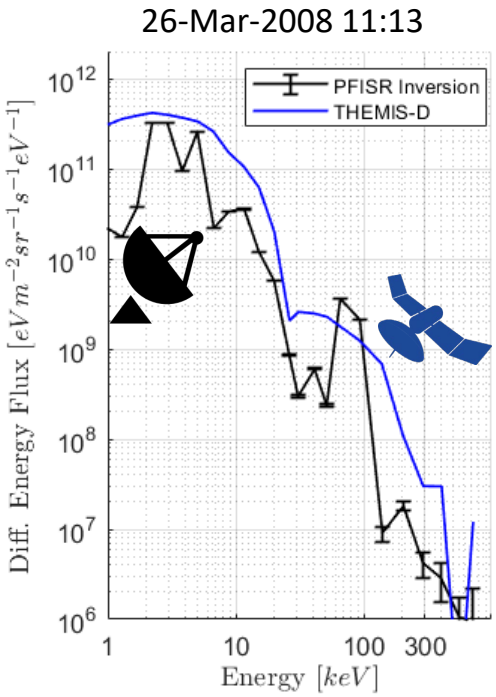

Figure 6.8: Precipitating electron energy flux estimated by magnetically conjugate measurements from the ionosphere and magnetosphere.

Magnetospheric Source of Precipitation	Energy	Altitude	Conductivity Increase in the Ionosphere
Scattering of cold plasma from the plasma sheet	<3 keV	>120 km	mainly σ_P
Auroral acceleration region	$\sim$ 10 keV	>100 km	mainly σ_H
Outer radiation belt boundary (current sheet scattering)	$\sim$ 100 keV	$>$ 80 km	transient layer of high electron mobility with high σ_H and σ_P in D-region

Table 6.1: The effect of precipitation from different magnetospheric sources on the conductivity of the ionosphere

electrons in the ionosphere estimated by PFISR when both instruments are magnetically closest. Unlike the temporal correlation observed with time-series plots of conductivity (figures 6.4,6.5), this is a correlation of energy spectra of precipitating electrons. It is double-humped, with the first peak at around 3–5 keV corresponding to auroral electrons, which are probably cold plasma accelerated at the auroral acceleration region. The second hump is around 70-100 keV, which is a result of the current sheet scattering near the magnetic equatorial plane at about 9 R_E in the plasma sheet.

Some magnetospheric sources of precipitation and its effect on ionospheric conductivity.

Table 6.1 lists the magnetospheric source regions we have explored in the previous chapters and their approximate effect on ionospheric conductivity. Energetic precipitation, such as that from the outer radiation belt boundary, causes an additional, transient layer of conductivity below or the lower end of the ionospheric dynamo layer. However, most conductance contributions are by the lower, auroral energy electrons from the plasma sheet, accelerated by the AAR.

Joule heating due to energetic precipitation during the growth phase is relatively high.

The conductance enhancement due to the outer radiation belt boundary can result in relatively high Joule heating rates. Joule heating, as a result of the collision of free electrons, accelerated due to an electric field into the surrounding plasma, can be expressed as $Q_J = \Sigma_P |E|^2$. We can estimate the electric field E from the drift velocity of ions measured by PFISR in the F-region, which is about $25mV/m^2$ with $V_D = 500m/s$. Assuming the Electric field gets translated to the upper D-region without attenuation, the total $Q_P \approx 1$ GW. This is double the total power of the precipitating energetic electrons with energy > 10 keV, which is $\sim$ 0.5 GW.

6.4 Conclusion

Our conductance measurements are mostly higher than that made by Kirkwood et al. (1988), by at least $1.5 - 2$ times in Pedersen and Hall conductances. The measurements suggest strongly that small-scale conductances are much higher than those predicted by global conductance models. The contribution of D-region to the total conductance is also non-negligible during energetic precipitation. It is highest at the outer radiation belt boundary during growth-phase, the substorm onset, and the expansion phase.

D-region contribution to Hall-conductance is higher than the Pedersen conductance. The charge carriers to ionospheric Hall conductivity are mostly electrons with high mobility in the D-region as opposed to the ions. The Hall conductance contribution reaches a maximum of about 60% during the expansion phase. Though the D-region Pedersen conductance contribution is low, here we have not taken into account the non-linear effects that can enhance Pedersen conductance

in the lower-E and -D region. The increase in conductance has a non-linear dependence on the electric field and electron temperature due to enhanced ion-electron coulomb collisions.

A significant realization that we had during this study is the lack of dependence of D-region conductivity estimates from ISRs on D-region ion chemistry. It is common to attribute uncertainties in any measurement of D-region quantities to the complex D-region chemistry. However, due to the high rate of ion-neutral collisions in the D-region, their mobility becomes insignificant, and electrons are the dominant (if not the only) charge carriers. As ISRs directly measure the D-region's electron concentrations, we can rely on its conductivity estimates without considering the contribution of ions at altitudes below ~ 97 km.

In the future, we ought to expand this study to use ISR-based electric field measurements to estimate Joule heating within the D-region more precisely. And also use the Hall conductance gradients to determine the magnitude of field-aligned currents. Finally, we can conclude that from the perspective of boundary conditions to MI coupling models, neglecting the D-region contribution during magnetically active periods such as a substorm can lead to uncertainty in the conductance values to about 15-60%.

CHAPTER 7

Multi-event Analysis of Energetic Precipitation from the Radiation Belt

Chapters 4–6 discusses specific sources and effects of energetic precipitation during a strong substorm on 26 March 2008. In this chapter, we address the natural question of the prevalence of the features observed during that substorm. Is the low-altitude D-region ionization caused by energetic precipitation, found on the 26 March 2008 substorm, seen in other substorms as well? This question has a broad scope, and to an extent, has been addressed by early riometer studies (Berkey et al., 1974). Narrowing down this question to focus specifically on the prevalence of energetic precipitation from the outer radiation belt and its optical signature discussed in chapter 5 make the goal more tractable. Since the visual signature of the outer radiation belt boundary has not been previously reported or identified in the literature, addressing this question becomes more pressing.

Given the large database of optical and ISR measurements, we need to devise a parsimonious technique to narrow down multiple substorms that are likely to manifest the signature of the radiation belt boundary. Hence, the first section of this chapter describes the methodology we used to arrive at a narrow set of substorms that are likely to exhibit the signatures we seek in optical and ISR data. In the next section, we list the substorms that exhibit these signatures and briefly present the observations from each event. Section 7.3 discusses key features from these observations. Finally, we conclude the chapter by presenting the results in a broader context of its implications on MI coupling.

7.1 Methodology

The straightforward way to address the question: How characteristic are the signatures of the outer radiation belt boundary (ORBB) during substorms?, is by verifying the optical and ISR measurements of all substorms. In light of results from Sivadas et al. (2019), we label a Structured Diffuse Aurora (SDA) to be an ORBB signature, if we find energetic precipitation conjugate to the SDA in the PFISR measurements, and if we observe it during the substorm growth phase. According to the SuperMag catalog, which classifies substorms based on ground magnetometer measurements of activity, there are about 17000 potential substorms that occurred in 13 years from 2005 to 2018. The type of ORBB signature driven by current sheet scattering observed in the 26 March 2008 substorm occurred during the substorms' growth phase. Other types of ORBB signature are out of the scope of the current work.

To meet the above constraints, we need to identify substorms whose growth phase occurs over Poker Flat, Alaska, as the instruments we use in this study - the digital all-sky camera (DASC) and the incoherent scatter radar (PFISR), are both located there. For this, we add a constrain on the latitude of substorm onset to be lower than the latitude of Poker Flat, Alaska. We base it on the fact that growth phase features mostly occur poleward of the substorm onset and before it. Also, during the growth phase, these features drift equatorward. This constraint considerably narrows the viable substorms to 494. In addition to this, PFISR will have to be operating and running the appropriate mode to measure D-region ionization.

Additionally, the DASC has to be recording, and this reduces the potential substorms with an identifiable ORBB signature to 26. And, the sky has to be clear and data available during the growth phase of the substorm. This results in the num-

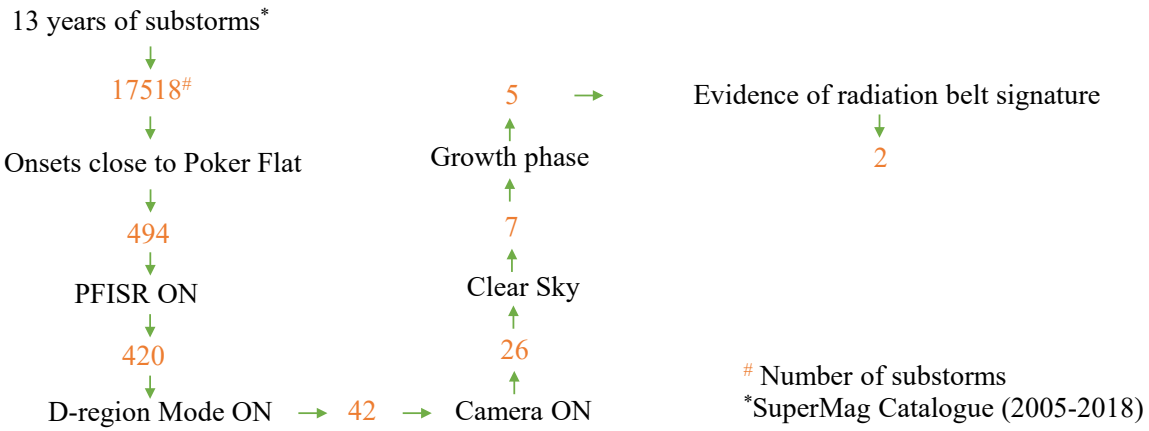

Figure 7.1: Selecting substorms with growth phases visible at Poker Flat, Alaska, with viable data from ISR and DASC.

ber of viable and recorded substorms from 2005 to 2018 to a mere five events. And out of the five, two substorms showed strong evidence of ORBB signature in both optical and ISR data. The whole process is summarized in figure 7.1.

7.2 Observations

Out of the five substorms filtered based on the viability of observing the growth phase features at Poker Flat, only two of them observed energetic electron precipitation during growth-phase simultaneously with structured diffuse aurora. This suggests that the SDA is an ORBB signature. It is worth noting here that the way we identify that an SDA is an ORBB, is by finding simultaneous EEP during the growth phase and confirming its relative location with respect to the diffuse aurora and growth-phase arc. Identifying EEP above the SDA using low earth orbiting satellite measurements will give us further confidence in this conclusion, however that is beyond the scope of this study. Details of these events are in table

7.1. All the substorm onsets occur very close in MLAT to PFISR ($\sim 65.47°$N). The MLT occurrence of these substorms is about an hour within the magnetic midnight meridian. It is also important to note that the latitudinal constraint of the substorm onset being equatorward of $\sim 65.47°$N selects for mostly strong substorms (>500 SML). These substorms usually have a long growth phase and substantial energy transfer from the solar wind, to cause a stretched magnetotail during an expanded polar cap. SML is a generalization of the AL (westward auroral electrojet) index constructed from the SuperMag database. It indicates the strength of the westward electrojet and consequently, the substorm (Newell & Gjerloev, 2011). In the rest of this section, we will describe the most relevant observations made of each of these substorms.

7.2.1 Event 1 (3339): 26 March 2008 substorm

We extensively discuss the observations of energetic precipitation and its effects during this substorm in chapters 4-6, however here we include a summary for completeness. The next four subsections share the same structure as this subsection, to allow for comparison between all the substorms. Associated with each subsection is an overview figure (e.g., figure 7.2) which provides: (Left column) an all-sky white-light image of the night-sky at poker flat, (Center column) estimates of electron density profiles, differential energy spectra of precipitating electrons, Hall conductivity profiles, and Pedersen conductivity profile, (Right column) IMF, AE, SYM-H, and solar wind dynamic pressure (P_{sw}). Some of the figures may include filtered all-sky-camera data at wavelengths 557.7 mm, 427.8 nm, and 630.0 nm.

Geomagnetic conditions: The IMF B_z is southward, driving dayside recon-

SuperMag Substorm ID	**Event 1 3339**	**Event 2 5504**	**Event 3 10023**	**Event 4 13816**	**Event 5 13879**
Substorm Onset Time (UT)	2008 26 Mar 11:46	2010 14 Dec 13:36	2014 02 Nov 12:30	2016 02 Nov 11:59	2016 13 Nov 11:37
Peak SML [nT]	-1426	-686	-458	-913	-668
Onset MLAT [°N]	65.47	66.24	65.62	65.62	65.62
Onset MLT [HH:MM]	23:48	03:36	01:07	00:35	00:14
PFISR MLT [HH:MM]	23:40	02:30	01:24	00:53	00:31
EEP Observed by PFISR	Yes	Yes	Yes	Yes	No
SDA Observed by DASC	Yes	Partly	Partly	Yes	Yes
Time of SDA Observation	11:18	13:17	12:30	11:51	11:40
ORBB Signature	**Yes**	No	No	**Yes**	No

Table 7.1: Selected substorms with growth-phase visible at Poker Flat, and onset occurring at Poker Flat or lower latitudes. The last row records whether there is evidence for the ORBB signature during the growth-phase of the selected substorm.

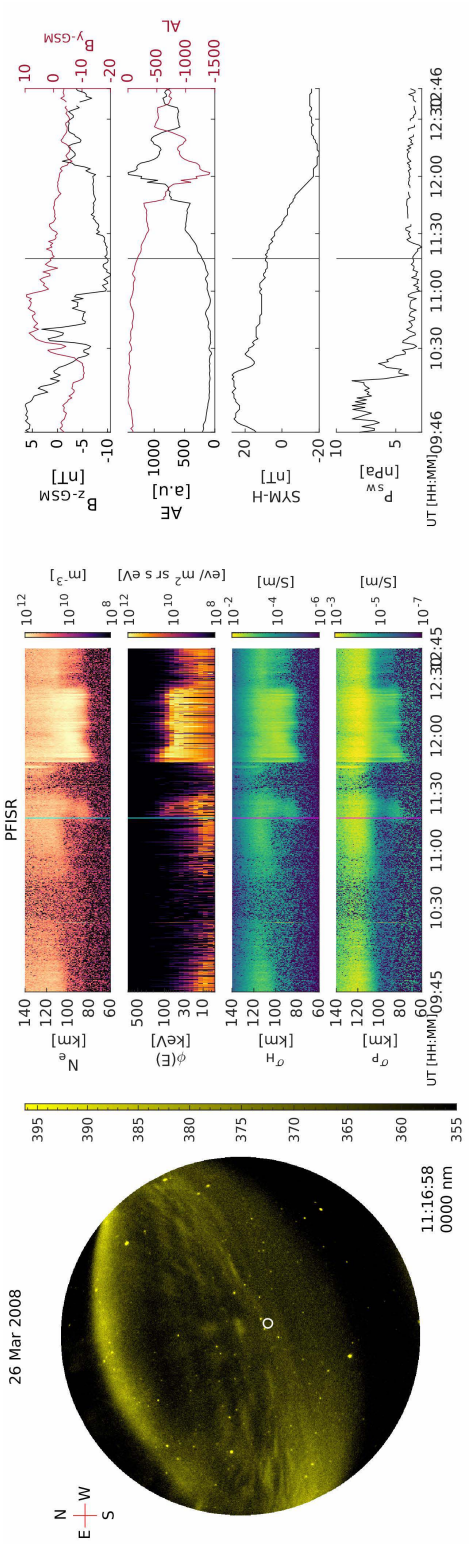

Figure 7.2: DASC and PFISR measurements of 26 March 2008 substorm showing the optical and ionospheric signature of the outer radiation belt boundary. Click *here* to watch a video of this substorm.

nection to transfer solar wind energy into the magnetosphere, causing magnetic energy to build-up in the magnetotail. As a result, from 11:00 to 11:44, one can observe the auroral electrojet indices increasing in its magnitude, before the onset at 11:46 UT. During the substorm growth phase, SYM-H is slowly decreasing - suggesting enhancement in the ring-currents. The AL index reaches a peak value of -1400 nT, indicating that what followed the growth phase was a strong substorm.

Auroral morphology: During the growth phase, the diffuse aurora slowly moves equatorward (or southward), with structured diffuse aurora observed at its poleward shoulder. The structures are correlated with energetic precipitation seen in Panel 2 of the center column. In the poleward edge of the SDA, a steady discrete arc known as the growth phase arc forms. It is more visible in the equatorward stations (See figure 5.1). A movie of the full time period shown in figure 7.2 is available *here*[1].

Precipitating electrons: PFISR measurements during this period show correlated (see chapter 5) and conjugate observations of energetic electron precipitation with the SDA. In Panels 1-2 of the center column of figure 7.2, we can see the temporal dispersion of energy or altitude, such that energetic electrons come first as the equatorward portion of the SDA passes over PFISR's FoV.

Conductivity: Panels 3-4 of figure 7.2 show the Hall and Pedersen conductivity extensively discussed in chapter 6. Here we note that the D-region enhancement in conductivity happens equatorward of the growth phase arc formation. This is more visible in figure 5.1b), where the pre-breakup arc forms poleward of the energetic electron arc measured by the NOAA-17 spacecraft.

The primary reason for concluding that the SDA is the optical signature of the

[1]https://youtu.be/V1asuVd38w8

ORBB is its strong spatial correlation with energetic electron precipitation. Additional evidence came from the latitudinal gradient in energy dispersion observed within the SDA that is consistent with current sheet scattering. In the next subsections, we have not evaluated the spatial correlation or energy dispersion. Instead, we chose to observe whether both SDA and energetic electron precipitation with similar features occur during the substorm's growth phase. If so, we conclude that the SDA is likely to be the optical signature of the ORBB. If we do not observe either of the two - energetic precipitation or SDA with satisfactory clarity, then we conclude that there is no evidence of the ORBB signature in the growth phase.

7.2.2 Event 2 (5504): 14 December 2010 substorm

According to the SuperMag catalog, the 14 December 2010 substorm onset happens at 13:36 UT (See Table 7.1). The onset location is 66.24°N and 03:36 MLT, which is east of the PIFSR location ∼2:30 MLT, at the time of onset. However, this is not a clean, isolated substorm since at 13:16 UT around 00:20 MLT (westward of PFISR), there seems to be some pre-breakup activity.

Geomagnetic conditions: IMF B_z time-shifted to the magnetopause fluctuates around zero for couple of hours from 11:15 UT, until it finally falls below 0 after 13:15 UT (See figure 7.3, column 3, panel 1). From 13:00 UT, AL starts to increase in magnitude, suggesting a thinning current-sheet and an increasing westward electrojet. The peak AL value is about -686 nT, which indicates that this is a strong substorm onset. SYM-H remains negative, suggesting an active ring current.

Auroral morphology: Figure 7.3 column 1, shows a bright and active growth phase arc bordering the diffuse aurora. The pre-breakup activity westward of PFISR might be the cause of the eastward traveling waves drifting across the arcs.

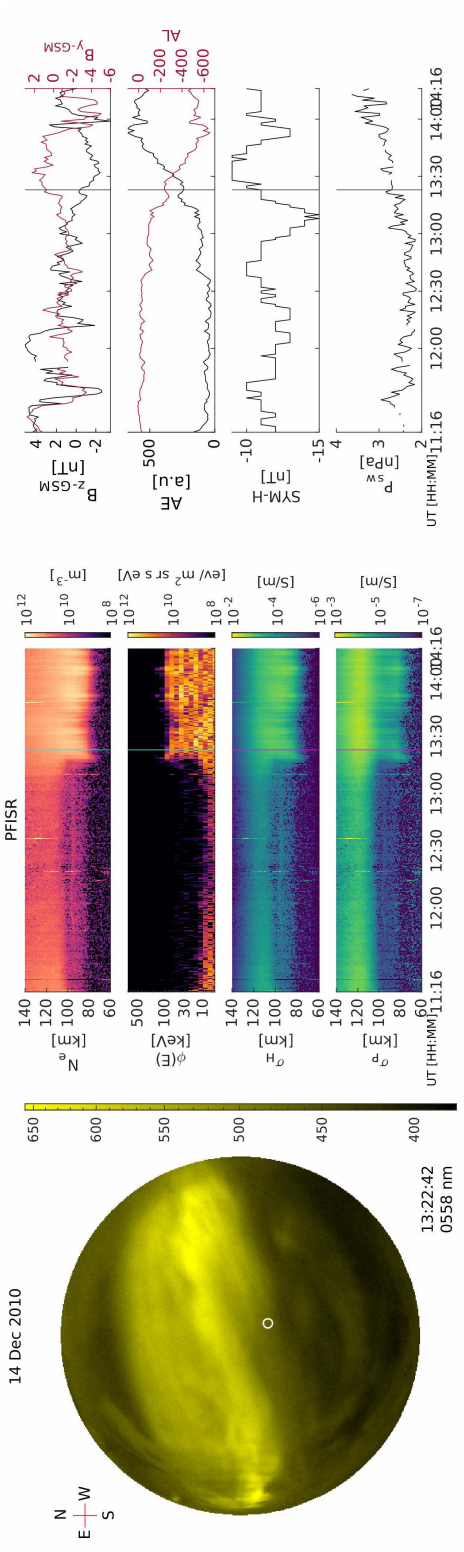

Figure 7.3: DASC and PFISR measurements of 14 December 2010 substorm showing the optical and ionospheric signature of the outer radiation belt boundary. Click *here* to watch the video if this event.

Clouds in the camera field of view seem to have rendered the finer features of the auroral morphology indecipherable. However, at 11:15-11:20 UT, much before the growth phase, narrow east-west aligned arc-like structures can be seen bordering the equatorward portion of what looks like multiple-arcs. The energy spectra over this period are more energetic (up to 30 keV) than when there is no arc overhead PFISR (figure 7.3 column 2, panel 2). These structures look similar to the SDA. Similar structures are likely to exist at 13:17-13:22. However, they are blurred and not distinctly visible, perhaps due to clouds in the camera FoV starting from 12:30 UT. However, we observe pulsating patches despite the blurriness of the images. They are likely to be associated with the energetic precipitation observed in figure 7.3 column 2). Before and after the onset at 13:36 UT, similar to the eastward-moving waves, large mesoscale patches are drifting east slowly, with pulsating patches in between them. See the video *here*[2].

Precipitating electrons: As mentioned earlier, PFISR detected energetic electron precipitation with narrow east-west aligned and faint arcs around 11:15 UT, but also from ∼13:15 UT to 13:25 UT. At the earlier period, we observed sparse fluxes of energetic electrons up to 30 keV, and the later time precipitating electrons of 100 keV and more were measured. However, there is no clear distinction between the growth phase and onset in this data set, and therefore no distinction between the precipitation. This is likely the consequence of the substorm happening at least ∼1 MLT away towards the east.

Conductivity: From 13:15 UT, when the energetic precipitation is observed over the PFISR field of view, it is clear that there is a D-region conductivity layer persisting through the precipitation, equatorward of the bright growth phase and

[2]https://youtu.be/-c8lRxY0TXg

multiple arc system.

Here it is difficult to conclude that SDA is visible clearly as in the case of Event 1. Hence we claim that we can mostly observe the SDA and most certainly pulsating patches during the growth phase and equatorward of a growth phase arc system. There is also energetic precipitation associated with this structure. However, due to the lack of clarity in the optical observations, we feel that evidence is insufficient to conclude there is an ORBB signature.

7.2.3 Event 3 (10023): 02 November 2014 substorm

According to the SuperMag database, this substorm on 02 November 2014 12:30 UT happens at an MLAT of 65.6°, MLT of 01:07, which is slightly east of Poker Flat whose MLT is 01:24.

Geomagnetic conditions: The IMF B_z is southward from ∼11:00 UT. The AL index starts to decrease at ∼12:00 UT, with the onset rapidly approaching at 12:30 UT. The peak AL value is -458 nT, making this the weakest substorm among the five, even though this is, on average, still a strong substorm. The SYM-H value is positive, but going towards negative, implying a slowly strengthening ring current.

Auroral Morphology: Figure 7.4 shows three all-sky-images. Each one is five seconds apart, and each a view of the sky through a different monochromatic filter. The wavelength is indicated on the right-bottom corner of each image panel in the figure. The growth phase starts from ∼12:00 UT, and we see a growth phase arc from 12:15 through a cloudy sky as it moves equatorward. At 12:24 UT, we can see auroral beading on the arc through the clouds. At 12:30 UT, east-west aligned streaks similar to the SDA in Event 1, are observed equatorward of the

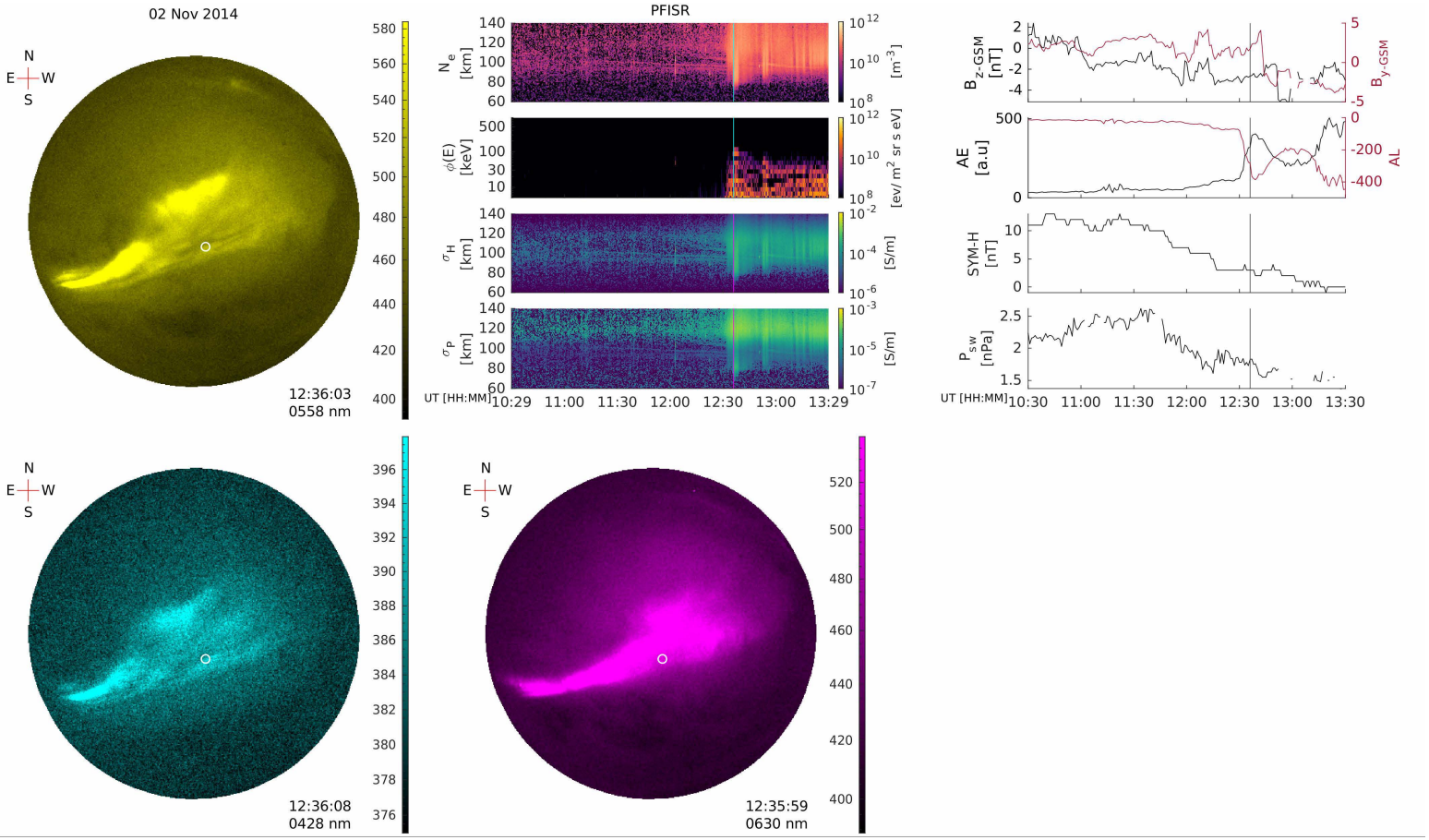

Figure 7.4: DASC and PFISR measurements of 02 November 2014 substorm showing the optical and ionospheric signature of the outer radiation belt boundary. Click *here* to see the video of this substorm.

growth-phase arc. However, it is not the field of view of PFISR's magnetic field-aligned beam indicated by the white circle. Additionally, for figures 7.4-7.6, we do not have accurate position calibration of the DASC. Hence, the location of the magnetic-field-aligned beam represented by the white circle has some error. See the video *here*[3].

Precipitating electrons: At 12:36:03 UT, after SuperMag's substorm onset, the auroral bulge hits the Poker Flat night sky. The growth phase arc swivels eastward, revealing SDA-like streaks within PFISR field-of-view. Associated with these streaks, we see energetic electron precipitation reaching 100 keV. As the substorm proceeds, the precipitating electron energies lower down to 30-50 keV in the expansion phase.

Conductivity There is transient D-region conductivity enhancement, between 12:33–12:37 UT, within the SDA-like features. And as the energy of the electron precipitation declines, most of the conductivity enhancement is seen in the E-region, along PFISR's magnetic field-aligned beam.

Though we see SDA-like features, we observe energetic electron precipitation only after the onset after the growth phase arc is blown away by the substorm-front to reveal SDA-like features underneath it. During the growth-phase ($\sim$12:30 UT) when SDA was visible above the white circle, no evidence of energetic precipitation was observed by PFISR, likely due to the error in calibration, which makes PFISR beam location more North than it is. And since there is evidence for energetic precipitation only at 12:36 UT after the onset (and not during the growth phase), we make a conservative determination that there is insufficient evidence to claim the existence of the ORBB signature during this event.

[3]https://youtu.be/CDVDcyaggTA

7.2.4 Event 4 (13816): 02 November 2016 substorm

This substorm is most similar to Event 1 (See figure 7.5). According to the SuperMag database, the onset is at 11:59 UT. Like Event 1, it occurs close to Poker Flat with an MLAT of 65.6°N and MLT of 00:35 when Poker Flat is at an MLT of 00:53. The AL index peaks at about -913 nT, making this substorm's strength second only to Event 1 amongst the five events described in this Chapter.

Geomagnetic Parameters: The IMF-B_z turns southward at ∼11:00 UT, after which there is no data for several hours. The auroral electrojet indices slowly increase in magnitude after 11:30 UT. SYM-H is more negative than Event 1, indicating a stronger ring-current.

Auroral Morphology: A steady east-west aligned growth-phase arc is visible in all-sky camera images before 10:00 UT. Equatorward of the arc, faint east-west aligned arcs and streaks are visible at such an early stage. The growth phase starts around ∼11:30 UT, as the arc moves equatorward. Diffuse aurora passes through the point along the magnetic-field-aligned beam of PFISR, up to ∼11:48 UT. At ∼11:49 UT, SDA-like features, east-west aligned streaks become prominent in the images. At 11:59 UT, the auroral breakup fills the sky. See the video *here*[4].

Precipitating electrons: As the SDA moves over PFISR, we observe low-altitude ionization reaching down to 75km, and electron precipitation as high as 50-100 keV. A latitudinal energy dispersion across the SDA features that manifests as a temporal dispersion, with energy decreasing with time or latitude within SDA, can be seen in figure 7.5 column 2, panel 1 and 2. At around 12:01 UT, substorm onset has begun, but the magnetic field-aligned beam finds itself in a region with no precipitation (a cavity). This cavity is bounded by the growth phase arc equa-

[4]https://youtu.be/RP2KOxgez4w

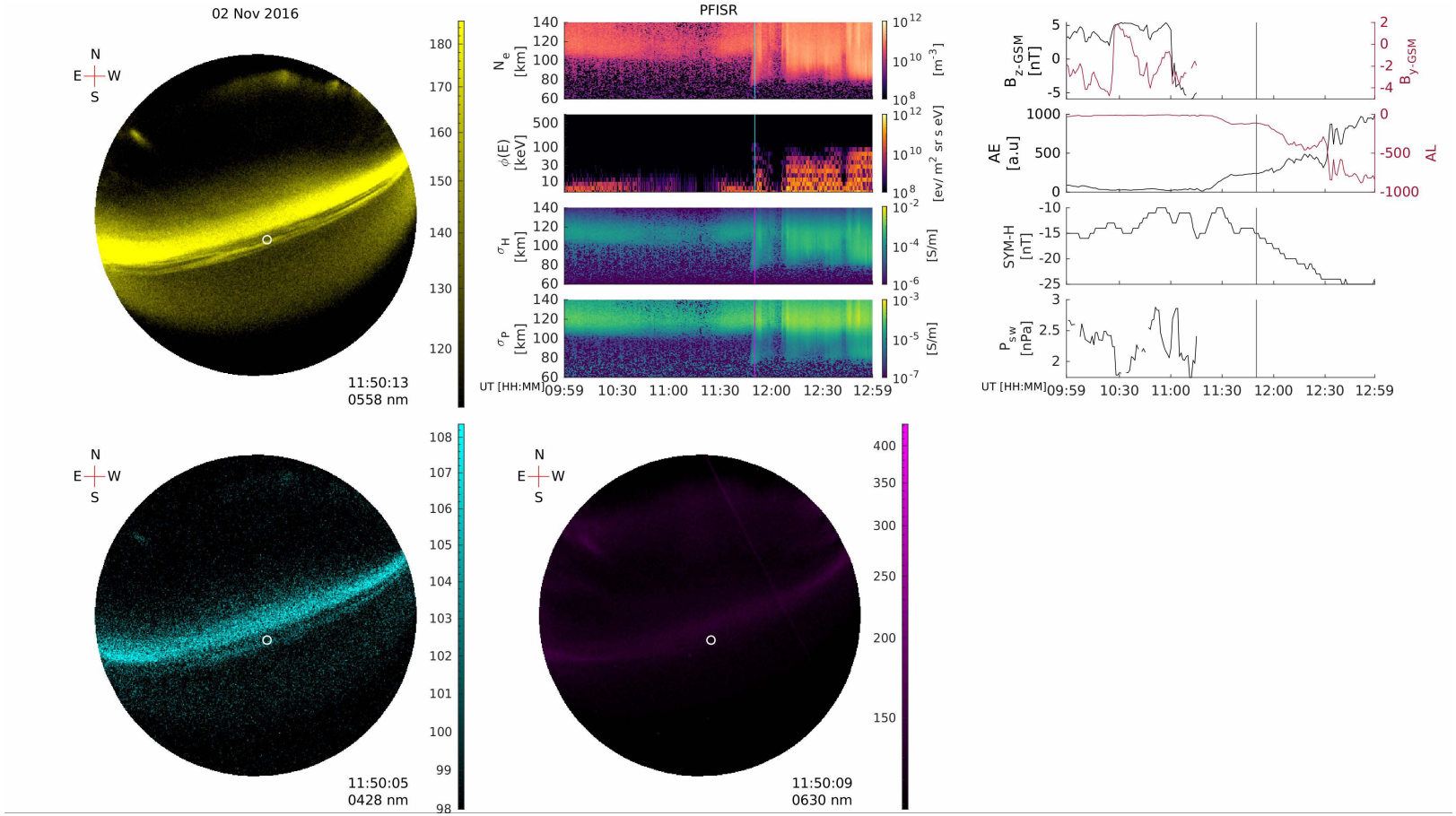

Figure 7.5: DASC and PFISR measurements of 02 November 2016 substorm showing the optical and ionospheric signature of the outer radiation belt boundary. Click *here* to see the video of this event.

torward, and possibly an extension of it poleward. Soon after, the sky is filled with aurora, and then energetic electron precipitation gets back to 50-100 keV and becomes more energetic later in the expansion phase at ∼12:50 UT.

Conductivity: During the SDA and expansion phase, we observe prominent conductivity enhancement in the D-region. We also note that similar to Event 1, SDA during the growth phase is equatorward of the growth phase arc. Therefore, there is a band of enhanced D-region conductivity and total conductance equatorward of the growth-phase arc.

In this event, during the growth phase, it is clear to see the SDA equatorward of the growth phase arc associated with energetic electron precipitation. The precipitation has a latitudinal (a.k.a temporal) energy dispersion with decreasing energy poleward within the SDA. These results lead us to conclude with high confidence that the observed SDA during the growth phase is a signature of the ORBB.

7.2.5 Event 5 (13879): 13 November 2016 substorm

This substorm occurs at 11:37 UT, also very close to Poker Flat, at an MLAT of 65.6°N and MLT of 00:14, when Poker Flat is at 00:31 MLT.

Geomagnetic parameters: The IMF B_z fluctuates about zero until ∼ 11:15 UT when it turns southward. The auroral electrojet indices begin to increase in magnitude around 11:28 UT, very close to the substorm onset, marking the beginning of the growth phase. The peak AL value is -668 nT, bringing the strength of the substorm on par with Event 2. SYM-H is quite negative, suggesting high ring current strength like the other substorms.

Auroral morphology: At about 11:20 UT, the growth phase arc appears close to the zenith of the camera field of view. Due to the moon above the horizon,

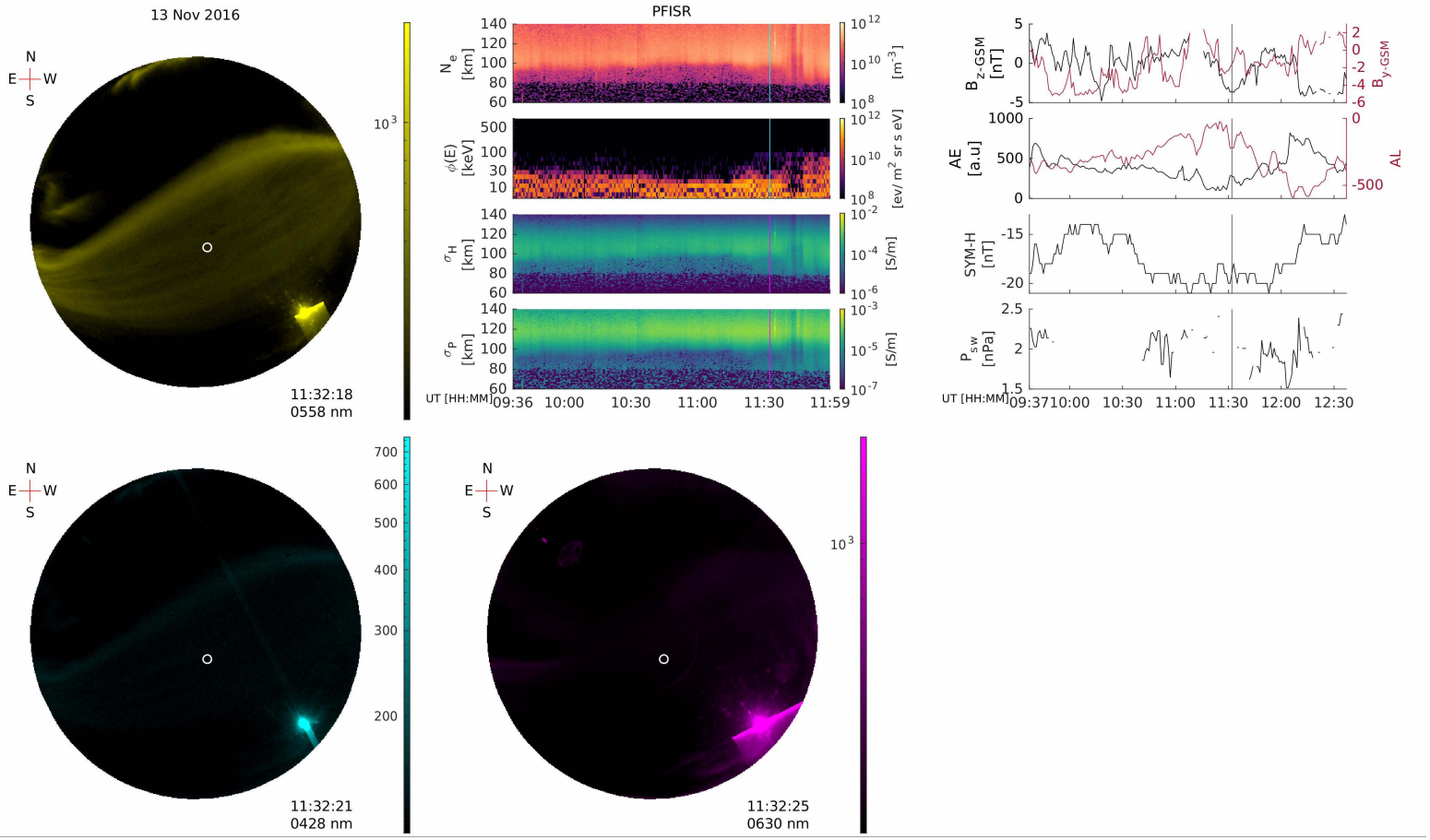

Figure 7.6: DASC and PFISR measurements of 13 November 2016 substorm showing the faint structuring of the diffuse aurora, but no significant enhancement in the precipitating energetic particles as one would expect. Click *here* to see the video.

the visibility of the sky is compromised. However, at 11:32 UT, we can see the faint growth phase arc move equatorward with the diffuse aurora equatorward of it. There is structuring within the diffuse aurora (see figure 7.6 column1 panel 1). However, they differ from the SDAs seen in other events. They contain long, faint, east-west aligned arcs without the short streaks. After 11:37 UT, the auroral breakup at the onset results in bright aurora filling the sky. However, after 11:50 UT, due to both clouds and the moon, it is impossible to decipher the morphology. See the video *here*[5].

Precipitating electrons: When the magnetic field-aligned beam is within the SDA equatorward of the growth phase arc, the electron precipitation becomes slightly more energetic, with the maximum energy increasing from 15 keV to 30 keV. It returns to 15 keV after the SDA moves out of the radar FOV. This energy is still very low for the equatorward portion of the SDA. However, after the substorm onset, the energies reach up to 100 keV during the expansion.

Conductivity: Conductivity enhancement in the D-region is observed only after the onset during this substorm.

In this event, we observe SDA, but the precipitating high energy electron flux is insufficient to confidently state that the SDA marks the outer radiation belt boundary.

7.3 Results and Discussion

40% of strong substorms have clear signatures of the ORBB.

Table 7.2 summarizes the evidence for ORBB signatures in five strong substorms selected based on the presence of an observable growth phase for Poker Flat, and

[5]https://youtu.be/M49G-rtXJoQ

Substorm ID	ORBB Signature	Justification
Event 1 3339	Yes	SDA and EEP both were observed at growth phase, equatorward of the growth-phase arc.
Event 2 5504	No	Though SDA-like structures and EEP were observed, the image is blurry and there is no clear distinction between growth and expansion phase in the data.
Event 3 10023	No	SDA-like structures and EEP were observed simultaneously only after the onset, and not during growth phase.
Event 4 13816	Yes	SDA and EEP were both observed during growth phase, equatorward of the growth-phase arc.
Event 5 13879	No	SDA was observed during growth phase, but conjugate EEP did not have sufficiently high energy.

Table 7.2: Summary of the evidence of ORBB signature in selected substorms.

other conditions described in section 7.1. Two out of five substorms have ORBB signature. If we loosen our criteria for finding SDA or SDA-like structures with conjugate EEP to any phase of the substorm, then the number of substorms that satisfy it will be four, i.e., 80% of the substorms from the sample. From table 7.1, it is clear that all viable substorms exhibit SDA or SDA-like features during the growth phase or at the onset. We also observe energetic electron precipitation (EEP) during all the substorms, especially during the expansion phase. However, in four out of the five substorms, they are seen during the growth phase.

D-region conductivity enhancement is common during strong substorms.

The presence of EEP during the substorm growth phase, and especially the expansion phase, make D-region conductivity layers during substorms a common

phenomenon. We can also expect such enhancements during magnetic storms, where large amounts of the radiation belt electrons >100 keV precipitate into the ionosphere. The Hall conductance value exceeds that of the Pedersen conductance. And, the charge carriers are predominantly electrons in the D-region.

The source of the structuring in SDA, maybe due to the spatial structure of the magnetospheric source population.

Lack of precise position calibration of the Digital All-sky camera images with color filters makes it challenging for us to determine the exact correlation with energetic precipitation measurements for Events 3–5. However, the present study indicates during magnetically active periods, SDA and SDA-like features are associated with energetic electron precipitation that reaches 100 keV energies. Several times the SDAs, e.g., during the recovery phase, are associated with pulsating patches McKay et al. (2018). These pulsating patches are also associated with high energies. If one can show this association to be statistically significant, it might suggest that the narrow features seen within SDA are related to the structuring of the source population or particle scattering mechanisms in the magnetosphere.

Types of SDA

We have found two types of SDA: 1) short east-west aligned streaks within diffuse aurora and 2) faint, long, narrow east-west aligned arcs. Both of them are dynamic. Sometimes we use the term SDA-like to identify the latter type of SDA. These SDAs seem to occur during the growth phase, onset and are also well-known to occur during recovery phases. Additionally, they are also observed on the dayside. On 18 October 2010, ∼10:37 UT, we observed an SDA that was far equatorward of the growth phase arc, and not embedded in any diffuse aurora. The source of this remains unknown, and given the large latitudinal distance from the growth phase

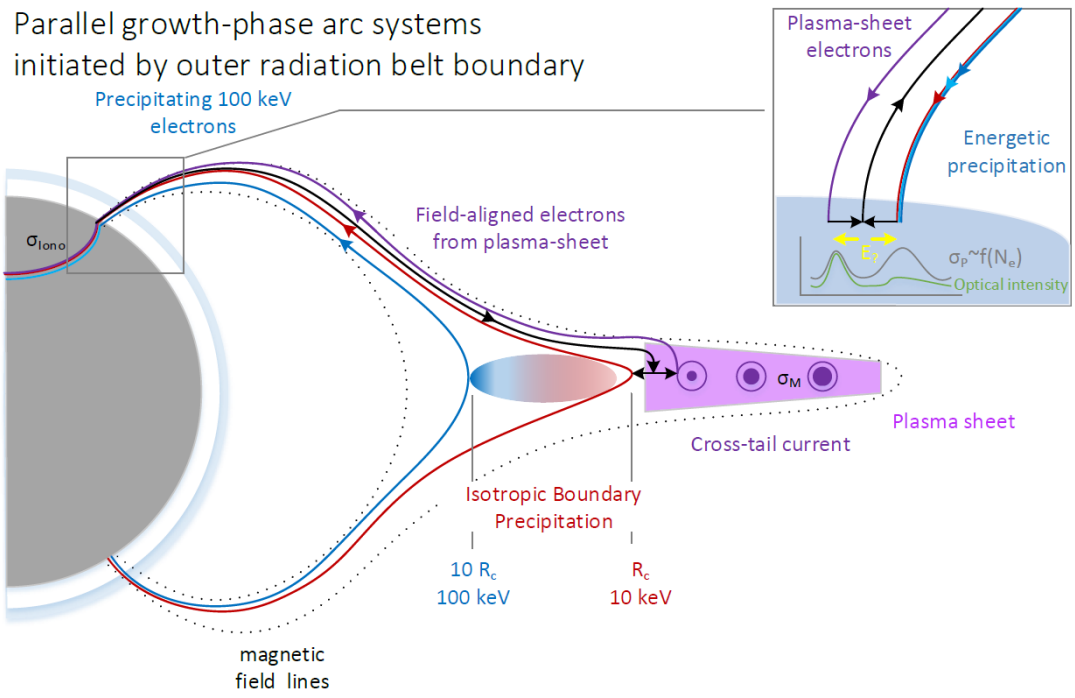

Figure 7.7: Growth phase arc brightening driven by enhanced ionospheric conductance generated by current sheet scattering of the outer radiation belt electrons.

arc, it seems unlikely that the current sheet scattering at the dipolar transition region could be a source.

Speculations on the origin of growth phase arcs.

The observation of SDAs adjacent to and equatorward of the growth-phase arc in events 1–5 brings us to ask the following question. If SDAs are associated with the ORBB during the growth phase, could ORBB provide a path for the initiation and brightening of the growth-phase arc? The hypothesis is pictured in figure 7.7.

During the substorm growth phase, the plasma sheet thins down, and the magnetotail stretches. This results in an increased current density of the cross-tail current. One theory of the source of the growth phase arc is the redirection of a part of the cross-tail current into the ionosphere through field-aligned currents. A

source of this redirection can be wave instabilities in near-earth current sheet or turbulence, resulting in increased resistance in the magnetosphere. This will force the current to look for an alternate path. The conductivity along the field lines is so high that the only limiting factor is the ionospheric conductivity. Ionospheric conductance during night-time is very low and is only enhanced by precipitation. Growth phase arcs do not usually exist during quiet periods. Therefore, the magnetosphere and ionosphere conductance ratios aren't ideal for cross-tail currents to be redirected during a quiet ionosphere.

When the magnetotail stretches during the growth phase, the outer radiation belt electrons scatter into the loss-cone due to a thinning, current sheet. That provides a way to kickstart an increase in conductance in the ionosphere by a mechanism completely independent of redirection of cross-tail currents. As we saw from the observations, the conductance can increase to about three times in a narrow region in the ionosphere < 10 km. This, coupled with decreasing conductivity in the cross-tail direction due to instabilities, might provide the incentive to set up a field-aligned current system between the ionosphere and the magnetosphere, thereby initiating the growth phase arc. Once this starts, a positive feedback loop can be set up, with field-aligned currents bringing in low energy electrons, which are accelerated by inverted V potentials in the auroral acceleration region to about 1–10 keV. This current, which is slightly poleward of the energetic electron precipitation, results in a further increase in ionospheric conductance, allowing more cross-tail current to be diverted and the subsequent brightening of the growth phase arc.

We have designed the above hypothesis to fit our observations. However, we can test this by using spacecraft such as SWARM to measure the field-aligned currents in LEO above such a growth phase arc system with an ORBB signature ad-

jacent to it. If we find a current system similar to that shown in figure 7.7, it will suggest that this system might be a MI coupling pathway that explains the brightening and origin of the substorm growth phase arc.

7.4 Conclusion

The multi-event analysis of substorm growth phases showed that 40% of strong substorms show optical signatures of energetic electron precipitation from the radiation belt. It is challenging to find the right conjunctions to evaluate if the observed structured diffuse aurora associated with a substorm growth phase is correlated with energetic precipitation. A more careful examination of the data sets should yield more samples of structured diffuse aurora with conjugate energetic electron precipitation, which can add to the statistics. Even if both are found within the same event, getting their spatial conjunction is not guaranteed, i.e., the SDA may not cross the radar FOV.

We also showed that energetic electron precipitation is frequent during the expansion phase of strong substorms. This results in enhanced D-region conductance during the substorm expansion phase and at least 40% of the time during the growth phase. The enhanced conductance during the growth phase due to energetic electron precipitation from the outer radiation belt boundary might also provide an electrical pathway to initiate the growth phase arc driven by field-aligned currents of colder plasma from the near-Earth plasma sheet.

CHAPTER 8

Summary and Outlook

8.1 Summary of contributions

In this thesis, we used an incoherent scatter radar to estimate the differential energy flux of precipitating electrons. By combining it with optical images from all-sky cameras, and magnetically conjugate spacecraft measurements, we demonstrated that we could constrain the source of energetic precipitation during substorms. This has been challenging due to difficulties associated with finding conjugate measurements and the unreliability of magnetic field models during substorm time. Using several techniques, we showed that during an intense substorm onset, the energetic electron precipitation originates in the plasma sheet tail-ward of 9 R_E likely due to scattering from electromagnetic ion cyclotron waves. Additionally, we were able to demonstrate the technique to estimate the energization of electrons by sources between the ionospheric and magnetosphere probe. In our example, we found that the Auroral Acceleration Region (AAR) between PFISR and THEMIS increases the characteristic energy of precipitation by ~ 10 keV.

We discovered the optical signatures of the outer radiation belt boundary (ORBB) for the first time with volumetric electron density profiles obtained from PFISR, all-sky camera, meridian scanning photometers, THEMIS, and NOAA spacecraft. Historically, it was considered that the energy flux of radiation belt precipitation is not sufficiently high to produce optical emissions. However, in our study, we showed that the energetic electron arc created by the electron isotropic boundary at the ORBB spatially correlates with a structured diffuse aurora, with an energy flux of ~ 1 mW/m^2 for electrons > 30 keV. Opgenoorth et al. (1983) and

Vondrak et al. (1983) reported the earliest SDA-like structures but did not identify them as related to the radiation belt boundary. Vondrak et al. (1983) observed sub auroral energetic electron arcs, which were narrow, aligned east-west, resembling multiple arcs. However, it was 3° in latitude, equatorward of the diffuse aurora, similar to what we observed in the 18 October 2010 substorm (which is not shown here). Opgenoorth et al. (1983) saw optical emissions in over-exposed frames correlated with the absorption arc (a manifestation of the ORBB in riometer data). Our work connected these optical observations to the ORBB. It also demonstrated that precipitation from the radiation belt boundary had spatial structure. Sergeev et al. (1996) described the energetic electron arc as "an intense, non-structured, isotropic electron precipitation" probably due to the limits in spatial resolution achieved by LEO satellites. However, now we know that ORBBs (and energetic electron arcs) are not uniform and they have small-scale spatial structure, which is likely associated with properties of the source plasma population or scattering mechanisms.

A multi-event analysis of energetic precipitation observed during the strong substorm's growth phase suggests that at least two out of five strong substorms show auroral signatures of the outer radiation belt boundary. We do not yet know whether these signatures exist in weak substorms, or during quiet periods. The study also affirms that structured diffuse aurora is typical during the growth phase of strong substorms. This result suggests that processes other than magnetopause shadowing on the dayside are associated with the structured diffuse aurora. Energetic electron precipitation from the dipolar transition region seems to be prevalent during substorm growth phases. They occur equatorward of the growth phase arc and are caused by the current sheet scattering of trapped electrons in the radiation belt. The sample size of the multi-event study was small, mounting only to

five viable substorms. The reason for the poor statistics is the challenge in finding conjunctions of the energetic electron arc moving across both the radar and camera field of view, given the radar beams have only a width of $\sim$5 km at $\sim$100 km altitude.

Finally, we explored the effect of energetic precipitation on ionospheric conductivity through incoherent scatter radars. We used electron density measurements, conductivity formulas, models of ionospheric composition, and assumptions of ionosphere chemistry. The results suggested that there is an additional conductivity layer in the D-region during the growth and expansion phases for strong substorms. This layer's contribution to total Pedersen and Hall conductance can reach up to 15% and 60%, respectively. This value will increase if we account for the non-linear increase in Pedersen conductivity with the electric field in the D-region. Most global conductance models use LEO satellite measurements of charged particle fluxes to estimate ionospheric conductance. Since most satellites measure electron fluxes up to 30 keV, they miss out on incorporating the high energy particles that contribute to D-region conductivity enhancements. Including the higher energy electrons will avoid uncertainties of $\sim$60% during magnetically active periods. Lastly, we showed that ISR estimates of D-region conductivity are more accurate than estimates based on satellite measurements of energetic precipitation. This is because D-region conductivity is driven by electron mobility, as ion collision frequencies are very high, and they remain chained to the neutrals. Therefore, since ISR measures the electron density directly, it makes the ISR conductivity estimates better than the satellite-based forward-modeled estimates of conductivity. The latter has uncertainties of $\sim$20% without using the complex D-region chemistry in the forward model.

8.2 Limitations and challenges

Our use of the maximum entropy inversion method to estimate precipitating electron energy spectra with ISR measurements was successful, as evidenced by the validation with magnetically conjugate THEMIS satellite measurements shown in figure 6.8. However, since THEMIS was at a distance of $\sim$ 9 R $_E$ in the magnetic equatorial plane, this validation is still unsatisfactory. The inversion technique needs to be validated by measurements of precipitating energetic electrons made by an LEO satellite with much less uncertainty regarding magnetic conjugacy. Furthermore, the inversion technique needs to incorporate the complex ionospheric chemistry using the SIC model instead of Vickrey et al. (1982), as we demonstrated in figure 4.6.

Though we can estimate the D-region conductivity without knowing the complex ion chemistry due to the low mobility of ions in the region, we cannot determine the conductivity enhancements due to its non-linear dependence on D-region electric fields. To enable this, we need to fit the power spectra of the back-scattered pulses from the ISR to extract parameters such as the plasma velocity, ion-neutral collision frequencies, temperature and composition ratios, electric fields, etc. This will allows us to calculate the non-linear Pedersen conductivity enhancements as well. SRI International is currently developing a model of the D-region ISR spectra, which will be available for fitting the measured ISR spectra soon.

A significant limitation of this study is also common in space physics: having access to global measurements of all parameters of interest. Incoherent scatter radar measurements and charged particle measurements in space do not yet offer high-resolution global coverage. There is reasonable global coverage for riometers and cameras. However, they alone do not help us constrain sources of energetic

precipitation. Therefore, It is important to look ahead to a future where we can develop low mass, low power, and low data sensor kits, which can record basic space physics data. Such a device might measure DC magnetic fields, radiation dose, charged particle spectra, etc. and be capable of piggybacking on large and small satellites alike. A network of diagnostic sensors around the near-Earth space is another logical step to understanding and forecasting space weather (as we currently do for terrestrial weather).

In this dissertation, we consciously decided to use the phrase '*constraining* the source of energetic precipitation' to acknowledge the great difficulties in establishing causality merely from data and without experiments. As discussed in section 3.3.1.4, a causal connection between two processes or events can only be made by making a causal assumption. In our case, we assumed that single-particle motion in a geomagnetic field was valid, and source mechanisms that violate adiabatic invariants were local and were located somewhere between or outside the two instruments measuring charged particles on the same field line. If this assumption is invalid, then we cannot claim causality between the ionospheric measurements of energetic electron precipitation and what we claim is its source. A deeper understanding of causal inference theory by Pearl (2009) is likely to allow our field to make more informed and better arguments of causal connections with the same data.

A considerable challenge that falls on researchers trying to use multiple instruments to uncover the physics behind observations in the near-Earth space environment is access to datasets. Over the decades, the community has invested in and developed excellent data sets and archives such as https://data.amisr.com/database/ and https://spdf.gsfc.nasa.gov/. Though the standardization of data

formats is always an issue, given the diversity of countries and researchers developing them, there is still a lot of historical data before 2010 that suffers from basic archiving requirements such as loss-less storage, availability of calibration files, and metadata. Fields such as sociology that require big data rely on external infrastructure to generate them (such as social networking websites). In contrast, almost all space physics data are produced from pre-planned research projects that know what data they will gather. Despite such awareness, there has been a widespread failure to put in the resources to archive them. Persuasion from the American Geophysical Union and space physics journals pushing for stricter data sharing standards is moving the community to follow better standards in the future. However, a structured program to recover and archive historical-data will become more critical with each passing day, given the increased difficulty of recovering them in the future.

Finally, it is clear that to make a better case for the frequency of ORBB signatures and energetic electron precipitation during substorms; we need to extend the study described in chapter 7 to include many more events. They will need to sample a broad set of parameters such as substorm strength (AL), MLT, MLAT, and season. We also need to explore the presence of ORBB signatures outside substorms. To do this, we will need to use an additional ISR. Resolute-bay ISR is north and east of PFISR - closer to the polar caps, and will easily observe substorm growth phases associated with weaker substorms. It will help address questions that remain: Do ORBB signatures occur in a weak substorm growth phase? Do they occur during periods outside substorms? Are the SDAs in the dayside and recovery phase magnetically conjugate to the radiation belt? What is the statistical extent and effect of energetic precipitation during substorms?

8.3 Future work

In this last section, we discuss several future projects that can potentially address some of the unanswered questions on this topic.

Quantifying D-region contribution to total ionospheric conductance:
Since ISRs can be used to make conservative estimates of D-region conductivity, a study that quantifies it through a long period that spans several geomagnetic and geographic parameters using one or more ISRs will be a novel contribution to the field. We can use the results to extend existing conductivity models to incorporate the D-region's contribution. A clearer picture of the magnitude and variance of D-region conductance will come about with such a statistical study, more than that of the multi-event study presented in this dissertation.

Characterizing ISR sensitivity to D-region ionization:
What is the lowest electron density that can be detected by an ISR from the D-region? One can characterize the sensitivity of ISRs to D-region ionization through the variance of backscattered power by developing a Monte-Carlo simulation. It will allow us to estimate the probability distribution of fitted parameters of ISR D-region power spectra. As mentioned earlier, scientists at SRI International are currently developing this.

Separating proton and electron flux while inverting ISR measurements to energy spectra of precipitating particles:
Our current method of inverting ionization profiles of electron density to estimate the energy spectra of primary precipitating particles assume the particles are pre-

dominantly electrons. However, expanding this capability by adding new constraints from conjugate measurements of optical H_β intensities to the maximum entropy inversion method will be very useful. To do this, one will need to use forward models of proton precipitation to predict the ionization rates caused by different energy protons (Rees, 1982). We will then have to validate the results with magnetically conjugate LEO satellite measurements.

Validating PFISR inverted energy spectra with ELFIN measurements:
As mentioned earlier, validating the ISR estimates of precipitating electron energy spectra is essential to gain confidence in ISR inversion techniques. This is a challenging task due to a sparsity of LEO satellites that measure energetic electrons and protons at sufficiently high energy and temporal resolution. However, we commissioned several PFISR experiments in 2019 and early 2020 to run in conjunction with ELFIN-A and -B spacecraft passes over Poker Flat. These LEO small satellites have particle detectors that measure energetic electrons >50 keV with sufficient energy resolution.

An empirical model of energetic electron precipitation:
To quantify the global effect of energetic electron precipitation on atmospheric chemistry, ionospheric conductance, and radio absorption, a global energetic precipitation model is essential. Using POES spacecraft and non-parametric nonlinear regression methods like a decision tree, one can construct a global empirical model of energetic precipitation with geomagnetic indices as input. Currently, there exist simpler empirical models such as the Ap-Energetic Electron Precipitation (APEEP) model, which, as the name suggests, is a model that uses a statistical

average of POES data and Ap index as its input. A more complex model with better spatial and energy distribution of precipitation is needed as input to NCAR's Whole Atmospheric Community Climate Model (WACCM) to characterize the full impact of energetic precipitation on atmospheric chemistry.

Characterizing radiation belt loss from current sheet scattering:
Most of the existing literature on the loss of trapped charged particles from the radiation belt focus on wave scattering as the primary loss mechanism. However, as chapter 5 shows, current sheet scattering can knock off trapped particles from the edge of the radiation belt. During the growth phase of substorms, it can cause losses similar in strength to relativistic dropouts during magnetic storms. Therefore, it becomes relevant to quantify the extent of the loss caused by current sheet scattering based on data and validate it with models. This will allow for a better understanding of the significance of this mechanism among the different loss processes that affect the radiation belt.

Identify solar-wind drivers of energetic precipitation:
It would be useful to identify combinations of solar-wind drivers that highly correlate with energetic precipitation, to develop a systems-level understanding of the drivers of energetic precipitation. It will provide us with effective lower-dimensional input vectors to global empirical models of precipitation that may improve performance. A preliminary analysis with canonical correlation analysis suggests that Kp and AU indices are predictors of the global-hemispheric average of electron precipitation. On the other hand, the solar-wind velocity and Kp are good predictors of the global-hemisphere average of proton precipitation.

The topic of energetic precipitation is broad, and covers a lot of ground in space physics, starting from the magnetotail to the lower-ionosphere. A considerable number of source mechanisms of energetic electrons lie at an unexplored region of the magnetosphere: the night-side dipolar transition region. Missions have been proposed to explore this region in the future. A ground-based network of cameras and riometers is being set up by the Canadians to study the ionospheric footpoints of this region. The scope and the effect of this phenomena on other subsystems of the near-Earth space environment and new missions are likely to open the doors to further questions and several new answers.

APPENDIX A

Supporting Information for Chapter 5

Contents

1. Text A.1 to A.2
2. Figures A.1 to A.4

Additional Supporting Information (Files uploaded separately)

1. Captions for Movie A.1

Introduction

Figure A.1 demonstrates the accuracy of the Tsyganenko 96 model estimate of the magnetic field at THEMIS-D coordinates. Figure A.2 shows the standard deviation of equatorial and northern magnetic foot points of THEMIS-D estimated using 11 magnetic field models, which we use as a proxy for magnetic field mapping error. Figure A.3 shows the time series measurements of electron energy flux measured by THEMIS-D and PFISR, along with the direct electron density measurements made by PFISR along the magnetic field direction. Figure A.4 presents THEMIS-D measurements of loss-cone pitch angle distribution, and its magnetically conjugate location at the magnetic equatorial plane. Text S1 discusses the error in the magnetic field mapping procedure by comparing *in-situ* magnetic field measurements with T96 model estimates, and discussing the variability of the mapping based on 11 different magnetic field models. Text S2 describes figure A.4 in detail, and

discusses possible reasons for the observed field-aligned loss-cone distribution in the early growth-phase. Table 5.1 provides details about the different instruments used for the analysis presented in the main article. Movie S1 shows how the small-scale structure evolves with time during the growth phase, and provides evidence for the structural correlation of the white-light emissions with energetic electron precipitation.

Text A.1

Quantifying magnetic field mapping error

Figure A.1 shows *in-situ* measurements of the magnetic field made by THEMIS-D spacecraft (red line), compared to estimates from the T96 magnetic field model (black dashed line). The figure shows that B_x, B_z and B_{mag} values have $<$25% error during the early growth-phase (10:30$-$11:20 UT). This period is where we observe current sheet scattering, and measure energetic precipitating using PFISR, and hence most relevant to our findings. However, this also suggests that at 11:29:30 UT, the magnetic field mapping of the NOAA-17 spacecraft from the southern hemisphere to Poker Flat cannot be trusted without additional methods to constrain the mapping.

Figure A.2 estimates the variance of the magnetically conjugate point of THEMIS-D spacecraft mapped to the magnetic equator and the norther hemisphere from its location near the magnetic equatorial plane by using several magnetic field models. The assumption we make here is that this provides us with a reasonable estimate of the spatial error that exists while mapping the foot points of the spacecraft. We use 11 magnetic field models, and produce a quartile representation of the magnetic equatorial point (figure A.2a-b), and northern hemispheric

foot point (figures A.2c-d). We can calculate the standard error from these plots, calculated as $\sigma/\sqrt{n}$, where σ is the standard deviation and n is the number of data points used to calculate the standard deviation - which is mostly 11. The maximum standard error we estimated was $\sim 1.5^{\circ}$ at around 10:15 UT.

Text A.2

Field-aligned loss-cone distribution observed at the magnetic equatorial plane during growth phase

Before the substorm growth phase from 8:30-11:00 UT, we believe that THEMIS-D and -E were likely tailward of the e-IB between ∼10–11 R_E, and ∼22–23 MLT. Figure A.4a shows the electron anisotropy A=$\phi_{\perp}/\phi_{\parallel}$-1 measured by THEMIS-D. It is very similar to that measured by THEMIS-E orbiting nearby. At 8:30 UT electrons ∼>300 keV are nearly field-aligned, and by 11:00 UT this extends towards lower energies of about ∼30 keV. Figure A.4c shows the distance of the magnetically conjugate location at the equatorial plane of the spacecraft tending to generally increase in time according to the T96 model, suggesting magnetotail stretching. This causes the minimum energy threshold required to isotropically scatter electrons to decrease within this time period (Figure A.4b). The minimum energy threshold is calculated by assuming the ratio of the minimum radius of curvature of a field line to that of the electron gyro radii to be ∼8 for non-adiabatic scattering (K_C =R_{Cmin}/ρ ∼<8). The threshold agrees with the decreasing lower energy limit of the anisotropy shown in figure A.4a. Tailward of the e-IB we expect strong isotropic pitch angle distribution in the loss-cone and not necessarily the observed field-aligned precipitation. Apart from the poor resolution associated with the THEMIS loss-cone measurements, there are two possible explanations for this incongruent

observation. 1. The THEMIS-D and -E are not close to the e-IB, but in the outer plasma sheet with decreasing energy of field-aligned precipitation as the the spacecraft finds itself moving out of the plasma sheet. 2. The spacecraft is close to the e-IB in the inner-plasma sheet from 08:30 to 11:00 UT, but additional scattering mechanisms that require a thin current sheet causes field aligned precipitation. Furthermore, the spacecraft crosses the entire outer plasma sheet between 11:00 to 11:15 UT, when the field lines stretch dramatically. We believe point 2 is more likely than point 1, in the light of the fact that: a) high energy electrons are not observed in the outer plasma sheet, b) the loss-cone energy flux measured by THEMIS-D for electrons >100 keV between 8:30 to 11:00 UT in figure A.3a is quantitatively similar to the energy flux estimated by PFISR for electrons $>$ 100 keV at $\sim$11:15 UT shown in figure A.3b. A more detailed analysis of the magnetic field mapping into the neutral sheet will allow us to evaluate this claim. Though it is challenging to estimate magnetic field lines within the night-side transition region, between 8:30–11:15 UT the T96 model estimate of the magnetic fields at THEMIS-D and -E coordinates are more or less accurate with the modelled Bx mostly within 25% of the measured value. (See figure A.1).

Movie A.1

Evolution of the small-scale structures of energetic electron arc (EEA)

The following image is a sample frame from movie S1.

Top-left panel shows contrast enhanced white-light images from DASC Poker Flat. In the middle of the image, the red pentagonal area represents the field of view of PFISR. The panel on the top-right shows the small-scale structure of white-

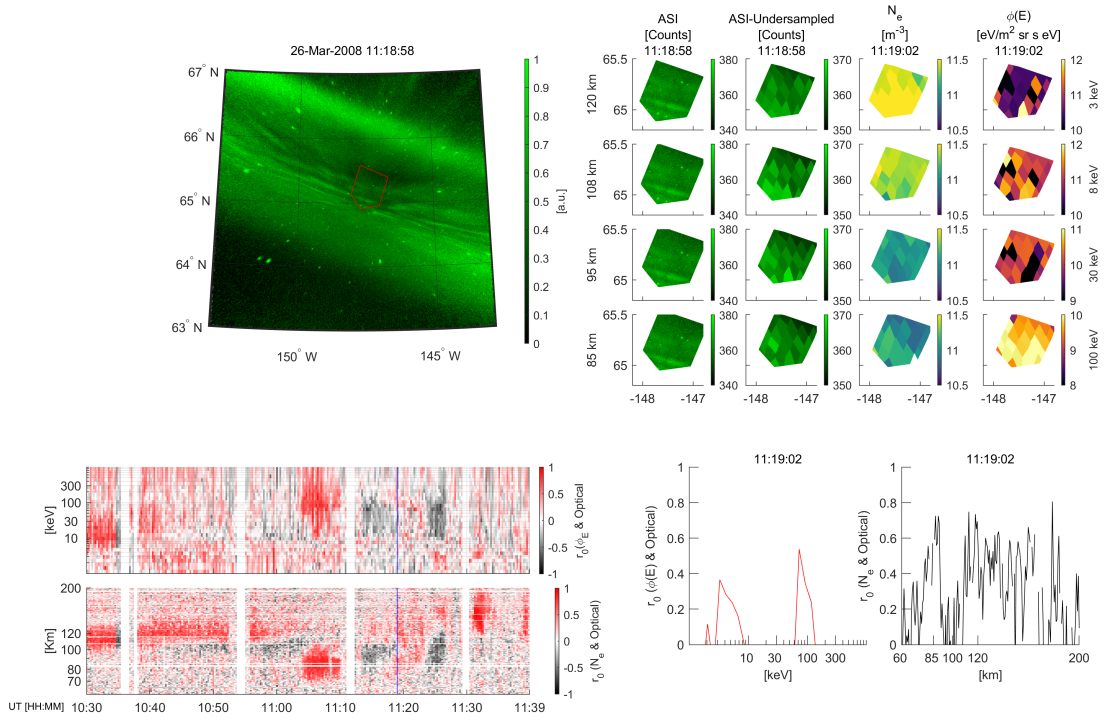

light images, white-light images under-sampled to match the spatial resolution of PFISR, PFISR electron density, and PFISR energy flux. Each row corresponds to an electron energy, and its corresponding peak-ionization altitude. The panel on the bottom-left, is the spatial correlation coefficient of energy flux (1) and electron density (2) with the white-light image. This is same as Figures 4d and 4e in the main article respectively. The bottom-right, shows the correlation coefficient varying with energy (1) and altitude (2) at the time instant marked by the blue time-marker in the bottom-left panel.

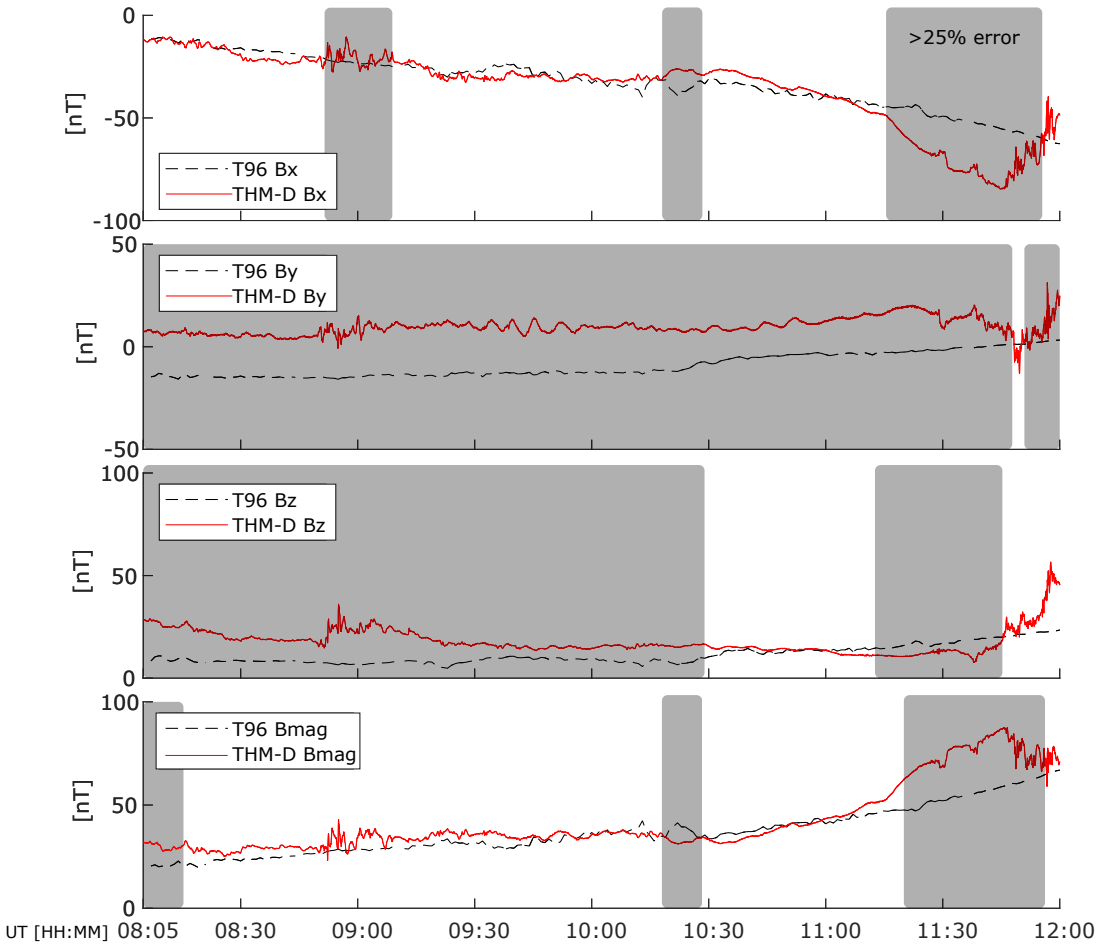

Figure A.1: Comparison of THEMIS-D magnetic field measurements with T96 estimate. The shaded regions show the time periods were the magnitude of the model estimate is greater than 25% of the local measurement.

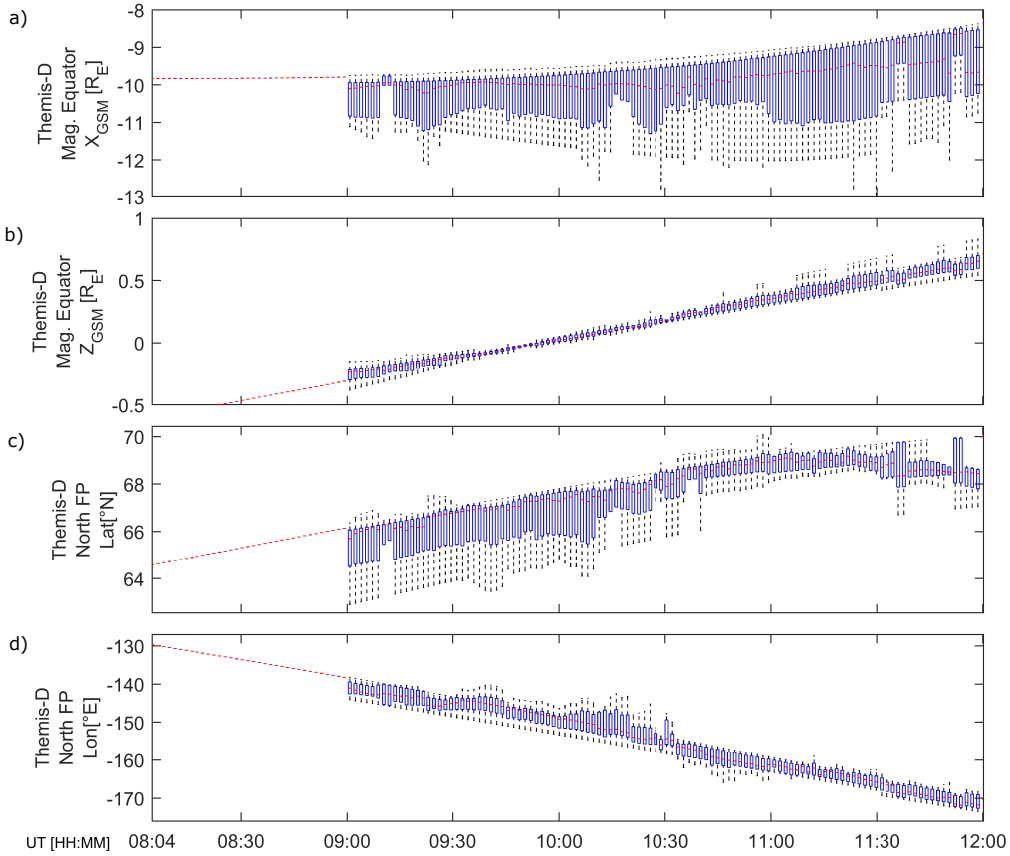

Figure A.2: Quartile representation of magnetic field model estimates of magnetically conjugate points in (a-b) the equator and (c-d) the ionosphere of THEMIS-D, calculated using 11 magnetic field models. The red dash is the median value, the lower and upper limit of the blue box corresponds to the 25th and 75th percentile, and the terminals of the dashed black lines shows the minimum and maximum values excluding outliers.The standard error from this plot ($\sigma/\sqrt{n}$) is used as the magnetic field mapping error in the main manuscript. Here n is number of data points in a time instance, and σ is the standard deviation. The magnetic field models used in this calculation are Mead & Fairfield (1975), Tsyganeko short (1987), Tsyganenko long (1987), Tsyganenko (1989c), Olson & Pfitzer quiet (1977), Olson & Pfitzer dynamic (1988), Tsyganenko (1996), Ostapenko & Maltsev (1997), Tsyganenko (2001), Tsyganenko (2001) storm, Tsyganenko (2004) storm.

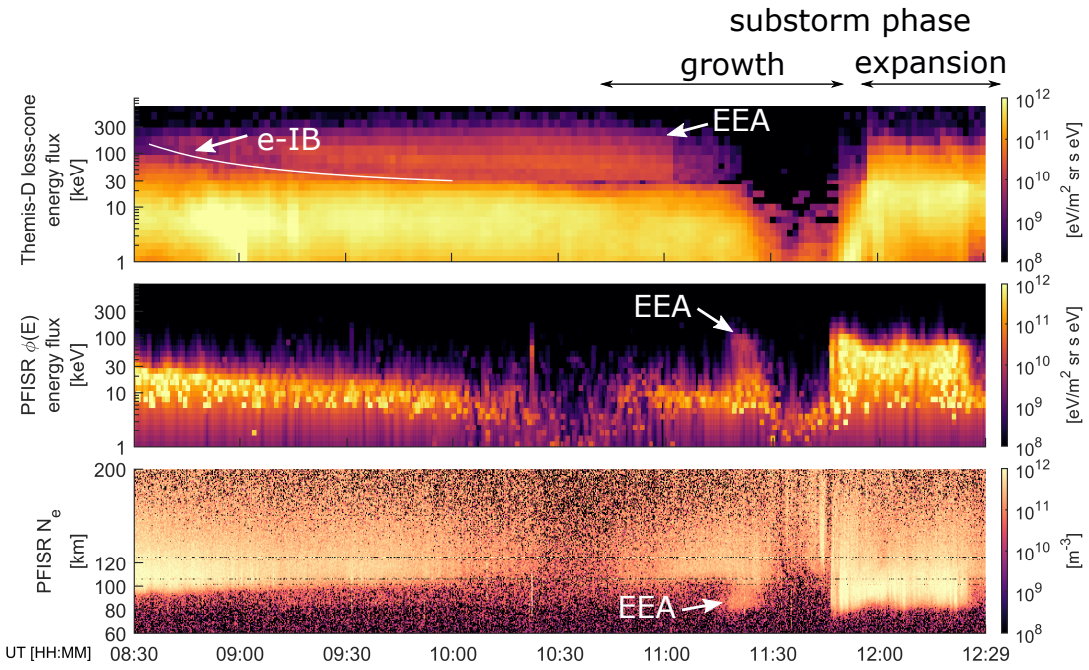

Figure A.3: Electron density, and energy flux estimated by PFISR, and electron energy flux measured by THEMIS-D from Sivadas et al., (2017).

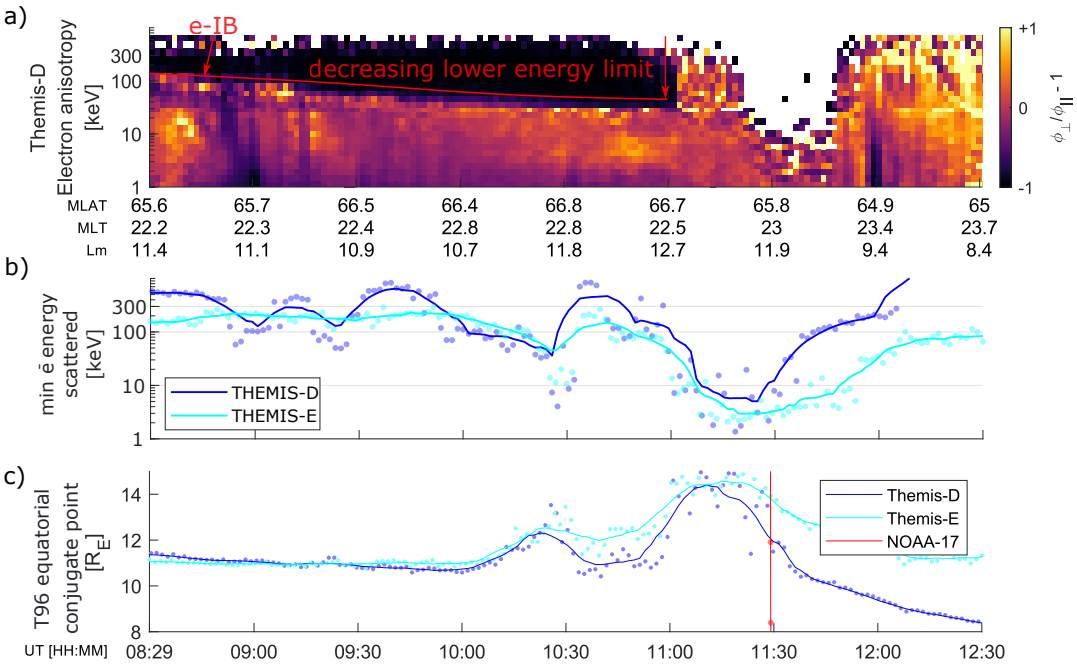

Figure A.4: Electron isotropic boundary from space: a) THEMIS-D electron anisotropy (A=$\phi_\perp/\phi_\parallel$-1), darker implies nearly field-aligned electrons, b) minimum electron energy of non-adiabatic scatter estimated from THEMIS-D and -E magnetic field measurements and T96 model, c) L-shell estimates of spacecraft from T96 model

BIBLIOGRAPHY

Akasofu, S. I. (1964). The development of the auroral substorm. *Planetary and Space Science*, *12*(4), 273–282.

Akasofu, S.-I. (2012). Auroral Morphology: A Historical Account and Major Auroral Features During Auroral Substorms. In *Geophysical Monograph Series*, vol. 197, (pp. 29–38). American Geophysical Union. http://www.agu.org/books/gm/v197/2011GM001156/2011GM001156.shtml.

Albert, J. M. (2003). Evaluation of quasi-linear diffusion coefficients for EMIC waves in a multispecies plasma. *Journal of Geophysical Research: Space Physics*, *108*(A6).

Alfonsi, L., Kavanagh, A. J., Amata, E., Cilliers, P., Correia, E., Freeman, M., Kauristie, K., Liu, R., Luntama, J. P., Mitchell, C. N., & Zherebtsov, G. A. (2008). Probing the high latitude ionosphere from ground-based observations: The state of current knowledge and capabilities during IPY (2007-2009). *Journal of Atmospheric and Solar-Terrestrial Physics*, *70*(18), 2293–2308.

Alfvén, H., & Fälthammar, C.-G. (1963). *Cosmical electrodynamics*. 2nd edition. Clarendon Press.

Amemiya, H., & Nakamura, Y. (1996). Measurement of Negative Ions in the Lower Ionosphere (D-Layer) in the Polar Region. *Journal of Geomagnetism and Geoelectricity*, *48*, 391–401.

Amm, O., Aksnes, A., Stadsnes, J., Østgaard, N., Vondrak, R., Germany, G., Lu, G., & Viljanen, A. (2005). Mesoscale ionospheric electrodynamics of omega bands determined from ground-based electromagnetic and satellite optical observations. *Annales Geophysicae*, *23*(2), 325–342.

Anderson, K. A., & Enemark, D. C. (1960). Balloon observations of X rays in the auroral zone II. *Journal of Geophysical Research*, *65*(11), 3521–3538.

Angelopoulos, V. (2008). The THEMIS mission. *Space Science Reviews*, *141*(1-4), 5–34.

Angelopoulos, V., McFadden, J. P., Larson, D., Carlson, C. W., Mende, S. B., Frey, H., Phan, T., Sibeck, D. G., Glassmeier, K. H., Auster, U., Donovan, E., Mann, I. R., Rae, I. J., Russell, C. T., Runov, A., Zhou, X. Z., & Kepko, L. (2008). Tail reconnection triggering substorm onset. *Science*, *321*(5891), 931–935.

Arnold, F., Kissel, J., Krankowsky, D., Wieder, H., & Zähringer, J. (1971). Negative ions in the lower ionosphere: A mass-spectrometric measurement. *Journal of Atmospheric and Terrestrial Physics*, *33*(8), 1169–1175.

Artemyev, A. V., Orlova, K. G., Mourenas, D., Agapitov, O. V., & Krasnoselskikh, V. V. (2013). Electron pitch-angle diffusion: resonant scattering by waves vs. nonadiabatic effects. *Annales Geophysicae*, *31*(9), 1485–1490.

Artemyev, A. V., Rankin, R., & Blanco, M. (2015). Electron trapping and acceleration by kinetic Alfven waves in the inner magnetosphere. *Journal of Geophysical Research: Space Physics*, *120*(12), 10305–10316.

Artemyev, A. V., Zelenyi, L. M., Malova, H. V., Zimbardo, G., & Delcourt, D. (2009). Acceleration and transport of ions in turbulent current sheets: formation of non-maxwelian energy distribution. *Nonlinear Processes in Geophysics*, *16*(6), 631–639.

Auster, H. U., Glassmeier, K. H., Magnes, W., Aydogar, O., Baumjohann, W., Constantinescu, D., Fischer, D., Fornacon, K. H., Georgescu, E., Harvey, P., Hillenmaier, O., Kroth, R., Ludlam, M., Narita, Y., Nakamura, R., Okrafka, K., Plaschke, F., Richter, I., Schwarzl, H., Stoll, B., Valavanoglou, A., & Wiedemann, M. (2008). The THEMIS fluxgate magnetometer. *Space Science Reviews*, *141*(1-4), 235–264.

Baker, D. N., Pulkkinen, T. I., Angelopoulos, V., Baumjohann, W., & McPherron, R. L. (1996). Neutral line model of substorms: Past results and present view. *Journal of Geophysical Research: Space Physics*, *101*(A6), 12975–13010.

Baker, W. G., & Martyn, D. F. (1953). Electric currents in the ionosphere - The conductivity. *Philosophical Transactions of the Royal Society of London. Series A, Mathematical and Physical Sciences*, *246*(913), 281–294.

Barcus, J. R., & Rosenberg, T. J. (1966). Energy spectrum for auroral-zone X rays: 1. Diurnal and type effects. *Journal of Geophysical Research*, *71*(3), 803–823.

Berkey, F. T., Driatskiy, V. M., Henriksen, K., Hultqvist, B., Jelly, D. H., Shchuka, T. I., Theander, A., & Ylindemi, J. (1974). A synoptic investigation of particle precipitation dynamics for 60 substorms in IQSY (1964-1965) and IASY (1969). *Planetary and Space Science*, *22*(2), 255–307.

Beynon, W. J. G., & Williams, P. J. S. (1978). Incoherent scatter of radio waves from the ionosphere. *Reports on Progress in Physics*, *41*(6), 909.

Birn, J., Artemyev, A. V., Baker, D. N., Echim, M., Hoshino, M., & Zelenyi, L. M. (2012). Particle acceleration in the magnetotail and aurora. *Space Science Reviews*, *173*(1-4), 49–102.

Bonnell, J. W., Mozer, F. S., Delory, G. T., Hull, A. J., Ergun, R. E., Cully, C. M., Angelopoulos, V., & Harvey, P. R. (2009). The Electric Field Instrument (EFI) for THEMIS. In *The THEMIS Mission*, (pp. 303–341). Springer New York. https://link.springer.com/chapter/10.1007/978-0-387-89820-9{_}14.

Borovsky, J. E. (1993). Auroral arc thicknesses as predicted by various theories. *Journal of Geophysical Research: Space Physics*, *98*(A4), 6101–6138.

Borovsky, J. E. (2018). The spatial structure of the oncoming solar wind at Earth and the shortcomings of a solar-wind monitor at L1. *Journal of Atmospheric and Solar-Terrestrial Physics*, *177*, 2–11.

Borovsky, J. E., & Denton, M. H. (2009). Electron loss rates from the outer radiation belt caused by the filling of the outer plasmasphere: The calm before the storm. *J. Geophys. Res*, *114*, 11203.

Borovsky, J. E., & Valdivia, J. A. (2018). The Earth's Magnetosphere: A Systems Science Overview and Assessment. *Surveys in Geophysics*, *39*(5), 817–859.

Bortnik, J., & Thorne, R. M. (2007). The dual role of ELF/VLF chorus waves in the acceleration and precipitation of radiation belt electrons. *Journal of Atmospheric and Solar-Terrestrial Physics*, *69*(3), 378–386.

Boyle, C. B., Reiff, P. H., & Hairston, M. R. (1997). Empirical polar cap potentials. *Journal of Geophysical Research A: Space Physics*, *102*(A1), 111–125.

Brekke, A., Hall, C., & Hansen, T. L. (1989). Auroral ionospheric conductances during disturbed conditions. *Annales Geophysicae*, *7*, 269–280.

Brekke, A., & Moen, J. (1993). Observations of high latitude ionospheric conductances. *Journal of Atmospheric and Terrestrial Physics*, *55*(11-12), 1493–1512.

Brown, R. R. (1966). Electron precipitation in the auroral zone. *Space Science Reviews*, *5*(3), 311–387.

Buchert, S. C., Tsuda, T., Fujii, R., & Nozawa, S. (2008). The Pedersen current carried by electrons: a non-linear response of the ionosphere to magnetospheric forcing. *Annales Geophysicae*, *26*(9), 2837–2844.

Callis, L. B., Natarajan, M., Lambeth, J. D., & Baker, D. N. (1998). Solar atmospheric coupling by electrons (SOLACE) 2. Calculated stratospheric effects of precipitating electrons, 1979-1988. *Journal of Geophysical Research Atmospheres*, *103*(D21), 28421–28438.

Cohen, R. H., Rowlands, G., & Foote, J. H. (1978). Nonadiabaticity in mirror machines. *Physics of Fluids*, *21*(4), 627–644.

Collis, P. N., & Korth, A. (1985). GEOS-2 observations of energetic electrons in the morning sector during auroral radio absorption events. *Journal of Atmospheric and Terrestrial Physics*, *47*(4), 327–339.

Cummer, S. A., Vondrak, R. R., Østgaard, N., Stadsnes, J., Bjordal, J., Chenette, D. L., Brittnacher, M. J., Parks, G. K., Sigwarth, J. B., & Frank, L. A. (2000). Global multispectral auroral imaging of an isolated substorm. *Geophysical Research Letters*, *27*(5), 637–640.

Danilov, A. D. (1970). Negative Ions and the Ionospheric D Region. In *Chemistry of the Ionosphere*, (pp. 129–171). Springer US.

Davis, T. N., & Sugiura, M. (1966). Auroral electrojet activity index AE and its universal time variations . *Journal of Geophysical Research*, *71*(3), 785–801.

De Mees, T. (2014). Thoughts on the Causality of the Maxwell Equations. *The General Science Journal*. https://www.gsjournal.net/Science-Journals/Essays-Mechanics%20/%20Electrodynamics/Download/5298.

De Pierro, A. R. (1991). Multiplicative iterative methods in computed tomography. (pp. 167–186). Springer, Berlin, Heidelberg.

del Pozo, C. F., Burns, C. J., & Hargreaves, J. K. (1993). Dual-beam EISCAT radar observations of the dynamics of the disturbed D- and E-regions in the early morning sector. *Journal of Atmospheric and Terrestrial Physics*, *55*(10).

Dessler, A. J., & Vestine, E. H. (1960). Maximum total energy of the Van Allen radiation belt. *Journal of Geophysical Research*, *65*(3), 1069–1071.

Doe, R. A., Kelly, J. D., Lummerzheim, D., Parks, G. K., Brittnacher, M. J., Germany, G. A., & Spann, J. (1997). Initial comparison of POLAR UVI and Sondrestrom IS radar estimates for auroral electron energy flux. *Geophysical Research Letters*, *24*(8), 999–1002.

Dougherty, J. P., & Farley, D. T. (1963). A theory of incoherent scattering of radio waves by a plasma: 3. Scattering in a partly ionized gas. *Journal of Geophysical Research*, *68*(19), 5473–5486.

Doupnik, J. R., Banks, P. M., Baron, M. J., Rino, C. L., & Petriceks, J. (1972). Direct measurements of plasma drift velocities at high magnetic latitudes. *Journal of Geophysical Research*, *77*(22), 4268–4271.

Ebihara, Y., & Tanaka, T. (2015). Substorm simulation: Formation of westward traveling surge. *Journal of Geophysical Research: Space Physics*, *120*(12), 10466–10484.

Ebihara, Y., & Tanaka, T. (2018). Why does substorm-associated auroral surge travel westward? *Plasma Physics and Controlled Fusion*, *60*(1), 014024.

Fang, X., Lummerzheim, D., & Jackman, C. H. (2013). Proton impact ionization and a fast calculation method. *Journal of Geophysical Research: Space Physics*, *118*(8), 5369–5378.

Farley, D. T. (1969). Incoherent Scatter Correlation Function Measurements. *Radio Science*, *4*(10), 935–953.

Foster, J. C., Erickson, P. J., Baker, D. N., Claudepierre, S. G., Kletzing, C. A., Kurth, W., Reeves, G. D., Thaller, S. A., Spence, H. E., Shprits, Y. Y., & Wygant, J. R. (2014). Prompt energization of relativistic and highly relativistic electrons during a substorm interval: Van Allen Probes observations. *Geophysical Research Letters*, *41*(1), 20–25.

Friedel, R. H. W., Korth, A., & Kremser, G. (1996). Substorm onsets observed by CRRES: Determination of energetic particle source regions. *Journal of Geophysical Research: Space Physics*, *101*(A6), 13137–13154.

Fritz, T. A. (1968). High-latitude outer-zone boundary region for $\geq$40-keV electrons during geomagnetically quiet period. *Journal of Geophysical Research*, *73*(23), 7245–7255.

Fritzenwallner, J., & Kopp, E. (1998). Model calculations of the negative ion chemistry in the mesosphere with special emphasis on the chlorine species and the formation of cluster ions. *Advances in Space Research*, *21*(6), 891–894.

Fuller-Rowell, T. J., & Evans, D. S. (1987). Height-integrated Pedersen and Hall conductivity patterns inferred from the TIROS-NOAA satellite data. *Journal of Geophysical Research*, *92*(A7), 7606.

Ganguli, G., Palmadesso, P. J., Fedder, J., & Lui, A. T. (1995). Role of Fermi acceleration in explosive enhancement of crosstail current in late substorm growth phase. *Geophysical Research Letters*, *22*(17), 2405–2408.

Gedalin, M., & Peter, W. (1992). Particle Acceleration Mechanisms in the Auroral Acceleration Region. *IEEE Transactions on Plasma Science*, *20*(6), 740–744.

Grandin, M., Kero, A., Partamies, N., McKay, D., Whiter, D., Kozlovsky, A., & Miyoshi, Y. (2017). Observation of pulsating aurora signatures in cosmic noise absorption data. *Geophysical Research Letters*, *44*(11), 5292–5300.

Grubbs, G., Michell, R., Samara, M., Hampton, D., & Jahn, J.-M. (2016). A synthesis of star calibration techniques for ground-based narrowband electron-multiplying charge-coupled device imagers used in auroral photometry. *Journal of Geophysical Research: Space Physics*, *121*(6), 5991–6002.

Guio, P., & Lilensten, J. (1999). Effect of suprathermal electrons on the intensity and Doppler frequency of electron plasma lines. *Annales Geophysicae*, *17*(7), 903–912.

Hada, T., Nishida, A., Teresawa, T., & Hones, E. W. (1981). Bi-directional electron pitch angle anisotropy in the plasma sheet. *Journal of Geophysical Research*, *86*(A13), 11211.

Han, D., Chen, X., Liu, J., Qiu, Q., Keika, K., Hu, Z., Liu, J., Hu, H., & Yang, H. (2015). An extensive survey of dayside diffuse aurora based on optical observations at Yellow River Station. *Journal of Geophysical Research: Space Physics*, *120*(9), 7447–7465.

Hansen, P. C. (2005). The L-curve and its use in the numerical treatment of inverse problems. Tech. rep., Technical University of Denmark. https://www.sintef.no/globalassets/project/evitameeting/2005/lcurve.pdf.

Hardy, D. A., Gussenhoven, M. S., Raistrick, R., & McNeil, W. J. (1987). Statistical and functional representations of the pattern of auroral energy flux, number flux, and conductivity. *Journal of Geophysical Research*, *92*(A11), 12275.

Hargreaves, J. K. (1969). Auroral Absorption of HF Radio Waves in the Ionosphere a Review of Results from the First Decade of Riometry. *Proceedings of the IEEE*, *57*(8), 1348–1373.

Hartz, T. R., & Brice, N. M. (1967). The general pattern of auroral particle precipitation. *Planetary and Space Science*, *15*(2), 301–329.

Heinselman, C. J., & Nicolls, M. J. (2008). A Bayesian approach to electric field and E -region neutral wind estimation with the Poker Flat Advanced Modular Incoherent Scatter Radar . *Radio Science*, *43*(5), n/a–n/a.

Henderson, M. G. (2009). Observational evidence for an inside-out substorm onset scenario. *Annales Geophysicae*, *27*(5), 2129–2140.

Herrera, D., Maget, V. F., & Sicard-Piet, A. (2016). Characterizing magnetopause shadowing effects in the outer electron radiation belt during geomagnetic storms. *Journal of Geophysical Research: Space Physics*, *121*(10), 9517–9530.

Hill, T. W., & Rassbach, M. E. (1975). Interplanetary magnetic field direction and the configuration of the day side magnetosphere. *Journal of Geophysical Research*, *80*(1), 1–6.

Holt, C., Landmark, B., & Lied, F. (1961). Analysis of riometer observations obtained during polar radio blackouts. *Journal of Atmospheric and Terrestrial Physics*, *23*(C), 229–243.

Honary, F., Marple, S. R., Barratt, K., Chapman, P., Grill, M., & Nielsen, E. (2011). Invited Article: Digital beam-forming imaging riometer systems. *Review of Scientific Instruments*, *82*(3), 031301.

Horne, R. B., & Thorne, R. M. (1998). Potential waves for relativistic electron scattering and stochastic acceleration during magnetic storms. *Geophysical Research Letters*, *25*(15), 3011–3014.

Horne, R. B., Thorne, R. M., Glauert, S. A., Albert, J. M., Meredith, N. P., & Anderson, R. R. (2005). Timescale for radiation belt electron acceleration by whistler mode chorus waves. *Journal of Geophysical Research: Space Physics*, *110*(A3).

Hosokawa, K., Kullen, A., Milan, S., Reidy, J., Zou, Y., Frey, H. U., Maggiolo, R., & Fear, R. (2020). Aurora in the Polar Cap: A Review. *Space Science Reviews*, *216*(1), 1–44.

Hosokawa, K., & Ogawa, Y. (2010). Pedersen current carried by electrons in auroral D-region. *Geophysical Research Letters*, *37*(18), L18103–L18108.

Hunsucker, R. D., & Bates, H. F. (1969). Survey of Polar and Auroral Region Effects on HF Propagation. *Radio Science*, *4*(4), 347–365.

Hysell, D. L. (2007). Inverting ionospheric radio occultation measurements using maximum entropy. *Radio Science*, *42*(4), RS4022–RS4030.

Imhof, W., Reagan, J., & Gaines, E. (1979). Studies of the sharply defined L dependent energy threshold for isotropy at the midnight trapping boundary. *Journal of Geophysical Research*, *84*(A11), 6371.

Imhof, W. L., Reagan, J. B., & Gaines, E. E. (1978). The energy selective precipitation of inner zone electrons. *Journal of Geophysical Research*, *83*(A9), 4245.

Jaynes, E. T. (1957). Information theory and statistical mechanics. *Physical Review*, *106*(4), 620–630.

Junginger, H., Geiger, G., Haerendel, G., Melzner, F., Amata, E., & Higel, B. (1984). A statistical study of dayside magnetospheric electric field fluctuations with periods between 150 and 600 s. *Journal of Geophysical Research*, *89*(A7), 5495.

Kaeppler, S. R., Sanchez, E., Varney, R. H., Irvin, R. J., Marshall, R. A., Bortnik, J., Reimer, A. S., & Reyes, P. M. (2019). Incoherent scatter radar observations of 10-100 keV precipitation: Review and outlook. In *The Dynamic Loss of Earth's*

Radiation Belts: From Loss in the Magnetosphere to Particle Precipitation in the Atmosphere, (pp. 145–197). Elsevier.

Kaufmann, R. L., Larson, D. J., Beidl, P., & Lu, C. (1993). Mapping and energization in the magnetotail: 1. Magnetospheric boundaries. *Journal of Geophysical Research*, *98*(A6), 9307.

Kelley, M. C. (2009). *The Earth's Ionosphere: Plasma Physics & Electrodynamics*, vol. 96. Ithaca, NY: Academic Press, 2 ed.

Kepko, L., McPherron, R. L., Amm, O., Apatenkov, S., Baumjohann, W., Birn, J., Nakamura, R., Lester, M., Sergeev, V., & Pulkkinen, T. I. (2015). Substorm Current Wedge Revisited. *Space Science Review*, *190*, 146.

Kero, A., Vierinen, J., McKay-Bukowski, D., Enell, C.-F., Sinor, M., Roininen, L., & Ogawa, Y. (2014). Ionospheric electron density profiles inverted from a spectral riometer measurement. *Geophysical Research Letters*, *41*(15), 5370–5375.

Kesavan, H. K. (2008). Jaynes' Maximum Entropy Principle. In *Encyclopedia of Optimization*, (pp. 1779–1782). Springer US.

Khazanov, G. V., Robinson, R. M., Zesta, E., Sibeck, D. G., Chu, M., & Grubbs, G. A. (2018). Impact of Precipitating Electrons and Magnetosphere-Ionosphere Coupling Processes on Ionospheric Conductance. *Space Weather*, *16*(7), 829–837.

Kirkwood, S., & Eliasson, L. (1990). Energetic particle precipitation in the substorm growth phase measured by EISCAT and Viking. *Journal of Geophysical Research*, *95*(A5), 6025.

Kirkwood, S., Opgenoorth, H., & Murphree, J. (1988). Ionospheric conductivities, electric fields and currents associated with auroral substorms measured by the EISCAT radar. *Planetary and Space Science*, *36*(12), 1359–1380.

Klaus, A., Bauer, J., Karner, K., Elbischger, P., Perko, R., & Bischof, H. (2004). Camera calibration from a single night sky image. In *Proceedings of the IEEE Computer Society Conference on Computer Vision and Pattern Recognition*, vol. 1.

Kosch, M. J., Honary, F., del Pozo, C. F., Marple, S. R., & Hagfors, T. (2001a). High-resolution maps of the characteristic energy of precipitating auroral particles. *Journal of Geophysical Research: Space Physics*, *106*(A12), 28925–28937.

Kosch, M. J., Scourfield, M. W., & Amm, O. (2001b). The importance of conductivity grandients in ground-based field-aligned current studies. *Advances in Space Research*, *27*(6-7), 1277–1282.

Kurita, S., Kadokura, A., Miyoshi, Y., Morioka, A., Sato, Y., & Misawa, H. (2015). Relativistic electron precipitations in association with diffuse aurora: Conjugate observation of SAMPEX and the all-sky TV camera at Syowa Station. *Geophysical Research Letters*, *42*(12), 4702–4708.

Lam, M. M., Horne, R. B., Meredith, N. P., Glauert, S. A., Moffat-Griffin, T., & Green, J. C. (2010). Origin of energetic electron precipitation >30 keV into the atmosphere. *Journal of Geophysical Research A: Space Physics*, *115*(A4).

Lathuillere, C., Wickwar, V. B., & Kofman, W. (1983). Incoherent scatter measurements of ion-neutral collision frequencies and temperatures in the lower thermosphere of the auroral region. *Journal of Geophysical Research*, *88*(A12), 10137.

Lejosne, S., & Kollmann, P. (2020). Radiation Belt Radial Diffusion at Earth and Beyond. *Space Science Reviews*, *216*(1), 1–78.

Lennartsson, W. (1987). Plasma sheet ion composition at various levels of geomagnetic and solar activity. *Physica Scripta*, *36*(2), 367–371.

Li, J. (1998). Notes on Adiabatic Invariants. Tech. rep., MIT, Boston. http://li.mit.edu/A/Papers/98/invariant.pdf.

Li, W., Bortnik, J., Nishimura, Y., Thorne, R. M., & Angelopoulos, V. (2012). The Origin of Pulsating Aurora: Modulated Whistler Mode Chorus Waves. In *Auroral Phenomenology and Magnetospheric Processes: Earth and Other Planets*, (pp. 379–388). Wiley Blackwell. http://www.agu.org/books/gm/v197/2011GM001164/2011GM001164.shtml.

Li, Z., Hudson, M., Patel, M., Wiltberger, M., Boyd, A., & Turner, D. (2017). ULF wave analysis and radial diffusion calculation using a global MHD model for the 17 March 2013 and 2015 storms. *Journal of Geophysical Research: Space Physics*, *122*(7), 7353–7363.

Lind, F. D., Grydeland, T., Erickson, P. J., Holt, J. M., & Sahr, J. D. (2001). Advanced Techniques for Incoherent Scatter Radar. Tech. rep. https://www.researchgate.net/publication/228970604{_}Advanced{_}Techniques{_}for{_}Incoherent{_}Scatter{_}Radar.

Lorentzen, K. R., McCarthy, M. P., Parks, G. K., Foat, J. E., Millan, R. M., Smith, D. M., Lin, R. P., & Treilhou, J. P. (2000). Precipitation of relativistic electrons by interaction with electromagnetic ion cyclotron waves. *Journal of Geophysical Research: Space Physics*, *105*(A3), 5381–5389.

Lu, G. (2016). Energetic and Dynamic Coupling of the Magnetosphere-Ionosphere-Thermosphere System. (pp. 61–77). American Geophysical Union (AGU). http://doi.wiley.com/10.1002/9781119066880.ch5.

Lui, A. T. Y. (2011). Revisiting Time History of Events and Macroscale Interactions during Substorms (THEMIS) substorm events implying magnetic reconnection as the substorm trigger. *Journal of Geophysical Research: Space Physics*, *116*(A3).

Lui, A. T. Y., Baumjohann, W., & Rostoker, G. (2000). Substorm expansion onset mechanism debated. *Eos, Transactions American Geophysical Union*, *81*(7), 70.

Lui, A. T. Y., Venkatesan, D., Anger, C. D., Akasofu, S. I., Heikkila, W. J., Winningham, J. D., & Burrows, J. R. (1977). Simultaneous observations of particle precipitations and auroral emissions by the Isis 2 satellite in the 19-24 MLT sector. *Journal of Geophysical Research*, *82*(16), 2210–2226.

Lyons, L. (1997). Magnetospheric Processes Leading to Precipitation. *Space Science Reviews*, *80*(1/2), 109–132.

Lyons, L. R. (1992). Formation of auroral arcs via magnetosphere-ionosphere coupling. *Reviews of Geophysics*, *30*(2), 93.

Lyons, L. R., & Fennell, J. F. (1986). Characteristics of auroral electron precipitation on the morningside. *Journal of Geophysical Research*, *91*(A10), 11225.

Maeda, K., & Kato, S. (1966). Electrodynamics of the ionosphere. *Space Science Reviews*, *5*(1), 57–79.

Matsui, H. (2003). Electric field measurements in the inner magnetosphere by Cluster EDI. *Journal of Geophysical Research*, *108*(A9), 1352.

McCoy, J. E. (1969). High-latitude ionization spikes observed by the POGO Ion, Chamber Experiment. *Journal of Geophysical Research*, *74*(9), 2309–2318.

McDiarmid, I. B., Burrows, J. R., & Budzinski, E. E. (1975). Average characteristics of magnetospheric electrons (150 eV to 200 keV) at 1400 km. *Journal of Geophysical Research*, *80*(1), 73–79.

McElroy, M. B. (2012). Ionosphere and magnetosphere. https://www.britannica.com/science/ionosphere-and-magnetosphere (Accessed:2020-06-23).

McKay, D., Partamies, N., & Vierinen, J. (2018). Pulsating aurora and cosmic noise absorption associated with growth-phase arcs. *Annales Geophysicae*, *36*(1), 59–69.

Mende, S. B., Eather, R. H., Rees, M. H., Vondrak, R. R., & Robinson, R. M. (1984). Optical mapping of ionospheric conductance. *Journal of Geophysical Research*, *89*(A3), 1755.

Mende, S. B., Harris, S. E., Frey, H. U., Angelopoulos, V., Russell, C. T., Donovan, E., Jackel, B., Greffen, M., & Peticolas, L. M. (2008). The THEMIS array of ground-based observatories for the study of auroral substorms. *Space Science Reviews*, *141*(1-4), 357–387.

Meredith, L. H., Gottlieb, M. B., & Van Allen, J. A. (1955). Direct detection of soft radiation above 50 kilometers in the auroral zone. *Physical Review*, *97*(1), 201–205.

Meredith, N. P., Horne, R. B., Sicard-Piet, A., Boscher, D., Yearby, K. H., Li, W., & Thorne, R. M. (2012). Global model of lower band and upper band chorus from multiple satellite observations. *Journal of Geophysical Research: Space Physics*, *117*(A10), n/a–n/a.

Meredith, N. P., Horne, R. B., Thorne, R. M., Summers, D., & Anderson, R. R. (2004). Substorm dependence of plasmaspheric hiss. *Journal of Geophysical Research: Space Physics*, *109*(A6).

Millan, R. M., & Baker, D. N. (2012). Acceleration of particles to high energies in earth's radiation belts. *Space Science Reviews*, *173*(1-4), 103–131.

Milovanov, A. V., & Zelenyi, L. M. (2001). Strange Fermi processes and power-law nonthermal tails from a self-consistent fractional kinetic equation. *Physical Review E - Statistical Physics, Plasmas, Fluids, and Related Interdisciplinary Topics*, *64*(5), 4.

Minnie, J., Matthaeus, W. H., Bieber, J. W., Ruffolo, D., & Burger, R. A. (2009). When do particles follow field lines? *Journal of Geophysical Research: Space Physics*, *114*(A1), n/a–n/a.

Mironova, I. A., Aplin, K. L., Arnold, F., Bazilevskaya, G. A., Harrison, R. G., Krivolutsky, A. A., Nicoll, K. A., Rozanov, E. V., Turunen, E., & Usoskin, I. G. (2015). Energetic Particle Influence on the Earth's Atmosphere. *Space Science Reviews*, *194*(1-4), 1–96.

Mitra, A. P., & Shain, C. A. (1953). The measurement of ionospheric absorption using observations of 18·3 Mc/s cosmic radio noise. *Journal of Atmospheric and Terrestrial Physics*, *4*(4-5), 204–218.

Miyoshi, Y., Oyama, S., Saito, S., Kurita, S., Fujiwara, H., Kataoka, R., Ebihara, Y., Kletzing, C., Reeves, G., Santolik, O., Clilverd, M., Rodger, C. J., Turunen, E., & Tsuchiya, F. (2015). Energetic electron precipitation associated with pulsating aurora: EISCAT and Van Allen Probe observations. *Journal of Geophysical Research: Space Physics*, *120*(4), 2754–2766.

Mohammad-Djafari, A. (1993). Maximum Entropy and Linear Inverse Problems. A Short Review. In *Maximum Entropy and Bayesian Methods*, (pp. 253–264). Springer Netherlands.

Murayama, T., & Hakamada, K. (1975). Effects of solar wind parameters on the development of magnetospheric substorms. *Planetary and Space Science*, *23*(1), 75–91.

Murphy, K. R., Mann, I. R., Rae, I. J., Walsh, A. P., & Frey, H. U. (2014). Inner magnetospheric onset preceding reconnection and tail dynamics during substorms: Can substorms initiate in two different regions? *Journal of Geophysical Research: Space Physics*, *119*(12), 9684–9701.

Newell, P. T., Feldstein, Y. I., Galperin, Y. I., & Meng, C.-I. (1996). Morphology of nightside precipitation. *Journal of Geophysical Research: Space Physics*, *101*(A5), 10737–10748.

Newell, P. T., & Gjerloev, J. W. (2011). Evaluation of SuperMAG auroral electrojet indices as indicators of substorms and auroral power. *Journal of Geophysical Research: Space Physics*, *116*(12).

Nicolls, M. J. (2015). Space Debris Measurements using the Advanced Modular Incoherent Scatter Radar. Tech. rep. https://amostech.com/TechnicalPapers/2015/Poster/Nicolls.pdf.

Nicolls, M. J., Heinselman, C. J., Hope, E. A., Ranjan, S., Kelley, M. C., & Kelly, J. D. (2007). Imaging of Polar Mesosphere Summer Echoes with the 450 MHz Poker Flat Advanced Modular Incoherent Scatter Radar. *Geophysical Research Letters*, *34*(20), L20102.

Nishimura, Y., Bortnik, J., Li, W., Thorne, R. M., Lyons, L. R., Angelopoulos, V., Mende, S. B., Bonnell, J. W., Le Contel, O., Cully, C., Ergun, R., & Auster, U. (2010). Identifying the driver of pulsating aurora. *Science*, *330*(6000), 81–84.

Nishimura, Y., Bortnik, J., Li, W., Thorne, R. M., Ni, B., Lyons, L. R., Angelopoulos, V., Ebihara, Y., Bonnell, J. W., Le Contel, O., & Auster, U. (2013). Structures of dayside whistler-mode waves deduced from conjugate diffuse aurora. *Journal of Geophysical Research: Space Physics*, *118*(2), 664–673.

Nishimura, Y., Lessard, M. R., Katoh, Y., Miyoshi, Y., Grono, E., Partamies, N., Sivadas, N., Hosokawa, K., Fukizawa, M., Samara, M., Michell, R. G., Kataoka, R., Sakanoi, T., Whiter, D. K., ichiro Oyama, S., Ogawa, Y., & Kurita, S. (2020). Diffuse and Pulsating Aurora. *Space Science Reviews*, *216*(1), 1–38.

Northrop, T. G. (1963). *The Adiabatic Motion of Charged Particles*. Interscience tracts on physics and astronomy, 21. Interscience Publishers. https://books.google.com/books?id=pPNQAAAAMAAJ.

Nygrén, T., Jalonen, L., & Huuskonen, A. (1987). A new method of measuring the ion-neutral collision frequency using incoherent scatter radar. *Planetary and Space Science*, *35*(3), 337–343.

Olsson, A., Persson, M. A. L., Opgenoorth, H. J., & Kirkwood, S. (1996). Particle precipitation in auroral breakups and westward traveling surges. *Journal of Geophysical Research: Space Physics*, *101*(A11), 24661–24673.

Opgenoorth, H. J., Pellinen, R. J., Baumjohann, W., Nielsen, E., Marklund, G., & Eliasson, L. (1983). Three-dimensional current flow and particle precipitation in a westward travelling surge (observed during the Barium-Geos Rocket Experiment). *Journal of Geophysical Research*, *88*(A4), 3138.

Osepian, A., Kirkwood, S., & Smirnova, N. (1996). Energetic electron precipitation during auroral events observed by incoherent scatter radar. *Advances in Space Research*, *17*(11), 149–155.

Ostgaard, N. (1999). The dynamics of energetic electron precipitation during substorms: Utilization of the remote sensing technique of X rays. *AGU Monograph*.

Otto, A. (1996). Mapping of magnetospheric boundaries. *Advances in Space Research*, *18*(8), 187–196.

Oyama, S., Kero, A., Rodger, C. J., Clilverd, M. A., Miyoshi, Y., Partamies, N., Turunen, E., Raita, T., Verronen, P. T., & Saito, S. (2017). Energetic electron precipitation and auroral morphology at the substorm recovery phase. *Journal of Geophysical Research: Space Physics*, *122*(6), 6508–6527.

Parham, J. B., Beukelaers, V., Leung, L., Mason, J., Walsh, B., & Semeter, J. (2019). Leveraging Commercial Cubesat Constellations for Auroral Science: A Case Study. *Journal of Geophysical Research: Space Physics*, *124*(5), 3487–3500.

Parks, G. K., McCarthy, M., Fitzenreiter, R. J., Etcheto, J., Anderson, K. A., Anderson, R. R., Eastman, T. E., Frank, L. A., Gurnett, D. A., Huang, C., Lin, R. P., Lui, A. T., Ogilvie, K. W., Pedersen, A., & Reme, H. (1984). PARTICLE AND FIELD CHARACTERISTICS OF THE HIGH-LATITUDE PLASMA SHEET BOUNDARY LAYER. *Journal of Geophysical Research*, *89*(A10), 8885–8906.

Partamies, N., Weygand, J. M., & Juusola, L. (2017). Statistical study of auroral omega bands. *Annales Geophysicae*, *35*(5), 1069–1083.

Parthasarathy, R., & Berkey, F. T. (1965). Auroral zone studies of sudden-onset radio-wave absorption events using multiple-station and multiple-frequency data. *Journal of Geophysical Research*, *70*(1), 89–98.

Paschmann, G., Haaland, S., & Treumann, R. (2003). Introduction. In *Auroral Plasma Physics*, (pp. 1–19). Springer Netherlands.

Pearl, J. (2009). Causal inference in statistics: An overview. *Statistics Surveys*, *3*, 96–146.

Pollock, C. J., Son-Brandt, C. P., Burch, J. L., Henderson, M. G., Jahn, J. M., McComas, D. J., Mende, S. B., Mitchell, D. G., Reeves, G. D., Scime, E. E., Skoug, R. M., Thomsen, M., & Valek, P. (2003). The role and contributions of energetic neutral atom (ENA) imaging in magnetospheric substorm research. *Space Science Reviews*, *109*(1-4), 155–182.

Pytte, T., Trefall, H., Kremser, G., Jalonen, L., & Riedler, W. (1976). On the morphology of energetic ($\geq$30keV) electron precipitation during the growth phase of magnetospheric substorms. *Journal of Atmospheric and Terrestrial Physics*, *38*(7), 739–755.

Pytte, T., & West, H. I. (1978). Ground-satellite correlations during presubstorm magnetic field configuration changes and plasma sheet thinning in the near-Earth magnetotail. *Journal of Geophysical Research*, *83*(A8), 3791.

Raeder, J., Berchem, J., & Ashour-Abdalla, M. (1996). The importance of small scale processes in global MHD simulations: Some numerical experiments, in The Physics of Space Plasmas . Tech. rep., MIT Cent. for Theoret. Geo/Cosmo Plasma Phys, Cambridge, Mass. https://pdfs.semanticscholar.org/1299/ac8e2ffa060eb0272b34bac673b7f0854174.pdf.

Raeder, J., McPherron, R. L., Frank, L. A., Kokubun, S., Lu, G., Mukai, T., Paterson, W. R., Sigwarth, J. B., Singer, H. J., & Slavin, J. A. (2001). Global simulation of the Geospace Environment Modeling substorm challenge event. *Journal of Geophysical Research: Space Physics*, *106*(A1), 381–395.

Ratcliffe, J. A. (1972). *An Introduction to Ionosphere and Magnetosphere*. CUP Archive.

Rees, M. (1982). On the interaction of auroral protons with the earth's atmosphere. *Planetary and Space Science*, *30*(5), 463–472.

Rees, M. H. (1969). Auroral electrons. *Space Science Reviews*, *10*(3), 413–441.

Rees, M. H. (1989). *Physics and Chemistry of the Upper Atmosphere*. Cambridge Atmospheric and Space Science Series. Cambridge University Press.

Rees, M. H., & Luckey, D. (1974). Auroral electron energy derived from ratio of spectroscopic emissions 1. Model computations. *Journal of Geophysical Research*, *79*(34), 5181–5186.

Reid, G. C. (1964). Physical processes in the D region of the ionosphere. *Reviews of Geophysics*, *2*(2), 311.

Reiff, P. H., Collin, H. L., Craven, J. D., Burch, J. L., Winningham, J. D., Shelley, E. G., Frank, L. A., & Friedman, M. A. (1988). Determination of auroral electrostatic potentials using high- and low-altitude particle distributions. *Journal of Geophysical Research: Space Physics*, *93*(A7), 7441–7465.

Ridley, A. J., Gombosi, T. I., & DeZeeuw, D. L. (2004). Ionospheric control of the magnetosphere: conductance. *Annales Geophysicae*, *22*(2), 567–584.

Robinson, R. M., Vondrak, R. R., Miller, K., Dabbs, T., & Hardy, D. (1987). On calculating ionospheric conductances from the flux and energy of precipitating electrons. *Journal of Geophysical Research*, *92*(A3), 2565.

Rodger, C. J., Clilverd, M. A., Kavanagh, A. J., Watt, C. E. J., Verronen, P. T., & Raita, T. (2012). Contrasting the responses of three different ground-based instruments to energetic electron precipitation. *Radio Science*, *47*(2), n/a–n/a.

Roederer, J., & Zhang, H. (2014). Drift Shells and the Second and Third Adiabatic Invariants. In *Dynamics of Magnetically Trapped Particles*, (pp. 57–88). Springer.

Rossberg, L. (1976). Prebay electron precipitation as seen by balloons and satellites. *Journal of Geophysical Research*, *81*(19), 3437–3440.

Rossolenko, S., Antonova, E., Yermolaev, Y., Kirpichev, I., Borodkova, N., & Budnik, E. (2008). Formation and characteristics of low latitude boundary layer. *Advances in Space Research*, *41*(10), 1545–1550.

Roux, A., LeăContel, O., Coillot, C., Bouabdellah, A., De La Porte, B., Alison, D., Ruocco, S., & Vassal, M. C. (2008). The search coil magnetometer for THEMIS. *Space Science Reviews*, *141*(1-4), 265–275.

Sadeghi, S., & Emami, M. R. (2018). Electric potential structures of auroral acceleration region border from multi-spacecraft Cluster data. *Advances in Space Research*, *61*(8), 2050–2056.

Saito, Y., Machida, S., Hirahara, M., Mukai, T., & Miyaoka, H. (1992). Rocket observation of electron fluxes over a pulsating aurora. *Planetary and Space Science*, *40*(8), 1043–1054.

Samara, M., Michell, R. G., Asamura, K., Hirahara, M., Hampton, D. L., & Stenbaek-Nielsen, H. C. (2010). Ground-based observations of diffuse auroral structures in conjunction with Reimei measurements. *Annales Geophysicae*, *28*(3), 873–881.

Schunk, R., & Nagy, A. (2009). *Ionospheres*. Cambridge: Cambridge University Press.

Seaton, M. (1954). Excitation processes in the aurora and airglow 1. Absolute intensities, relative ultra-violet intensities and electron densities in high latitude aurorae. *Journal of Atmospheric and Terrestrial Physics*, *4*(6), 285–294.

Semeter, J., Butler, T. W., Zettergren, M., Heinselman, C. J., & Nicolls, M. J. (2010). Composite imaging of auroral forms and convective flows during a substorm cycle. *Journal of Geophysical Research: Space Physics*, *115*(8), n/a–n/a.

Semeter, J., & Kamalabadi, F. (2005). Determination of primary electron spectra from incoherent scatter radar measurements of the auroral e region. *Radio Science*, *40*(2), 1–17.

Semeter, J., & Zettergren, M. (2014). Model-Based Inversion of Auroral Processes. In *Modeling the Ionosphere-Thermosphere System*, vol. 9780875904917, (pp. 309–321). Wiley Blackwell. http://doi.wiley.com/10.1002/9781118704417.ch25.

Seppälä, A., Clilverd, M. A., & Rodger, C. J. (2007). NO _x enhancements in the middle atmosphere during 20032004 polar winter: Relative significance of solar proton events and the aurora as a source. *Journal of Geophysical Research*, *112*(D23), D23303.

Sergeev, V. A., Apatenkov, S. V., Angelopoulos, V., McFadden, J. P., Larson, D., Bonnell, J. W., Kuznetsova, M., Partamies, N., & Honary, F. (2008). Simultaneous THEMIS observations in the near-tail portion of the inner and outer plasma sheet flux tubes at substorm onset. *Journal of Geophysical Research*, *113*, A00C02.

Sergeev, V. A., Liou, K., Newell, P. T., Ohtani, S.-I., Hairston, M. R., & Rich, F. (2004). Auroral streamers: characteristics of associated precipitation,convection and field-aligned currents. *Annales Geophysicae*, *22*(2), 537–548.

Sergeev, V. A., Nishimura, Y., Kubyshkina, M., Angelopoulos, V., Nakamura, R., & Singer, H. (2012). Magnetospheric location of the equatorward prebreakup arc. *Journal of Geophysical Research: Space Physics*, *117*(A1).

Sergeev, V. A., Pulkkinen, T. I., & Pellinen, R. J. (1996). Coupled-mode scenario for the magnetospheric dynamics. *Journal of Geophysical Research: Space Physics*, *101*(A6), 13047–13065.

Sergeev, V. A., Sazhina, E., Tsyganenko, N., Lundblad, J., & Søraas, F. (1983). Pitch-angle scattering of energetic protons in the magnetotail current sheet as the dominant source of their isotropic precipitation into the nightside ionosphere. *Planetary and Space Science*, *31*(10), 1147–1155.

Sergienko, T., Sandahl, I., Gustavsson, B., Andersson, L., Brändström, U., & Steen, Å. (2008). A study of fine structure of diffuse aurora with ALIS-FAST measurements. *Annales Geophysicae*, *26*(11), 3185–3195.

Sergienko, T. I., & Ivanov, V. E. (1993). A new approach to calculate the excitation of atmospheric gases by auroral electron impact. *Annales Geophysicae*, *11*(8), 717–727.

Shelley, E. G. (1995). The auroral acceleration region: The world of beams, conies, cavitons, and other plasma exotica. *Reviews of Geophysics*, *33*(1 S), 709.

Shprits, Y. Y. (2009). Potential waves for pitch-angle scattering of near-equatorially mirroring energetic electrons due to the violation of the second adiabatic invariant. *Geophysical Research Letters*, *36*(12).

Shprits, Y. Y., Subbotin, D. A., Meredith, N. P., & Elkington, S. R. (2008). Review of modeling of losses and sources of relativistic electrons in the outer radiation belt II: Local acceleration and loss. *Journal of Atmospheric and Solar-Terrestrial Physics*, *70*(14), 1694–1713.

Shpynev, B. G. (2017). Refraction and Faraday rotation in the incoherent scatter radar technique. *Radio Science*, *52*(9), 1067–1080.

Simon Wedlund, C., Lamy, H., Gustavsson, B., Sergienko, T., & Brändström, U. (2013). Estimating energy spectra of electron precipitation above auroral arcs from ground-based observations with radar and optics. *Journal of Geophysical Research: Space Physics*, *118*(6), 3672–3691.

Sinnhuber, M., Nieder, H., & Wieters, N. (2012). Energetic Particle Precipitation and the Chemistry of the Mesosphere/Lower Thermosphere. *Surveys in Geophysics*, *33*(6), 1281–1334.

Siscoe, G. L. (2002). Hill model of transpolar potential saturation: Comparisons with MHD simulations. *Journal of Geophysical Research*, *107*(A6), 1075.

Sivadas, N., Semeter, J., Nishimura, Y., & Kero, A. (2017). Simultaneous Measurements of Substorm-Related Electron Energization in the Ionosphere and the Plasma Sheet. *Journal of Geophysical Research: Space Physics*, *122*(10), 10,528–10,547.

Sivadas, N., Semeter, J., Nishimura, Y., & Mrak, S. (2019). Optical Signatures of the Outer Radiation Belt Boundary. *Geophysical Research Letters*, *46*(15), 8588–8596.

Solomon, S. C. (2017). Global modeling of thermospheric airglow in the far ultraviolet. *Journal of Geophysical Research: Space Physics*, *122*(7), 7834–7848.

Spanswick, E., Donovan, E., Kepko, L., & Angelopoulos, V. (2017). The Magnetospheric Source Region of the Bright Proton Aurora. *Geophysical Research Letters*, *44*(20), 10,094–10,099.

Spjeldvik, W. N., & Thorne, R. M. (1975). The cause of storm after effects in the middle latitude D-region. *Journal of Atmospheric and Terrestrial Physics*, *37*(5), 777–795.

Stenbaek-Nielsen, H. C., Hallinan, T. J., Osborne, D. L., Kimball, J., Chaston, C., McFadden, J., Delory, G., Temerin, M., & Carlson, C. W. (1998). Aircraft observations conjugate to FAST: Auroral are thicknesses. *Geophysical Research Letters*, *25*(12), 2073–2076.

Sulzer, M. (2015). RADAR | Incoherent Scatter Radar. *Encyclopedia of Atmospheric Sciences*, (pp. 422–428).

Swift, D. W., & Gorney, D. J. (1989). Production of very energetic electrons in discrete aurora. *Journal of Geophysical Research*, *94*(A3), 2696.

Tanskanen, E. I. (2009). A comprehensive high-throughput analysis of substorms observed by IMAGE magnetometer network: Years 1993-2003 examined. *Journal of Geophysical Research: Space Physics*, *114*(A5), n/a–n/a.

Tepley, C. A., & Mathews, J. D. (1985). An incoherent scatter radar measurement of the average ion mass and temperature of a nighttime sporadic layer. *Journal of Geophysical Research*, *90*(A4), 3517.

Thayer, J. P. (2000). High-latitude currents and their energy exchange with the ionosphere-thermosphere system. *Journal of Geophysical Research: Space Physics*, *105*(A10), 23015–23024.

Thorne, R. M., Ni, B., Tao, X., Horne, R. B., & Meredith, N. P. (2010). Scattering by chorus waves as the dominant cause of diffuse auroral precipitation. *Nature*, *467*(7318), 943–946.

Tong, D. (2005). Cambridge Lecture Notes on Classical Dynamics. Tech. rep., University of Cambridge, Cambridge. http://www.damtp.cam.ac.uk/user/tong/dynamics.html.

Tsyganenko, N. A. (1995). Modeling the Earth's magnetospheric magnetic field confined within a realistic magnetopause. *Journal of Geophysical Research*, *100*(A4), 5599.

Turunen, E., Kero, A., Verronen, P. T., Miyoshi, Y., Oyama, S.-I., & Saito, S. (2016). Mesospheric ozone destruction by high-energy electron precipitation associated with pulsating aurora. *Journal of Geophysical Research: Atmospheres*, *121*(19), 11,852–11,861.

Turunen, E., Matveinen, H., Tolvanen, J., & Ranta, H. (1996). D-region ion chemistry model. In R. W. Schunk (Ed.) *STEP Handbook of Ionospheric Models*, (pp. 1–25). Boulder,CO: SCHOSTEP Secretariat.

Vanhamäki, H., Aikio, A., Nygrén, T., Yoshikawa, A., Ieda, A., & Fujii, R. (2015). Altitude dependent polarization electric field in the ionospheric E-region. In *26th IUGG General Assembly, Session A25*. Prague. http://www.czech-in.org/cmdownload/IUGG2015/presentations/IUGG-2516.pdf.

Vasyliunas, V. M. (1972). Magnetospheric Plasma. In *The Magnetosphere*, (pp. 192–211). Dordrecht: Springer Netherlands. http://link.springer.com/10.1007/978-94-010-3130-1{_}6.

Verronen, P. T., Andersson, M. E., Kero, A., Enell, C. F., Wissing, J. M., Talaat, E. R., Kauristie, K., Palmroth, M., Sarris, T. E., & Armandillo, E. (2015). Contribution of proton and electron precipitation to the observed electron concentration in October-November 2003 and September 2005. *Annales Geophysicae*, *33*(3), 381–394.

Verronen, P. T., Seppälä, A., Clilverd, M. A., Rodger, C. J., Kyrölä, E., Enell, C. F., Ulich, T., & Turunen, E. (2005). Diurnal variation of ozone depletion during the October-November 2003 solar proton events. *Journal of Geophysical Research: Space Physics*, *110*(A9).

Vickrey, J. F., Vondrak, R. R., & Matthews, S. J. (1982). Energy deposition by precipitating particles and Joule dissipation in the auroral ionosphere. *Journal of Geophysical Research: Space Physics*, *87*(A7), 5184–5196.

Virtanen, I. I., Gustavsson, B., Aikio, A., Kero, A., Asamura, K., & Ogawa, Y. (2018). Electron Energy Spectrum and Auroral Power Estimation From Incoherent Scatter Radar Measurements. *Journal of Geophysical Research: Space Physics*, *123*(8), 6865–6887.

Vondrak, R., Harris, S., & Mende, S. (1983). Ground-based observations of subauroral energetic-electron arcs. *Geophysical Research Letters*, *10*(7), 557–560.

Vondrak, R. R., & Baron, M. J. (1977). A method of obtaining the energy distribution of auroral electrons from incoherent scatter radar measurements. In *Radar Probing of the Auroral Plasma*, (pp. 315–330). Norway: Tromsoe Univ. https://inis.iaea.org/search/search.aspx?orig{_}q=RN:11499528.

Walt, M. (1971). Radial diffusion of trapped particles and some of its consequences. *Reviews of Geophysics*, *9*(1), 11.

Wang, C. P., Zaharia, S. G., Lyons, L. R., & Angelopoulos, V. (2013). Spatial distributions of ion pitch angle anisotropy in the near-Earth magnetosphere and tail plasma sheet. *Journal of Geophysical Research: Space Physics*, *118*(1), 244–255.

Watkins, N. W., Chapman, S. C., Gough, M., & Forsberg, P. (2013). In-Situ Spacecraft Particle Autocorrelation and Cross-Correlation- Theory and Practice. In *Geophysical Monograph Series*, vol. 102, (pp. 319–324). Blackwell Publishing Ltd. http://doi.wiley.com/10.1029/GM102p0319.

Whalen, B. A., Miller, J. R., & McDiarmid, I. B. (1971). Sounding rocket observations of particle precipitation in a polar-cap electron aurora. *Journal of Geophysical Research*, *76*(28), 6847–6855.

Wisemberg, J., & Kockarts, G. (1980). Negative ion chemistry in the terrestrial D region and signal flow graph theory . *Journal of Geophysical Research: Space Physics*, *85*(A9), 4642–4652.

Yu, Y., Jordanova, V. K., McGranaghan, R. M., & Solomon, S. C. (2018). Self-consistent modeling of electron precipitation and responses in the ionosphere: application to low-altitude energization during substorms. *Geophysical Research Letters*.

Zettergren, M., Semeter, J., Blelly, P. L., Sivjee, G., Azeem, I., Mende, S., Gleisner, H., Diaz, M., & Witasse, O. (2008). Optical estimation of auroral ion upflow: 2. A case study. *Journal of Geophysical Research: Space Physics*, *113*(7).

CURRICULUM VITAE